Report No. FRA-RT-73-27

PRELIMINARY DESIGN STUDIES OF MAGNETIC SUSPENSIONS FOR HIGH SPEED GROUND TRANSPORTATION

JOHN R. REITZ
ROBERT H. BORCHERTS
L. C. DAVIS
T. K. HUNT
DENNIS F. WILKIE

MARCH 1973

FINAL REPORT

Prepared for

FEDERAL RAILROAD ADMINISTRATION
Office of Research, Development, and Demonstrations
Washington D. C. 20590

TECHNICAL REPORT STANDARD TITLE PAGE

1. Report No.	2. Government Accession No.	3. Recipient's Catalog No.
FRA-RT-73-27		

4. Title and Subtitle	5. Report Date
Preliminary Design Studies of Magnetic Suspensions for High Speed Ground Transportation	March 1973
	6. Performing Organization Code

7. Author(s)	8. Performing Organization Report No.
John R. Reitz, Robert H. Borcherts, L. C. Davis, T. K. Hunt, Dennis F. Wilkie	

9. Performing Organization Name and Address	10. Work Unit No.
Ford Motor Company Transportation Research and Planning Office 23400 Michigan Avenue Dearborn, Michigan 48124	11. Contract or Grant No. DOT-FR-10026
	13. Type of Report and Period Covered Final Report (Tasks II&III) Feb. 1972-March 1973
12. Sponsoring Agency Name and Address U. S. Department of Transportation Federal Railroad Administration 400 Seventh Street, S.W., Room 5416 Washington, D. C. 20591	14. Sponsoring Agency Code

15. Supplementary Notes

See also "Study of a Magnetically Levitated Vehicle" Stanford Research Institute, February (1973 NTIS Accession # PB 221696)

16. Abstract

This report examines certain critical problem areas relative to magnetic suspension of high-speed vehicles and develops a baseline design for a TMLRV (tracked magnetically levitated research vehicle). Both types of magnetic suspension, the repulsive-force suspension and the attractive-force suspension, are considered. The present study has not turned up any problems serious enough to completely eliminate one of these competing suspensions.

Areas considered in this report include propulsion systems and their compatibility with magnetically-levitated high-speed vehicles, aerodynamic effects, failure modes, studies of ride quality, and criteria for maximum allowable track roughness. In regard to the repulsive-force suspension, experiments have been carried out to measure ac loss in the superconducting magnets and an assessment of the magnetic shielding requirement has been made. Two model electromagnets for the attractive-force suspension, and their feedback control systems, were built and tested during the present study.

17. Key Words	18. Distribution Statement
Tracked levitated vehicles, magnetic levitation, vehicle dynamics, ride quality, superconducting magnets, feedback control systems, suspension, electrical propulsionguideways and structures high speed ground transportation	Document is available to the public through the National Technical Information Service, Springfield, Virginia 22151

19. Security Classif. (of this report)	20. Security Classif. (of this page)	21. No. of Pages	22. Price
Unclassified	Unclassified	299	

Form DOT F 1700.7 (8-69)

SUMMARY

This report and Report PB210-506 cover work performed by the Ford Motor Company under Contract DOT-FR-10026 with the Federal Railway Administration, U.S. Department of Transportation. Whereas PB210-506 addressed the technical feasibility of magnetic suspension of high-speed vehicles, the present report is concerned with certain critical problem areas in the two most promising magnetic suspension schemes.

The present report includes work in the following areas:

Repulsive-Force Suspension

(1) parameter optimization,

(2) studies of ac loss in the cryogenic magnets,

(3) magnet shake tests and experimental studies of damping and control,

(4) control requirements,

(5) assessment of the magnetic shielding requirement,

(6) propulsion systems and their compatibility with the high-clearance suspension,

(7) baseline design of a research vehicle including a full-scale, superconducting magnet design;

Attractive-Force Suspension

(1) design and construction of two model electromagnets and their feedback control systems,

(2) basic control strategy,

(3) magnetic saturation and eddy-current drag at high speeds,

(4) control requirements,

(5) criterion for maximum allowable track roughness,

(6) need for a secondary suspension.

Other aspects considered in the report are aerodynamic effects, system failure modes, and studies of ride quality. The present study has not turned up any problems serious enough to completely eliminate one of the two competing suspension schemes.

PREFACE

This report covers work performed by Ford Motor Company under Contract DOT-FR-10026 with the Office of Research, Development, and Demonstration of the Federal Railroad Administration, U.S. Department of Transportation.

The authors would like to express their appreciation to Dr. John T. Harding of the Office of Research, Development, and Demonstration for his close liaison with the project, for a number of suggestions which improved the study, and for help in tracking down technical information related to the project. Thanks are also due to supporting members of Scientific Research Staff, Ford Motor Company, who contributed to the program; in particular, we would like to acknowledge Mr. John D. Zbrozek who joined the program in June 1972 and who played a major role in the design, construction, and testing of feedback control systems for studies of the attractive-force magnetic suspension.

The results of the present study were augmented by tasks performed by other groups under subcontract. These include a full-scale, superconducting magnet design by Magnetic Corporation of America, a vehicle aerodynamic study by AVco Systems Division, Avco Corporation, and a study of vehicle dynamics and a research vehicle layout by Aeronutronics Division, Philco-Ford Corporation. We would like to express our appreciation to all of the subcontractors for their efforts. And in particular we would like to thank R. L. Pons, R. R. Auelmann and H. W. Schaefgen of Philco-Ford Corporation for their contributions to Chapters 6 and 7.

TABLE OF CONTENTS

		Page
1.	INTRODUCTION	
2.	ELECTRODYNAMIC (REPULSIVE) SUSPENSION	
	2.1. Parametric Study of Vehicle Magnets	
	2.1.1. Parametric Study	11
	2.1.2. Other Magnet Configurations	14
	2.1.3. Quadrupole Arrangement of Lift Magnets	21
	2.2. Characteristics of Guidance Forces	23
	2.3. Effect of Ferromagnetic Backing on the Aluminum Track	28
	2.4. Passive Damping	29
	2.4.1. Experimental Studies of Damping	33
	2.5. Control Requirements	34
	2.6. Superconducting Magnet Design and Construction	40
	2.6.1. Design of Ford Model Magnet	41
	2.6.2. Fatigue Testing of Magnet Struts	49
	2.6.3. Magnet Tests	49
	2.7. AC Loss Studies	61
	2.8. Magnetic Shielding	70
3.	ELECTROMAGNETIC (ATTRACTIVE) SUSPENSION	79
	3.1. Parametric Study	79
	3.2. High-Speed Drag Problem	85
	3.2.1. Rotating Wheel Experiments	89
	3.3. Control Requirements	94
	3.4. Criterion for Maximum Track Roughness	101
	3.5. Analysis and Demonstration of Magnet Control System	103
	3.5.1. Small Magnet Analysis	103
	3.5.2. Design of Control System	113
	3.5.3. Large Magnet Analysis	135
	3.5.4. Experimental Study of Control System	124
4.	PROPULSION	150
	4.1. LIM Studies	151
	4.2. Integration of LIM with High Clearance Suspension	157

		Page
4.3.	Rotating Superconducting Motors	166
4.3.1.	Superconducting Paddle Wheel	166
4.3.2.	Superconducting Helix	174
4.3.3.	End Effects in Linear Induction Propulsion Systems	180
4.4.	LSM Studies	181
4.5.	Propulsion by a Turbojet Engine	194
5.	VEHICLE AERODYNAMICS	202
5.1.	Aerodynamic Drag	202
5.1.1.	Nose Drag	202
5.1.2.	Base Drag	203
5.1.3.	Skin Friction Drag	203
5.1.4.	Protuberance Drag	205
5.1.5.	Total Drag Coefficient	205
5.2.	Aerodynamic Effects on Yaw and Transverse Oscillation	206
5.2.1.	Side Winds	211
5.3.	Use of Flaps for Damping	211
5.3.1.	Lift and Drag Coefficients	213
5.3.2.	Required Flap Rate	214
6.	VEHICLE DYNAMICS AND RIDE QUALITY	217
6.1.	Dynamics of Various Guideways	217
6.2.	Ride Index Criterion	223
6.3.	Secondary Suspension	234
6.4.	Dynamics of Vehicle Including Pitch	238
6.5.	System Failure Analysis	247
7.	BASELINE DESIGN OF RESEARCH VEHICLE AND GUIDEWAY	253
7.1.	Research Vehicle Specification	253
7.1.1.	Primary Suspension	256
7.1.2.	Alternate Suspension	256
7.1.3.	Propulsion and Power Conversion	258
7.1.4.	Accommodations	258
7.1.5.	Braking	258
7.1.6.	Life Support	259
7.2.	Undercarriage Design	259

Page

7.3. Guideway 260
7.3.1. Aluminum Specification 261
7.3.2. Inductance Studies of Guideway Joints 263
7.3.3. Radius of Curves 265
7.3.4. Switching 266
7.4. Cryogenic Magnet Design and Refrigeration Requirement 267
8. CONCLUSIONS 273
9. RECOMMENDATIONS 279
10. REFERENCES 281
APPENDICES 287

LIST OF FIGURES

		Page
Fig. 2.1	Lift force F_L and F_L/F_D on a coil above an aluminum plate	6
Fig. 2.2	Drag force as a function of speed	8
Fig. 2.3	Lift and transverse force on a coil	10
Fig. 2.4	Lift and guidance force near a corner	12
Fig. 2.5	Effect of track thickness on F_L/F_D	13
Fig. 2.6	F_L/F_D as a function of magnet length	15
Fig. 2.7	Ratio of lift at 50 mi/h to lift at 300 mi/h	16
Fig. 2.8	Two levitation coils separated longitudinally	17
Fig. 2.9	F_L and F_L/F_D for two coils separated longitudinally	18
Fig. 2.10	A levitation coil with rounded ends	19
Fig. 2.11	Speed dependence of F_L and F_G for a 2 x 4 inch coil	24
Fig. 2.12	Inductance of a coil near a L-shaped channel	26
Fig. 2.13	Inductance of lift-guidance coils near a channel	27
Fig. 2.14	Drag force on a coil as a function of the permeability of the backing material	30
Fig. 2.15	Levitation and control coils and their images	35
Fig. 2.16	Effectiveness ratio for a control coil	37
Fig. 2.17	5 ft diameter rotating wheel facility	42
Fig. 2.18	Cryostat for Ford experimental magnet	43
Fig. 2.19	Cross-section of the Ford magnet	46
Fig. 2.20	Superconducting coil and coil form	47
Fig. 2.21	Epoxy fiberglas strut for experimental magnet	48
Fig. 2.22	Epoxy fiberglas columns	50
Fig. 2.23	Magnet mounted above rotating wheel	51
Fig. 2.24	Control coil for the experimental magnet	54

		Page
Fig. 2.25	AC loss in the Ford magnet versus frequency	55
Fig. 2.26	AC loss versus control current amplitude	56
Fig. 2.27	Dynamic response of magnet to current in control coil	58
Fig. 2.28	Vertical response of magnet to a step displacement	59
Fig. 2.29	Diagram of apparatus for measuring ac loss	64
Fig. 2.30	Energy loss per cycle vs driving field level	67
Fig. 2.31	AC loss in ventilated coils	68
Fig. 2.32	Effect of shielding with various thicknesses of iron	75
Fig. 2.33	Field above levitation coil vs shield thickness	76
Fig. 2.34	Shielding by means of a superconducting coil	77
Fig. 3.1	Magnet and track in the attractive-force suspension	81
Fig. 3.2	Simplified model of the attractive-force suspension	82
Fig. 3.3	Magnetic circuit of the attractive-force suspension	86
Fig. 3.4	Experimental results for lift and drag	90
Fig. 3.5	Variation of magnetic field in air gap	93
Fig. 3.6	Dynamic model of a vehicle with an attractive-force suspension	95
Fig. 3.7	Guideway force on magnet	98
Fig. 3.8	Schematic design of small electromagnet	105
Fig. 3.9	Method for restricting motion of small magnet	106
Fig. 3.10	Air gap flux density of small electromagnet	107
Fig. 3.11	Same as preceding figure	108
Fig. 3.12	Inductance vs air gap for small magnet	110
Fig. 3.13	Levitation current vs air gap	112
Fig. 3.14	Schematic diagram of feedback control system	115
Fig. 3.15	Schematic of large electromagnet	118
Fig. 3.16	Large electromagnet and experimental setup	119

		Page
Fig. 3.17	Flux density vs current (large magnet)	120
Fig. 3.18	Inductance vs gap	122
Fig. 3.19	Levitation current vs gap	123
Fig. 3.20	Magnet and Track coordinates	126
Fig. 3.21	Block diagram of linearized magnet equations	126
Fig 3.22	Schematic of magnet control system	128
Fig. 3.23	Block diagram - magnet with feedback control	131
Fig. 3.24	Frequency response: type I control	133
Fig. 3.25	Frequency response: type II control	136
Fig. 3.26	Transfer function: type III control	139
Fig. 3.27	Control limit versus frequency	142
Fig. 3.28	Vertical acceleration psd using various controls	149
Fig. 4.1	Schematic model of LIM	152
Fig. 4.2	Thrust vs slip for a series connected LIM	155
Fig. 4.3	Efficiency vs slip for same LIM	156
Fig 4.4	Thrust vs slip for a parallel connected LIM	158
Fig. 4.5	Efficiency vs slip for same LIM	159
Fig 4.6	Active suspension of LIM	161
Fig. 4.7	Lateral acceleration psd for various control cutoff frequencies	164
Fig. 4.8	Superconducting paddle wheel in high speed vehicle	167
Fig. 4.9	Two dimensional model of the paddle wheel	169
Fig. 4.10	Propulsive force as a function of relative speed	171
Fig. 4.11	Lift force and efficiency vs relative speed	173
Fig. 4.12	Superconducting screw in high speed vehicle	175
Fig. 4.13	Schematic diagram of section of double helix	176

		Page
Fig. 4.14	Thrust and transverse force vs relative speed	179
Fig. 4.15	Thrust vs slip	182
Fig. 4.16	Efficiency vs slip	183
Fig 4.17	Thrust versus slip for larger v_{ϕ}/w	184
Fig. 4.18	Efficiency vs slip. Same parameters as Fig. 4.17	185
Fig. 4.19	Schematic diagram of LSM	187
Fig. 4.20	Effective potential energy V(x') vs x'	192
Fig. 4.21	Configuration of lift and propulsion magnets for LSM	195
Fig. 4.22	LSM peak thrust vs magnet length	196
Fig. 4.23	Efficiency and track current vs coil length	197
Fig. 4.24	Resistance/km of track	198
Fig. 4.25	Volume of conductor/km of track	199
Fig. 5.1	Yaw and transverse oscillation in guideway	207
Fig. 5.2	Use of flaps for damping vertical motion	212
Fig 6.1	Levitation-guidance magnets in various guideways	218
Fig. 6.2	Vehicle above inverted vee guideway	219
Fig. 6.3	Vehicle above vee guideway	219
Fig. 6.4	Vehicle above canted inverted T guideway	222
Fig. 6.5	Urban TACV ride quality specification	225
Fig. 6.6	Single frequency ride quality specification	228
Fig. 6.7	Vertical acceleration psd for vehicle with passive damping	230
Fig. 6.8	Vertical acceleration psd for vehicle with control	231
Fig. 6.9	Several different ride quality standards	323
Fig. 6.10	Vehicle with secondary suspension	236
Fig. 6.11	Vertical acceleration psd for vehicle with secondary suspension	237

Page

Fig. 6.12 Vehicle undergoing pitch oscillations 240

Fig. 6.13 Vertical acceleration psd for vehicle with passive damping 243

Fig. 6.14 Vertical acceleration psd for front end of vehicle (feedback control) 245

Fig. 6.15 Same as 6.14. Center of gravity and rear eng 246

Fig. 7.1 Layout of TML research vehicle system 254

Fig. 7.2 "U" shaped guideway option 257

Fig. 7.3 Inductance measurement of coil in guideway with a butt joint 264

Fig. 7.4 Basic configuration of MCA magnet and dewar 268

LIST OF SYMBOLS

A	statistical roughness parameter [Eq. (6.5)]; also used for vehicle cross-sectional area (Chapter 5); aspect ratio (Section 5.3).
A_g	cross-sectional area of air gap
$A_{\alpha\beta}$	matrix coefficient
a,b,c	coil parameters (see Fig. 2.8)
$\underline{B}$	magnetic flux density
b,c	flap parameters (Chapter 5; see Fig. 5.2)
C_D	drag coefficient [Eq. (5.1)]
C_n	yawing moment coefficient (Chap. 5)
C_y	side force coefficient (Chap. 5)
DI	discomfort index
D_ℓ	damping characteristic
$\underline{E}$	electric field
F_L, F_D	lift and drag forces
F_T, F_G	transverse and guidance forces
F_I	image force
F_{AD}	aerodynamic drag force
f	frequency
$\underline{f}$	force on source due to image
g	acceleration due to gravity
H_n	Fourier component of track roughness
h	height of levitation magnet (or height of propulsion magnet in LSM) above the track; gap between magnet and track in attractive system
h′	lateral distance between coil and vertical guidance panel; also used for height of damping plate above track
I	current
$\underline{i}$	current density
k	wave number ($2\pi/\lambda$)
k_x, k_y, k_z	wave vector components
k_ℓ	spring constant
L	self inductance; also used for length of magnet (or motor) in direction of vehicle motion

List of Symbols (Continued)

ℓ	length
M	mutual inductance; also used for sprung mass or vehicle mass
M_z	torque component
N	number of turns
P	power
P_{zz}, P_{nn}	power spectral density function
$P_{\ddot{x}\ddot{x}}$	acceleration psd function
p	pole face width of magnet; also used for number of wire bundles in motor
q	wave number ($2\pi/\lambda$); also used for dynamic pressure (Chap. 5)
R	resistance; also used for reluctance in Sects. 3.2 and 3.5
Re_L	flow Reynold's number
s	slip (in a linear motor)
T	thickness of track or reaction plate
T_x, T_y, T_z	components of torque
V	voltage; also used for volume
v, v_o	vehicle speed
v	also used for relative speed [see Eq. (4.25)]
v_ϕ	phase velocity
v(t)	time dependent voltage
W	field energy; also used for vehicle width (Chap. 5)
w	material parameter with dimensions of velocity [Eq. (2.2)]
x	distance from origin in direction of vehicle motion
y	transverse distance
z	vertical height from some reference level
z_G	height of guideway above a reference level
α	defined by $\alpha = (k^2+ik_x\mu\sigma v)^{1/2}$ (Chapters 2 and 3); also used for roll angle (Chapt. 6)
β	α/k; also used for damping coefficient; also $\beta = v_\phi/w$ (Chap. 4)
Γ	defined by Eq. (3.6)
γ	effectiveness ratio [Eq. (2.16)]; also used for angular frequency ($2\pi f$); also a damping coefficient
δ	electromagnetic skin depth; also used for damping ratio $(2\pi f\tau)^{-1}$; used in Chapter 5 for boundary layer thickness

List of Symbols (Continued)

$\langle \delta^2 \rangle$	mean square mid-chord offset (Chap. 6)
η	random track roughness
θ	half angle inverted vee guideway (Chap. 6)
κ	relative permeability
λ	wavelength
μ	permeability
ξ	ratio of lateral displacement to vehicle width (Chap. 5)
ρ	resistivity; used for density of air in Chapter 5
σ	electrical conductivity
τ	damping time
Φ	magnetic flux
$\Phi(\Omega)$	power spectral density of a surface
ψ	yaw angle (Chap. 5); half angle of vee guideway (Chap. 6)
Ω	wave number ($2\pi/\lambda$)
ω	angular frequency ($2\pi f$)

1. INTRODUCTION

This report covers work performed by the Ford Motor Company under Contract DOT-FR-10026 (Task II) with the Office of Research, Development, and Demonstration of the Federal Railroad Administration, U.S. Department of Transportation. It represents a continuation of earlier work under the same contract (Task I) which has been reported in an earlier report.[1] Task I effort established the feasibility of magnetic levitation as a suspension system for high-speed guided vehicles, but it also indicated a need for further studies of certain critical aspects of the levitation problem. These aspects have been addressed in the present study.

At the conclusion of Task I effort, it was apparent that two types of magnetic suspensions had merit. These are the high-clearance electrodynamic (repulsive force) suspension which uses superconducting magnets in the vehicle, and the low-clearance electromagnetic (attractive force) suspension which uses ordinary ac electromagnets. Of the two suspensions, it appeared to us at the time, that the first one was better able to provide all the desired features of a 300 mi/h transportation system; namely, good ride quality, moderate guideway tolerance, basic stability, and moderate drag forces. The advantages of this suspension were somewhat offset by a substantial magnetic shielding problem and uncertainty as to the severity of the ac losses in the superconductors resulting from non-steady fields and vehicle oscillation.

Concurrent with our Task I program, a similar study was conducted for DOT by Stanford Research Institute (SRI). Their conclusions relative to the feasibility of magnetic suspension for high-speed guided transportation are similar to ours, and are summarized in reference 2.

In a follow-on program, SRI designed and built a small vehicle supported

and guided by four superconducting magnets, and has recently towed this vehicle at speeds up to 30 mi/hr in an aluminum channel.[3] Larger scale experiments have already been carried out in Japan and Germany. As part of its centenary celebration, Japan National Railways (JNR) carried out a public demonstration run on October 14, 1972, of a 4-passenger magnetically-suspended (but guided by physical contact) vehicle at its Railway Technology Research Institute near Tokyo. The experimental vehicle is 7 m long, 2 m wide, and 1.7 m high, uses superconducting magnets, and is powered by a linear induction motor. It will be test run over a 400 m track at speeds up to 60 km/hr. This is the first test of a large vehicle using the electrodynamic suspension. (JNR uses a discrete-loop track instead of the continuous sheet track proposed by both Ford Motor Company and SRI.) Research vehicles using an electromagnetic suspension, large enough to carry passengers, were demonstrated in Germany by Messerschmitt-Bölkow-Blohm and Krauss-Maffei during 1971; one of these has been run at speeds up to 163 km/hr.

The goals of the present program (Tasks II and III) are twofold: to examine certain aspects of a magnetic suspension system which can affect its operation in a critical way, and to provide baseline specifications for a TMLRV (tracked magnetically levitated research vehicle). The situation is complicated by the fact that the critical problem areas for the two competing magnetic suspensions are different. For the attractive-force suspension the unresolved problem areas are: control system design and basic control strategy, high-speed performance, maximum allowable track roughness, and the possible need for a secondary suspension. For the repulsive-force suspension the problem areas are: superconducting magnet design, ac loss in the superconducting magnets, magnetic shielding, and the choice of a compatible propulsion system.

The present study has not turned up any problems serious enough to completely eliminate one of the competing magnetic suspensions. Regarding the electromagnetic suspension, we have developed a criterion for maximum track roughness; and we have shown that high-speed performance will be degraded by skin-depth-induced saturation of the magnetic field in the track. These considerations are important but can probably be accommodated by the appropriate system design. We have also built and tested two model electromagnets and their feedback control systems, and have studied various control strategies. The static and dynamic control power requirements have been determined for this suspension. Regarding the electrodynamic suspension, experiments performed during the present study show that ac losses in the superconductor are smaller than were originally thought, and these losses can be further minimized by appropriate magnet design. Thus ac loss is not a major problem. Concerning magnetic shielding of the superconducting magnets, it appears that the magnetic field in the passenger compartment can be attenuated to the 200 gauss level without an excessive weight penalty. In the absence of adequate statistical data on possible biological effects of magnetic fields it is prudent to keep fields near the natural value of one gauss. Should this prove necessary the weight penalty of the shields will be severe not only for magnetically levitated vehicles but also for vehicles using electromagnetic propulsion.

The present report discusses parameter optimization and the critical problem areas which can affect system performance for both types of suspension. Experimental studies involving vibration and control have been carried out for both cases. However, baseline specification of the guideway and research vehicle, including a full-scale magnet design, has been carried out only for the electrodynamic (repulsive type) suspension. Other aspects considered in this report are propulsion systems and their compatibility with magnetically-levitated vehicles, aerodynamic effects, failure modes, and studies of ride quality.

2. ELECTRODYNAMIC (REPULSIVE) SUSPENSION

In this suspension, current-carrying coils (or magnets), moving with the vehicle, induce eddy currents in a conducting roadbed or guideway, and these eddy currents interact with the coil such as to repel and support it. There is no lift at zero speed so the vehicle must be supported in some other way at low speeds (presumably by wheels). As the vehicle speed increases, the lift force F_L (for a magnet at constant height) first increases rapidly, then levels off, approaching the image force F_I at high speeds. F_I is the force between the coil and its image in the guideway. In addition to F_L, there is also a magnetic drag force F_D and possibly also a transverse force F_T. If the transverse force is such as to provide guidance, we call it a guidance force F_G.

Report No. PB210-506[1] discussed analytic methods for calculating F_L, F_D, and F_T for various rectangular coils moving over flat guideways or over corner-channel guideways. It also discussed the experiments which were done to establish the validity of the analytic methods. A parametric study of the magnetic forces established that to reduce drag forces on a revenue vehicle to an acceptable level at 300 mi/h the aluminum guideway should be approximately 2.5 cm (one inch) thick and the vehicle magnets should be at least 2 m long. A 1 m x 2 m coil was a frequently used example in ref. 1. However, a narrow magnet is desirable in order to reduce the track width and thereby lower the aluminum requirement for the system. Furthermore, a longer magnet appears desirable in order to obtain a somewhat more desirable lift/drag ratio. We are, therefore, proposing that each of the magnets for a revenue vehicle be a 1/2 m x 3 m coil. For a research vehicle, shorter magnets (with a somewhat smaller F_L/F_D) can be tolerated; we propose: 1/2 m x 2 m coils. For ease in fabrication and structural

stability, coils with rounded ends are preferred to purely rectangular coils; the effect of this geometric modification on F_L/F_D is explored in 2.1.2.

2.1. Parametric Study of Vehicle Magnets

We have made calculations of F_L and F_D vs. velocity v for a 1/2 x 3 m coil at 0.3 m elevation over a 25 mm aluminum plate. The plate is assumed to be wide enough that edge effects are negligible. In Figure 2.1, we show F_L amd F_L/F_D. Compared to the 1 x 2 m coil at the same height and with the same plate thickness, F_L approaches the image force F_I more slowly. Also, the lift-to-drag ratio at 300 mi/h is higher (58 compared to 52), but still significantly below the thin-plate value of 76. It is found that 8 magnets (1/2 x 3 m), each carrying 2.6×10^5 A, will support 100,000 lbs. at 300 mi/h with a height of 0.3 m.

In Figure 2.2, the drag force at constant height (h = 0.3 m) is shown as a function of velocity. The drag peak is substantially lower ($\sim 0.1\ F_I$ compared to $\sim 0.2\ F_I$ the thin-plate limit) than the 1 x 2 m case, although F_L/F_D is essentially the same at low speeds. Therefore, the power requirements to overcome drag are the same in the two cases at low speeds as long as the vehicle is supported by the magnets. But, in regions of the track where both wheels are used and the guideway is lined with aluminum, the drag should be smaller.

To determine the effects of the finite width of the track, the lift force F_L and the transverse force F_T were calculated for a 1/2 x 3 m magnet at the edge of a semi-infinite plate. Only the high-speed limit was considered. From Figure 2.3, we see that at $h' = h$, $F_T \tilde{=} 5\%$ of F_L and F_L is approximately F_I, the image force far from the edge. h' is the horizontal distance from the edge of the magnet to the edge of the plate and h is the height. F_T tends to push the magnet away from the plate.

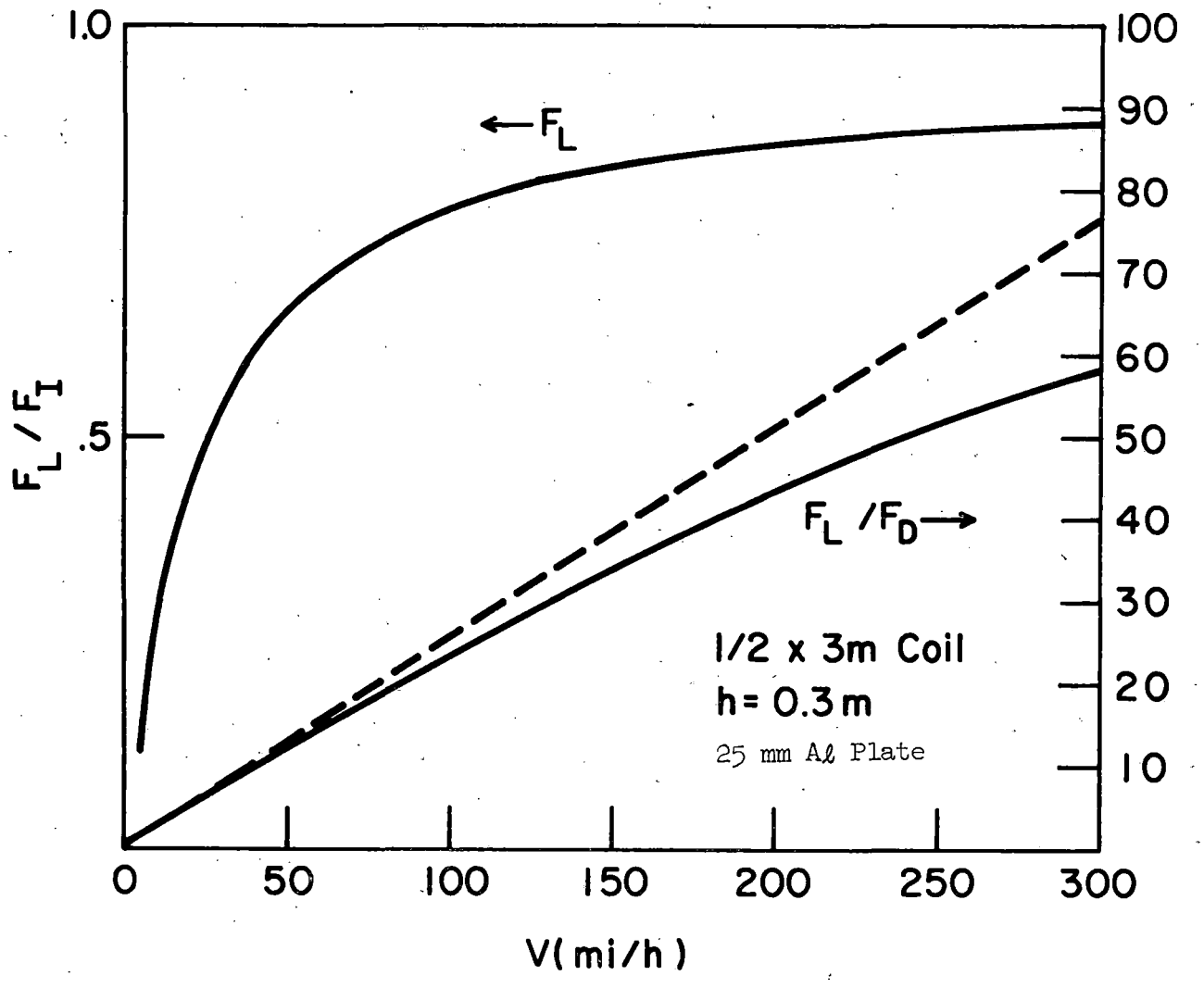

Fig. 2.1. Lift force F_L and F_L/F_D (lift-to-drag ratio) on a coil above an aluminum plate as a function of speed. F_I is the image force.

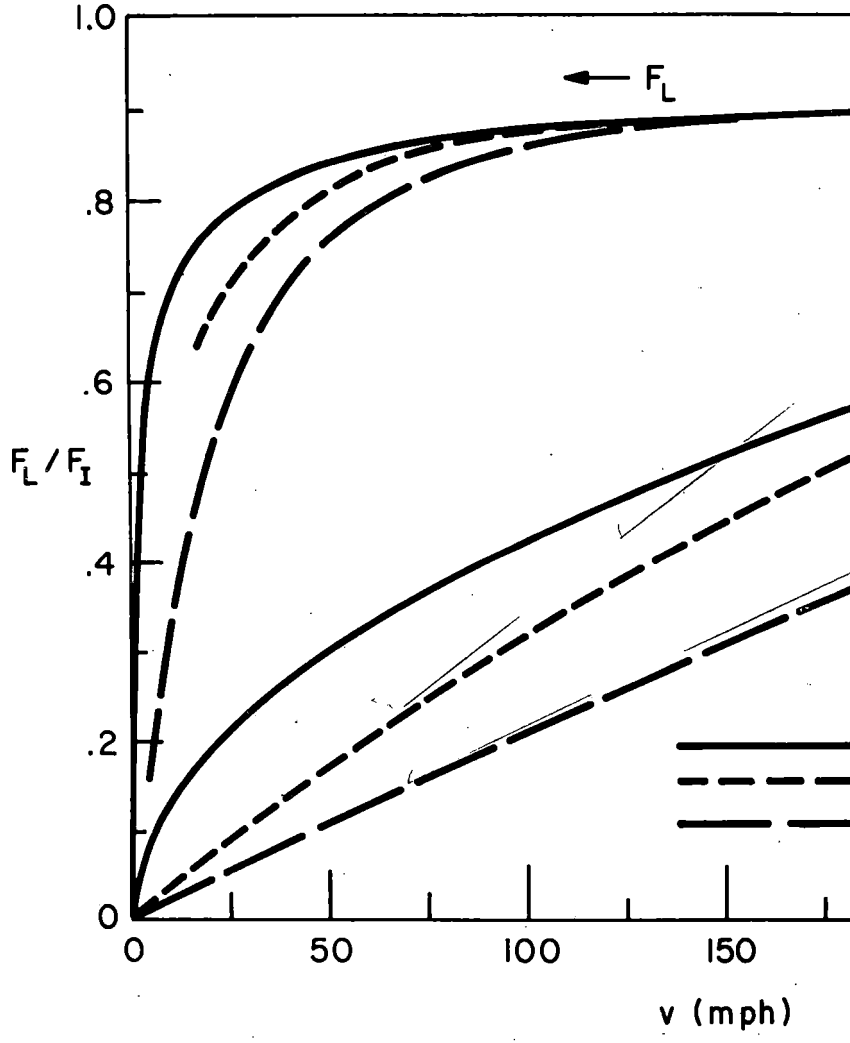

Fig. 2.1.a. Same data as Fig. 2.1

74.6

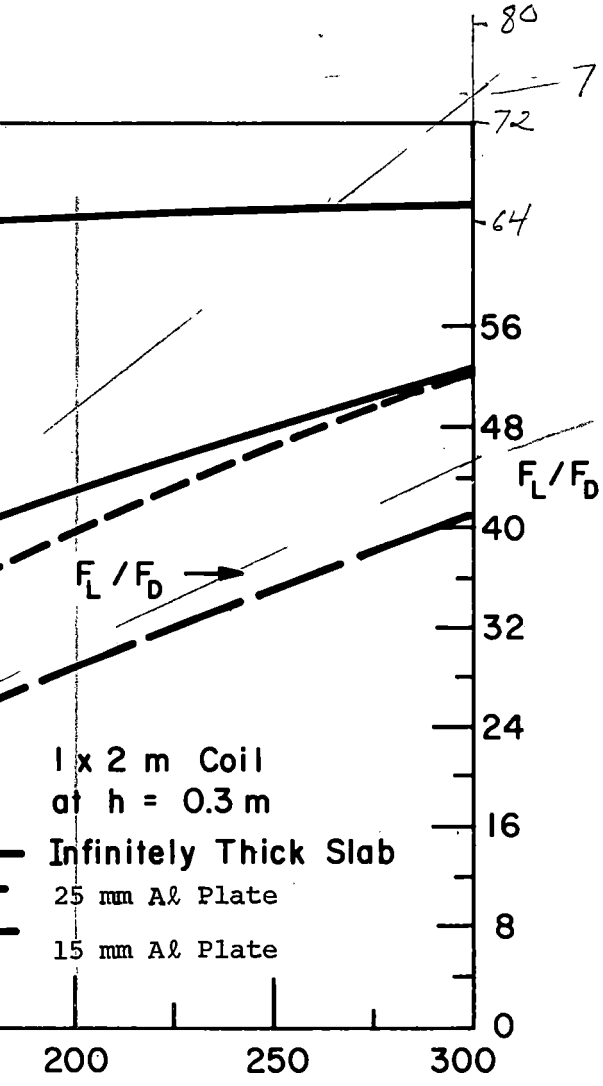

, but for a 1 x 2 m coil.

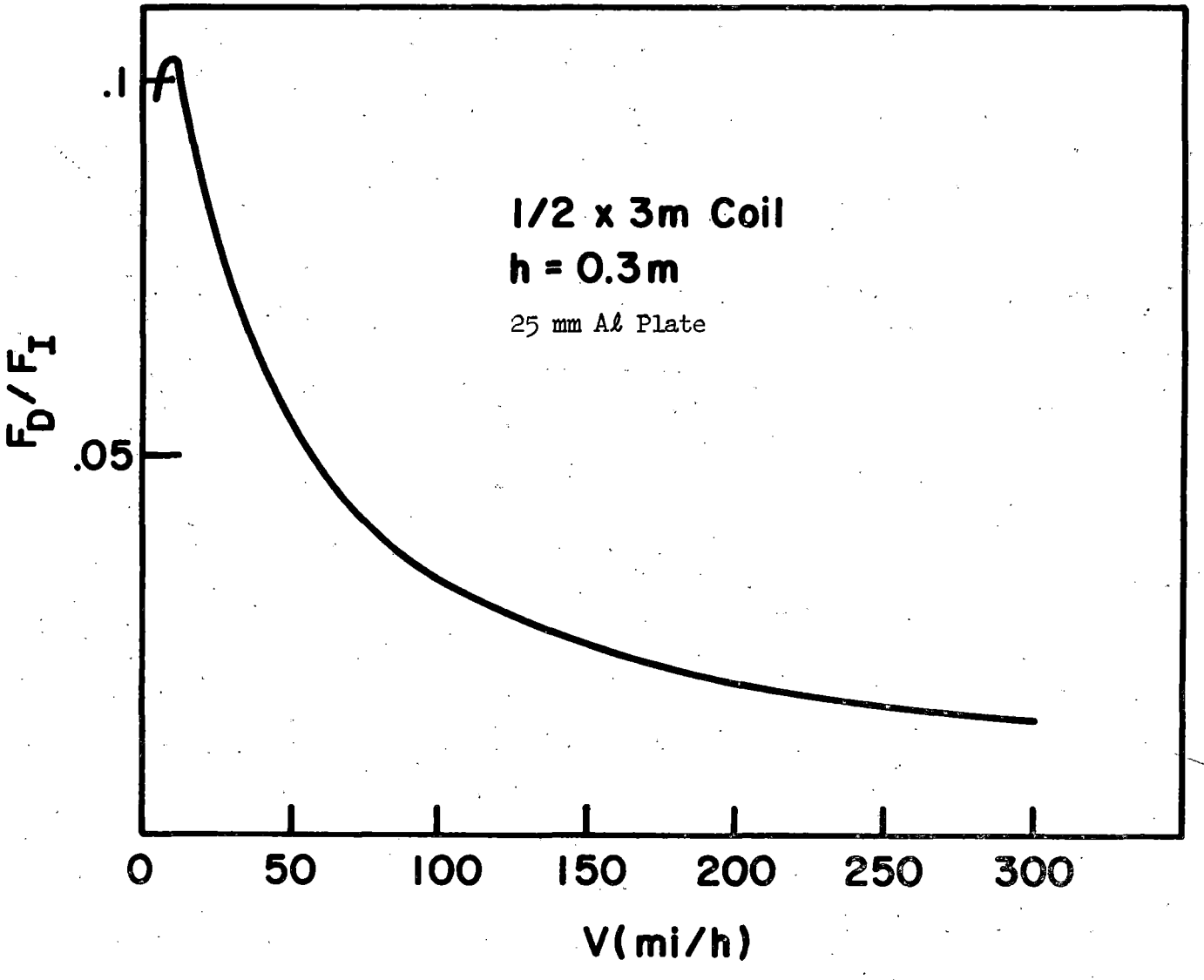

Fig. 2.2. Drag force F_D as a function of speed.

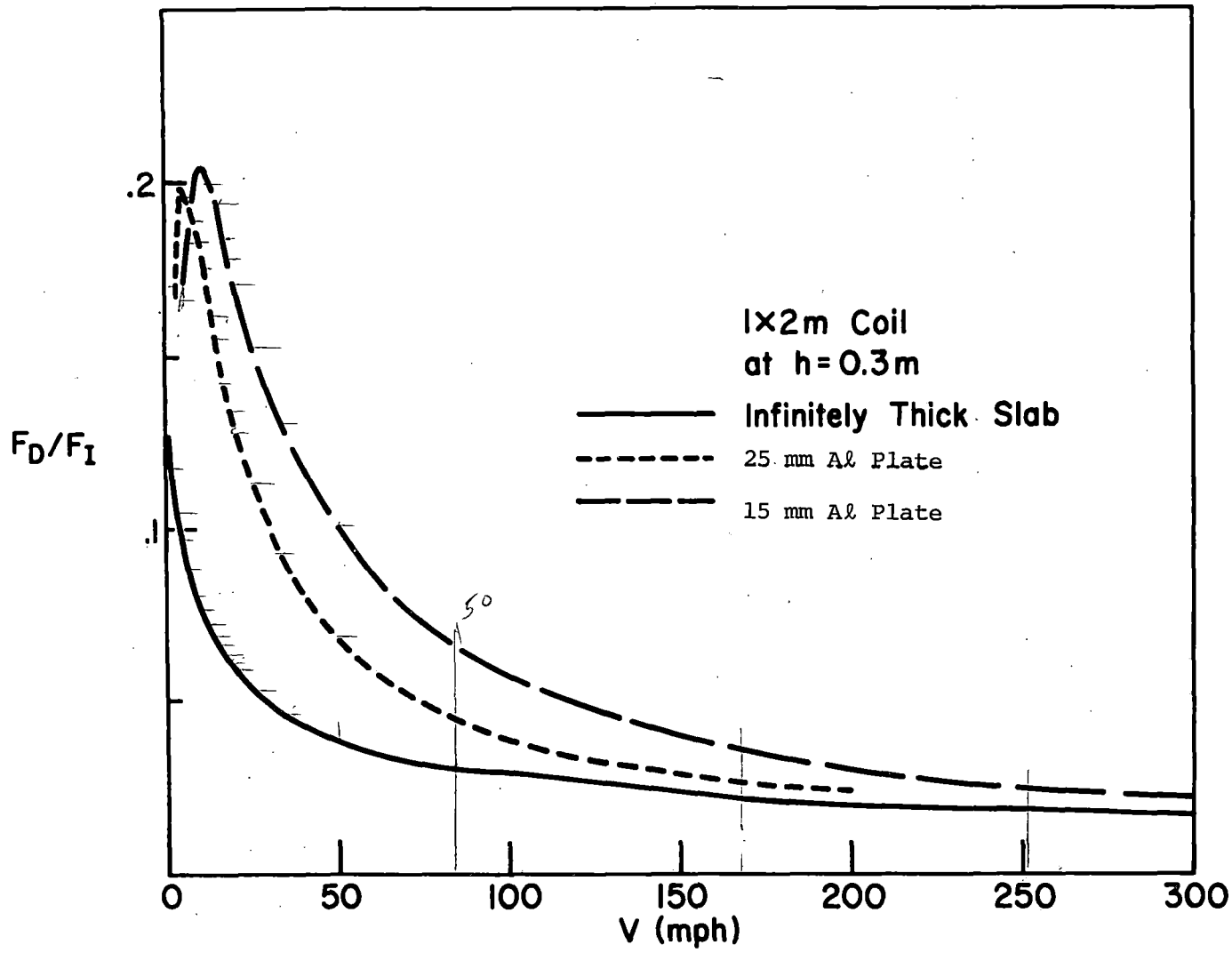

Fig. 2.2.a. Same data as Fig. 2.2, but for a 1 x 2 m coil.

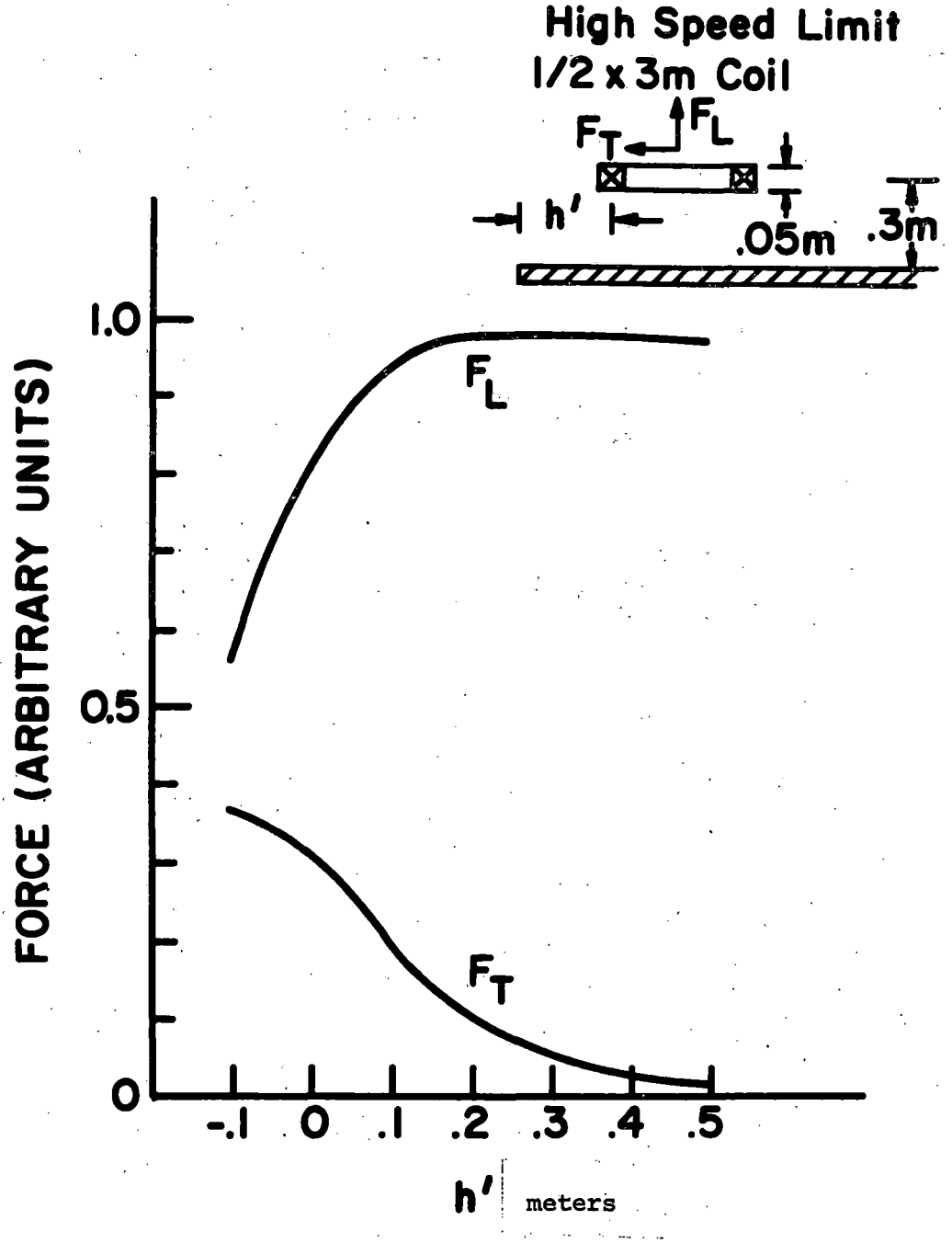

Fig. 2.3. Lift and transverse force on a coil near the edge of a conducting plate.

For smaller h′, F_T increases and F_L drops. Since we have found experimentally and theoretically[54] that

$$F_D = \frac{w}{v} (F_L + F_T) \tag{2.1}$$

$$w = 2/\mu_o \sigma T \tag{2.2}$$

we expect the drag force to be given approximately by Equation 2.1 for the geometry of Figure 2.3. Hence, we require the track width to exceed the magnet width by 2 h in order that the degradation of F_L/F_D is less than 10% (5% from each edge). It appears that better use of aluminum would be made if the track were shaped as a right-angle corner. Then the edge effects would give guidance and would be useful.

To complete the essential information, we have calculated the forces on the magnet near a right-angle corner in the high-speed limit. The lift force F_L and the guidance force F_G are shown as functions of the separation of the magnet from the vertical panel, h′, in Figure 2.4. Also shown is $F_L + F_G$ since the drag force $F_D = \frac{w}{v} (F_L + F_G)$. At about h′ = 0.2 m, $F_G = F_L$ so that considerable guidance force can be obtained from a guideway utilizing such a configuration.

2.1.1. Parametric Study

To justify that the 1/2 x 3 m shape over a 25 mm Al track is reasonable, we present the results of a parametric study. First, we show in Figure 2.5 the effect of track thickness T on F_L/F_D at 300 mi/h. A linear increase of F_L/F_D with T (thin-plate behavior) occurs up to about 1.5 cm but above that the curve begins to flatten out as the skin depth becomes smaller than the plate thickness. Little is gained by going to thicknesses greater than 1 inch = 2.54 cm. For longer magnets, the curves retain the linear behavior to slightly higher T.

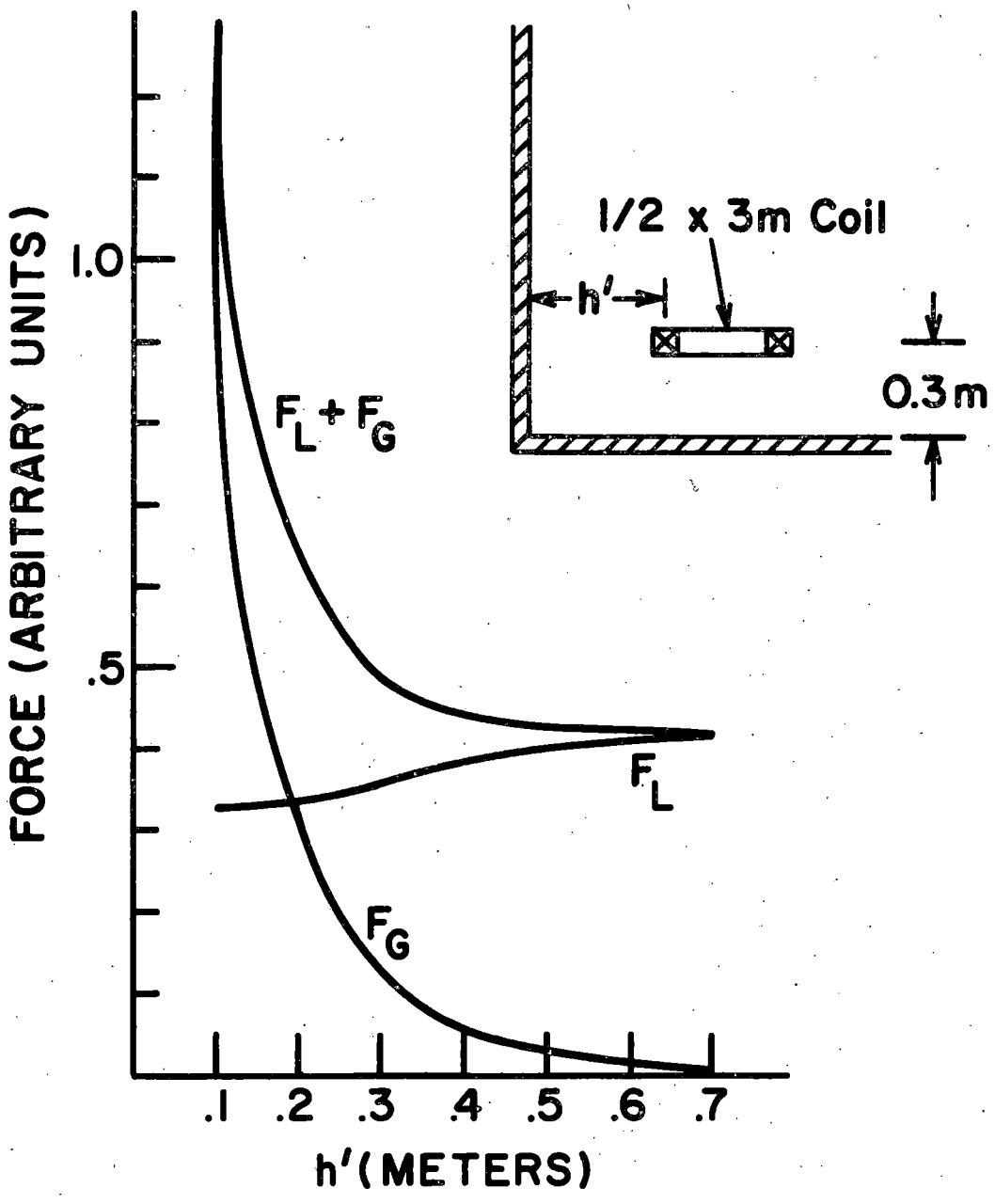

Fig. 2.4. Lift and guidance force on a coil near a conductor shaped as a right-angle corner.

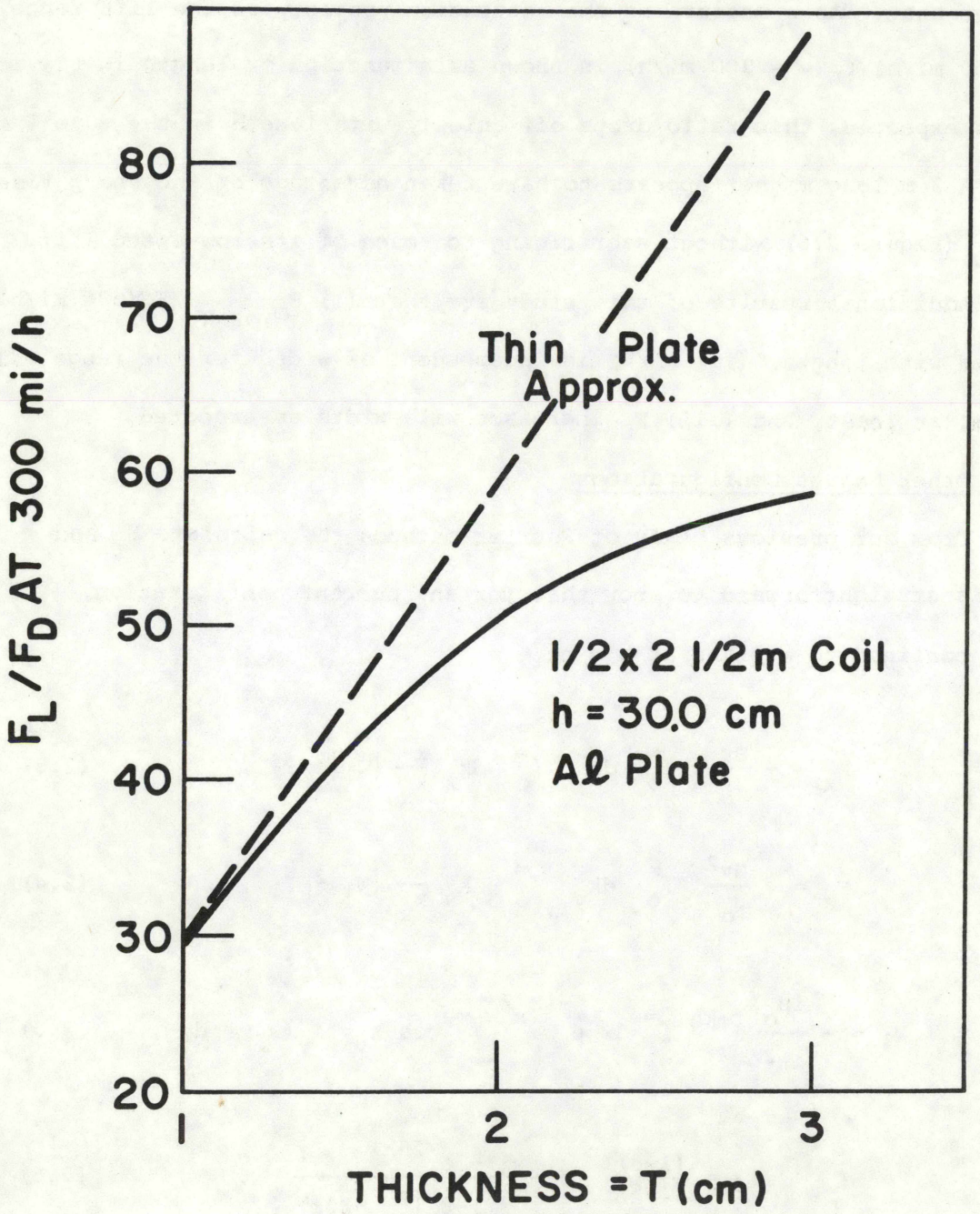

Fig. 2.5. Effect of track thickness T on F_L/F_D.
(The thin plate approximation applies when the skin depth is greater than the plate thickness; in this approximation: $F_L/F_D = \mu_o \sigma v T/2$.)

In Figure 2.6 for a fixed width (1/2 m), F_L/F_D at 300 mi/h is shown as a function of the length of the magnet, 2 b. There is a rapid increase of F_L/F_D with length in the range 2 to 4 m, but the curve tends to flatten out above that. As a measure of the saturation property of the lift force, $F_L(v = 50 \text{ mi/h})/F_L(v = 300 \text{ mi/h})$ is shown as a function of length in Figure 2.7. As expected, this ratio drops off quickly with length in the 2 to 4 m range. A 3 m long magnet appears to have taken advantage of the sharp rise in F_L/F_D (Figure 2.6) without sacrificing too much of its low-speed lift.

Additional results of this study are that (i) $F_{D,peak}/F_L(300 \text{ mi/h})$ decreases with length, (ii) F_L/F_D is independent of width for the range 0.1 to 0.6 m, at least, and (iii) F_L increases with width as expected.

2.1.2. Other Magnet Configurations

From our previous study of Fourier methods[4] to calculate F_L and F_D, it is straightforward to show that for any current configuration, $\underline{i}(x,y)$, confined to a plane at $z = h$

$$F_x = -\frac{8\pi^2}{\mu_o} \int_o^\infty dk_y \int_o^\infty dk_x \frac{k}{k_x} |W_1|^2 \Gamma_2 , \qquad (2.3)$$

$$F_z = -\frac{8\pi^2}{\mu_o} \int_o^\infty dk_y \int_o^\infty dk_x \frac{k^2}{k_x^2} |W_1|^2 \Gamma_1 , \qquad (2.4)$$

where

$$W_1 = -\frac{i\mu_o}{4\pi^2} e^{-kh} \int_{-\infty}^{\infty} dx\, e^{-ik_x x} \int_{-\infty}^{\infty} \cos k_y y\, i_y(x,y)\, dy , \qquad (2.5)$$

and

$$\Gamma_1 + i\Gamma_2 = \frac{(1-\beta)}{(1+\beta)} \frac{1 - e^{-2\beta kT}}{1 - \left(\frac{1-\beta}{1+\beta}\right)^2 e^{-2\beta kT}} . \qquad (2.6)$$

The remaining quantities are defined in Reference 4.

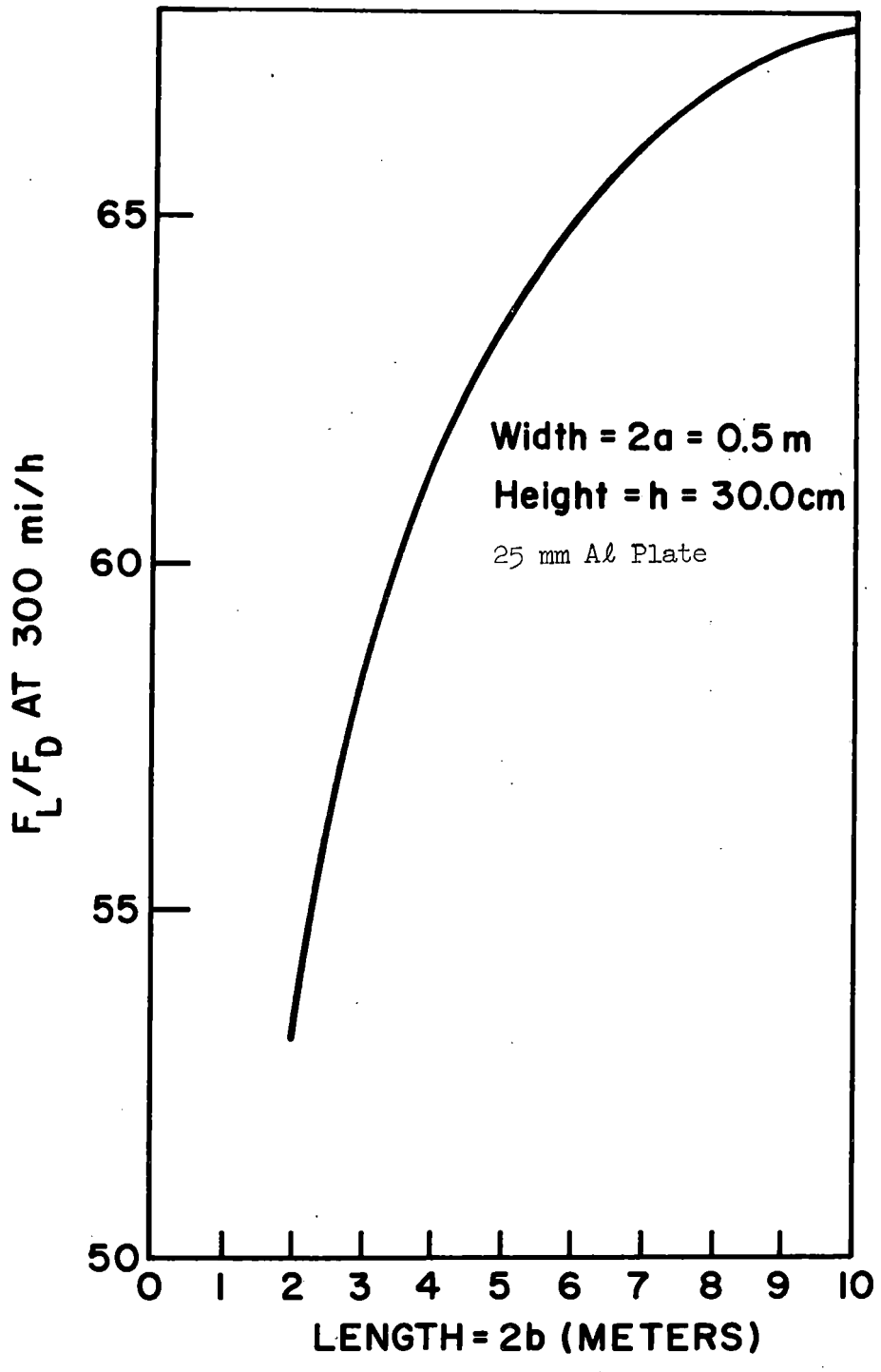

Fig. 2.6. F_L/F_D as a function of magnet length.

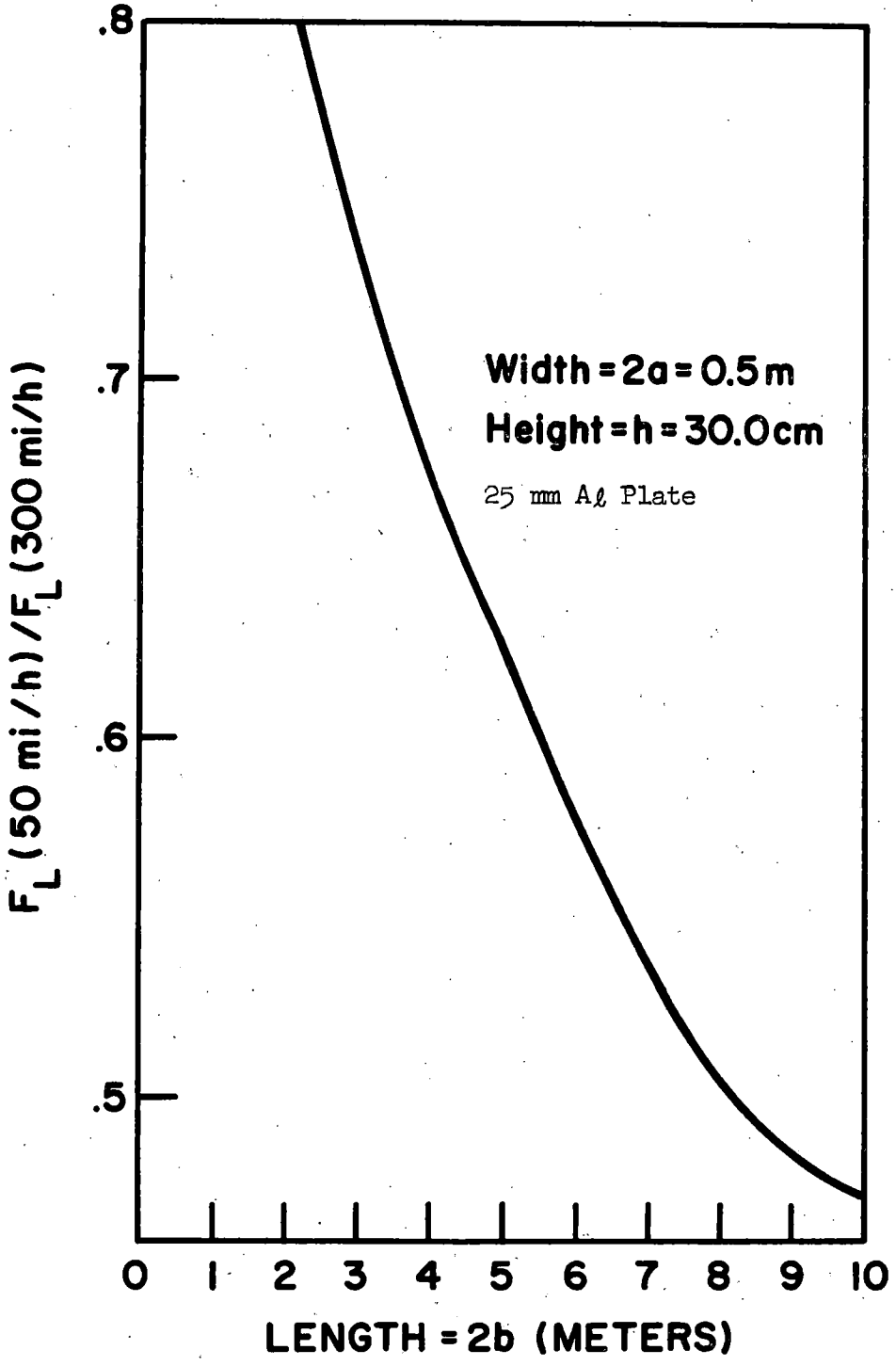

Fig. 2.7. Ratio of lift at 50 mi/h to lift at 300 mi/h as a function of magnet length.

For two rectangular magnets 2a x 2b separated longitudinally by 2c (see Figure 2.8),

$$W_1 = -\frac{\mu_o}{\pi^2} e^{-kh} \frac{\sin k_y a}{k_y} \sin k_x b \, [(I_1+I_2) \cos k_x(c+b) + i(I_2-I_1) \sin k_x(c+b)] \, . \quad (2.7)$$

For a north pole - north pole arrangement (N-N), $I_2 = I_1$ and for a north pole - south pole arrangement (N-S), $I_1 = -I_2$. A calculation of F_L and F_L/F_D as a function of velocity v is shown in Figure 2.9 comparing N-N, N-S, and two widely separated coils (for which the relative polarity is unimportant). We note that N-S has the highest lift whereas N-N has the highest F_L/F_D as might be expected. For $c > h = 0.3$ m, the difference in F_L/F_D is not large.

Two coils separated longitudinally by a small amount look very much like a single coil of double length provided they carry the same currents I circulating in the same sense. This observation allows a certain flexibility in design of the magnet system. We have seen that long magnets are desirable in order to obtain a high F_L/F_D ratio. But the force transmittal struts on long magnets are subjected to substantial longitudinal shearing forces due to thermal contraction of the magnet system under cooling (see Section 7.2); the use of two shorter magnets in tandem reduce the magnitude of these shearing forces. Since some redundancy in the magnet support system is required anyway, to ensure continued support and guidance following loss of cryogenic temperature in one of the magnets, this arrangement does not complicate the magnet support system.

The lift and drag forces, and F_L/F_D, are given in Table 2.1 for two 0.5 x 1.5 m coil separated longitudinally by various distances 2c. Note that 2c = 0 corresponds to a single 0.5 x 3 m coil. It is evident that

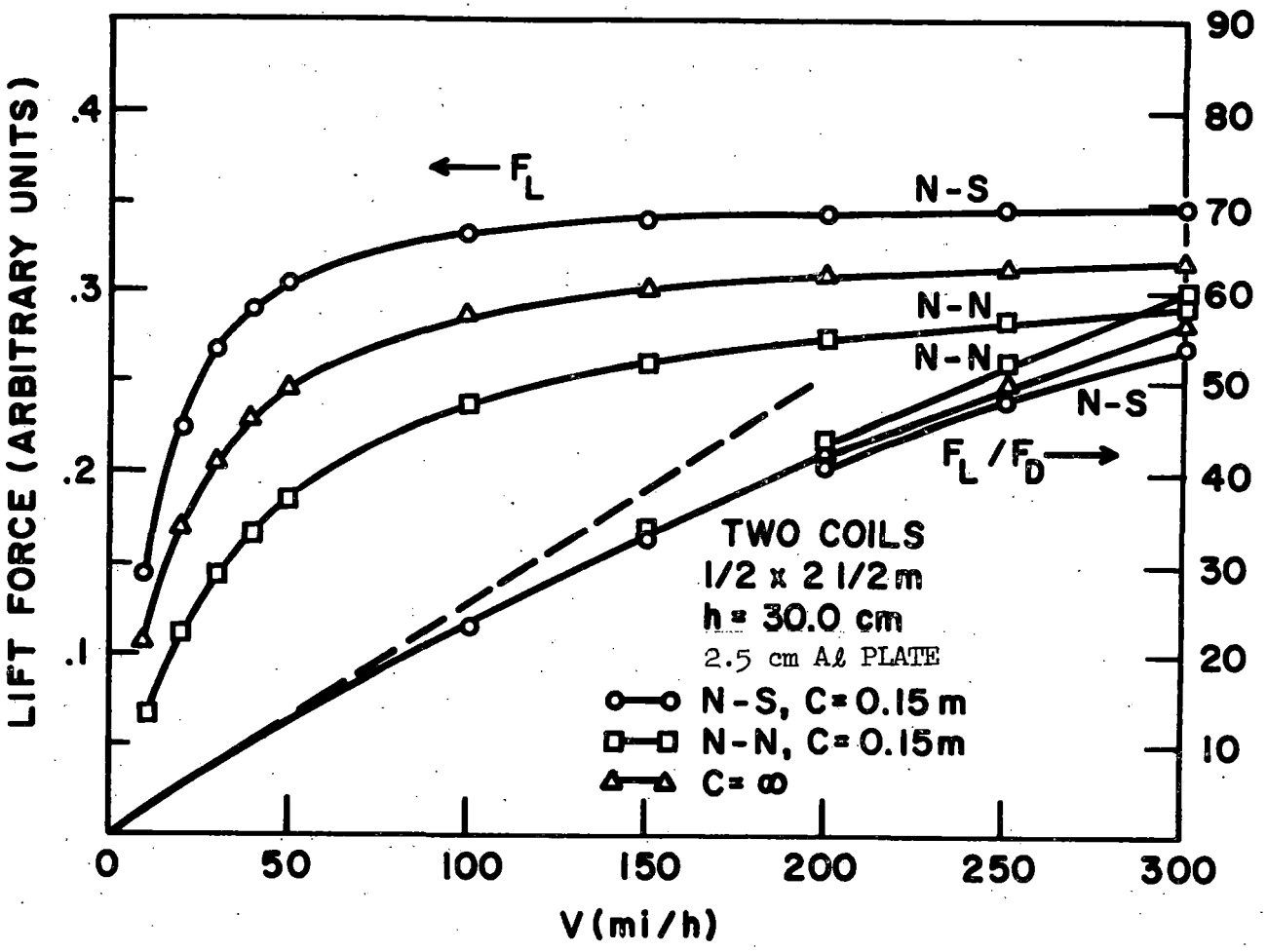

Fig. 2.9. F_L and F_L/F_D for two coil separated longitudinally by 2c.

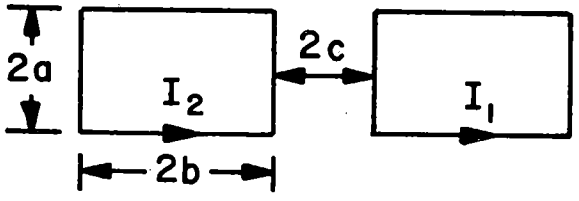

Fig. 2.8. Two levitation coils separated longitudinally by a distance 2c.

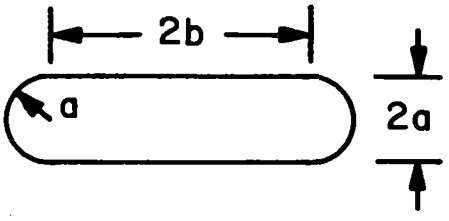

Fig. 2.10. A levitation coil with rounded ends.

the reduction in F_L/F_D is small even when the coils are separated by as much as 0.3 m.

TABLE 2.1. Lift and drag forces on two N-N coils separated by 2c as shown in Figure 2.8. 2 a = 0.5 m, 2 b = 1.5 m, $F_1 = \mu_o (NI)^2 (a+2b)/\pi h$. Track is one inch thick aluminum.

Velocity (mi/h)	F_L/F_1	10 F_D/F_1	F_L/F_D
	2c = 0		
50	0.236	0.194	12.1
100	0.282	0.120	23.4
150	0.300	0.0894	33.6
200	0.306	0.0725	42.7
250	0.315	0.0619	50.9
300	0.319	0.0547	58.3
	2c = 0.2m		
50	0.227	0.189	12.0
100	0.270	0.118	22.9
150	0.289	0.0888	32.5
200	0.298	0.0727	41.0
250	0.304	0.0625	48.6
300	0.308	0.0555	55.4
	2c = 0.3m		
50	0.228	0.191	11.9
100	0.271	0.120	22.6
150	0.289	0.0910	31.8
200	0.299	0.0750	39.8
250	0.304	0.0648	47.0
300	0.308	0.0577	53.4

For a magnet with rounded ends of radius of curvature a, length 2b (see Figure 2.10), we find that

$$W_1 = -\frac{\mu_o Ia}{2\pi^2} e^{-kh} \text{ Im} \left\{ e^{-ik_x b} \int_{-\pi/2}^{\pi/2} d\phi \cos \phi \exp[-i(k_x a \cos \phi + k_y a \sin \phi)] \right\}. \tag{2.8}$$

For a magnet of this configuration with a = 0.25 m and 2b = 2.5 m, F_L and F_L/F_D are found to be essentially the same as that of a rectangular magnet of dimensions 1/2 x 3 m.

2.1.3. Quadrupole Arrangement of Lift Magnets

It has been suggested that partial magnetic shielding can be accomplished by placing an opposing coil above the main levitation coil. If the upper coil is the same size as the lower one and carries an equal, but opposite current, then a quadrupole arrangement is formed.

To find the forces on this configuration, we can modify the force expressions, Equations 2.3 and 2.4. We see that W_1, the Fourier transform of the magnetic field at the track surface from a coil at height z_1, is proportional to e^{-kz_1}. Now the magnetic field at a height z_2, due to the eddy currents induced in the track (by the coil at z_1) involves a factor $e^{-kz_2} W_1$, which is proportional to $e^{-k(z_1 + z_2)}$. Therefore, in the expression for F_x and F_z we have the following factors:

i) eddy currents due to lower coil acting on lower coil: + e^{-2kh}

ii) eddy currents due to lower coil acting on upper coil: $-e^{-k(2h+c)}$

iii) eddy currents due to upper coil acting on lower coil: $- e^{-k(2h+c)}$

iv) eddy currents due to upper coil acting on upper coil: + $e^{-2k(h+c)}$.

The total is $e^{-2kh}(1-e^{-kc})^2$. Hence, an additional factor of $(1-e^{-kc})^2$ must appear in F_x and F_z, i.e.,

$$F_x = \frac{-8\pi^2}{\mu_o} \int_0^\infty dk_y \int_0^\infty dk_x \frac{k}{k_x} |W_c|^2 \Gamma_2 (1-e^{-kc})^2 , \qquad (2.9)$$

$$F_z = \frac{-8\pi^2}{\mu_o} \int_0^\infty dk_y \int_0^\infty dk_x \frac{k^2}{k_x^2} |W_c|^2 \Gamma_1 (1-e^{-kc})^2 \qquad (2.10)$$

where

$$W_c = \frac{\mu_o NI}{\pi^2} \frac{\sin k_x b \sin k_y a \, e^{-kh}}{k_y} \qquad (2.11)$$

for a rectangular coil of dimensions 2a x 2b. c is the vertical separation of the two coils. Other quantities have been defined previously.

For a 1/2 x 3 m levitation coil with c = h = 0.3, sample results are shown in Table 2.2 comparing the quadrupole arrangment to the single coil. We note that the lift force is reduced significantly, but the lift-to-drag ratio remains about the same. The track is taken to be aluminum, 25 mm thick.

TABLE 2.2. Comparison of quadrupole to single coil. $F_1 = \mu_o (NI)^2 (a+b)/\pi h$.

v (mi/h)	F_L/F_1 Quad.	F_L/F_1 Single	F_L/F_D Quad.	F_L/F_D Single
50	.089	.236	11.9	12.1
100	.110	.282	22.7	23.4
150	.120	.300	32.3	33.6
200	.125	.310	40.9	42.7
250	.128	.315	48.6	50.9
300	.130	.319	55.5	58.3

2.2. Characteristics of Guidance Forces

Calculations of guidance forces have been made only in the high-speed limit, and only for rather simple guideway geometries (flat track of finite width and the L-shaped channel). Guidance from more complicated guideways and the speed dependence of the guidance forces must be determined experimentally.

The speed dependence of the guidance force on a 2" x 4" coil, displaced laterally in the channel guideway of our 24" aluminum wheel, was measured during Task I. This was alluded to in Reference 1 and in the paper by Borcherts and Davis,[5] but the data were never published. We show these data together with the lift force on the coil in Figure 2.11. The guidance force rises more slowly as a function of speed than does the lift force, but this is most likely due to the finite thickness of the side panels whereas the bottom of the channel is very thick aluminum. Certainly, at higher speeds where the skin depth is less than the thickness of the panel, the velocity dependence of F_L and F_G is similar.

The low speed "anomaly" or turn up in the F_G curve is probably due to the slightly ferromagnetic nature of the welds in the stainless steel Dewar. This causes an attraction at zero speed; then at low speed, there appears to be a slight enhancement of the "weld magnet" due to the small image induced in the aluminum wheel. Finally, at higher speed the image becomes large enough that it dominates the interaction with the superconducting magnet. This is not seen in the other cases since the magnet remained in the center of the Dewar. Only for these experiments where the magnet was moved relative to the Dewar was this effect noticeable.

In order to investigate guidance forces from finite width guideways, we employed experimental guideway models and used an ac impedance bridge

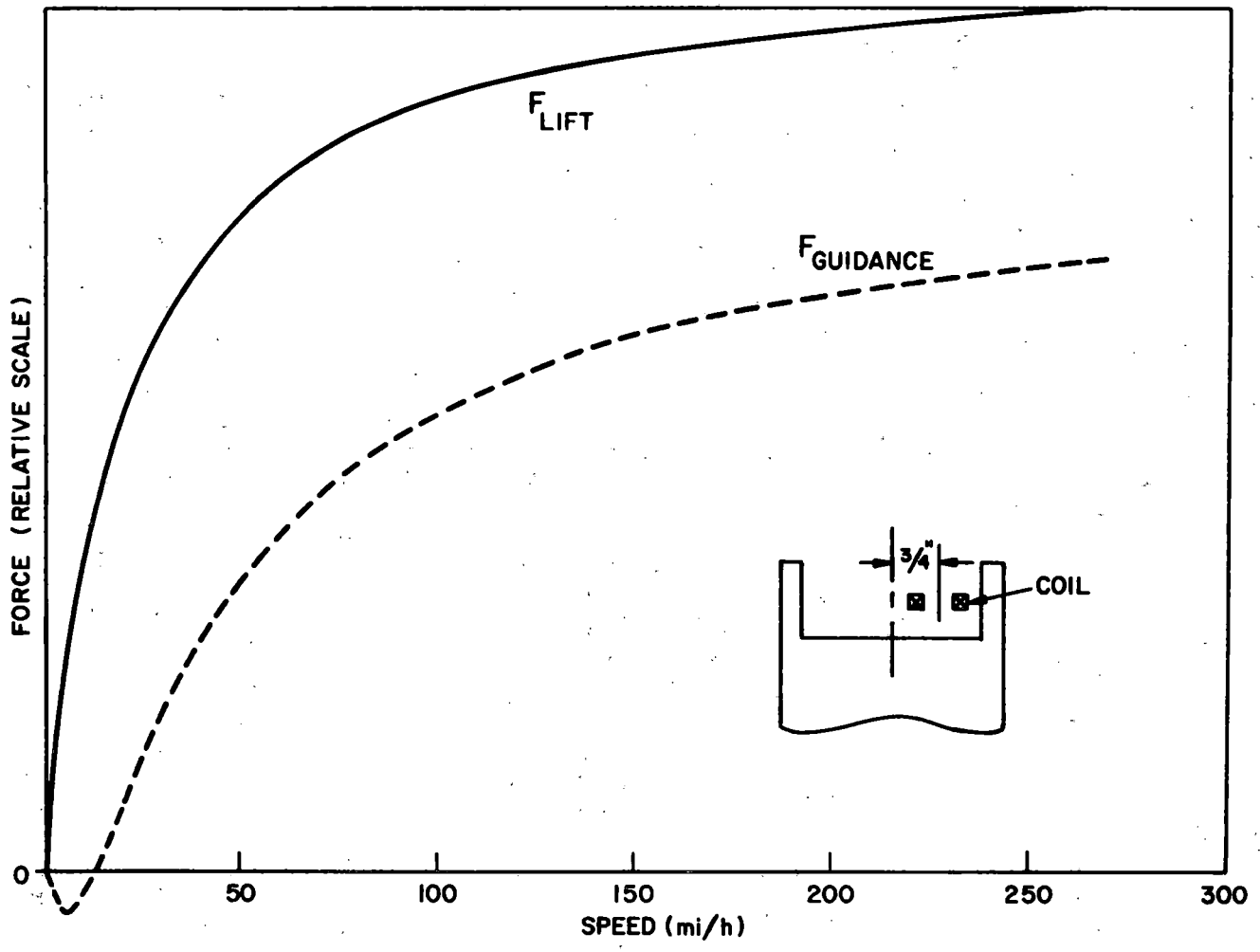

Fig. 2.11. Speed dependence of F_L and F_G for a 2 x 4 inch coil in an aluminum channel.

operated at 1 k Hz. In this technique, the inductance of the coil is measured as a function of its position in the guideway.[6] The current pattern established in the aluminum guideway is similar to that which would be produced by a moving coil at high speed. Since the coil energy $E = (1/2)\ Li^2$, and $F = \nabla E$, the force is proportional to the gradient of L.

To verify that the technique gives correct results, we first measured the inductance of a 2" x 4" coil (180 turns) as a function of its height above a flat aluminum plate. The force law obtained in this way agreed quite well with that found experimentally with a 2" x 4" superconducting coil above the rotating aluminum wheel.

Fig. 2.12 shows the inductance of a coil near one of two L-shaped guideways, one made by bending a single piece of aluminum, the other made of two pieces in close proximity but not in electrical contact. The results show that one does get a guidance force from the bent corner guideway; but from the one <u>not</u> in electrical contact, there is actually a force tending to push the coil into the side panel. This can be explained from the fact that without the side panel the inductance of the coil is increasing as it is moved to the side and the addition of the side panel does not subtract sufficient inductance to offset this effect. A positive guidance force was obtained by significantly extending the bottom plate beyond the edge of the guidance panel (making the bottom plate appear infinite in extent). However, the force, $F \sim dL/dx$, was not as large as that obtained by the single "L" guideway.

Figure 2.13 shows the inductance obtained from separate lift and guidance coils in an L-shaped channel. In this experiment, the coils are mechanically fastened as shown and then the inductance measured by connecting them in series. The two curves are obtained by fixing the height and then varying the guidance clearance, or vice versa.

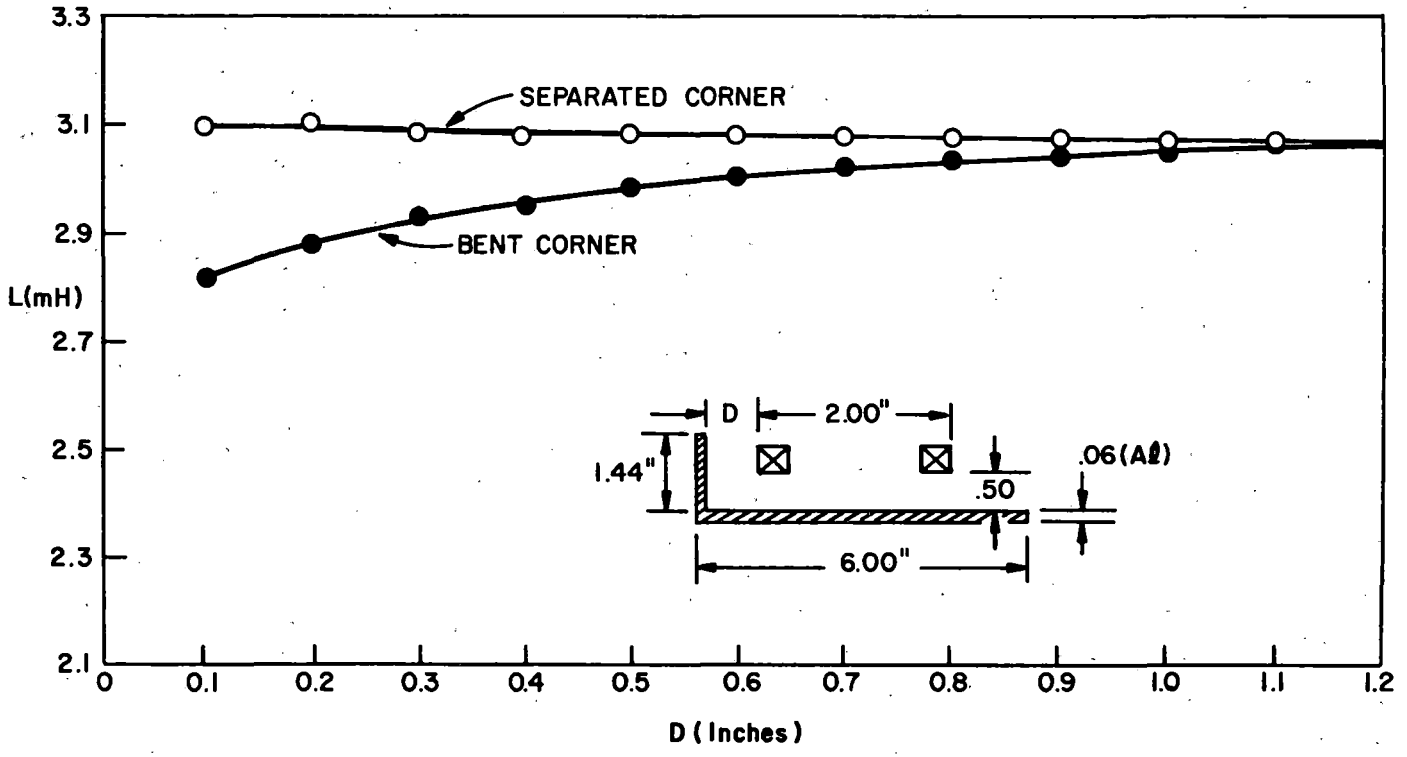

Fig. 2.12. Inductance of a coil near an L-shaped channel.

(experimentally determined).

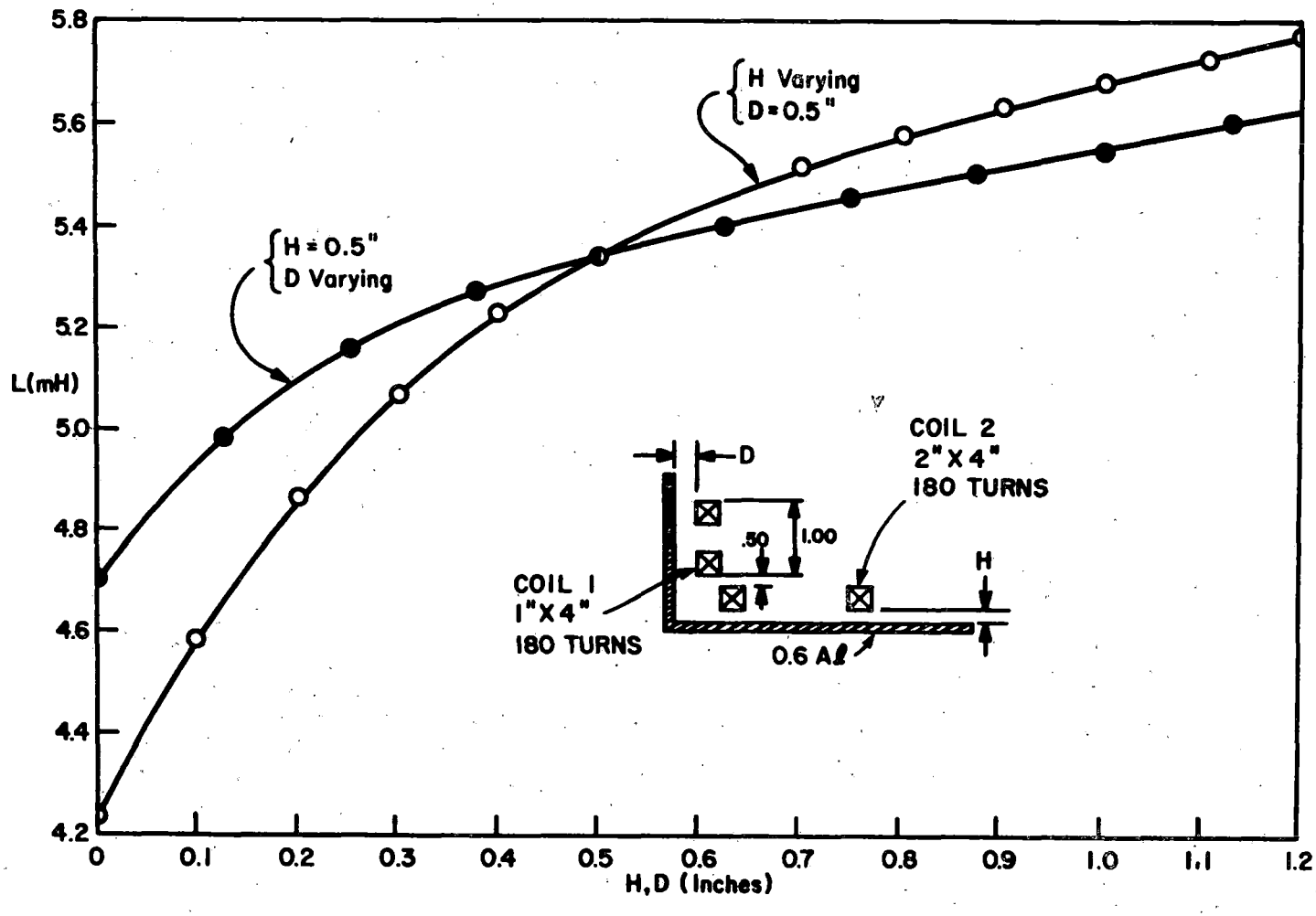

Fig. 2.13. Inductance of lift-guidance coils near an L-shaped channel.

These experiments confirm our analytic techniques, but at the same time provide an opportunity for studying finite width guideways in more detail. It is evident from Figures 2.12 and 2.13 that a larger guidance force can be obtained by using a separate guidance coil; however, with high enough side panels a single coil should be capable of providing both lift and guidance.

2.3. Effect of Ferromagnetic Backing on the Aluminum Track

All calculations made thus far for the electrodynamic suspension have assumed that the conducting track is structurally supported with non-ferromagnetic material. In fact, no criteria have been established as to the location and amount of ferromagnetic material that can be used in the guideway. From an economic point of view, the use of some steel in the guideway is probably desirable, particularly in the form of reinforcing material for concrete. Although aluminum can be used in concrete, its use would certainly lead to increased cost.

In order to get some idea as to the effect of ferromagnetic structural material, we have examined what might be considered a worst case: the ferromagnetic material is placed immediately below the aluminum track. We first analyzed a number of "single-Fourier-component levitation coils" moving over a one inch thick aluminum plate backed by ferromagnetic material characterized by a relative permeability κ and a conductivity σ. It was found that the high-speed performance of the coil was unaffected by the ferromagnetic material due to effective shielding by the aluminum plate. The low-speed performance (below 50 mi/h) was affected, however. The conductivity of the ferromagnetic material is unimportant (essentially no difference was observed for conductivities in the range: zero to $10^5\ \Omega^{-1}\ cm^{-1}$); the important parameter is κ. The effects noted are: (1) below about 5 mi/h the lift force is negative (i.e., attractive), (2) the height of the

low-speed drag peak is increased substantially, and (3) low-speed performance is affected even with moderately permeable material ($\kappa = \mu/\mu_o = 10$).

We next analyzed the performance of a 0.5 x 3 m coil moving at height 0.3 m over a 25 mm thick plate of aluminum backed by permeable material of zero conductivity. This was accomplished by modifying Equation 2.6 to read:

$$\Gamma_1 + i\Gamma_2 = \frac{1-\beta - (1+\beta)\ (1-\beta\kappa)\ e^{-2\beta kT}/(1+\beta\kappa)}{1+\beta - (1-\beta)\ (1-\beta\kappa)\ e^{-2\beta kT}/(1+\beta\kappa)} \qquad (2.12)$$

The results, which are shown in Figue 2.14, are similar to those of the "single-Fourier coefficient coil" just described. The curve labeled $\kappa = 1$ in Figure 2.14 is the same as shown in Figure 2.2. It is evident that a permeable backing material increases the height of the low-speed drag peak substantially; with $\kappa = 1000$ the height of the drag peak is almost doubled. The attractive force at zero speed is $-0.89\ F_I$ for $\kappa = 1000$ and is $-0.72\ F_I$ for $\kappa = 10$. On the other hand, the high-speed performance is affected very little; at 300 mi/h the lift force is degraded only slightly by the presence of the permeable material, the drag force is unaffected, and F_L/F_D goes from 58.3 for $\kappa = 1$ to 56.8 for $\kappa = 1000$.

In summary, then, the two effects of ferromagnetic structural material in the vicinity of the tracks are (1) an attractive force on the magnet at very low speeds, and (2) an increased drag at low speeds. If conductor is to be left out of the low-speed acceleration section of the guideway, then the increased height of the drag peak poses no real problem; but it does increase the braking of the vehicle and puts larger longitudinal forces on the magnet suspension struts during braking. The attractive force on the magnets means the force transmittal struts have to withstand a much larger tensile load than they would if there were no ferromagnetic material in the system.

2.4. Passive Damping

The final report for Task I [1] discussed two methods for increasing the passive damping of the electrodynamic (repulsive force) suspension. These

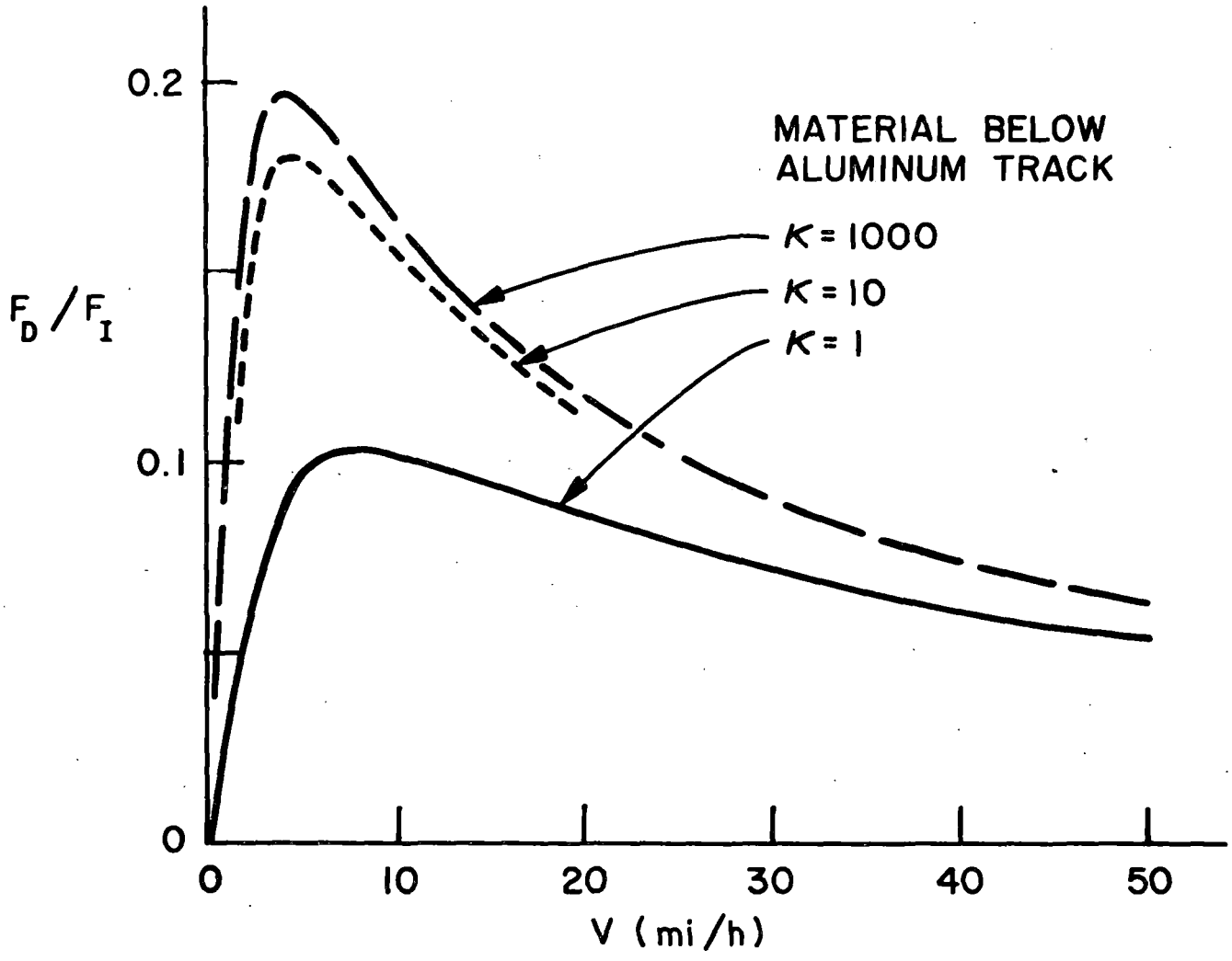

Fig. 2.14. Drag force on a 0.5 x 3m coil moving over one-inch thick aluminum backed by material of relative permeability K.

are conducting-plate damping and damping with a tuned coil. In both cases, the plate or coil is placed between the levitation magnet and guideway, and is rigidly attached to the magnet. Neither case provided sufficient damping to give acceptable ride quality to the passengers in the levitated vehicle for the expected roughness of guideway surfaces. Thus, it was indicated that either a secondary suspension or some form of active control is needed.

Several refinements in the analysis of passive damping forces have been made in the present study. These indicate that conducting-plate damping is somewhat more effective and tuned-coil damping is somewhat less effective than were originally calculated. We have also made measurements of the damping which can be achieved by means of a conducting plate located below the levitation coil and these experimental results agree rather well with the theoretical predictions.

In the final report for Task I,[1] Appendix F, an expression for the eddy-current damping time τ of a conducting plate was given:

$$\frac{1}{\tau} = \frac{2g}{w_p} \frac{F_I(2[h + h'])}{F_I(2h)} I\left(\frac{2(h + h')\gamma}{w_p}\right) \tag{2.13}$$

where $w_p = 2/\mu_o \sigma_p T_p$, σ_p is the conductivity and T_p the thickness of the conducting plate, $\gamma = 2\pi f_o$ is the frequency of oscillation, and $F_I(x)$ is the force due to its image at distance x. h is the height of the levitation magnet above the track and h' is the height of the plate. The function $I(x)$, $x = 2(h + h')\gamma/w_p$ was given for a long wire as the levitation magnet. Although we used the I(x) derived for a long wire for all magnets, it has become clear to us that this underestimates the damping (i.e., makes τ too long). For example, if the force between the levitation magnet and its image can be represented by (constant)/z^n where z is the separation and

n = a positive integer, then I(x) should be replaced by $I_n(x)$ where

$$I_1(x) = I(x) = 1-xf(x) ,$$

$$I_2(x) = 1-x^2g(x) ,$$

$$I_3(x) = 1 - \frac{x^2}{2} I_1(x) ,$$

$$I_4(x) = 1 - \frac{x^2}{6} I_2(x) ,$$

$$f(x) = Ci(x) \sin x - si(x) \cos x$$

and

$$g(x) = - Ci(x) \cos x - si(x) \sin (x)$$

Ci(x) and si(x) are given in Reference 7. In general, it appears that

$$I(x) = I_1(x) \leq I_2(x) \leq I_3(x) \leq I_4(x) .$$

Qualitatively, all the $I_n(x)$ are similar since $I_n(x) \to 1$ as $x \to 0$ and $I_n(x) \propto x^{-2}$ for $x \to \infty$. Hence, we note that as a function of the conductivity σ_p, $1/\tau$ has the form

$$\frac{1}{\tau} \propto \frac{1}{\sigma_p} , \quad \sigma_p \to \infty \tag{2.14}$$

and

$$\frac{1}{\tau} \propto \sigma_p , \quad \sigma_p \to 0 . \tag{2.15}$$

It turns out that τ^{-1} has a broad maximum as a function of σ_p and this explains why σ_p can change by significant amounts and τ change only slightly. The same general behavior also occurs for a shorted, multiturn copper coil.

In Reference 1 (Appendix F), we found that the maximum of $xI_1(x)$ is 0.41, occurring at x = 1.7. For the levitation coil at h = 0.3 m, h′ = 0.2 m, and f_o = 1 Hz , this gave an optimum plate thickness of 1 cm Al at room temperature or 1 mm Cu at liquid N_2. The damping time τ for a 1 x 2 m coil

was found to be 2 sec. The maximum of $xI_2(x)$ is 0.86 occurring at $x = 2.8$. This gives a somewhat larger optimum thickness and a smaller damping time. As noted earlier, the damping time can be further decreased by putting the plate closer to the track.

The force law (constant/z^n) for the 0.5 x 3 m levitation coil has an n in the vicinity of 2.0; taking into account the various factors in Equation 2.13, we find $\tau = 1.7$ sec for the 0.5 x 3 m coil. This gives (at $f_o = 1.35$ Hz)

$$\delta = (2\pi f_o \tau)^{-1} = 0.07$$

which is still far below the value for critical damping ($\delta = 1$). From studies of ride quality, it would appear that δ should be greater than 0.71 in order to insure good ride quality without a secondary suspension.

2.4.1. Experimental Studies of Damping

Experiments were carried out to study the damping due to a copper plate moving rigidly with a levitation coil over a conducting plate. A 0.095 inch copper plate was attached 1/4 inch below the bottom of a Dewar containing a 7-1/2 x 11-1/2 inch superconducting magnet. The Dewar was attached to a long support structure which was pivoted at one end. The Dewar, magnet, and copper plate were effectively constrained to oscillate vertically above a 4 foot diameter, rotating, aluminum wheel (rim speed 110 mi/h). The copper plate was cooled to 77°K before the experiment and allowed to warm up as data were taken. After an initial perturbation, the decaying oscillations were recorded on an x-y recorder. From each recorder, tracing a frequency f_o and a damping time τ (1/e reduction in amplitude) were calculated.

In a typical series of runs, we found that for h = 3 inches, h′ = 2 inches, $f_o = 2.5$ Hz; with the plate at -40°F, $\tau = 1.2$ sec; and at -160°F,

τ = 1.0 sec. When the experiment was repeated with no copper plate, the damping time was considerably longer: 3.3 sec. The mechanisms responsible for this 3.3 sec damping time are not known with certainty. Some possible causes are eddy current damping in the side plates of the wheel, aerodynamic forces, and eddy currents in the Dewar.

The calculated value of f_o (based on h and coil geometry) is 2.6 Hz. From the analysis of the preceding section, damping times of 1.8 sec and 1.3 sec were calculated for the two cases described above. If one adds the 3.3 sec damping due to other sources (by adding reciprocals of the damping times), then the calculations yield 1.2 sec and 0.9 sec. Considering the inaccuracies in the determination of the experimental numbers, the close agreement of theory and experiment should probably be viewed as fortuitous, although it is clear that the calculations give reliable estimates of the damping.

2.5. Control Requirements

Because the amount of passive damping which can be built into the system is so limited, acceptable ride quality can only be obtained either by a secondary suspension or by active control. Active control is preferred because it allows more freedom in meeting ride quality objectives, and it also allows the use of a rougher guideway. The control power requirement is modest provided the guideway is not too rough. (The use of a secondary suspension will be discussed in Chapter 6.)

Separate control coils are a virtual necessity, both to allow the option of persistent-mode operation of the levitation coils and to keep the current-voltage product of the control system as low as possible. A possible control coil arrangement is shown in Figure 2.15. The effectiveness ratio

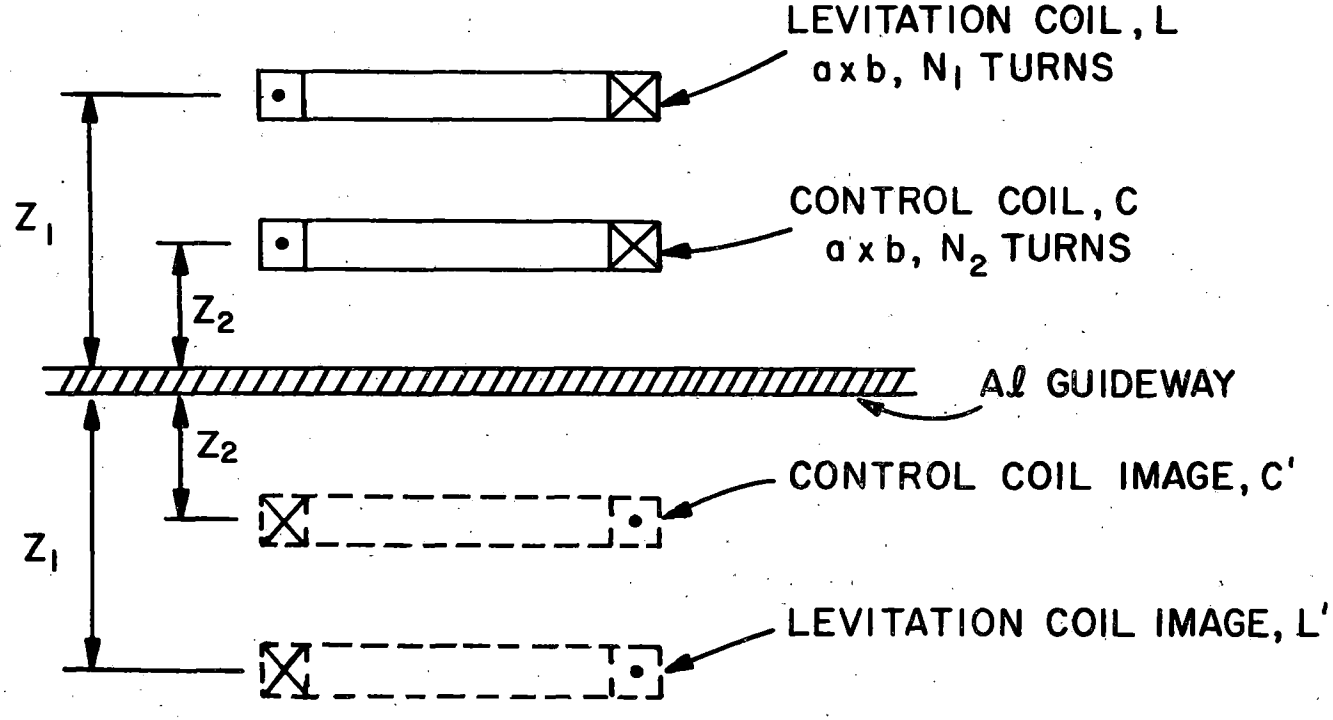

Fig. 2.15. Levitation and control coils and their images.

γ is defined by

$$\gamma = \frac{\text{Change in } N_1 I_e \text{ to Produce } \Delta F_L}{\text{Control Ampere Turns to Produce } \Delta F_L} \qquad (2.16)$$

where I_e is the equilibrium current in the levitation coil. Thus, $\gamma = 1$ implies that the same control current is needed in the separate control coil as would be required in the main levitation coil. The effectiveness ratio as a function of control coil height and dimensions is plotted in Figure 2.16. The levitation coil is 0.5 x 3 m at height 0.3 m. The curves in Figure 2.16 show both constant-current and persistent-mode operation of the levitation coil.

With the 0.5 x 3 m levitation coil at 0.3 m height and a control coil of the same size at 0.2 m height, the effectiveness ratio $\gamma = 1.03$. The control currents required for this case are shown in Table 2.3 for various suspension parameters.

TABLE 2.3. Control currents for various suspension parameters. Levitation coil at 0.3 m; control coil at 0.2 m. Control current: rms value expressed as percent of I_e.

$\hat{f}_o$ (Hz)	δ	i_c (%)
0.6	0.445	4.07
0.6	0.707	4.09
0.6	2.68	4.60
1.18	0.707	2.71
1.18	1.35	3.42

Let us now determine the control power that must be delivered to the control coil. Define the resistance of the control coil as R_C and its self

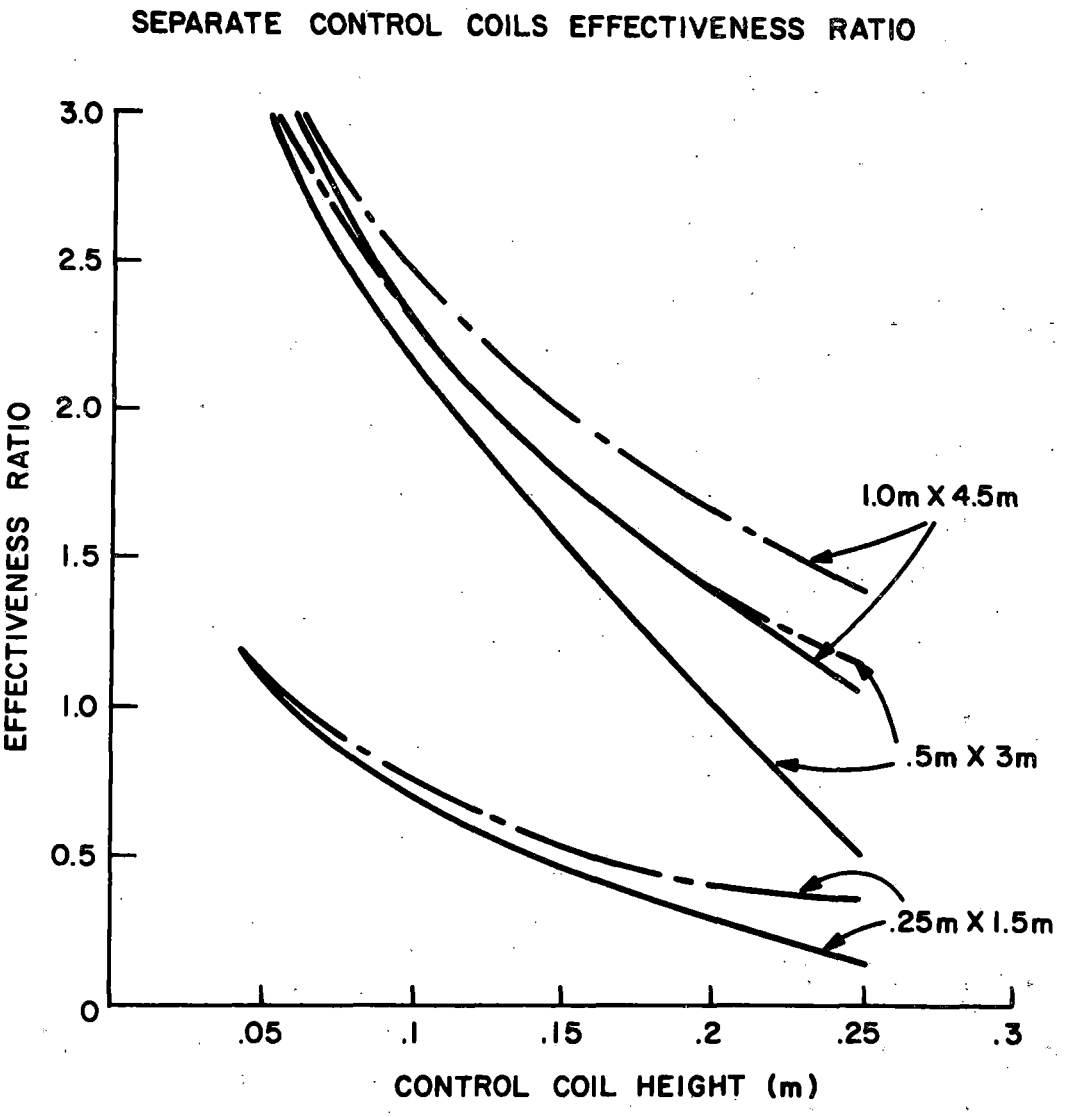

Fig. 2.16. Calculated effectiveness ratio for a control coil.

inductance as L_C. Suppose we apply a sinusoidal voltage to the coil

$$v(t) = V \sin \omega t \ . \tag{2.17}$$

Then, using phasor notation, the current through the coil is

$$I = \frac{V}{R_C + j\omega L_C} \ , \tag{2.18}$$

the real power dissipated in the coil is

$$\begin{aligned} P_{real} &= 1/2 \ \mathrm{Re} \ [VI^*] \\ P_{real} &= I^2_{rms} \cdot R \ , \end{aligned} \tag{2.19}$$

and the apparent power delivered by the power supply is

$$P_{app} = V_{rms} \ I_{rms} \ . \tag{2.20}$$

We have the power spectral density of the control current induced by random track irregularities, $P_{\Delta I}(\omega)$, and thus I^2_{rms} can be determined as

$$I^2_{rms} = \int_0^{\omega_C} P_{\Delta I} \, d\omega \ , \tag{2.21}$$

where ω_C is an upper cutoff frequency above which there is no feedback current control. A natural value for ω_C would be the frequency for which the wavelength at 300 mi/h is the magnet length. Any shorter wavelengths would essentially be filtered by the magnet. For the magnet length of 3 m, f_c = 44 Hz. In order to determine the rms voltage, it is necessary to determine the power spectral density of the voltage, P_V. From Equation 2.18, it follows that

$$P_V = (R^2_C + \omega^2 L_C^2) \ P_{\Delta I} \tag{2.22}$$

and thus

$$V^2_{rms} = \int_0^{\omega_C} P_V \, d\omega \ . \tag{2.23}$$

In the derivations to this point, the self inductance of the control coil L_C has been used. However, an equivalent inductance which accounts for the mutual inductance between the coils and the various images should be used in determining the rms voltage and thus the control power. The coils and images considered in the case of a separate control coil located below the levitation coil are shown in Figure 2.15. The mutual inductances between the various coils and images are given in Table 2.4, normalized to the self inductance of the control coil L_C. Since the equivalent inductance of the control coil involves terms like $(M/L_C)^2$, it is obvious that the only term with a considerable influence is M_{LC}. The equivalent inductance for the control coil is then

$$L_{eq} = L_C \left[1 - \left(\frac{M_{LC}}{L_C} \right)^2 \right] . \qquad (2.24)$$

TABLE 2.4. Normalized mutual inductances for the control problem (see Figure 2.15). L_C = 40 henries for a 3000-turn coil.

	M/L_C
M_{LC}/L_C	0.47
$M_{CC'}/L_C$	0.15
$M_{LC'}/L_C$	0.09
$M_{LL'}/L_C$	0.07

The voltage power spectrum is

$$P_V = (R_C^2 + \omega^2 L^2_{eq}) \, P_{\Delta I} . \qquad (2.25)$$

Calculations of the real and apparent control power were made using these results and assuming a guideway with roughness parameter $A = 5 \times 10^{-6}$ feet and for a coil supporting 25,000 pounds. Since 4 coils would be required to support a 100,000 pound vehicle, the control powers associated with the lift coils would be four times these values. If guidance coils are also used, we need to add the equivalent of 2 more coils since each guidance coil will supply essentially 1/2 the lift force of a single coil. With all these factors, we obtain a control power requirement of

$$P_{real} = 1.15 \text{ kW/ton} ,$$
$$P_{apparent} = 1.8 \text{ kW/ton} . \qquad (2.26)$$

Since both the rms voltage and current scale as $A^{1/2}$, the power required over any rougher or smoother guideway will scale directly with the A value.

2.6. Superconducting Magnet Design and Construction

The use of a superconducting magnet as a levitation or guidance pad for a high-speed vehicle poses certain problems which must be evaluated before a research vehicle using the repulsive suspension can be built. Although not necessarily unique to this application, the central problems to be considered are:

i) a low heat loss mechanism for transmittal of the levitation and guidance forces from the superconducting wire at 4.2 K to the room temperature vehicle.

ii) means for reducing the ac environment (and the resulting heat loss) seen by the superconducting wire. This ac environment arises from changes in the magnet current due to magnet vibration or from current changes in the control coil.

iii) a light weight for the overall magnet system. The magnet system includes the superconducting coils, the dewars, the magnet control system and the refrigeration requirement.

iv) choice of superconducting wire and coil fabrication technique to best meet the requirements in i), ii), and iii).

Two superconducting magnets were considered in this program. One magnet, a levitation-guidance pad for a 50,000 lb. research vehicle was designed on a subcontract to the Magnetic Corporation of America, 179 Bear Hill Road, Waltham, Mass; the other, a small 6 x 21 inch (15 cm x 53 cm) low-heat-loss experimental magnet was designed and built by Ford Scientific Research Staff. This latter magnet was built with a curved coil to fit the 5 ft. diameter experimental wheel (shown in Fig. 2.17) so that experimental information could be obtained about the effects of a vibratory environment and a magnet control system.

The magnet designed by MCA is discussed briefly in Section 7.4 and in detail in the MCA report.[8] The rest of this section will deal with the smaller superconducting magnet designed, built and tested by the Ford Scientific Research Staff.

2.6.1. Design of Ford Model Magnet

The 6 x 21 inch experimental magnet, shown complete in Fig. 2.18, incorporates a number of features which we wanted to evaluate before proposing their use in a larger magnet for a research vehicle. The basic features of the magnet are:

a) All aluminum cryostat (except for the stainless steel fill and vent tubes). The use of aluminum was felt to be necessary in order to minimize weight as well as to provide good internal heat conduction in the nitrogen and helium regions.

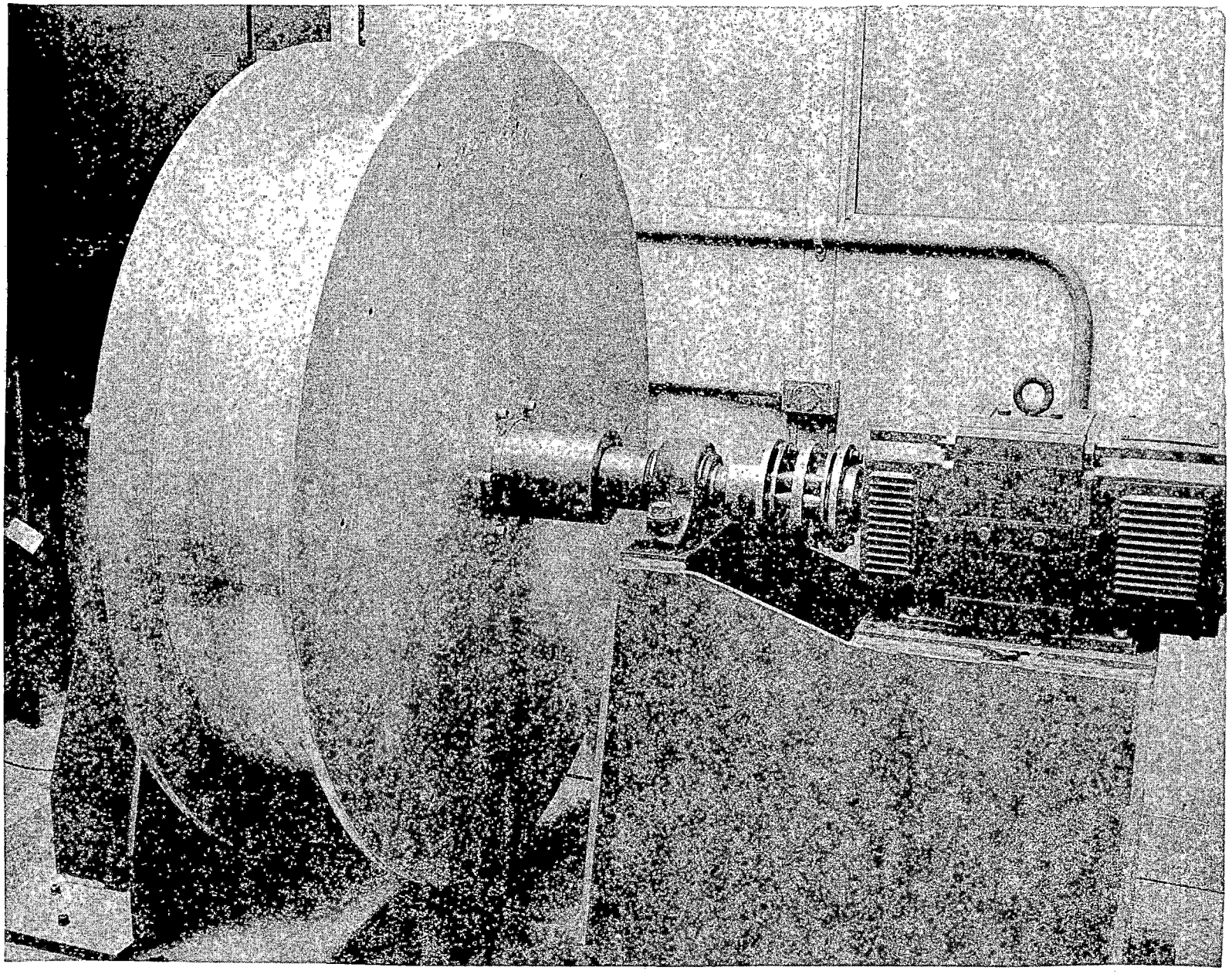

Fig. 2.17 5 ft diameter rotating wheel facility.

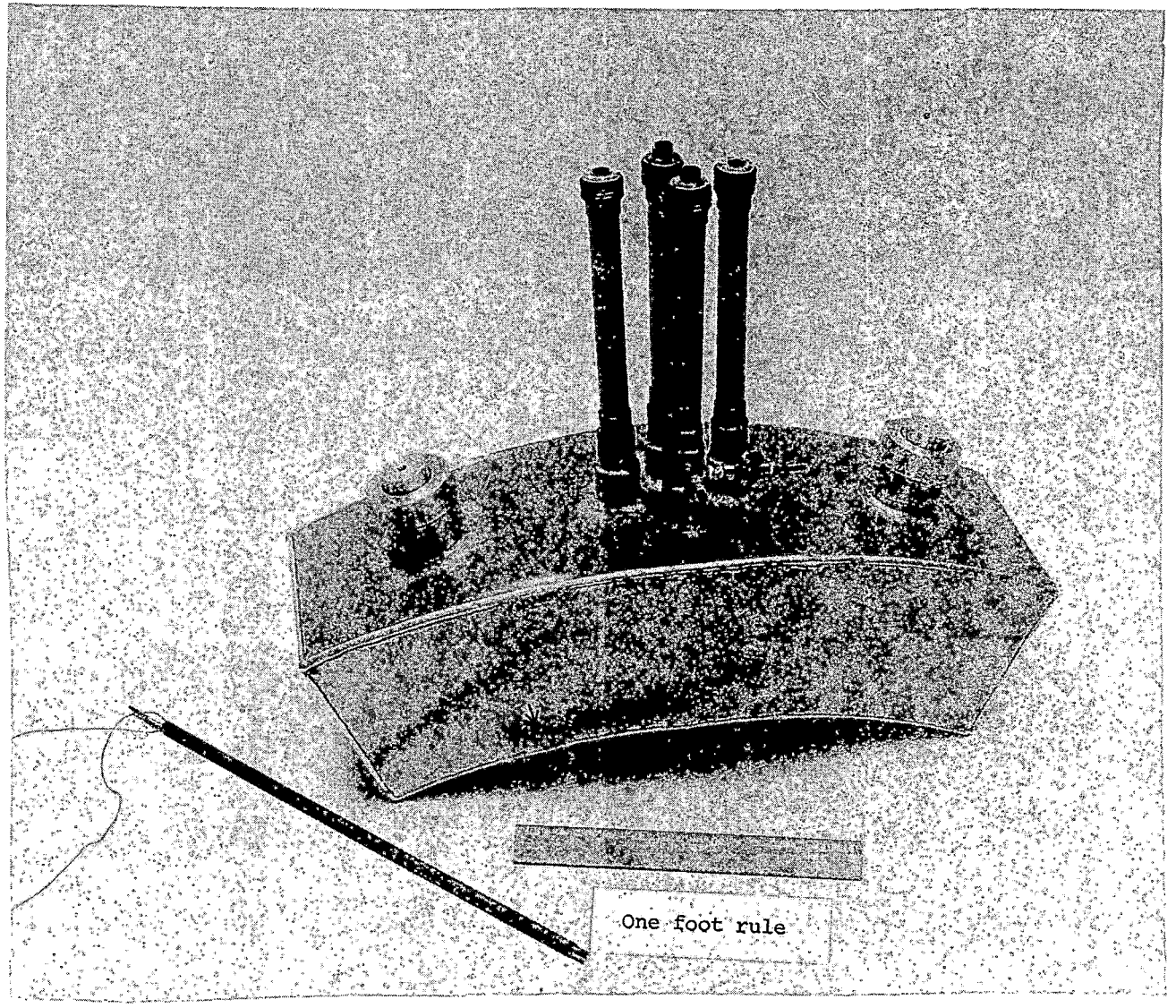

Fig. 2.18 Cryostat for Ford experimental magnet.

b) Persistent switch. This device removes the need for a low-voltage power supply and eliminates the heat losses associated with the current leads.

c) Removable magnet and heater leads. Since one of the goals of this program is to provide data for heat leak mechanisms, removal of the current leads reduces the ambient heat leak to that from radiation between the nitrogen and helium surfaces and conduction down the force transmittal struts and the fill and vent tubes.

d) Twisted multi-filament NbTi wire in a copper matrix wound in an intrinsically stable configuration. Whereas aluminum-clad NbTi or V_3Ga wire has considerable potential for a magnet material, such wire has not been adequately investigated at the present time. We chose the intrinsically stable configuration (fully potted) rather than the fully stabilized configuration of the MCA design; both configurations are candidates for the full-scale magnet but the fully stabilized one is somewhat more conservative.

e) Epoxy fiberglas (G-10) force transmittal struts. The extremely low heat conduction and high strength of this material make it desirable to attempt its incorporation into the magnet design.

f) Nitrogen tank with nearly optimum heat shield thickness for eddy-current damping. The use of liquid nitrogen to provide an intermediate surface was again felt to be necessary to reduce the ambient heat loss to the $4^{\circ}K$ surface to a minimum. It was also expected that the heat input into the damper shield could be measured by the nitrogen boil off rate.

These features are shown in cross section in Fig. 2.19. The magnet coil itself (Fig. 2.20) consists of 985 turns of 241 filament NbTi copper clad wire (Cu/Supercond. = 1.2/1, twisted 2 turns/inch) manufactured by MCA and wound on an aluminum coil form and potted with pliobond glue. The coil is 6 inches wide (centerline to centerline) with semicircular ends; the overall length of the coil is 21 inches. As shown in Fig. 2.19 the two epoxy fiberglas struts are designed to be removable through caps containing an "O" ring seal. Thus, the removal of these struts for examination or the use of other struts is possible. One of the struts is shown in Fig. 2.21.

Some properties of the magnet-cryostat assembly are given in Table 2.5.

TABLE 2.5. Properties of the 6 x 21 inch Ford Magnet

LIQUID CAPACITY:		
Nitrogen	5.2 liters	
Helium	6.3 liters	
AMBIENT BOIL OFF RATE:		
Nitrogen	0.21 l/hr (9.4 watts)	
Helium	0.21 l/hr (0.17 watts)	
CRITICAL CURRENT:		
65 amperes		
AXIAL FIELD AT CENTER OF CRYOSTAT		
Undersurface: 45 gauss/ampere		
DRY WEIGHT:		
He cryostat & coil	15.4	
N_2 cryostat	7.3	
77°K radiation shield	5.4	
Room temp. container	14.1	
Struts, strut ends & locking caps	1.9	
Total	44.1	lbs.

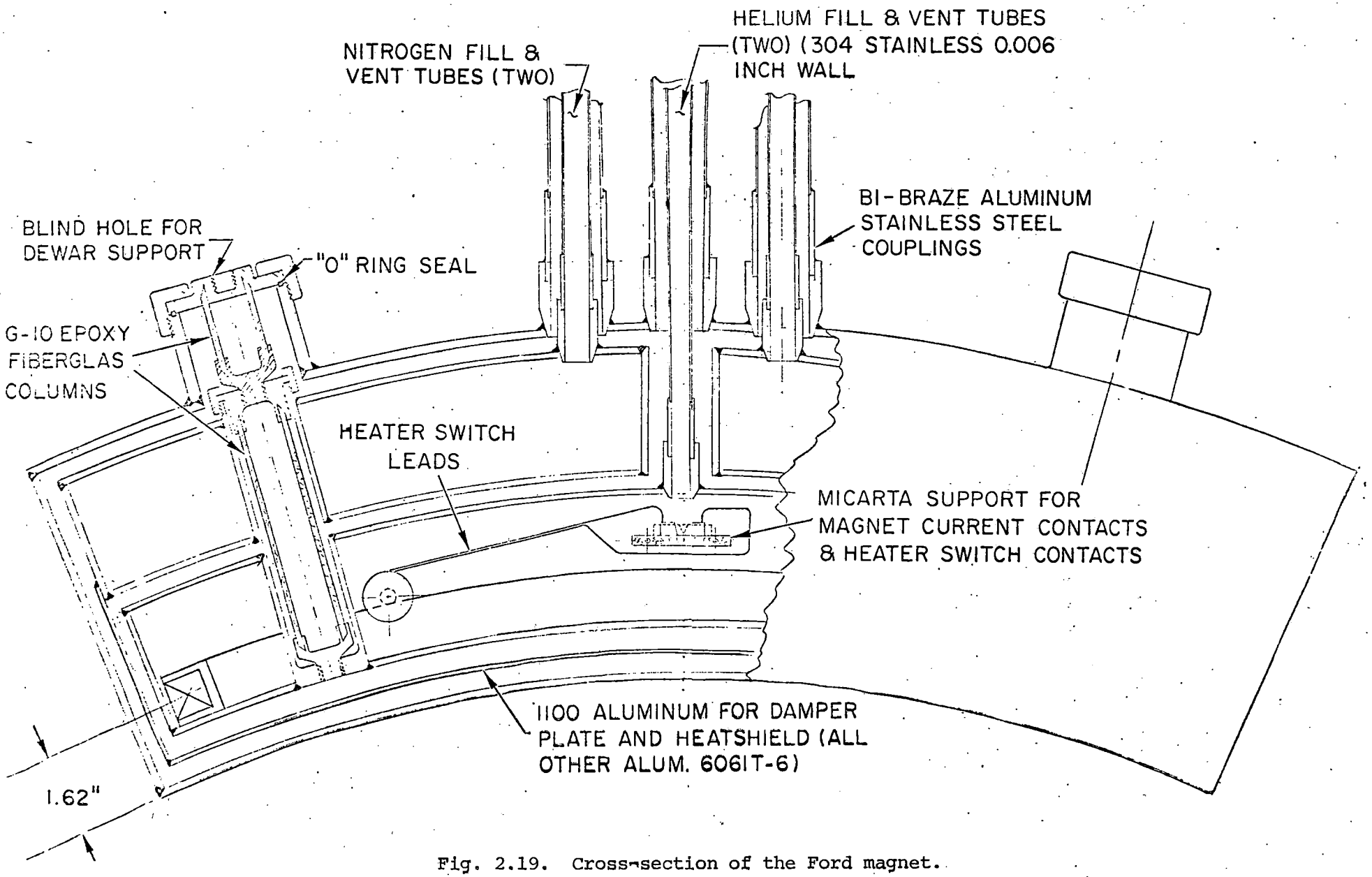

Fig. 2.19. Cross-section of the Ford magnet.

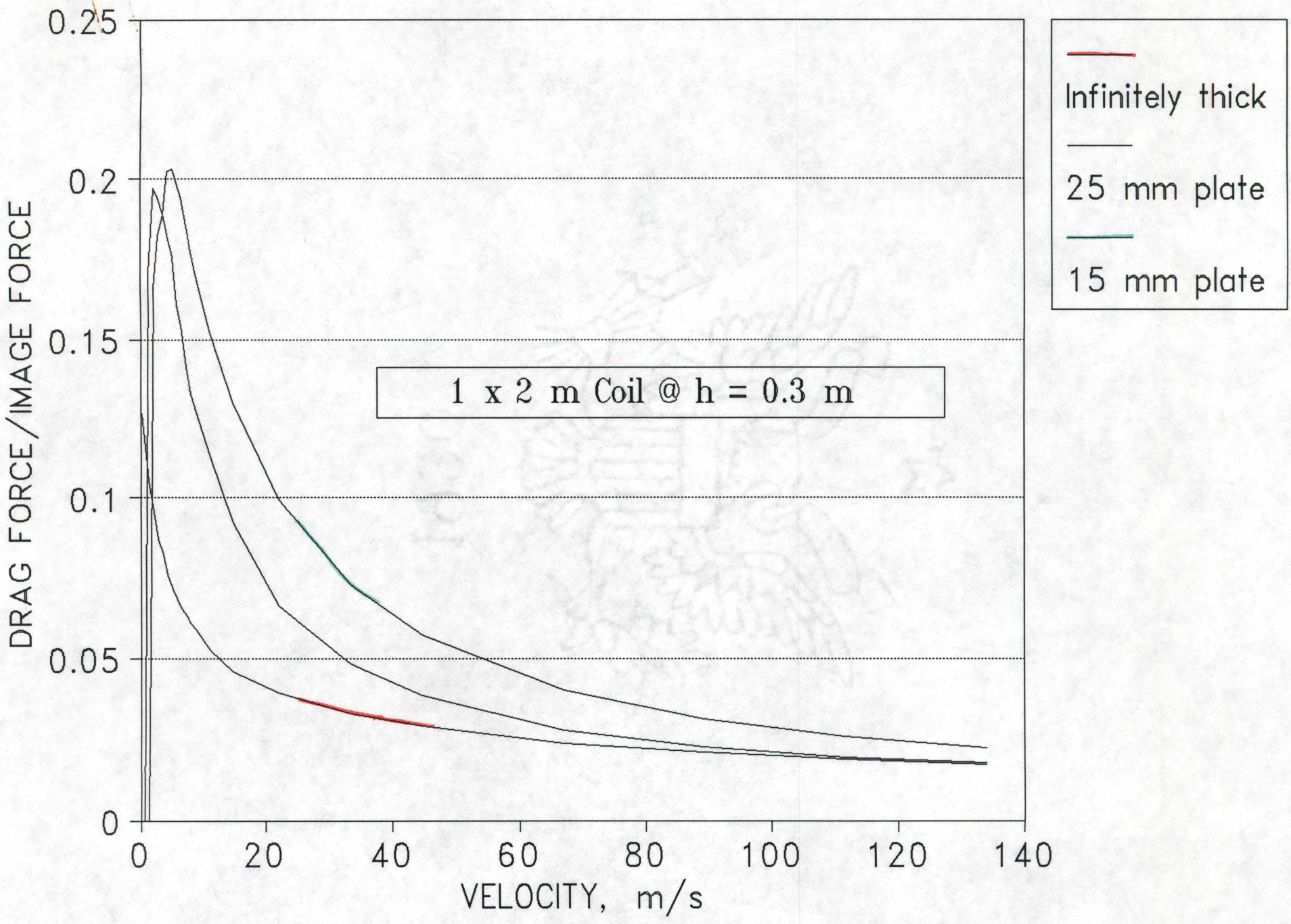
0.25
0.2
0.15
0.1
0.05
0
DRAG FORCE/IMAGE FORCE
1 x 2 m Coil @ h = 0.3 m
0
20
40
60
80
100
120
140
VELOCITY, m/s
Infinitely thick
25 mm plate
15 mm plate

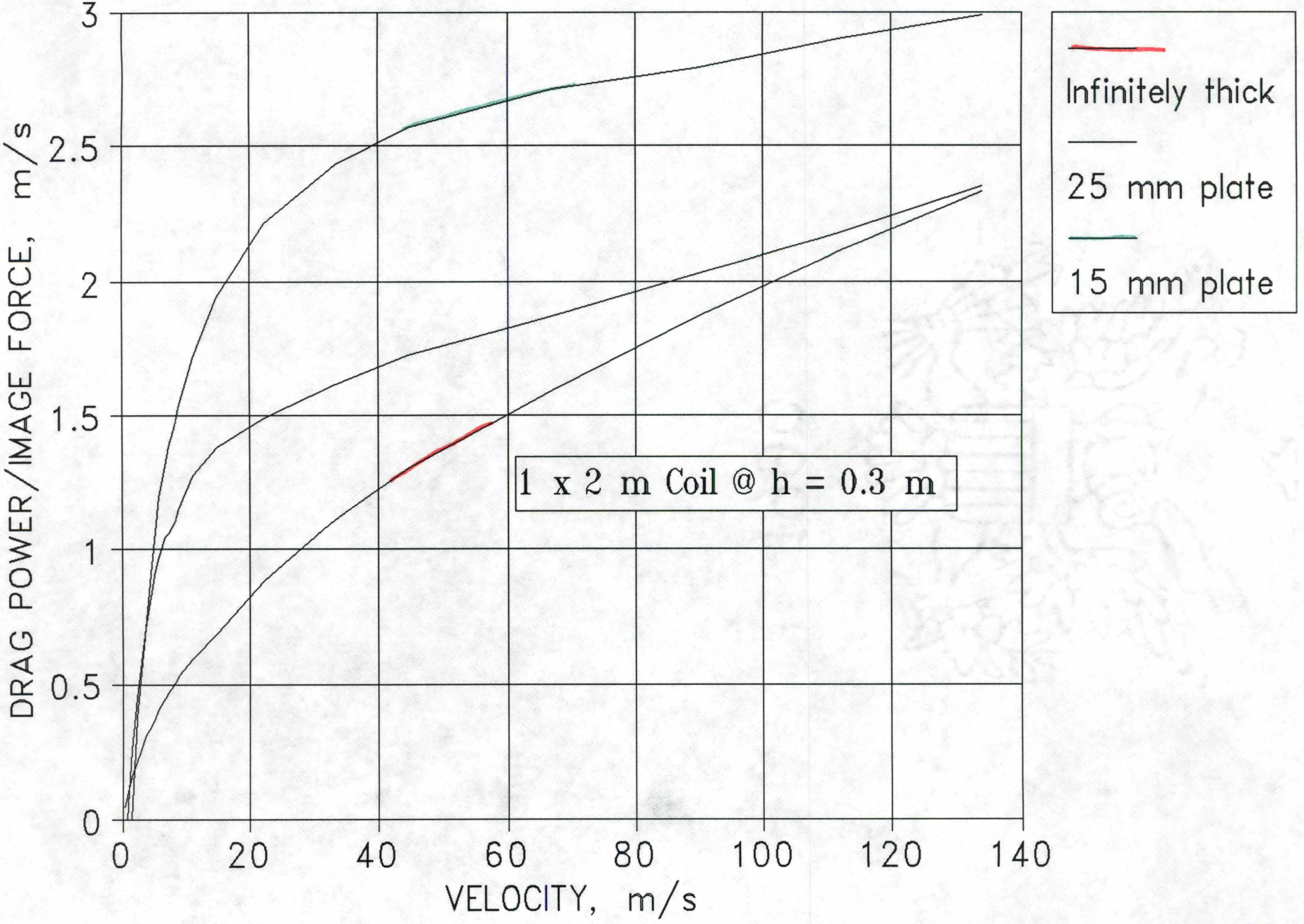
DRAG POWER/IMAGE FORCE, m/s
3
2.5
2
1.5
1
0.5
0
0
20
40
60
80
100
120
140
VELOCITY, m/s
1 x 2 m Coil @ h = 0.3 m
Infinitely thick
25 mm plate
15 mm plate

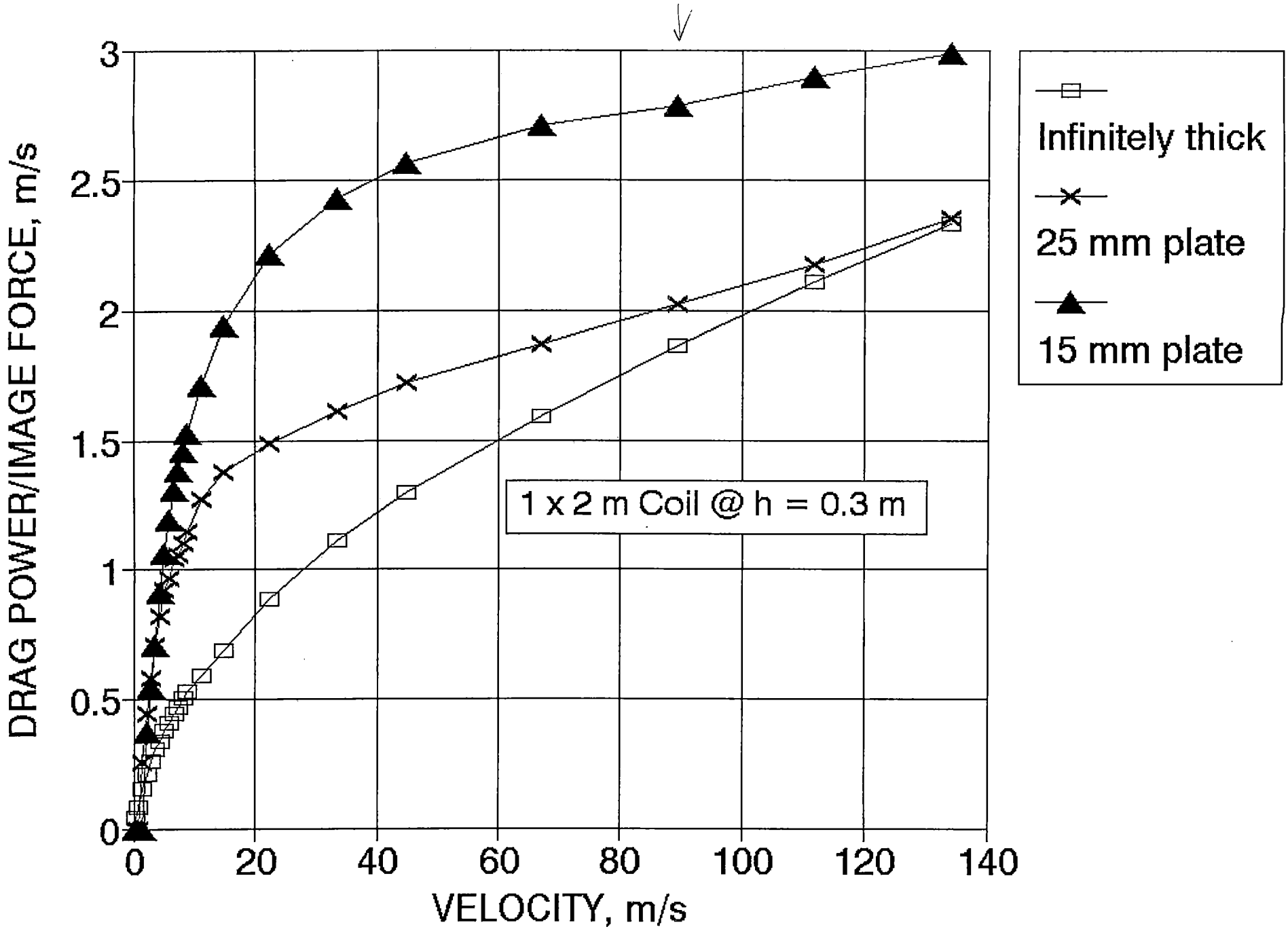
DRAG POWER/IMAGE FORCE, m/s
VELOCITY, m/s
0
0.5
1
1.5
2
2.5
3
0
20
40
60
80
100
120
140
1 x 2 m Coil @ h = 0.3 m
Infinitely thick
25 mm plate
15 mm plate

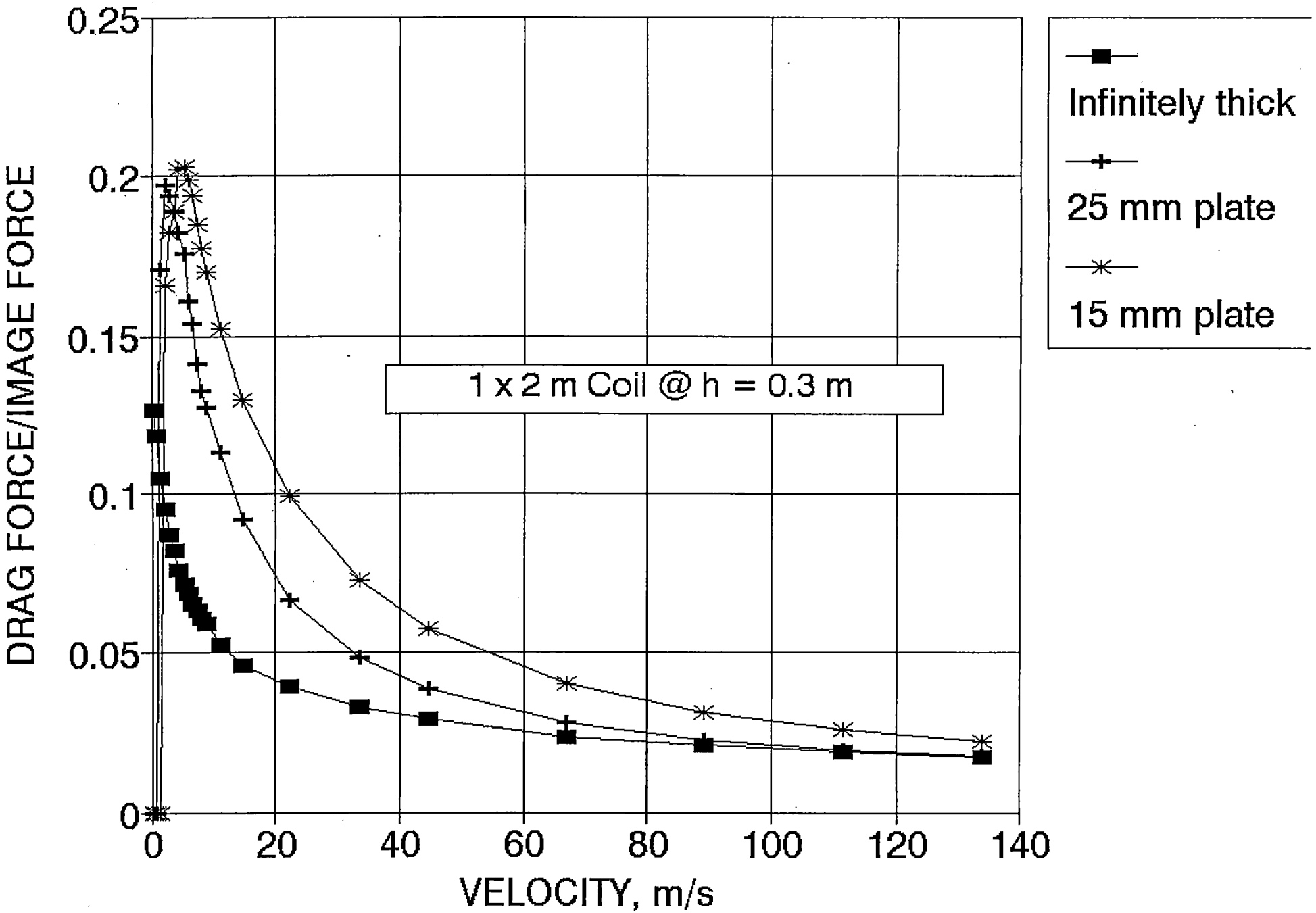
0.25
0.2
0.15
0.1
0.05
0
DRAG FORCE/IMAGE FORCE
0
20
40
60
80
100
120
140
VELOCITY, m/s
1 x 2 m Coil @ h = 0.3 m
Infinitely thick
25 mm plate
15 mm plate

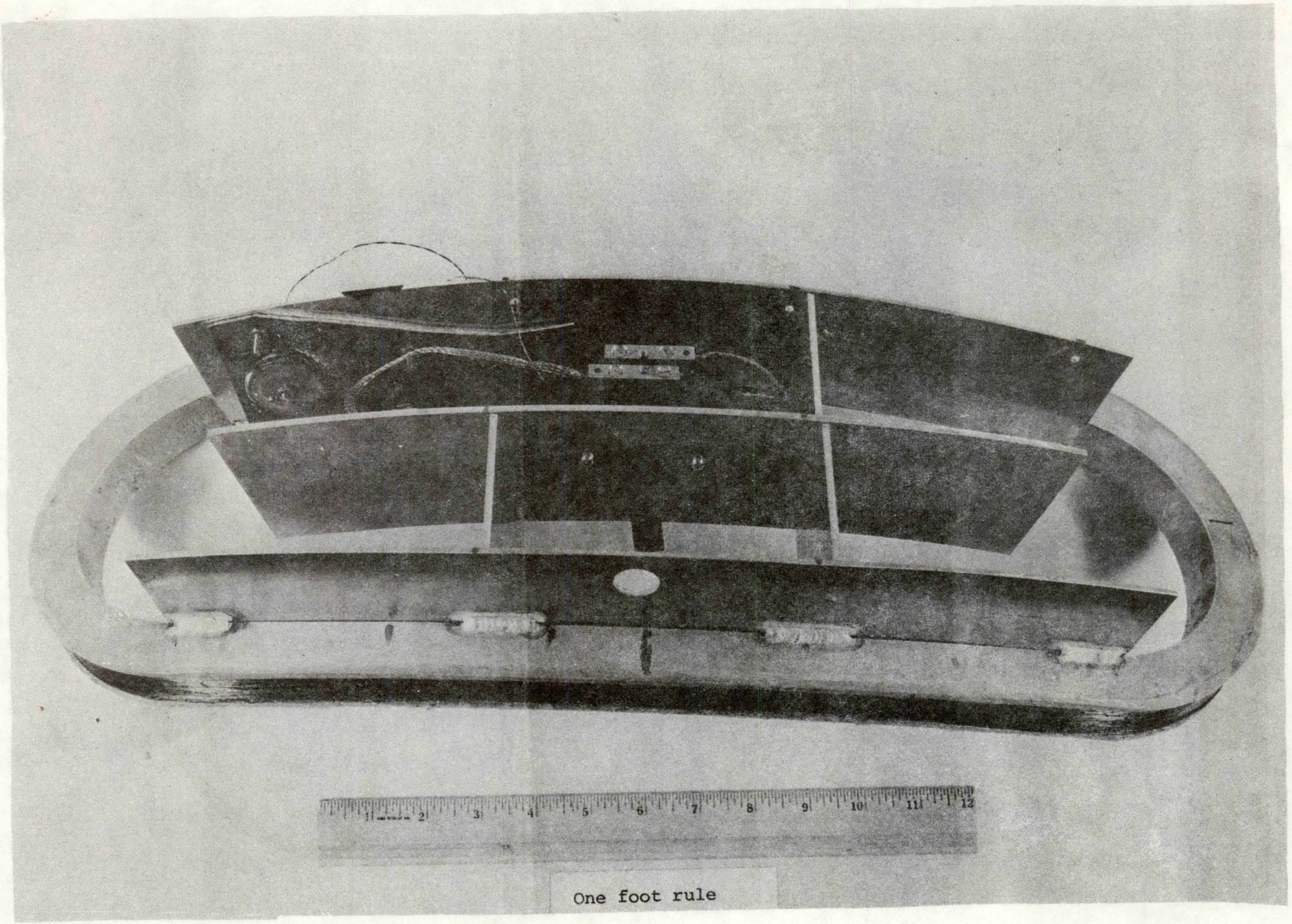

Fig. 2.20 Superconducting coil and coil form for the experimental magnet.

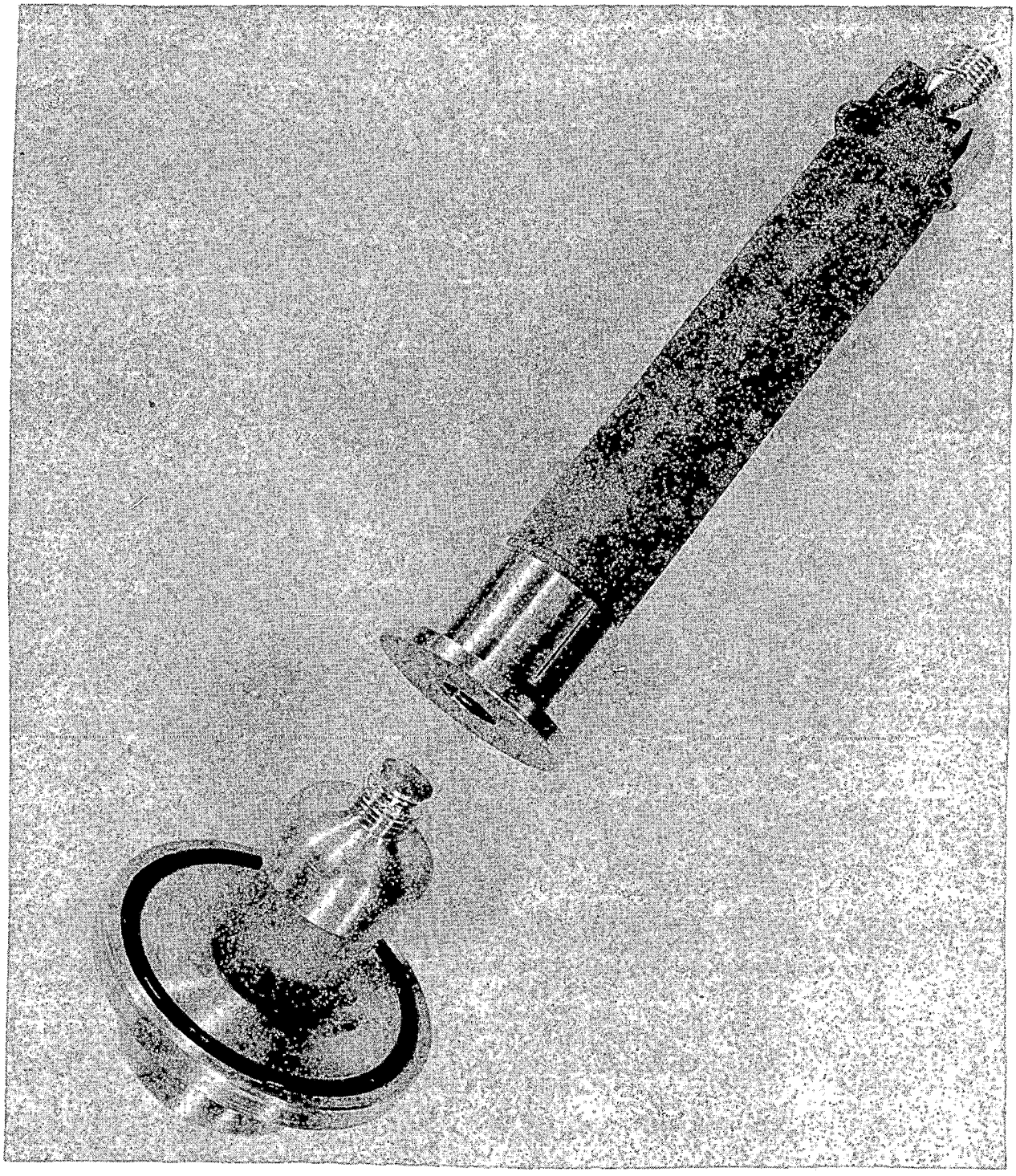

Fig. 2.21 Epoxy fiberglas strut for experimental magnet.

2.6.2. Fatigue Testing of Magnet Struts

Before the magnet was built force transmittal struts similar to those being considered in the magnet design were assembled and tested for ultimate strength and fatigue life. Tests were carried out at both room and liquid nitrogen temperatures. The test specimens (see Fig. 2.22) consisted of 1.5 inch diameter G-10 epoxy fiberglas columns 6 inches long with epoxied aluminum end caps.[9] The cross sectional area of the fiberglas column is 0.54 in^2 and the wetted epoxy area is 3.4 in^2. As shown in Fig. 2.22 two types of columns were tested -- one with a scarfed joint,[10] the other with a butt joint. The results are shown in Table 2.6.

The compressive strength value found, 59,000 lbs/in^2, is close to the handbook value for the G-10 material. The compressive strength test was the only one in which the G-10 material itself failed; in all the other tests failure, if it occurred at all, occurred at the glue joint between the column and the end cap. As Table 2.6 shows the scarfed joint performs better than the non-scarfed or butt joint in straight tension. However, the fatigue tests show a more dramatic difference -- the scarfed test specimen lasting over 5 times as long. Both joints were found to be stronger at low temperature than at room temperature.

2.6.3. Magnet Tests

The Ford magnet was operated at various persistent current levels from 22 to 45 amperes. The magnet was mounted on a tubular-frame lever arm so that it could be suspended over our 5 ft diameter, rotating aluminum wheel. This arrangement is shown in Fig. 2.23. The back end of the lever arm is pivoted at a fulcrum and the front end can either float free or be connected to our electrohydraulic shaker as shown in the figure. When the magnet was charged with 32 amperes it was able to support 50 kg at a suspension height of 8.6 cm.

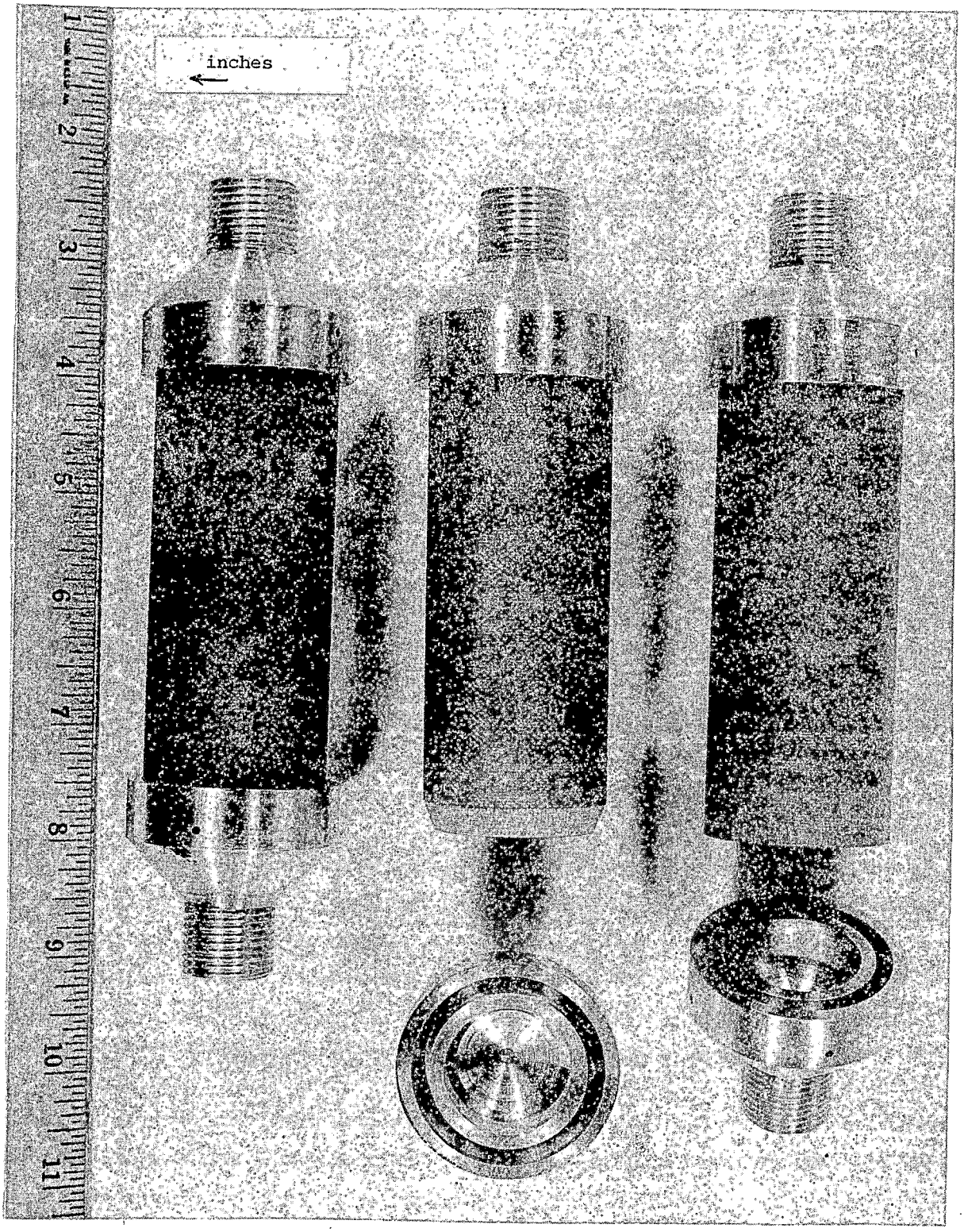

Fig. 2.22 Epoxy fiberglass columns for fatigue and strength tests.

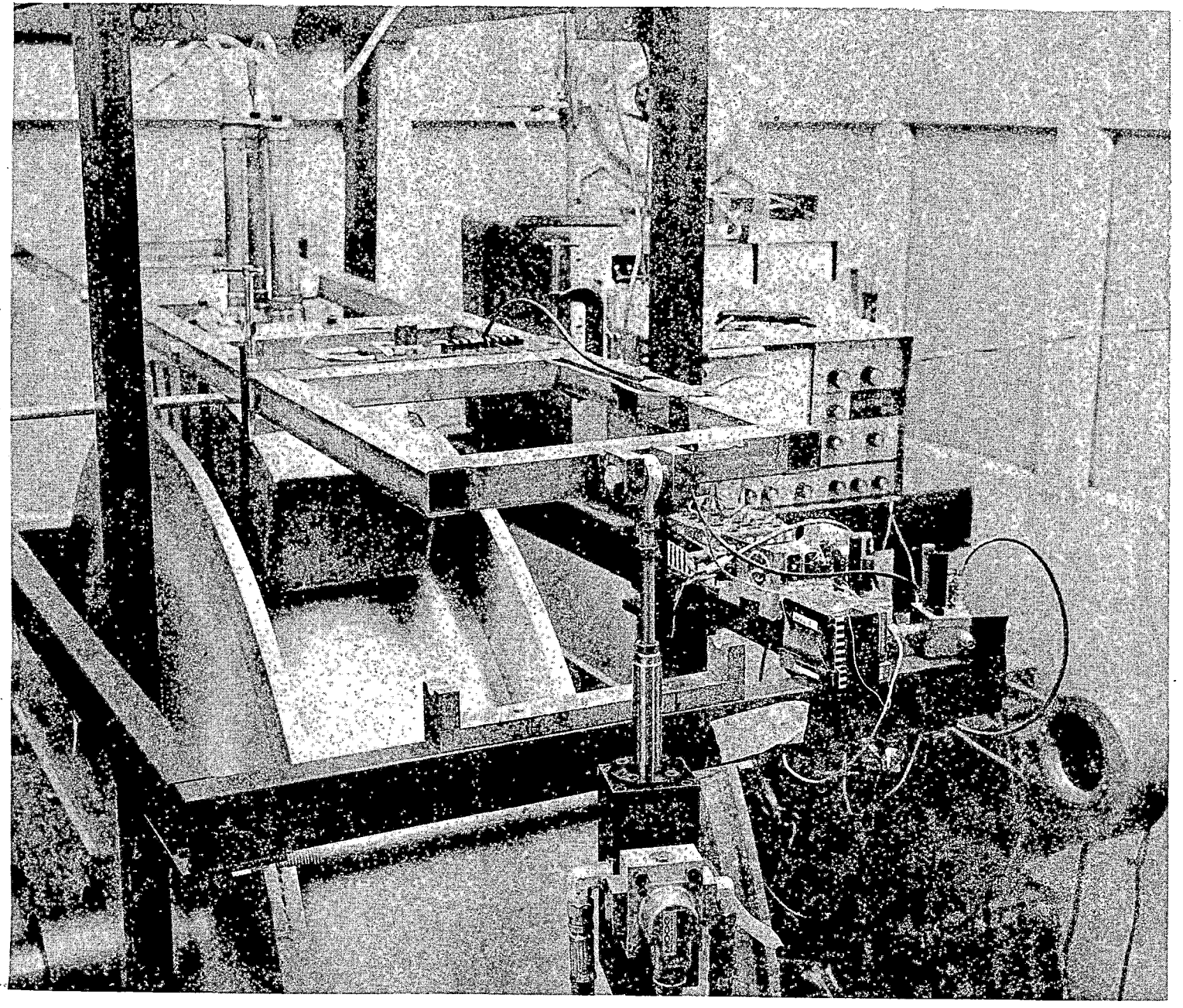

Fig. 2.23 Mounting of the experimental magnet for measurements above the rotating wheel.

As mentioned in Section 2.6.1. the helium and nitrogen boil off rates were both about 0.21 l/hr. These are low enough that the fully charged magnet-cryostat will operate up to 23 hours without refilling. It might be instructive to scale up the helium loss rate to that of a full-size coil for a revenue system (0.5 x 3 m) -- by multiplying by the ratio of coil areas. If we do this, we obtain 4.6 l/hr. We expect that this loss rate is higher than need be since no superinsulation was used in the small cryostat; nevertheless, the small dewar appears faily representative of the larger magnet on a unit area basis.

Table 2.6. Strength and Fatigue Testing of Magnet Struts

Sample	Joint	Temp. (°K)	Test	Failure	Remarks
1	Non-Scarfed	300	Tension	5000 lbs.	None
2	Non-Scarfed	300	Tension	4400 lbs.	11 Thermal Cycles
3	Scarfed	300	Tension	6600 lbs.	11 Thermal Cycles
4	Non-Scarfed	300	Fatigue	14,300 cycles	10 Hz Sinusoidal 2500 lbs. Tension 5000 lbs. Compression
5	Scarfed	300	Fatigue	71,300 cycles	"
6	Non-Scarfed	300	Fatigue	14,800 cycles	"
7	Scarfed	77	Fatigue	No Failure at 158,000 cycles	"
7	Scarfed	77	Tension	9,750 lbs.	Performed After Fatigue Test
8	Non-Scarfed	300	Compression	32,000 lbs.	None

The testing program for the Ford magnet had two major goals: (1) to determine ac losses produced either by mechanical vibration or by changing the current in a nearby control coil, and (2) to demonstrate that the magnet's vertical motion can be effectively damped with an active control system. In order to carry out this program a 400-turn control coil of the same dimensions as the superconducting magnet coil was mounted on the bottom plate of the outer vacuum can of the cryostat (See Fig. 2.24). ac losses were determined by measuring the increase in helium boil off rate.

(1) AC Loss

The control coil was connected to a variable frequency power supply and used as a source of ac field for the superconducting coil. The results of these experiments are shown in Figs. 2.25 and 2.26; in those figures the relative boil-off rate is plotted against frequency or amplitude of the control current. (Note that control current amplitude is listed in ampere-turns.) It will be shown later that the control current is of the right order of magnitude for control of magnet acceleration in the 0.2 to 0.3 g range, so that we are working at meaningful ac fields.

As shown in Fig. 2.25 the boil-off rate barely goes above background in the 1-2 Hz range, the dominant region of interest for control; on the other hand boil-off in the 10-20 Hz range is appreciable. The drop off in boil off at the higher frequencies is believed to be due to eddy-current shielding by both the intermediate temperature ($77^{o}K$) shield and the outer aluminum can.

The magnet was next mounted on its lever arm, but held rigidly, suspended over the rotating aluminum wheel, and the preceding set of experiments with the control coil were repeated. It was found that the ac fields produced by the control coil cause an 8% lower boil-off rate when the wheel is running compared to when it is stopped. (i.e., compared to results in Fig. 2.25). This is reasonable since when the wheel is

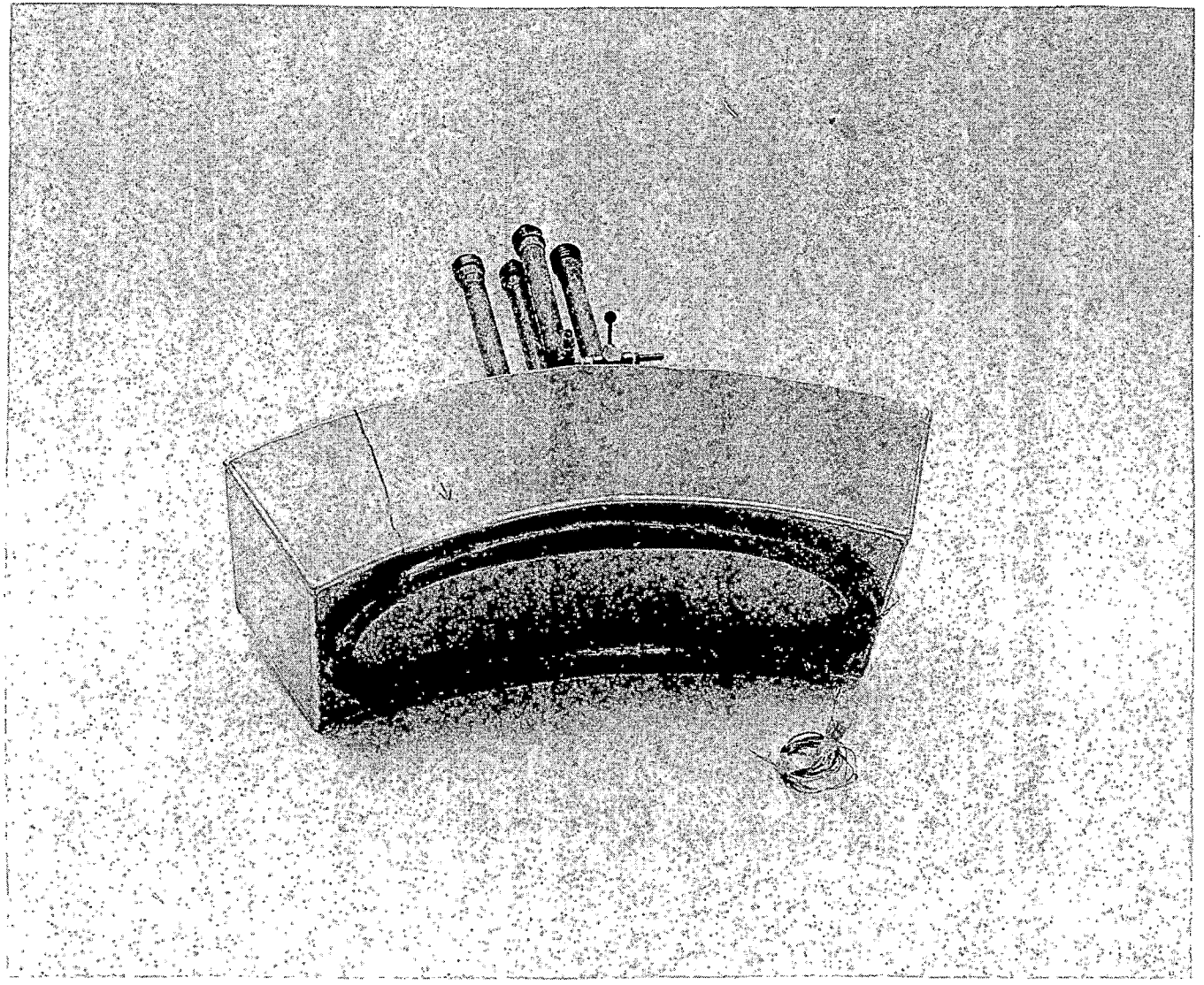

Fig. 2.24 Control coil for the experimental magnet.

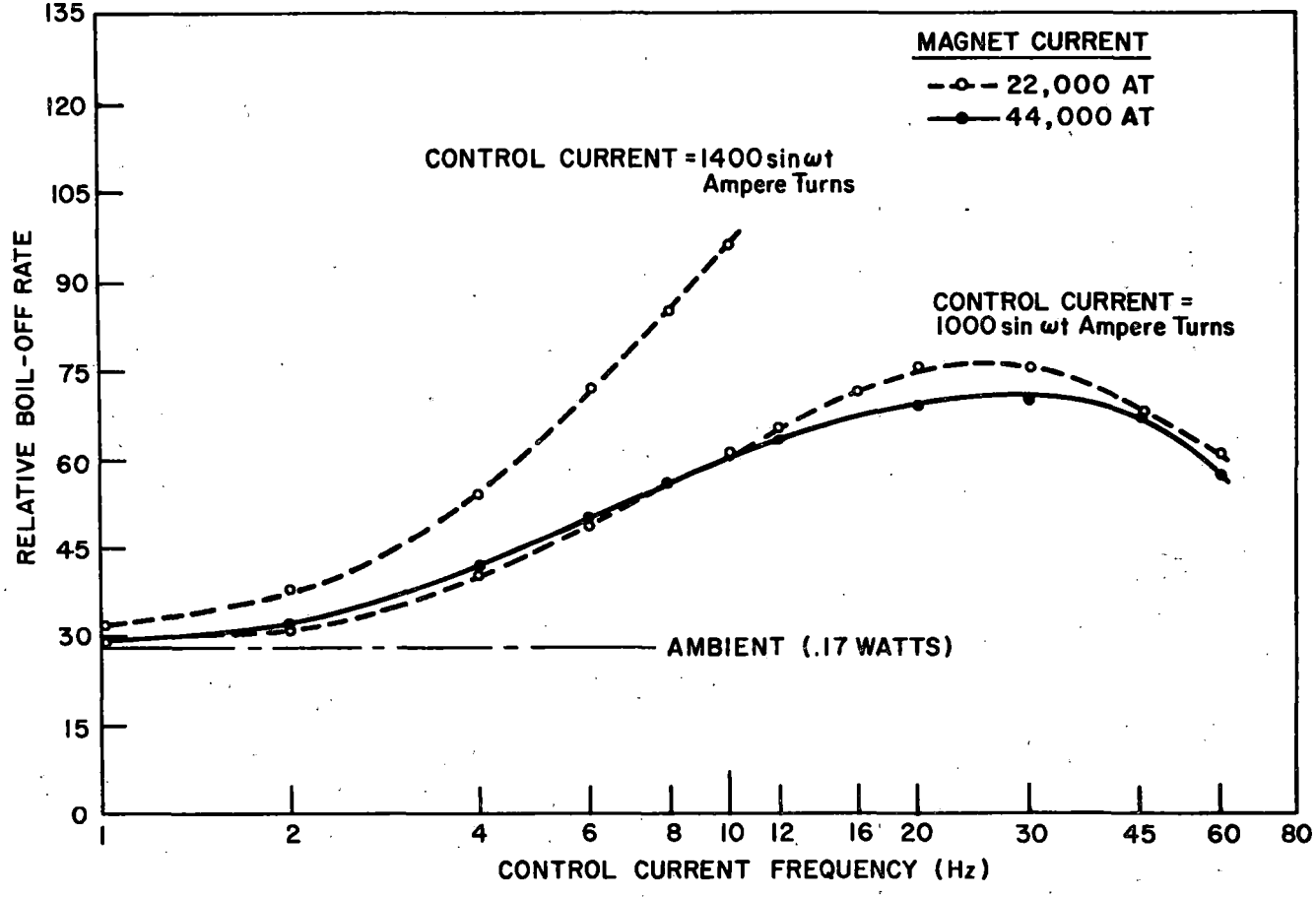

Fig. 2.25. AC loss in the Ford magnet versus frequency of the control coil current.

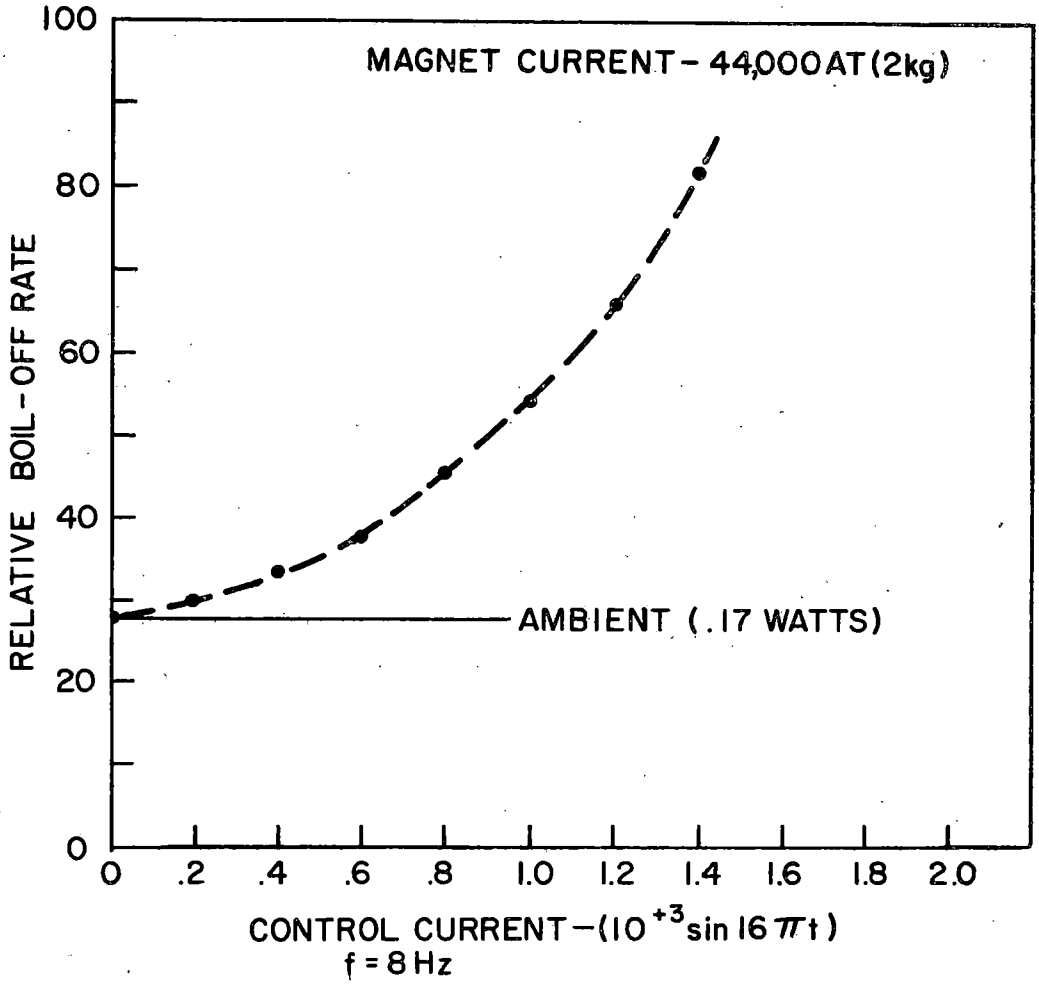

Fig. 2.26. AC loss versus control current amplitude.

moving there are additional image coils coupled into the system.

An ac current in the control coil causes an ac component in the levitation force when the coil is floating above the rotating wheel. The dynamic response of the floating magnet to constant amplitude ac current of various frequencies is shown in Fig. 2.27; it is largest at the natural frequency of the magnet (2.3 Hz for the case shown) and the width of the resonance is a measure of the damping.

Experiments were also done in which the lever arm holding the magnet was shaken by the electrohydraulic shaker (See Fig. 2.23) which was controlled by the Ford Mini-Servo System built by the Product Test Operations Office. (This device is capable of exerting a dynamic force of 700 lbs. over a range from 0.01 to 30 Hz.) The magnet was shaken at a variety of frequencies; measurement of helium boil off was made only at resonance (2.3 Hz). At 2.3 Hz, a magnet vertical amplitude of $\pm$ 0.57 cm (corresponding to a peak acceleration of 0.13 g) caused excess boil off equivalent to 0.027 watts. An amplitude of 1.14 cm (corresponding to 0.26 g) caused excess boil off equivalent to 0.12 watts.*

(2) Experiments Demonstrating Control

Figure 2.28 shows measurements of the vertical response of the magnet to a step displacement, both with and without active control. Without control the magnet is rather poorly damped, with a damping time $\tau \sim 1$ second. The calculated damping times for the various aluminum shields in the cryostat are given in Table 2.7. It is seen that the damping time for the intermediate temperature shield is fairly close to that which is observed for the system. In fact, since the intermediate temperature shield is near the optimum thickness for maximum damping, the effect of the other two aluminum plates is such as to decrease the damping somewhat from that of the predicted 0.85 sec.

* Calculations based on the equations in Section 5.2 of reference 1 give ac losses of 0.02 watts and 0.04 watts for these two cases, respectively.

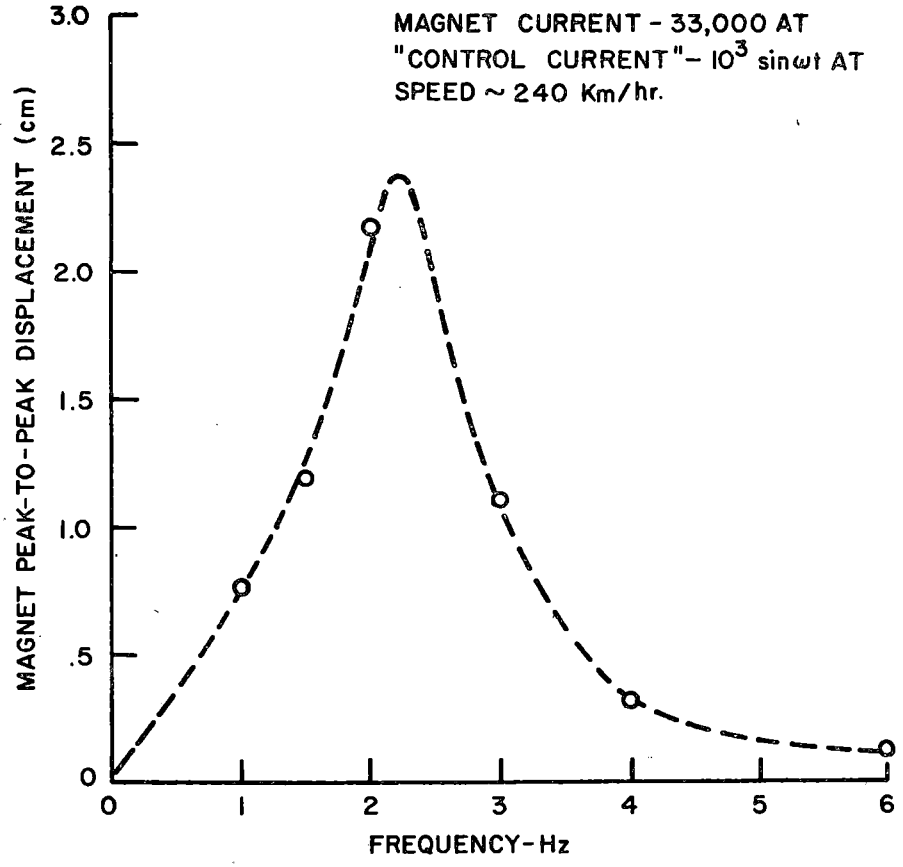

Fig. 2.27. Dynamic response of magnet to constant-amplitude ac current in the control coil.

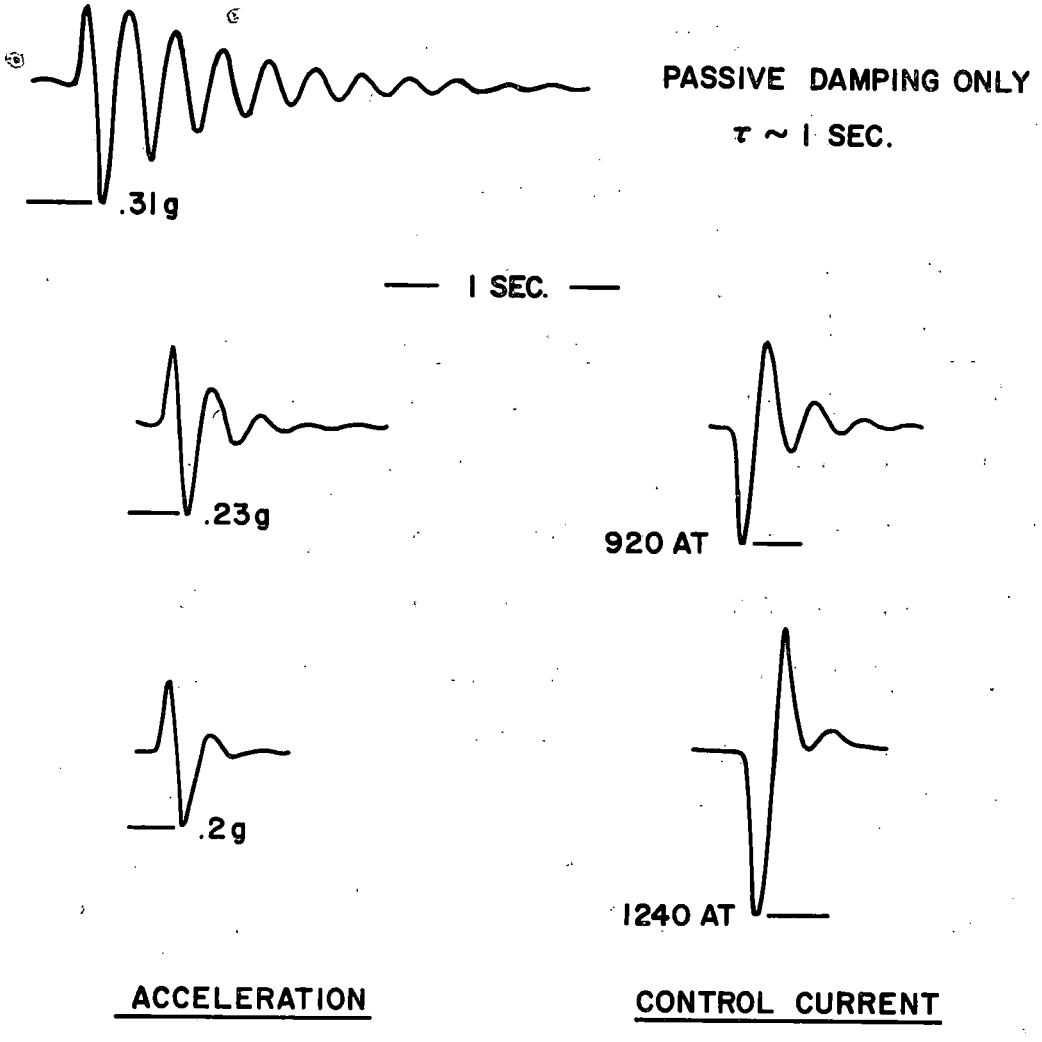

Fig. 2.28. Vertical response of magnet to a step displacement, with and without active control.

TABLE 2.7. Calculated Damping Times for the Various Damping Plates in the Ford Cryostat

Plate	τ (Calculated)*
Liquid He Plate	2.0 sec
Intermediate Temp. Shield (Liq. N_2)	0.85 sec
Outer Can	2.9 sec

Active control was achieved by sensing the magnet acceleration with an accelerometer and using a signal proportional to velocity to control the current in the control coil. As seen from Fig. 2.28 disturbances with peak accelerations of 0.25 g can be damped out in about 1 cycle with control currents of the size studied in (1) above.

(3) Effect of Helium Motion

The magnet was also shaken by the electrohydraulic shaker when there was no current in the magnet in order to determine the effect of sloshing the liquid helium. With accelerations of 0.3 to 0.4 g the increase in helium boil off was less than 5% over ambient. This implies that the boil off results described on the preceding page are due to ac loss.

* Each τ is calculated as if only one damping plate is present.

2.7. AC Loss Studies

One of the serious problems anticipated in the operation of a superconducting magnetically-levitated vehicle is the large loss expected in the superconducting coils when they are disturbed from their equilibrium current by interaction with irregularities in the guideway and by the active control magnets used to improve the ride quality of the vehicle over such irregularities.[1] An understanding of the magnitude of cryogenic losses from this source is important since some estimates[1,55] suggest that they will contribute from 1/3 to more than 1/2 the total cryogenic losses. A general review of ac loss has been given by Wipf.[11]

In conducting modeled experiments on ac loss one hopes to be able to use realistic values for both the static magnetic field and the ac field so that no theoretical interpretation will be necessary on these aspects. We operate with smaller coils for which the overall field configuration is quite different from that of the projected revenue vehicle though the field variations at the surface of the coil of wire will be quite similar. We have attempted to calculate the loss expected for the model coils and for the different types of wire under consideration using a variety of approximations. Although incomplete theoretical understanding of the detailed mechanisms still leads to discrepancies with the experiments we believe that the present experiments do model the behaviour of the projected revenue vehicle in a straightforward way which is essentially independent of the details of the theory.

2.7.1. Modeling

For lift coils on a revenue vehicle having a design current of 2.6×10^5 ampere-turns in a 3m x 0.5m coil and with an average current density of $10^8 A/m^2$ we can deduce a reasonable figure for the operating

dc field at the windings. For a wire packing fraction of 0.75 to allow for liquid helium ventilation, the field at the surface of the bundle will be of order 1.6 tesla. It should be possible to reduce the peak fields and decrease the loss significantly by winding the coil with an expanded wire bundle of still lower average current density.

We consider the ac loss situation for three different control strategies, for which other relevant calculations are performed in this report. Each is expected to give acceptable ride quality for a guideway roughness $A = 5 \times 10^{-6}$ ft. Case 1 involves control using compensating current directly in the windings of the lift magnets and requires at 1.2 Hz an rms ac current 2.71% of the dc level. Case 2 uses a separate control coil and requires only ±1.27% at 1.2 Hz. Case 3 uses a secondary suspension with optimum passive damping and requires ±1.12% at 3 Hz. We have performed our experiments to investigate the losses through this amplitude range as a function of frequency and dc field.

The actual loss mechanism involves the motion of trapped flux vortices against their pinning centers but this process itself is not subjected to detailed calculation here. Rather the penetration of the ac field into the superconductors is assumed to follow according to the Bean-London critical state model[12] and Maxwell's equations are then used to deduce the resulting loss when a current flows by employing the relation

$$\text{Loss per unit volume} = \int_V \underline{E}(\dot{\underline{B}}) \cdot \underline{J} \, dV \quad . \tag{2.27}$$

Calculations using this approach are presented in Appendix A for the sample coils used in the present experiments and predict quite different loss rates for multicore wire and for single core wire. These differences result from the size of the superconducting strands which in typical multicore and single core wires straddle a critical size region.

2.7.2. Experimental Approach

The ac loss in our experimental coils was measured using the helium boil off technique[13] which consists simply of monitoring the increase in gas flow from the dewar under ac excitation and calibrating this against a known heat input, provided, in this case, by joule heating in a resistor contained in the sample chamber. In order to avoid possible uncertainties due to variable input currents to the sample coil, an inductive technique was used to induce the ac currents in the persistent mode test coil. This also provides a more accurate simulation of the conditions anticipated for a real vehicle since the sample coil is also in the persistent mode during the model experiment. The experimental arrangement is shown in Fig. 2.29. A nested set of 3 dewars is used so that the large superconducting driving coil may be run independently of the sample coil which has its own dewar. Trapped fields are introduced into the sample coil by operating a heater switch while a dc field is applied using the drive coil. Trapped currents up to the critical current of the sample coil may be introduced by this method.

In order to avoid ambiguities in the determination of the equilibrium flow the flow was monitored every 10 seconds using a Precision Scientific Co. "Wet Test" flow meter with a digital shaft encoder readout, an averaging electronic counter, a digital to analogue converter and a strip chart recorder. This system allows the approach to equilibrium to be monitored even for the rather low differential flow rates of order 1 ml/sec which are often encountered in these experiments on small sample coils (see Fig. 2.29).

The field trapped in the sample coil is monitored using a small bismuth magnetoresistance probe (American Aerospace Controls, Inc.-MRA-11) mounted at the center of the sample coil. From this and the known coil

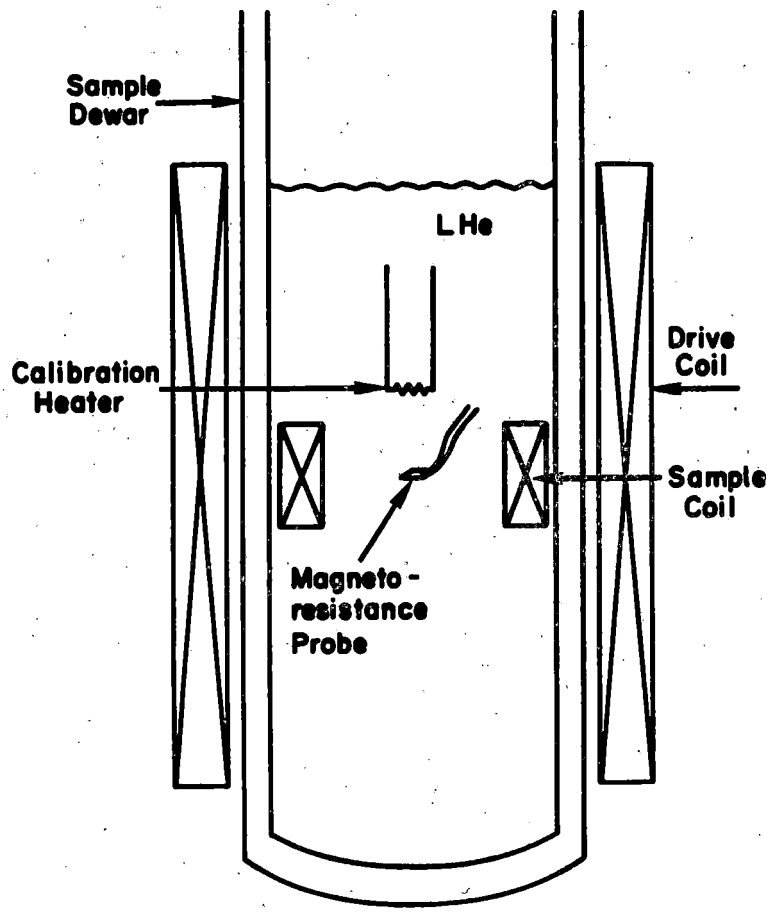

FLOW MONITORING SYSTEM

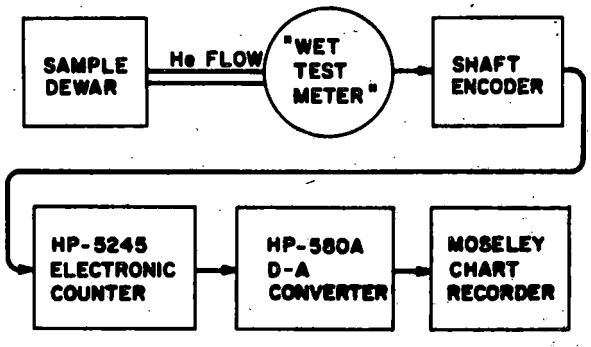

Fig. 2.29. Diagram of the apparatus for measuring power dissipation in a persistent mode superconducting coil subjected to an ac magnetic field.

geometry the trapped current is easily deduced. The additional heat loss introduced by this measurement is less than a microwatt and is negligible.

The coupling between the drive and sample coils can be readily calculated. Using this relation we have measured the critical current in the sample by noting the drive current at which substantial flux leakage into the sample coil first occurs.
Typical calculations are discussed in Appendix A. In this report we shall discuss mainly the loss results for three "ventilated" coils for which the sample coil current $I_s = 1.94\ I_d$ (I_d = the drive coil current). Two of these coils were wound with a multicore NbTi wire ("Kryoconductor"-180 strands) and the other one with a single core NbTi wire ("SC 8-15"). Both wires have the same outer diameter and all three coils have essentially identical dimensions and number of turns.

Initial calibration runs were made in the absence of a sample coil so that the bismuth magnetoresistance probe could be calibrated against the known field of the superconducting drive coil without the shielding effect of the sample coil. A check was made at this point to see if ac excitation of the drive coil (which produces boiloff from the drive-coil dewar) had any effect on helium loss from the sample dewar. For the experimental configuration used, such effects were found to be negligible.

Typical procedure involves a background boil off rate determination with no ac excitation, a loss test with excitation and a $2^{\underline{nd}}$ background level reading. Typical equilibrium times (to ~95% of final value) range from 2 to ~10 minutes and are shorter for the ventilated sample coils than for the potted coils tested earlier. Measurements of the critical current obtained by noting the drive coil current at which flux leaks

into the sample coil yields values in rather good agreement with the manufacturer's data for the sample coil wire, thus lending further support to the calculations performed on the drive coil fields and the coupling.

In the early experiments with potted coils (Torr-seal epoxy; Pliobond) difficulties were encountered for loss rates above about 60 to 80 milliwatts as the result of internal heating of the coils. For the multicore coils this led at higher frequencies and drive levels to thermal runaway and extreme losses. Those tests were terminated to prevent the coil from reaching its transition temperature. For the ventilated coils there is no evidence of inadequate cooling at the test levels we have employed.

In Fig. 2.30 we have plotted for both single core and multicore ventilated coils the loss per cycle Q/f as a function of the driving field level which is indicated by I_{do} (the peak amplitude of the current in the drive coil). In Appendix A it is shown that anticipated revenue vehicle conditions are simulated by I_{do} from 0.3 to 1.0A. The losses have been plotted for experiments run at a variety of frequencies as shown and illustrate the expected fact that at these field and frequency levels the losses are linearly proportional to the frequency of the applied signal. At higher frequencies this is direct evidence that there is no thermal runaway problem which would necessarily bring in non-linear terms. This is further evidence in the multicore case that eddy current losses due to insufficient decoupling of the filaments are not important at these levels since eddy current losses scale with f^2 rather than with f linearly.

In Fig. 2.31 we have shown the actual loss rate $\dot{Q}$ as a function of driving field for three coils at a variety of persistent current levels. As will be readily seen from the consistency of the data for both types of

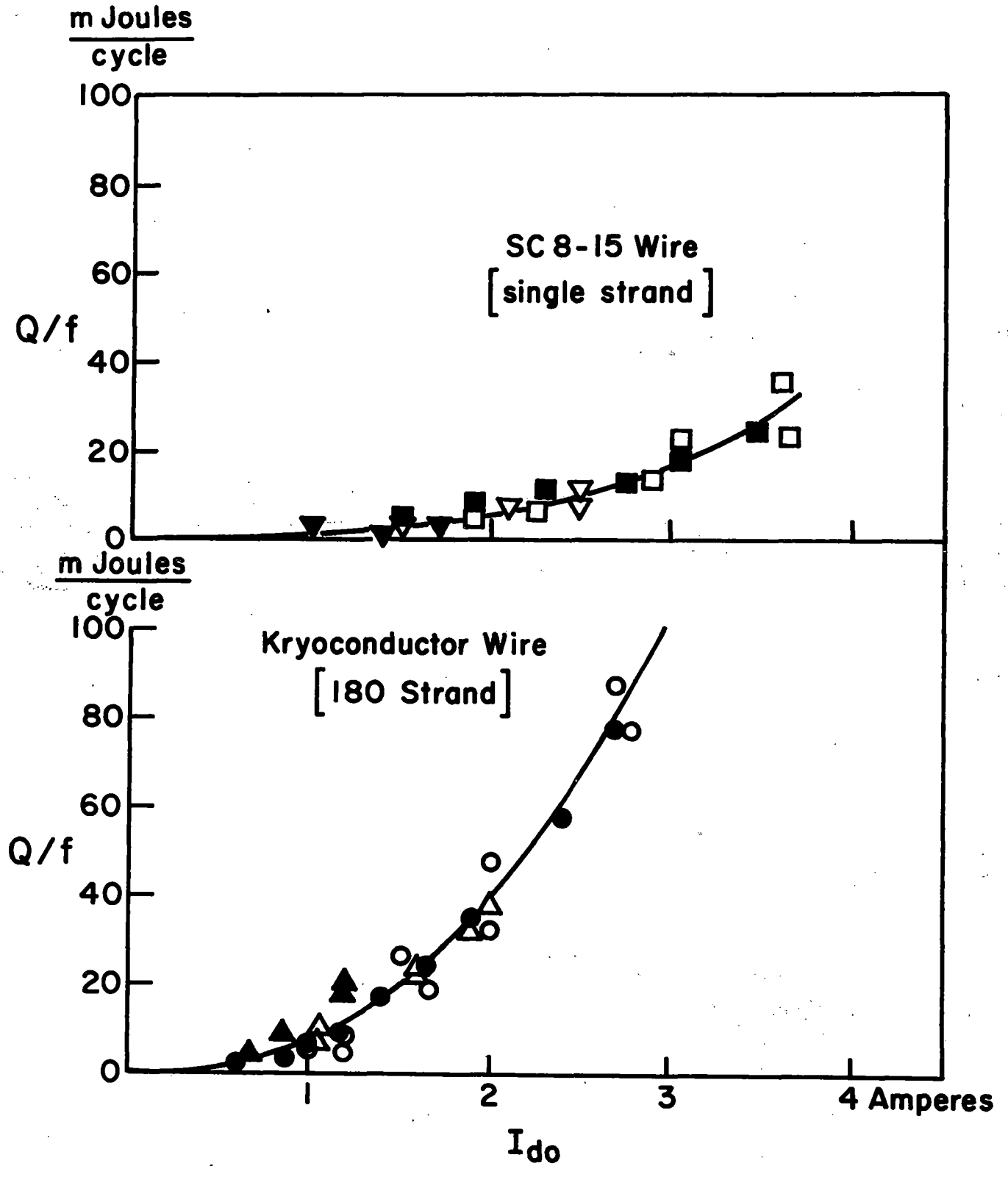

Fig. 2.30. Energy loss per cycle vs. driving field level.

Single core wire SC 8-15 - Coil #7, □ 1.0 Hz I_p = 0; ■ 2.0 Hz I_p = 0; ▽ 3.0 Hz I_p = 7.3A; ▼ 4.0 Hz I_p = 27.5A.

Multicore Wire. Kryoconductor - Coil #8, ○ 1.0 Hz I_p = 0; ● 2.0 Hz I_p = 0; △ 4.0 Hz I_p = 0; Coil #9. ▲ 7.0 Hz I_p = 29A.

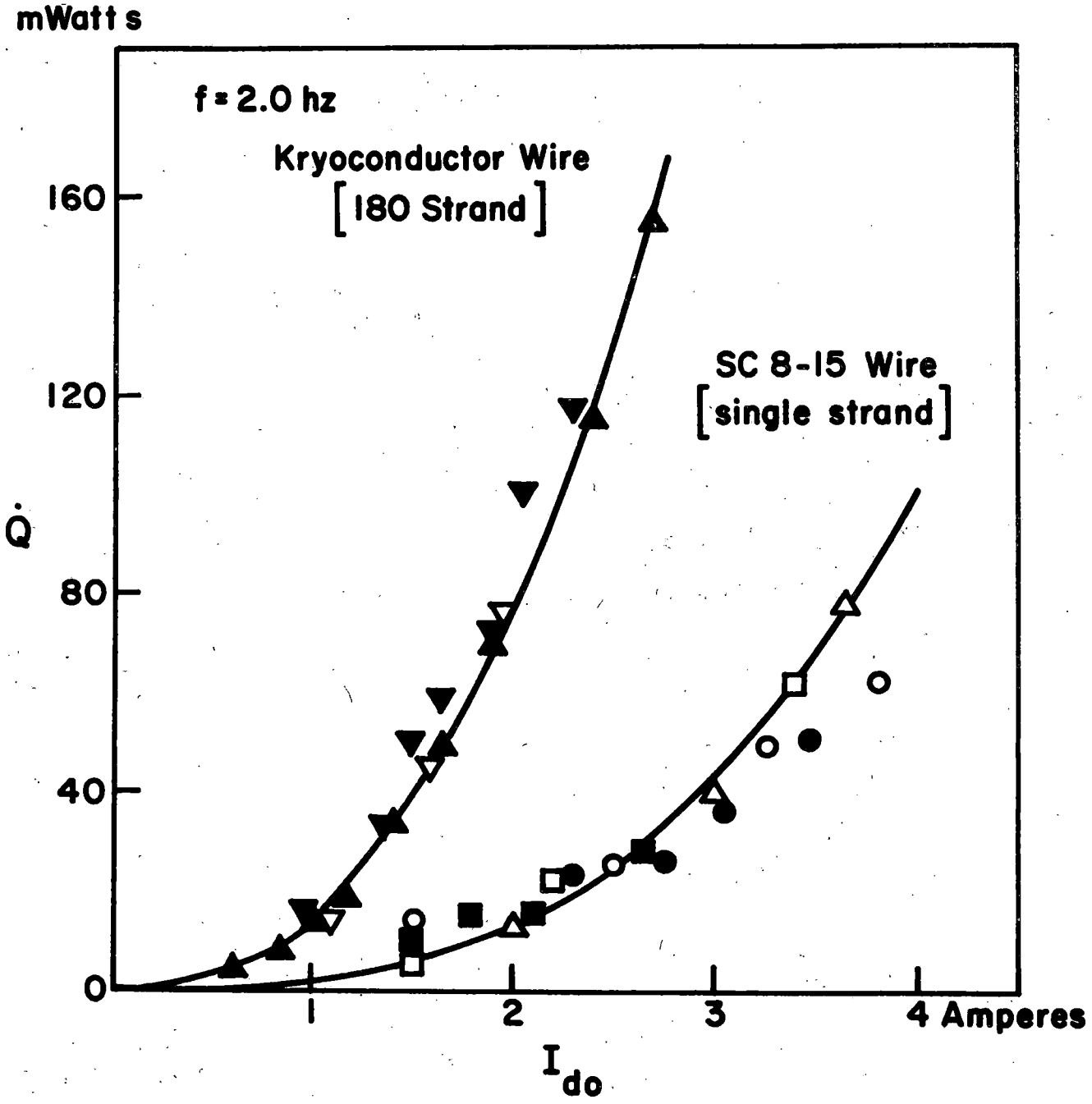

Fig. 2.31. AC loss in ventilated coils at 2.0 Hz.

Kryoconductor-Multicore Wire Coil #8, ▲ I_p = 0; Coil #9, ▽I_p = 0; ▼ I_p = 20.2A.

SC 8-15 - Single Core Wire. Coil #7, ● I_p = 0; ○ I_p = 7.3A; ■ I_p = 14.3A; □ I_p = 24.1A; Δ I_p = 26.9A.

coil the loss rate is not appreciably affected by the presence of a persistent current within the range studied. For this coil geometry the persistent current needed to simulate the dc field levels expected for revenue vehicle coils is about 30 amperes. Note that because these experimental coils have a smaller bundle size (2 cm diameter vs 4 cm) a smaller effective coil diameter the and/much/ current densities required to achieve these full scale fields are larger, and closer to the critical value. Nevertheless the dc <u>self field</u> levels at I_p = 30 A are not sufficient to appreciably lower the critical current density of the NbTi and we thus do not expect much change in the loss rate at these dc levels.

It may easily be seen that the losses for the multicore wire are much greater than for the single core wire throughout the range studied and at all persistent current levels. This is a result of the fact that the maximum penetration depth of the ac field is larger than the multicore filament radius and smaller than the single core radius throughout the experimental field ranges.

The solid curve for the single core wire is a cubic fit to the data, as suggested by the analysis discussed in Appendix A. The solid curve for the multicore wire is merely drawn through the data points. Eq. (A2) can give nearly as good a fit, but only if we permit an adjustment of J_c. Data are shown for both coils #8 and #9 made of the same multicore wire and in the standardized configuration. The results are quite reproducible suggesting that accidents of the assembly process do not bear strongly on the observed loss.

In the course of these experiments with the persistent coils subjected to ac currents some 4 to 5 times larger than we normally

anticipate for the revenue vehicle we do not see any evidence for substantial decay of the persistent current over periods of several hours. The stability of the single core wire may well turn out to be adequate for the purposes envisioned and one can expect to find significantly lower losses for this material than for the multicore wire generally proposed for these magnets.

2.7.3. Conclusions

The implications of these results are rather striking. It is clear from our early work that adequate ventilation of the levitation coils to liquid helium is essential to avoid excess loss due to thermal runaway. For the 1.2 Hz separate control coil case discussed above we project a per coil loss on the revenue vehicle of $\dot{Q} \approx 2.5$ watts for the 180 strand Kryoconductor wire and $\dot{Q} = 0.08$ to 0.3 watts for the SC 8-15 wire (see Appendix A for details).

It would appear advisable to learn more about the stability of ventilated coils made from single-core wire since for small ac fields these coils have losses lower than their multicore twins by as much as a factor of 6. Expansion of the wire bundle to provide better cooling will also reduce the average current density and ac field levels seen by the wire, and thus should further reduce the loss. In this connection it appears likely that the single-core wire will be more responsive to such field reductions, with anticipated losses dropping as a^{-3} where a is the radius of the wire bundle forming the coil.

2.8. Magnetic Shielding

The superconducting magnets required for the repulsive-force magnetic suspension must produce a 0.15 to 0.2 tesla field at the track in order to support the weight of the vehicle. With no shielding the

magnets will produce a comparable field 0.3m above the magnet. Calculations show that the maximum field produced by the 0.5 x 3m coil at the floor of the passenger compartment (70 cm above coil) is around 0.05 T (500 gauss). Such fields are probably not harmful to human beings, but they may cause a certain amount of inconvenience. A magnetic field of 200 gauss or larger will affect the operation of some watches, and such a field may also influence the operation of certain electronic equipment such as electronic pacemakers. It is believed, therefore, that some magnetic shielding will be required in the revenue vehicle to reduce the field in the passenger compartment.

Reduction to below 50 gauss at all parts of the passenger compartment would be a desirable goal, but it is not clear whether this can be accomplished without either an excessive shield weight or the loss of potential passenger space.

There is substantial literature on the biological effects of magnetic fields.[14] The breadth of the biomagnetic experiments which have been reported is large; however, the depth of the experimentation has been quite limited. In very few cases have more than one author done the same experiment, and in essentially no case has a clear-cut physical or chemical interpretation of the experimental data been established. Concerning static field biomagnetic phenomena, which is the area of interest here, the principal deliterious effects which have been reported involve either large magnetic fields (>5000 gauss) or large field gradients (>5000 gauss/mm). An exception to this, and one which bears directly on the problem at hand, is the observation[14a] that persons exposed to low intensity magnetic fields under industrial conditions often show a short term desynchronization in their electroencephalogram (EEG). On the other hand,

Friedman, Becker and Bachman[14b] studied the response time of humans subjected to static fields of 5 to 17 gauss and found no effect; when this was changed to a slowly modulated field (0.1 to 0.2 Hz) it was found that the subjects exposed to the magnetic field had a decreased response time. This area, functional changes in the central nervous system produced by low intensity static fields, is one which deserves further study. Other low field effects involve the observation that certain animals, such as migratory birds and insects, are sensitive to small magnetic fields and do in fact use the geomagnetic field for orientation, but such effects do not appear to have any analogue in terms of human response.

Among the high field effects studied[14c] M. and J. Barnothy exposed mice to fields of 9000 gauss and found that platelets in the blood increased 25% by the third day, then decreased to normal by the 10th day; the amount of platelets also increased upon removal of the field. It is believed that the amount of platelets in the blood is affected by stress; however, it is not known whether the magnetic field effect is proportional to the field or requires a threshold. Beischer exposed squirrel monkeys to fields up to 92,000 gauss; he noted an increase in both the frequency and amplitude of the EEG traces. A number of investigators have exposed pupating insects to large field gradients ($\sim 10^4$ gauss/mm) for periods of several minutes to an hour and have observed effects such as increased development time, sterility, and in some cases death to the insect.

Since there are no decisive low-field biomagnetic experiments which show harmful effects to man, we conclude that the levels suggested in the first paragraph are reasonable; i.e., the passenger compartment should be shielded to below 200 gauss; and a 50 gauss goal would be desirable.

It should be noted that the maximum field in the passenger compartment occurs at floor level. As will be seen in Fig. 2.33 the field drops by more than a factor of two for a 40 cm increase in distance above the coil. Thus a 200 gauss field at the floor would translate to somewhat less than 100 gauss at seat level. Further research on changes in the electro-encephalogram of persons exposed to static fields in the range of 50 to 500 gauss would be desirable, to establish whether there are any low grade effects (such as fatigue) or long term effects.

2.8.1. Types of Magnetic Shields

Shielding of the superconducting magnets can be accomplished in one of three ways: through the use of (i) ferromagnetic shielding material, (ii) a superconducting shielding coil or coils or (iii) a sheet of superconducting material. The simplest shield uses ferromagnetic material (e.g., iron) placed between the magnet and passenger compartment. There is no need to put the shield inside the dewar. For the same magnet current the lift force is increased somewhat by using the shield. The disadvantage of this scheme is the added weight of the shield; with the weight of material that one can afford to carry, shielding is incomplete and the material is magnetically saturated.

Schemes (ii) and (iii) should be capable of much better shielding per unit weight of shield material but do require that the shield material be at liquid helium temperature. In scheme (iii) the shielding can be quite effective provided the shield material extends considerably beyond the coil dimensions; this would require a larger and more complicated dewar system. In both schemes (ii) and (iii) the currents in the diamagnetic shield reduce the net lift force achievable with a fixed magnet current.

Consider first ferromagnetic shielding (scheme i). The configuration would be something like that shown in Fig. 2.32. The shield material is iron or some other ferromagnetic alloy of similar density. Because we want the shield to be relatively thin (to reduce shield weight), the material will be at or near magnetic saturation. We can reduce the tendency toward saturation by placing the shield farther from the coil, but then the shield must overlap the coil more and this adds weight to the system. Because of magnetic saturation the analytic problem is non-linear; the only practical method of solution is to use a relaxation procedure. Magnetic Corporation of America (see reference 8) has used this technique to evaluate various thickness iron shields for a 0.5 x 3m coil carrying 3.0×10^5 ampere turns. Actually the relaxation procedure used is a two-dimensional one so that the coil length does not enter except in the calculation of shield weights. Since the levitation coils are quite long compared to their width, the procedure is fairly accurate for fields in a vertical plane which passes transversely through the midpoint of the coil.

Fig. 2.32 shows the magnetic field at various heights z above the 0.5 x 3m coil for two different shield thickness (2 and 4 cm of iron). z = 70 cm might perhaps be taken as the floor of the passenger compartment although from the dewar design of Section 7.4, the floor of the compartment could be situated as low as z = 50 cm. The shield weights for the 2 and 4 cm shields are 2250 lbs and 4300 lbs respectively. The maximum field at several heights above the coil as a function of shield thickness is shown in Fig. 2.33. (The field of the unshielded coil can be obtained from Fig. 2.34; since that figure pertains to a coil with NI = 2.6×10^5 A-turns, the field of the 3×10^5 A-turn coil is 15% larger.)

Fig. 2.34 shows the effect of shielding with a superconducting coil. The 0.5 x 3m suspension coil carrying 2.6×10^5 ampere turns is

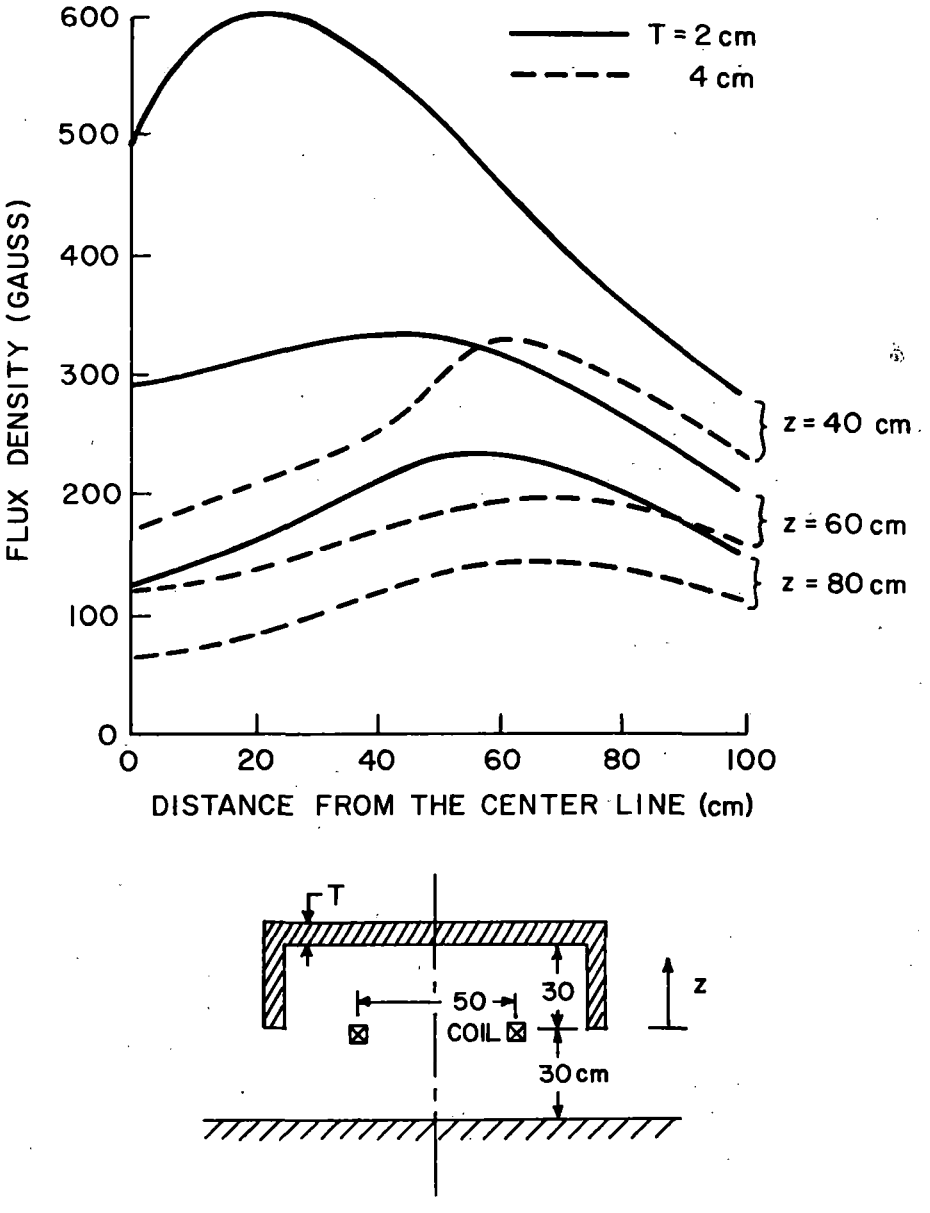

Fig. 2.32. Effect of shielding the levitation coil with various thicknesses of iron.

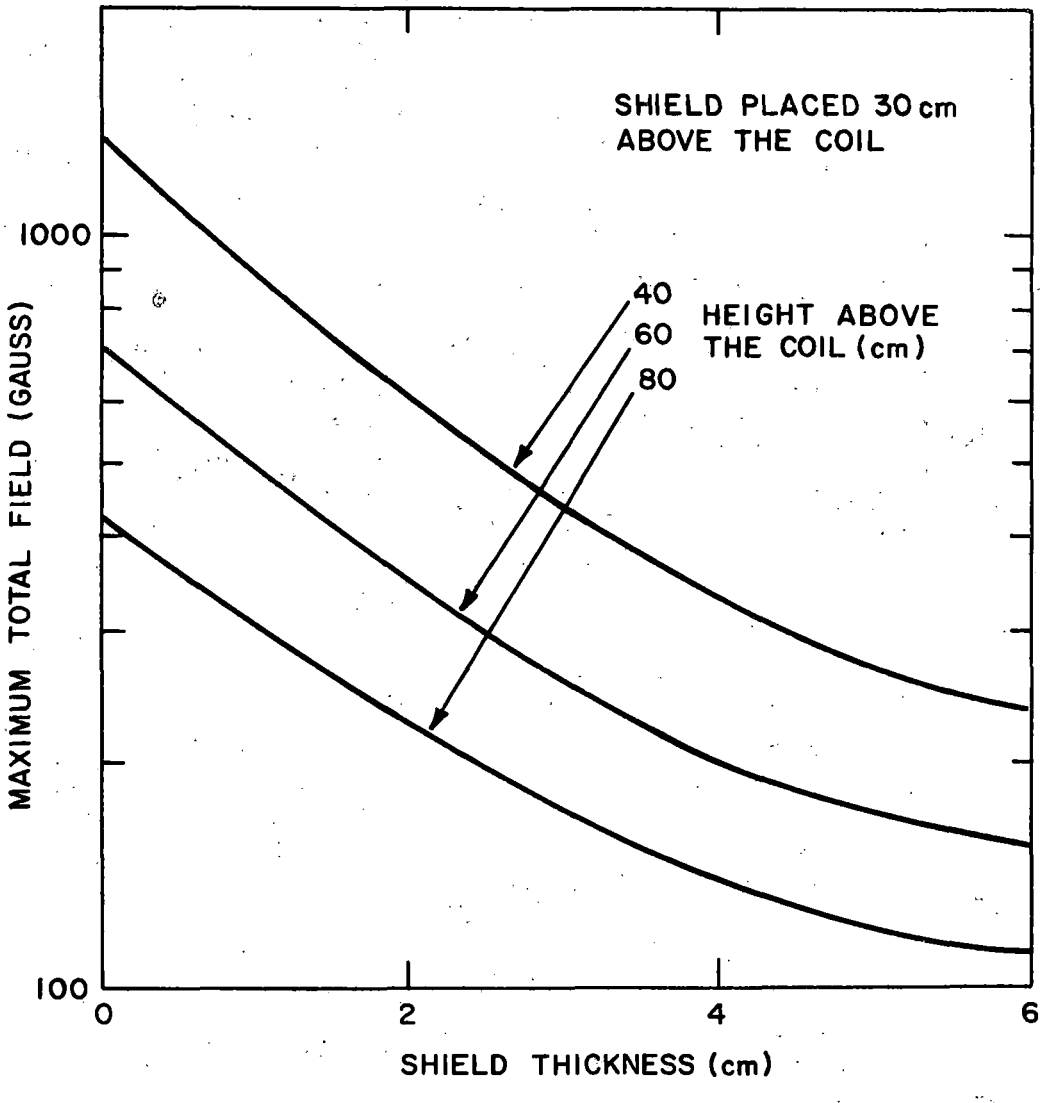

Fig. 2.33. Maximum field above the levitation coil as a function of shield thickness

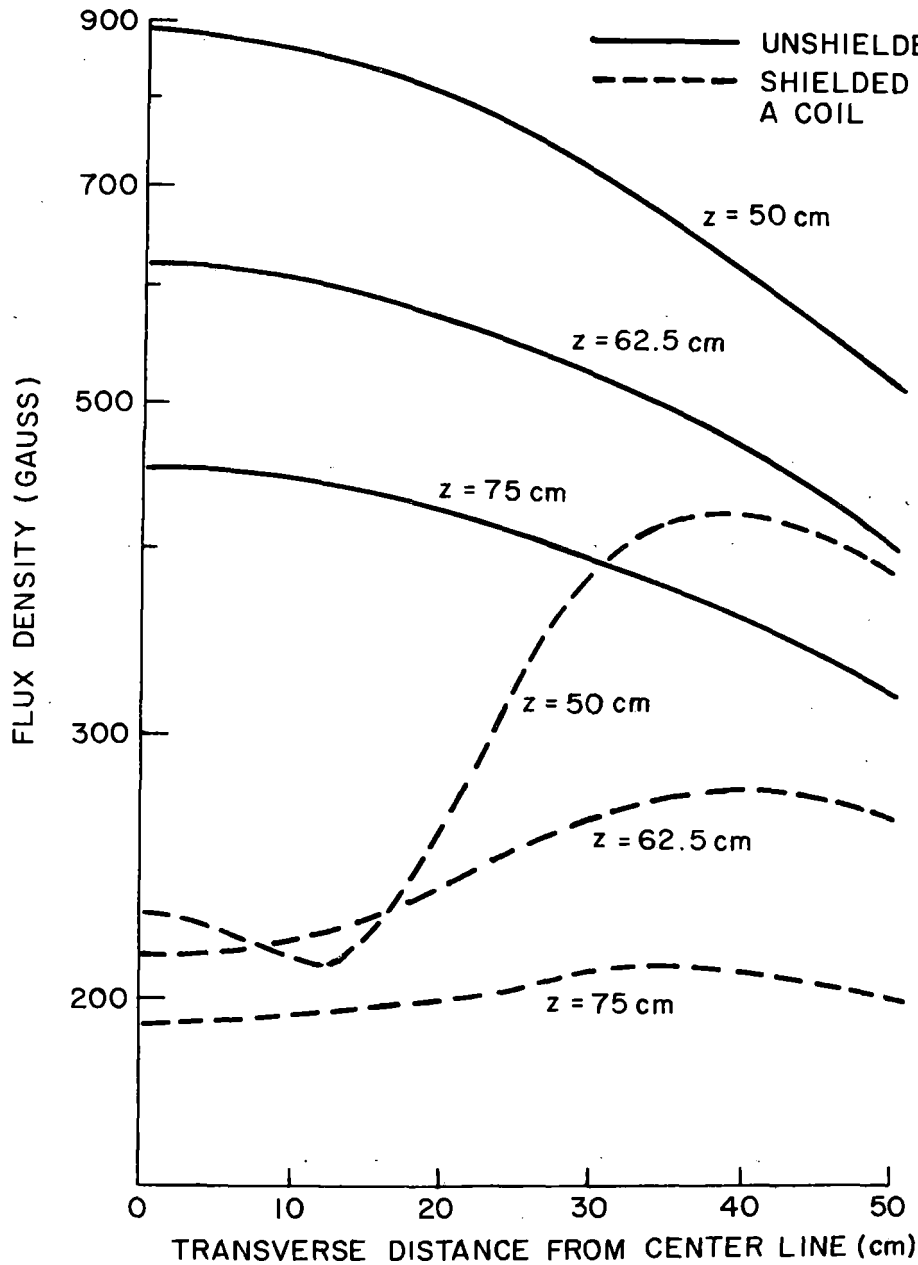

Fig. 2.34. Effect of shielding the levitation coil with another superconducting coil.

shielded by an identical coil, carrying -0.65×10^5 ampere turns, which is situated 30 cm above the suspension coil. The reduction in lift caused by the shielding coil is about 14%; i.e., the currents in the magnets would have to be increased by about 7% to get the same lift as the unshielded magnet. Even so this seems to be more effective shielding than 2 cm of iron. The extra weight needed for the shielding requirement is estimated as 200 lbs for the shielding coil and its helium can, 130 lbs for enlarging the outer dewar, and 40 lbs for additional structural support.

Of the two methods the second is the better one because the weight penalty is so much smaller. Nevertheless, even with an optimization of the latter scheme it does not appear possible to reduce the field in the passenger compartment much below 200 gauss unless one uses more than one shielding coil.

The most effective shielding is a sheet of superconducting material. The local supercurrent required to shield a magnetic field B is B/μ_o; thus a 0.2 T field requires a shielding current of 160,000 amperes. But the critical current density of both Nb_3Sn and NbTi alloys is larger[14b] than 10^6 amperes/cm^2 at 2000 gauss; thus a 2 mm shield thickness is adequate magnetically. Of course such a thickness would not be adequate from a structural point of view since there are large magnetic forces on the shield. Thus the shield must be reinforced with light-weight ribbed structures. Furthermore, to be effective the sheet shield must extend considerably beyond the levitation coil dimensions, and all parts of the shield must be maintained at liquid helium temperature. No design of a sheet superconducting shield has been made, but it seems clear that the weight penalty would be substantially larger here than for the coil shield discussed in the preceeding paragraphs.

3. ELECTROMAGNETIC (ATTRACTIVE) SUSPENSION

In this suspension ordinary electromagnets, moving with the vehicle are suspended below a steel track. This type of arrangement is unstable, so that the position of the magnets relative to the track must be sensed and the current in the magnets controlled by a feedback-control system. In order to operate with reasonable amounts of suspension powers the nominal gap between magnets and track should be 15 mm or smaller.

The attractive suspension achieves its maximum lift F_L at zero speed; at higher speeds the lift force is degraded due to the generation of eddy currents in the track. This eddy current generation also produces a drag force F_D at the higher speeds. Guidance forces can be produced by appropriate design of the magnet and track or by the use of separate guidance magnets.

PB-210-506 (reference 1) discussed some early calculations made by us of the lift and drag forces, and their dependence on the material parameters of the track, for a flat, rectangular, levitation coil. Such a coil is not very realistic for a levitation magnet, however, since its magnetic circuit has rather large reluctance. In Section 3.1 we make a similar parametric study for U-shaped electromagnets of the type used by MBB and Krauss-Maffei.[15]

3.1. Parametric Study of the Lift and Drag Forces

In this section we shall determine the lift and drag forces, F_L and F_D, on an electromagnet consisting of a coil of wire surrounding a U-shaped iron core, which is suspended below a plate of relative permeability $\kappa = \mu/\mu_o$ and conductivity σ. The magnet is moving with velocity v relative to the plate, but the gap between magnet and plate is held constant. Non-linear effects of saturation are neglected; i.e., both κ of the plate and the magnetization of the iron core are assumed constant as a function of velocity.

In Fig. 3.1 a schematic of this type of magnet suspension is shown. The length of the magnet in the direction of motion is 2b, the pole width is 2a, the pole separation c, and the gap is h. To model such a configuration exactly would be difficult. A simple model that contains the main features of the real system, for which the calculation of F_L and F_D versus v is still tractable, is shown in Fig. 3.2. The magnetized core is replaced by surface magnetization currents J. These currents are assumed uniform. Furthermore, the actual current windings are taken to be far from the track. The track is to be infinitely wide and of arbitrary thickness T. The permeability $\mu = \kappa\mu_o$ is an effective permeability which depends upon the required lift, velocity, and detailed magnetic circuit; (this will be discussed in more detail in Section 3.2). Although still a somewhat crude model, it is more realistic than considering single coils[1] or the single Fourier component model of Meissenholder and Wang.[16]

Referring to Fig. 3.2, consider the nth current element at height h_n whose center is at y = 0. The eddy currents induced by this current element give rise to a magnetic field above the track whose Fourier transform involves

$$\left\{ \begin{matrix} \cos k_y y \\ \sin k_y y \end{matrix} \right\} e^{-kz} \; W_n \text{ for } \left\{ \begin{matrix} x,z \\ y \end{matrix} \right\} \text{ components,}$$

where

$$W_n = I_n \; W_o \; e^{-k(h_n - h)}, \tag{3.1}$$

$$W_o = (\mu_o/\pi^2 \; k_y) \sin k_x b \sin k_y a \; e^{-kh}, \tag{3.2}$$

and

$$I_n = J\Delta h. \tag{3.3}$$

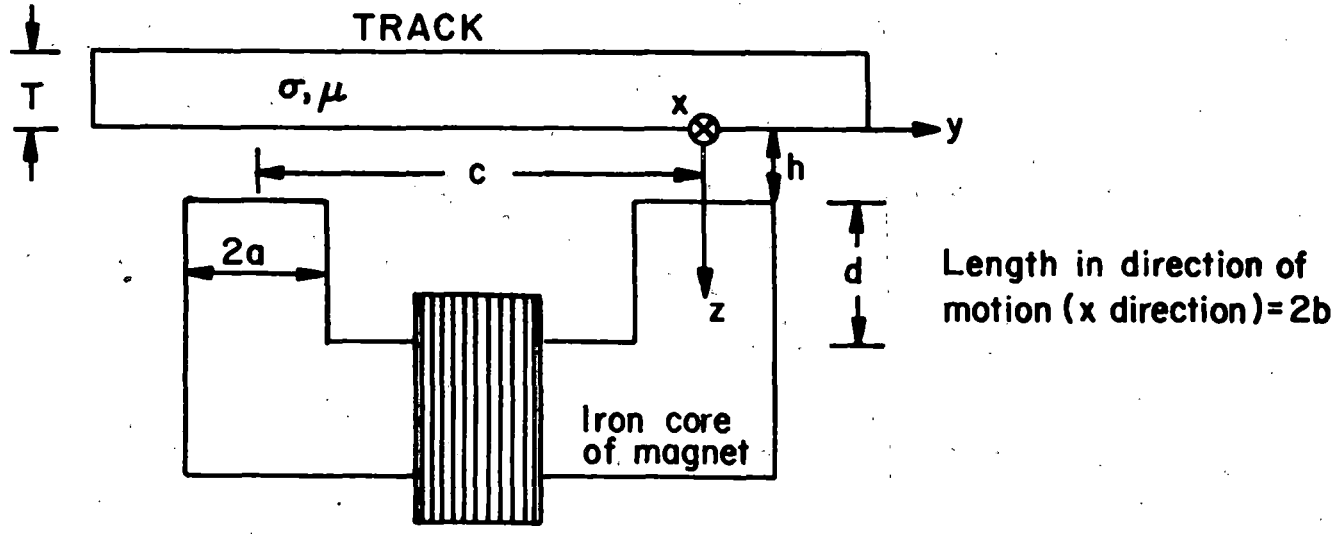

Fig. 3.1. Schematic design of magnet and track in the attractive-force suspension.

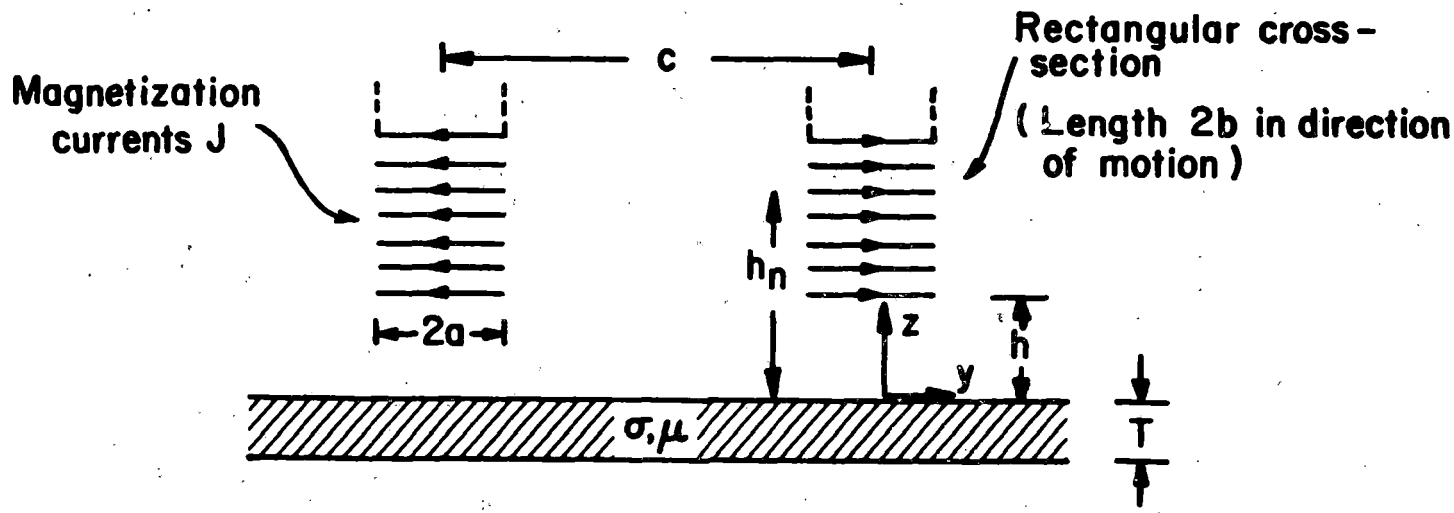

Fig. 3.2. Model of the attractive-force suspension, simplified for calculational purposes.

The corresponding loop at y = -c involves

$$- \begin{Bmatrix} \cos k_y\ (y+c) \\ \sin k_y\ (y+c) \end{Bmatrix} e^{-kz}\ W_n .$$

Now it is straightforward to show that the force on the mth loop with center at y = 0, z = h_m involves[4] $W_m W_n\ (1 - \cos k_y c)$. The total force on the loops at the right involves the sum:

$$\sum_{m,n} I_m\ I_n\ e^{-k\ (h_n + h_m - 2h)}\ (1 - \cos k_y c)\ W_o{}^2 .$$

Letting $h_n = h + (n - 1)\Delta h$, n = 1, 2, . . . , we find in the limit that $\Delta h \to 0$ the total lift and drag forces on the magnet are

$$F_L = (16\pi^2 J^2/\mu_o)\int_o^\infty dk_y \int_o^\infty dk_x\ |\ W_o\ |^2 \Gamma_1\ (1 - \cos k_y c)\ /k_x^2 , \quad (3.4)$$

$$F_D = (16\pi^2 J^2/\mu_o)\ \int_o^\infty dk_y \int_o^\infty dk_x\ |\ W_o\ |^2 \Gamma_2\ (1 - \cos k_y c)/k\ k_x . \quad (3.5)$$

where

$$\Gamma_1 + i\ \Gamma_2 = \frac{(1 - \beta/\kappa)}{(1 + \beta/\kappa)}\ \frac{1 - e^{-2\beta kT}}{1 - \left(\frac{1 - \beta/\kappa}{1 + \beta/\kappa}\right)^2 e^{-2\beta kT}} \quad (3.6)$$

The remaining quantities are defined in reference 4.

Some sample results are shown in Tables 3.1 and 3.2. Our numerical studies indicate that $F_L/F_D \approx C_1\ (\kappa/\sigma v)^{1/2}$ where C_1 depends upon a, b, c, and h. F_L/F_D is also proportional to (length of magnet)$^{1/2}$ and is larger for narrower magnets. Tables 3.1 and 3.2 are for an infinitely-thick iron-alloy plate, but the results are changed very little for a plate of thickness 2.5 cm; the zero velocity lift would be slightly smaller, but above a few miles/hour the skin depth would be less than 2.5 cm and thus the results would be almost identical.

It is evident that a large F_L/F_D can be obtained over the entire speed range, provided the magnets are long enough and the ratio κ/σ is large enough. In the next section we shall discuss the high-speed performance in more detail; in particular we show that because of saturation effects in the track κ drops substantially below 1000.

TABLE 3.1. Lift and Drag Forces in the Attractive System [2a = 2cm, 2b = 1.0m, c = 18cm, h = 1.5cm, κ = 50, $T = \infty$ σ^{-1} = 50 $\mu\Omega$-cm, $F_1 = 2\mu_o [(Jh)^2 (a + b)/h]$

v (mi/h)	F_L/F_1	F_D/F_1	F_L/F_D
0	0.741	0	∞
100	0.653	.0195	33.5
200	0.610	.0242	25.3
300	0.579	.0269	21.5

TABLE 3.2 Lift and Drag Forces in the Attractive System (Parameters the same as Table 3.1 except c = 7cm, κ = 1000)

V (mi/h)	F_L/F_1	F_D/F_1	F_L/F_D
0	0.661	0	∞
100	0.648	.00226	287
200	0.642	.00312	206
300	0.638	.00374	170

3.2 High-Speed Drag Problem

An analytic study of the lift and drag forces in a electromagnetic (attractive) suspension has uncovered a serious problem for high-speed operation. As reported in Section 3.1, the lift-to-drag ratio for a ferromagnetic suspension is proportional to $(\mu\rho/v)^{\frac{1}{2}}$ where μ is the permeability, ρ the resistivity of the alloy in the track, and v is the vehicle speed. A practical upper limit for the resistivity of metallic, ferromagnetic alloys is 50-100 $\mu\ \Omega$ cm. If the relative permeability κ is greater than 1000 there is no problem with the lift-to-drag ratio at 300 mi/h, but as we shall see shortly such large values of κ cannot be obtained.

The problem arises because the magnetic flux in the track must be carried in the skin depth. The skin depth is proportional to $(\rho/\mu v)^{\frac{1}{2}}$. As the vehicle speed increases the skin depth becomes smaller; this causes the flux density in the track to approach saturation and μ to drop precipitously. This situation cannot be avoided because efficient magnet design requires them to operate at high flux density.

Let us consider the problem in more detail. A long electromagnet of length L is suspended below a ferromagnetic track as shown in Fig. 3.3 (transverse section through the coil and track).
According to Reitz and Davis[4] the skin depth for penetration of the electromagnetic field is

$$\delta = 2^{1/2} / [\{(\mu\sigma v k_x)^2 + k^4\}^{1/2} + k^2]^{1/2} \qquad (3.7)$$

where $k^2 + k_x^2 + k_y^2$, $\sigma = 1/\rho$ and k_x, k_y are appropriate wave numbers; x is in the direction of motion. We are dealing with a range of material parameters such that, except at the lowest speeds,

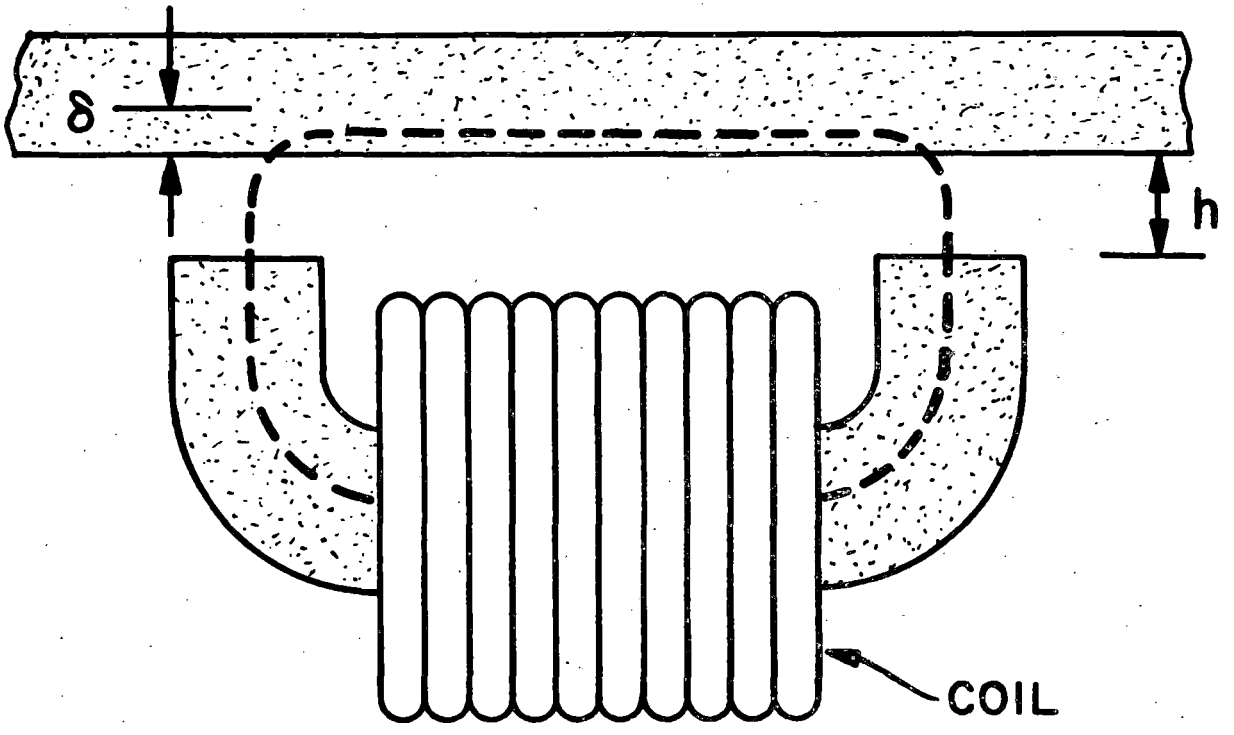

Fig. 3.3. Magnetic circuit of the attractive-force suspension.

$$\mu\sigma v k_x \gg k^2 \ , \tag{3.8}$$

so that

$$\delta \approx (2/\kappa\mu_o\sigma v k_x)^{1/2} \ . \tag{3.9}$$

$k_x \approx \pi/L$. κ depends on the flux density B which in turn depends on the total flux in the magnetic circuit and on δ.

Now the electromagnet and track form a magnetic circuit. The flux through the magnet Φ is given by

$$\Phi = NI/R \tag{3.10}$$

where the reluctance R is

$$R = R_o + R_1R_2/(R_1 + R_2) \ . \tag{3.11}$$

Here R_o is the reluctance of the magnet core, R_1 is the reluctance of the track and the air gap, and R_2 is leakage reluctance. The energy of the magnetic circuit

$$W = (NI)^2/2R \ , \tag{3.12}$$

and the lift force is given by

$$F_L = - (N^2I^2/2) \ d(1/R)/dz. \tag{3.13}$$

If we neglect R_o since it is small compared to either R_1 or R_2, and if we assume that the leakage flux does not depend upon gap height, and since

$$R_1 = \ell_t/\kappa\mu_o A_t + 2z/A_g\mu_o, \tag{3.14}$$

where ℓ_t, A_t are the length and cross-section of the flux path in the track, z = h is the gap, and A_g is the flux cross-section in the gap, we find

$$\Phi = \Phi_1 + \Phi_2 \tag{3.15}$$

and

$$F_L = \Phi_1^2/\mu_o A_g. \tag{3.16}$$

Here Φ_1 is the flux through the track.

Now the flux in the track can be expressed as the flux density B times the area through which it passes ($L\delta$):

$$\Phi = BL\delta \quad . \tag{3.17}$$

Combining (3.9), (3.12) and (3.13), we obtain

$$\kappa = \frac{2L^3B^2}{\mu_o{}^2\sigma\pi A_g F_L v} \quad , \tag{3.18}$$

and since the pole face area $A_g = pL$ where p is the pole face width:

$$\kappa = \frac{2L^2B^2}{\mu_o{}^2\sigma\ \pi p F_L v} \quad . \tag{3.19}$$

Equation (3.19) can be combined with the characteristic B-H curve for the material to obtain both κ and B. However, a simpler procedure is to anticipate that B is in the vicinity of the saturation field B_S and obtain κ directly from (3.19). If we take the following set of magnet and track material parameters: $B_S = 2T$, $\sigma = 2 \times 10^6$ mho/m (appropriate to a 4% Si-Fe alloy), L = 1m, p = .03m, v = 134 m/sec, and if we assume that 32 of these magnets support a 50 ton vehicle ($F_L = 1.38 \times 10^4$ N), then $\kappa \approx 16$.

This is clearly a serious problem since such a low value of κ will adversely affect the lift/drag ratio. Calculations show that at 300 mi/h the lift/drag ratio of a 1 m × 0.15 m U-channel electromagnet cruising at 1.5 cm below a 4% Si-Fe plate is only 18. How then can we effectively increase κ? The most obvious way is to increase the resistivity of the track. It does not appear that one would want to use a ceramic material such as a ferrite since these materials are brittle and not suitable for tensile loads. One can effectively increase the resistivity of a metallic track by laminating it; however, it appears that vertical laminations will be required. The weight of the vehicle would then be supported by a series

of cross bolts through the laminations. Laminating the track will increase its cost substantially.

Equation (3.19) suggests several other methods for increasing κ One can increase the number of support magnets, thus decreasing F_L; this possibility is quite limited, however. A better solution is to make the individual magnets longer. If we support the entire vehicle with four magnets, each 10 meters long, κ could be increased to about 200. The longer magnets would also improve the lift/drag ratio (in addition to the improvement obtained with the higher κ). However, from the control viewpoint it would seem that more numerous, shorter magnets would be desirable.

Although the model discussed in this section is somewhat crude, we believe that the conclusions which have been obtained are essentially correct. Other studies which support these conclusions are some analog modeling studies by Oberretl[17] and rotating wheel experiments. Oberretl used an analog method to determine the magnetic field penetration and eddy current losses in ferromagnetic material when the material is near saturation. His results for large magnetic fields (field at the surface of 2 tesla) show that the penetration depth is much more sharply defined than that for simple exponential penetration, and his $\kappa_{effective}$ values are indeed rather low (in the range which we would predict from our model).

3.2.1. Rotating Wheel Experiments

A series of lift and drag force measurements were made on a 5 × 10 cm superconducting coil (mounted in a Dewar) situated above a rotating steel wheel. The wheel is 1 ft. in diameter.* The experimental results for two different heights are shown in Fig. 3.4.

Calculations of lift and drag were made for a 5 × 10 cm coil suspended at 3.0 cm below a ferromagnetic plate at coil speeds up to

* The material constants, σ and κ, are not known very well. They had to be inferred from the experimental data as described below.

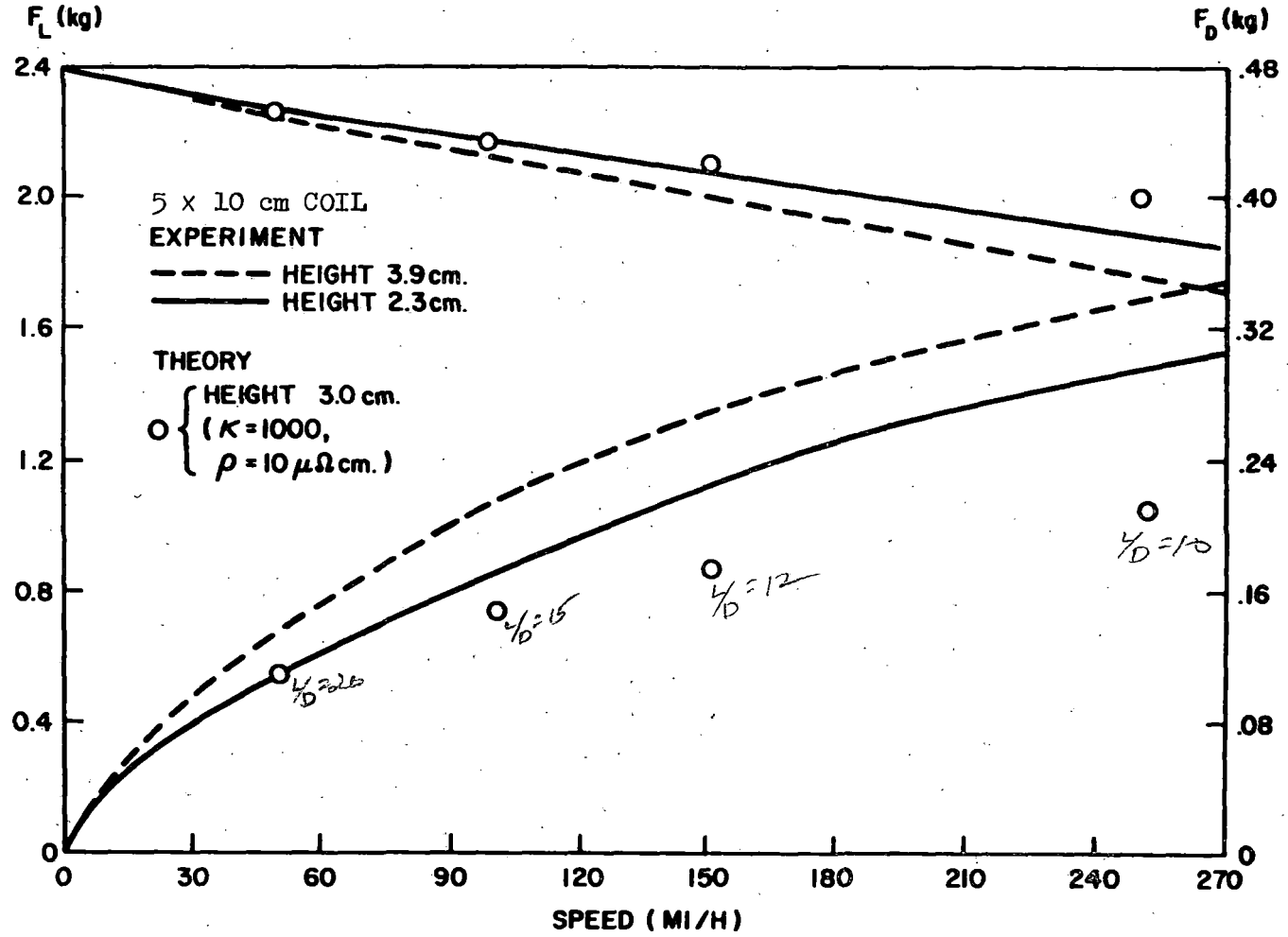

Fig. 3.4. Experimental results for lift and drag using the rotating steel wheel.

300 mi/h. A resistivity of 10 μ Ω-cm was assumed; several different values of κ were used. In comparing the experimental results with the calculations it is evident that κ is not a constant, independent of velocity. In fact, if the calculations are "fit" to experiment we can determine κ as a function of speed. These results are given in Table 3.3. If ρ is actually larger than 10 μ Ω-cm, then the κ-values would be smaller than shown in the table.

TABLE 3.3. Effective relative permeability of a cold-rolled steel wheel as a function of rim speed when subjected to the field of a current-carrying coil. ρ assumed to be 10 μ Ω-cm.

v(mi/h)	κ
50	1000
100	690
250	450

Now the coil above the steel wheel does not form a very good magnetic circuit. We can, however, use magnetic circuit analysis and skin depth concepts to estimate κ and see how it compares with the results from Table 3.3. The lift force on the coil is calculated to be

$$F_L = 0.234\ \mu_o (NI)^2 (\text{perimeter})/4\pi h \quad , \tag{3.20}$$

and the flux generated by the coil is estimated to be

$$\Phi = 0.7\ \mu_o NI.(\text{length}) \quad . \tag{3.21}$$

We assume that 3/4 of this flux is channeled through the steel, and we estimate that this flux is channeled through an effective area equal to 1.5 × (perimeter of coil) × δ. Using an analysis very similar to that of Eqs. 3.9 through 3.19, and choosing ρ = 10 μ Ω-cm we obtain κ = 23

for v = 250 mi/h. This does not agree very well with the last entry in Table 3.3. We can, however, repeat the calculations for other assumed values of ρ; the results are given in Table 3.4.

TABLE 3.4. Effective relative permeability of a cold-rolled steel wheel at 250 mi/h rim speed when subjected to the field of a current-carrying coil.

ρ ($\mu\ \Omega$ cm)	κ (from fit to experimental L/D)	κ (from magnetic circuit-skin depth analysis)
10	450	23
20	225	46
30	150	69
40	112	92

We see that if ρ is 45 $\mu\ \Omega$ cm the two analyses give about the same value for κ. It seems very unlikely, however, that ρ of cold-rolled steel is larger than 25 $\mu\ \Omega$ cm, so the crude magnetic circuit analysis can probably not be trusted in this case. Nevertheless, the effective reduction in κ, which was predicted, appears to be well documented.

Several other experiments were performed with the rotating steel wheel using a small iron-core magnet (7 cm wide and 12.5 cm long) shaped to fit the wheel. Fig. 3.5 shows the variation of the magnetic field in the air gap for high-speed operation. This is just what is expected; the skin depth is largest near the trailing edge of the magnet, and hence the reluctance of the parallel magnetic circuits is lowest in this region. Measurements of F_L/F_D at v = 130 m/sec were also made as a function of current

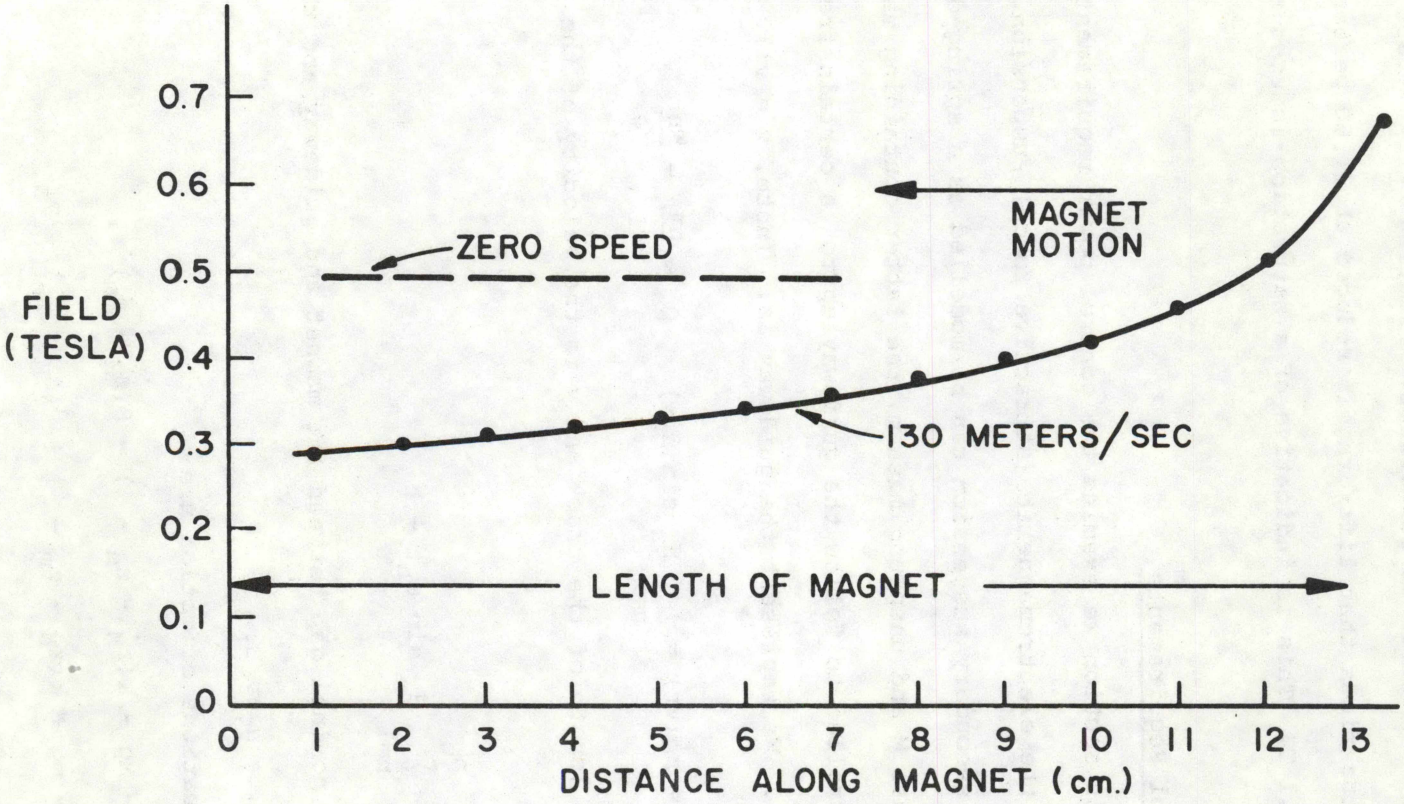

Fig. 3.5. Variation of magnetic field in air gap between an iron-core electromagnet and the rotating steel wheel.

in the magnet windings. These latter measurements were difficult to make on an absolute basis because of the large forces involved, but the relative measurements are believed to be correct. Plotting F_L/F_D versus field in the air gap, one finds that lift/drag is reduced about 60 percent in going from 0.3 to 1.1 T. This is indicative of a saturation-induced reduction in κ.

3.3. Control Requirements

In this section we examine the control power requirement for a vehicle using the electromagnetic (attractive force) suspension. Such a system with a secondary suspension can be modelled as a spring-damper with sprung mass M and unsprung mass m, the latter containing magnets which are controlled to follow the guideway up to a certain frequency (see Fig. 3.6). We represent the guideway as: (note, x = vt)

$$z_G(x) = z_G(vt) = \sum_{n=1}^{\infty} H_n \sin(\Omega_n x) \quad , \; \Omega_n = \frac{n\pi}{L} = \frac{\omega_n}{v} \tag{3.22}$$

where L is the length of the track and v is the velocity of the vehicle. Then

$$z_m(t) = \sum_{n=1}^{n_c} H_n \sin \omega_n t + h \tag{3.23}$$

where h is the nominal gap between the magnet and guideway and the cutoff frequency is $\omega_c = n_c \pi v/L$.

The equations of motion are:

$$\begin{aligned} M\ddot{z}_M &= - Mg - k(z_M - z_m - \ell) - \beta(\dot{z}_M - \dot{z}_m) \quad , \\ m\ddot{z}_m &= - mg + k(z_M - z_m - \ell) + \beta(\dot{z}_M - \dot{z}_m) + F_z \end{aligned} \tag{3.24}$$

where F_z is the magnetic force on m.

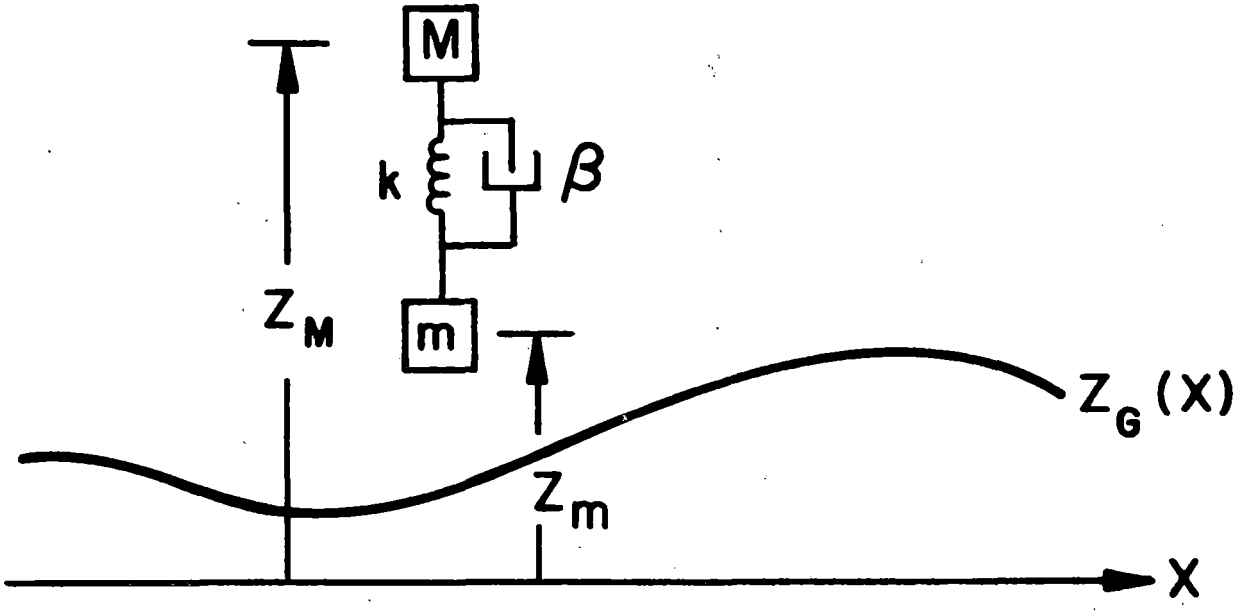

Fig. 3.6. Dynamic model of a vehicle with an attractive-force suspension following a guideway Z_G.

It can be shown that

$$z_M(t) = h_M + \mathrm{Im}\ \{ \sum_{n=1}^{n_c} a_n\, e^{i\omega_n t} \} \tag{3.25}$$

where

$$k(h_M - h - \ell) = Mg \quad , \tag{3.26}$$

$$a_n = \frac{\omega_o^2 + 2i\gamma\omega_n}{\omega_o^2 - \omega_n^2 + 2i\gamma\omega_n} H_n \quad , \tag{3.27}$$

$$\omega_o^2 = \frac{k}{M} \quad , \tag{3.28}$$

and

$$\gamma = \frac{\beta}{2M} \quad . \tag{3.29}$$

h_M is the nominal height of M and Im $\{ \cdots \}$ means the imaginary part of ... and ℓ is the unloaded separation of m and M. The force, F_z, necessary to give the prescribed $z_m(t)$ is then

$$F_z = (m + M)g - \mathrm{Im}' \{ \sum_{n=1}^{n_c} H_n \omega_n^2 e^{i\omega_n t} \left(m + M \frac{\omega_o^2 + 2i\gamma\omega_n}{\omega_o^2 - \omega_n^2 + 2i\gamma\omega_n} \right) \} \tag{3.30}$$

The average mechanical power (work done by F_z per sec) is

$$\langle F_z \dot{z}_m(t) \rangle = \gamma M \sum_{n=1}^{n_c} \frac{\omega_n^6 H_n^2}{(\omega_o^2 - \omega_n^2)^2 + (2\omega_n\gamma)^2} \tag{3.31}$$

Now H_n^2 is related to the power spectral density of the guideway, $\Phi(\Omega)$, by

$$H_n^2 = \frac{2\pi}{L} \Phi(\Omega_n) = \Phi \left(\frac{\omega_n}{v} \right) \tag{3.32}$$

where, in the usual approximation,

$$\Phi(\Omega) = A/\Omega^2 \quad . \tag{3.33}$$

The average mechanical power can then be converted to the following integral

$$< F_z \dot{z}_m(t) > = 2\ MAv \int_o^{\omega_c} \frac{d\omega\ \omega^4}{(\omega_o^2-\omega^2)^2 + (2\gamma\omega)^2} \quad . \tag{3.34}$$

This power is supplied by the propulsion system, not the control system, and is dissipated in the damper. This can be seen as follows. Ignoring the high frequency components (i.e., $\omega > \omega_c$), the magnet follows the guideway. The guideway exerts a force on the magnet, F_N, normal to the guideway surface (as shown in Fig. 3.7), where $F_N \cos \alpha = F_z$. The drag force on the magnet is then $F_D = F_N \sin \alpha = F_z \tan \alpha$. $\tan \alpha$ is related to the slope of the guideway by

$$\tan \alpha \doteq \frac{dz_G}{dx} = \frac{1}{v} \frac{dz_G}{dt} = \frac{1}{v} \dot{z}_m \tag{3.35}$$

Hence the drag power is

$$F_D v = F_z \dot{z}_m \quad . \tag{3.36}$$

This power is then supplied by the propulsion system. (Obviously this argument can be extended to account properly for the high frequency components.) One can also show, by direct calculation of $< \beta (\dot{z}_M - \dot{z}_m)^2 >$, that this power is dissipated in the damper.

The average mechanical power can be written as

$$< F_z \dot{z}_m > = 2\gamma MAv\ \omega_o\ J(\omega_c/\omega_o, \delta) \tag{3.37}$$

where

$$J(\omega_c/\omega_o, \delta) = \int_o^{\omega_c/\omega_o} \frac{dx\ x^4}{(x^2-1)^2 + (2\delta\ x)^2} \quad , \tag{3.38}$$

and

$$\delta = \gamma/\omega_o = \beta/2M\omega_o \quad . \tag{3.39}$$

Fig. 3.7.

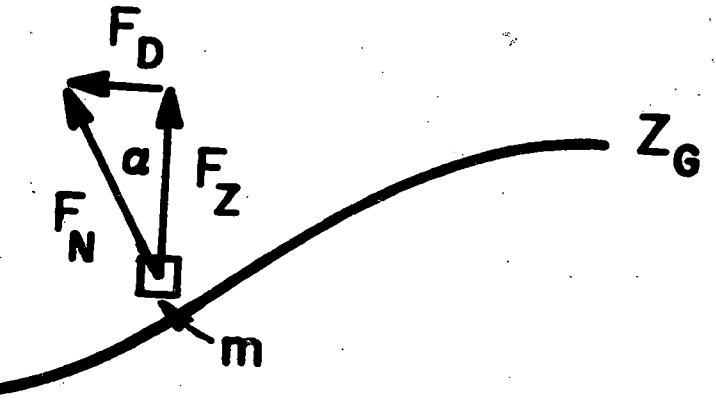

. Guideway force on magnet.

For critical damping ($\delta = 1$), J is given in Table 3.5

TABLE 3.5. Tabulation of the Functions $J(\omega_c/\omega_o, 1)$ and $I^{1/2}$ $(\omega_c/\omega_o, 1, 0.1)$ versus ω_c/ω_o

ω_c/ω_b	J	$I^{1/2}$
1	0.0072	0.551
2	0.539	2.53
3	1.28	5.43
4	2.13	8.98
5	3.04	13.1
8	5.89	
10	7.84	40.8
20		136.

For $\omega_c/\omega_o >> 1$, $\delta \leq 1$

$$J \simeq \frac{\omega_c}{\omega_o} + \frac{\pi}{4\delta}(1 - 4\delta^2) \quad . \tag{3.40}$$

The control power is the product of the voltage $V = \frac{d}{dt}(LI)$ and the current I,

$$P = VI = I\frac{d}{dt}(LI) \quad . \tag{3.41}$$

We neglect the resistive loss in the windings. To a good approximation, the gap $(z_G - z_m)$ is held constant so that

$$P = \frac{dW}{dt} \quad , \quad W = \tfrac{1}{2} LI^2 \quad . \tag{3.42}$$

W is the field energy and is given approximately by

$$W = F_z h. \tag{3.43}$$

Hence,

$$P \simeq \frac{dF_z}{dt}\ h\ . \tag{3.44}$$

The average power $< P >$ vanishes, but the rms power is given by

$$P_{rms} = < P^2 >^{1/2} = h\ [<(dF_z/dt)^2>]^{1/2} \tag{3.45}$$

Hence, after some manipulation we find that,

$$P_{rms} = h\ [Av\omega_o^5\ M^2\ I(\omega_c/\omega_o,\ \delta,\ m/M)]^{1/2} \tag{3.46}$$

$$= h\ (Av)^{1/2}\ \omega_o^{5/2}\ MI^{1/2}$$

where

$$I(\omega_c/\omega_o,\ \delta\ ,\ m/M) = \int_0^{\omega_c/\omega_o} dx\ x^4\ \left|\frac{m}{M} + \frac{1 + 2i\delta x}{1 - x^2 + \delta 2i\ x}\right|^2 \tag{3.47}$$

For critical damping ($\delta = 1$) and $m/M = 0.1$, $I^{1/2}$ is given in Table 3.5.

For $\omega_c/\omega_o >> 1$, $\delta = 1$

$$I = 0.2\ (m/M)^2\ (\omega_c/\omega_o)^5 + (4 + 6\ m/M)\ (\omega_c/\omega_o)^3/3. \tag{3.48}$$

For some typical parameters ($A = 5 \times 10^{-6}$ ft. $v = 300$ mi/h, $M + m = 50$ tons, $m/M = 0.1$, $\delta = 1$, $\omega_o = 8.5\ sec^{-1}$, $h = 15$ mm), we find that

$$< F_z\ \dot{z}_m > = 1.3 \times 10^3 \times J \quad \text{(watts)} \tag{3.49}$$

$$P_{rms} = 1.93 \times 10^3\ I^{1/2} \quad \text{(watts)} \tag{3.50}$$

For $\omega_c = 5\ \omega_o$, this gives a mechanical power

$$< F_z \dot{z}_m > = 0.08 \text{ kW/ton supported weight,} \tag{3.51}$$

and a control power

$$P_{rms} = 0.5 \text{ kVA/ton supported weight,} \tag{3.52}$$

which are not large. For fixed ω_c/ω_o , $\langle F_z \dot{z}_m \rangle$ is proportional to Av and P_{rms} is proportional to $(Av)^{1/2}$. Thus even a roadbed with a 16 x larger A coefficient (4 times rougher) does not use exhorbitant amounts of power. It should be noted, however, that the $(Av)^{1/2}$ dependence for P_{rms} is based on a small signal theory, and probably underestimates the control power for rougher tracks.

If ω_c is increased to $10 \times \omega_o$ the power increases substantially: the mechanical power is increased by 260% and the control power by 310% relative to $\omega_c/\omega_o = 5$. An increase in m/M also increases the control power.

3.4. Criterion for Maximum Track Roughness

In any noncontact suspension system there is a maximum track roughness which can be tolerated in order to prevent vehicle contacts with the track. Such considerations are independent of those involving ride quality. For large-gap magnetic suspensions, ride quality considerations will limit the maximum allowable track roughness, but this is not necessarily so for small-gap, ferromagnetic suspensions of the attraction type. In this section we derive a criterion for maximum allowable track roughness for the electromagnetic suspension.

We assume that the guideway roughness z_G is given by a power spectrum of the usual type:

$$\overline{z_G^2} = \int_{\Omega_1}^{\infty} \phi(\Omega) d\Omega = Av \int_{\omega_1}^{\infty} d\omega/\omega^2 \quad . \tag{3.53}$$

We want the primary suspension to follow track irregularities accurately up to some cutoff frequency ω_c. Ride quality is not considered; it will be handled by the secondary suspension. The maximum roughness criterion arises because (i) displacement amplitude in the uncontrolled frequencies ($\omega > \omega_c$) must be less than the gap; this puts a lower limit on ω_c.

(ii) The vehicle with a controlled ferromagnetic suspension cannot fall away from the track with accelerations greater than g; this puts an upper limit on ω_c. (i) and (ii) are incompatible if Av exceeds a maximum value.

From (i):

$$Av \int_{\omega_c}^{\infty} d\omega/\omega^2 \quad < \quad h^2/4 \tag{3.54}$$

where h is the gap. The factor 1/4 on the right hand side is the product of 1/2 (to convert peak to rms) and another 1/2 (a factor of safety to handle statistical variations in amplitude). This gives:

$$\omega_c > 4Av/h^2 \quad . \tag{3.55}$$

In the controlled frequency range the magnet's acceleration should respond to the control strategy; however, the vehicle cannot fall away from the track with accelerations greater than g. On the other hand the initial downward acceleration of the primary suspension can be as large as (M/m)g where M is total vehicle mass and m is the mass of the primary suspension. This is due to the release of energy in the compressed spring between primary and secondary. Again, to convert peak to rms and provide some factor of safety, we assume the maximum allowed acceleration in the controlled range to be 0.5 (M/m)g. Then (ii) yields

$$g^2 \ (M/m)^2/4 > Av \int_{\omega_1}^{\omega_c} \omega^2 d\omega \approx Av \ \omega_c{}^3/3 \quad . \tag{3.56}$$

Using (3.55) and (3.56) to eliminate ω_c yields

$$(A_v)^4_{max} = 3g^2h^6(M/m)^2/256 \quad , \tag{3.57}$$

or $(A_v)_{max} = 60 \times 10^{-4}$ m^2/sec for h = 12.5 mm, M/m = 10. (Remember that A = 5×10^{-6}ft and v = 300 mph gives Av = 2.2×10^{-4}m^2/sec.) Thus this maximum roughness corresponds to 136 x 10^{-6} ft which is somewhat rougher than an average highway.

It is not completely clear that we have used large enough factors of safety to reduce magnet-guideway contacts to insignificance. Nevertheless, it does not appear that these considerations would reduce $(Av)_{max}$ by more than a factor of 4. With $(Av)_{max} = 60 \times 10^{-4}$ m^2/sec, the cutoff frequency $\omega_c/2\pi = 17$ Hz which from a practical point of view may be larger than desired for the control system. On the other hand $\omega_c/2\pi$ should probably be at least 8 Hz. (At 300 mph, using an elevated guideway with a 75 ft span, there would be appreciable guideway irregularity power in the vicinity of 6 Hz and one would hope to control beyond this frequency.)

It thus appears that a control system can be designed in the ferromagnetic attraction case to follow guideways which are about as rough as an average highway. ($A = 35$ to 70×10^{-6} ft) if $h \geq 0.5$ inches and M/m is ~ 10. $(Av)_{max}$ is proportional to the 3/2 power of the gap and is proportional to $(M/m)^{1/2}$. This says nothing about ride quality which must be handled by the secondary suspension (either passive or active).

3.5 Analysis and Demonstration of Magnet Control System

The use of a feedback control system is necessary to control the current to stabilize the equilibrium position of the magnet. We have built two electromagnets with their required feedback control systems, both for purposes of demonstration and for studying the characteristics of the suspension obtained using ordinary electromagnets. These two magnets are discussed in the following sections.

3.5.1. Small Magnet Analysis

Our first model magnet for demonstrating the electromagnetic suspension and studying its characteristics is shown schematically in

Figure 3.8. The weight of the magnet including the coil and iron core was 25.4 lb. The magnet was restricted to vertical motion only by placing it on the end of a rather long lever arm as shown in Figure 3.9. Data were taken which give the air gap flux density, $B_{ag,}$ as a function of coil current for gaps ranging from 1/16 in. (1.59 mm.) to 3/4 in. (19.1 mm.). These data were taken by holding the magnet at a given gap and passing a dc current through the coil. Thus, they do not correspond to the magnet levitating in an equilibrium position with feedback control. The data for air gap flux density versus coil current are shown in Figures 3.10 and 3.11. It should be noted in Figure 3.10 that some residual magnetism is present since a non-zero flux density is measurable at the smaller gaps with zero current.

From these curves of flux density versus coil current, the coil inductance can be calculated. The reluctance of the magnet core can probably be neglected with respect to both the air gap reluctance and leakage reluctance to a good approximation. Thus, from equations (3.10) and (3.11), the coil inductance is found to be

$$L = \frac{N\Phi_T}{I} = \frac{N(\Phi_{ag} + \Phi_e)}{I} \tag{3.58}$$

where

N = number of turns in the coil

I = coil current

Φ_T = total flux linking the coil

Φ_{ag} = air gap flux

Φ_e = leakage flux

If we neglect leakage flux,

$$L \cong \frac{N \cdot B_a \cdot A}{I} \tag{3.59}$$

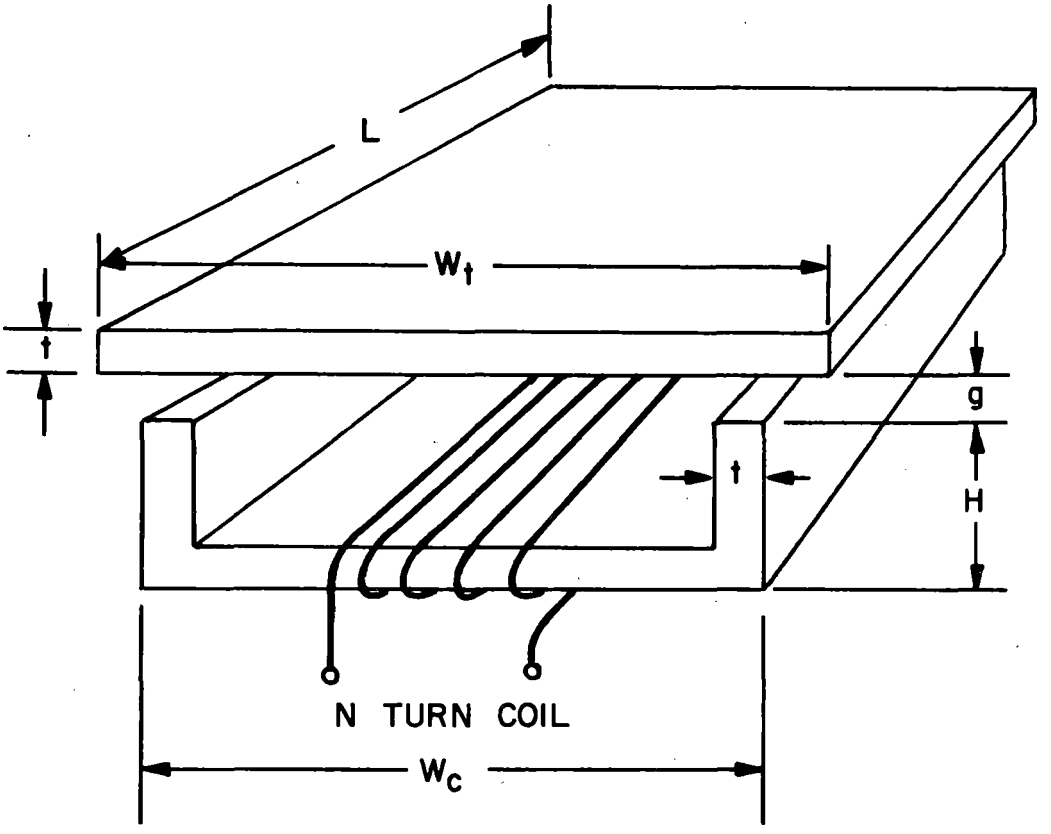

SMALL MODEL ELECTROMAGNET

L = 11 1/16 IN.	H = 1 1/2 IN.
W_t = 6 7/8 IN.	N = 418 (13 GAUGE WIRE)
W_c = 6 IN.	t = 1/2 IN.

CORE & PLATE MATERIAL - ARMCO IRON

R_{COIL} = 1.7 Ω

1/16 IN. ≤ g ≤ 3/4 IN.

Fig. 3.8. Schematic design of small electromagnet.

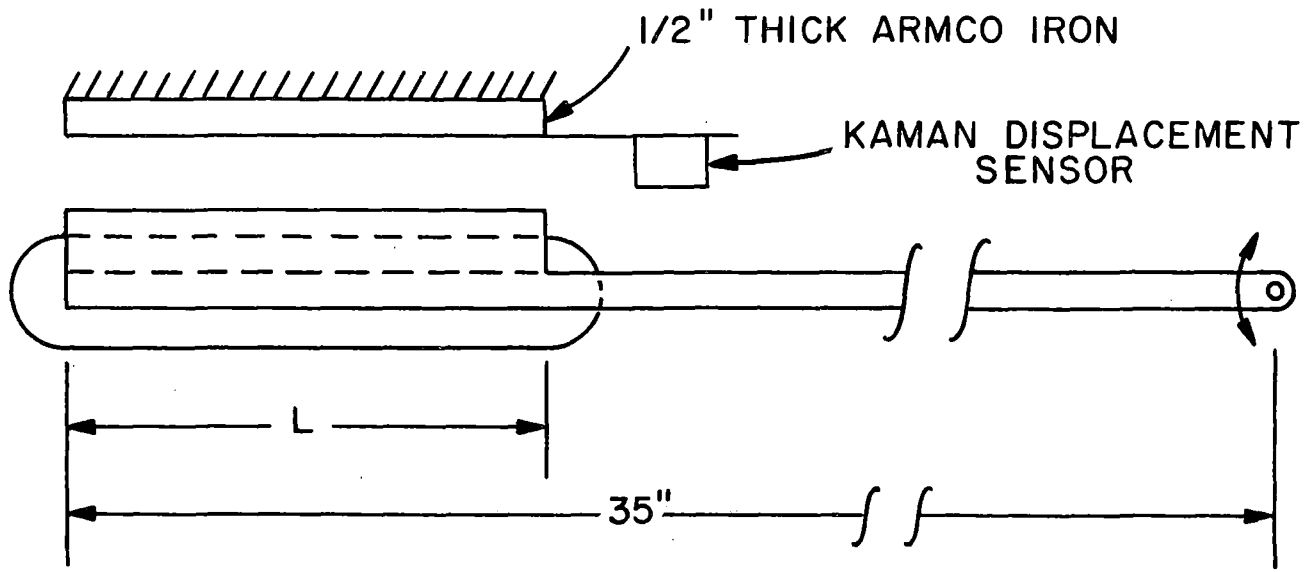

Fig. 3.9. Method for restricting motion of small magnet.

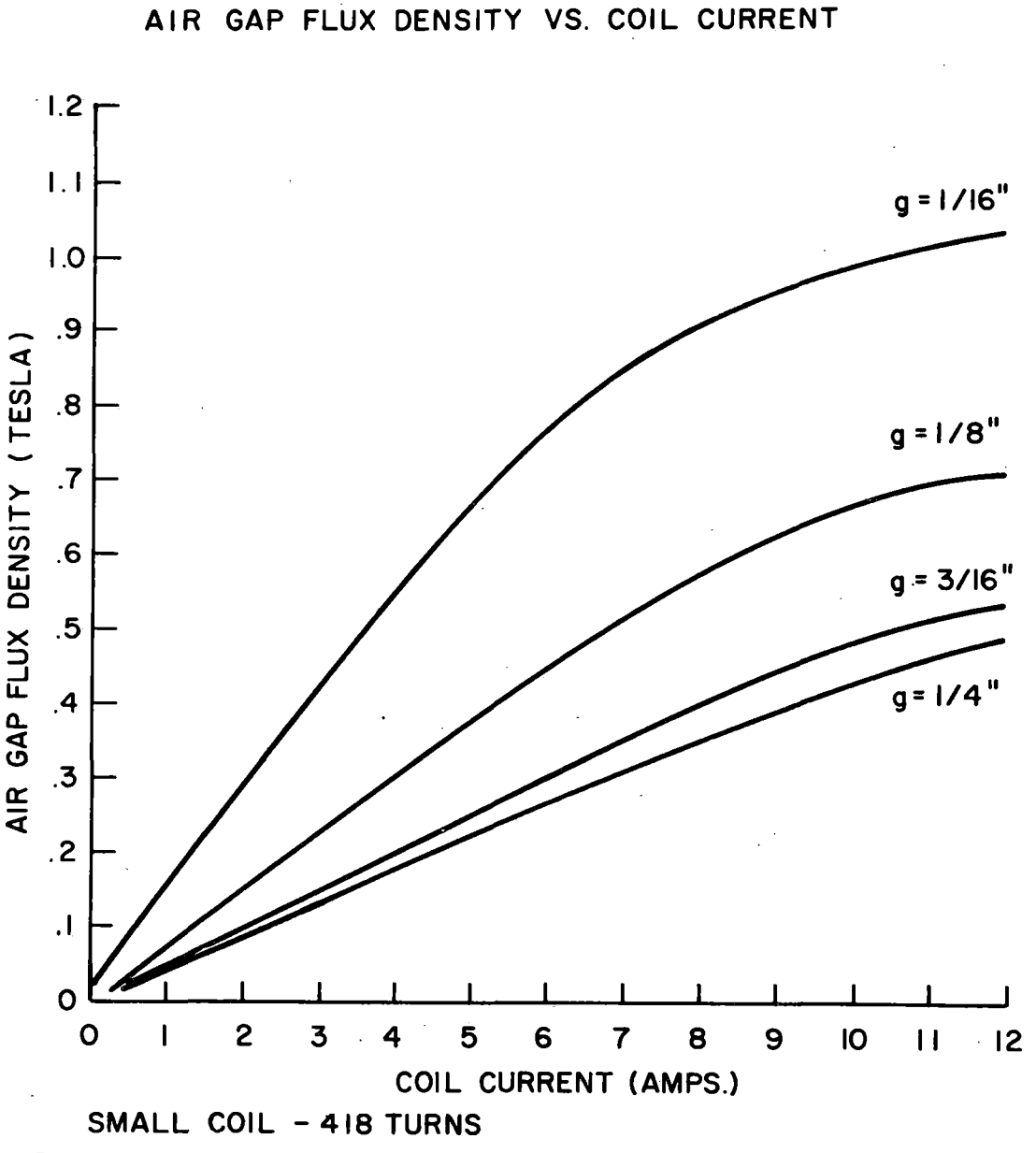

Fig. 3.10 Air gap flux density of small electromagnet.

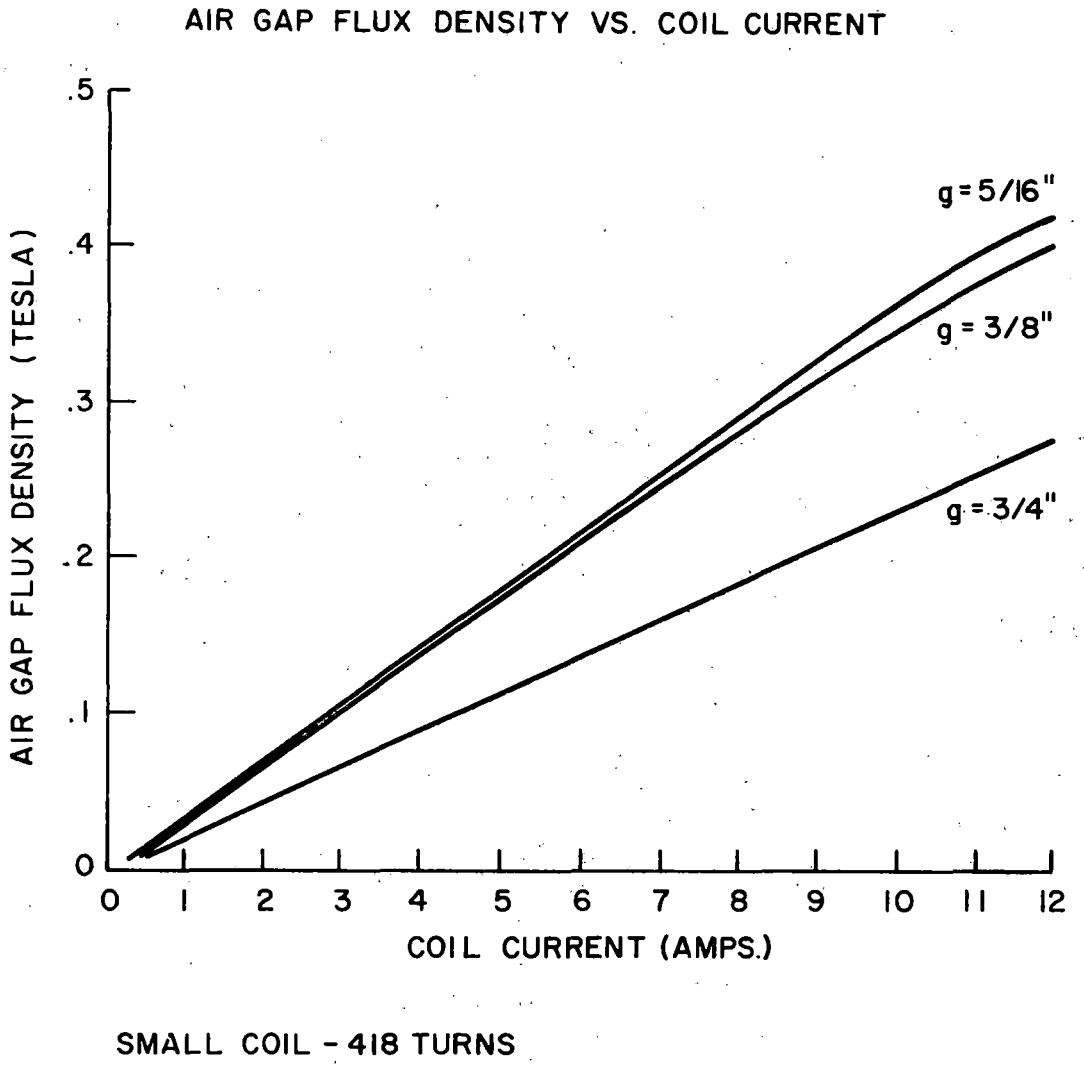

Fig. 3.11. Air gap flux density of small electromagnet.

where

B_a = air gap flux density

A = cross sectional area of air gap ($3.57 \times 10^{-3} m^2$ for magnet of Figure 3.8)

From the data of air gap flux density versus coil current, a plot of inductance can be made. Theoretically the inductance should be independent of the current, but experimentally there is some variation. The inductance versus air gap as calculated from (3.59) using Figs. 3.10 and 3.11 for current values of 2A, 5A and 7A are indicated in Figure 3.12, and the solid curve represents an approximate fit to these data.

The inductance can also be theoretically calculated from the magnet geometry. The inductance is

$$L = \frac{N}{I} (\Phi_{ag} + \Phi_e) \tag{3.60}$$

or

$$L = N^2 \left(\frac{1}{R_1} + \frac{1}{R_2} \right) \tag{3.61}$$

Again, we neglect the leakage term; if we also neglect the track reluctance compared to the air gap reluctance in (3.14), we obtain

$$L = N^2 \frac{\mu_o A}{2z} \tag{3.62}$$

The values of L calculated from (3.62), are also plotted in Figure 3.12. It is seen that the agreement between the two procedures is quite good, differing by at most 15% over the range of gaps considered. Recall that leakage flux, and thus a leakage inductance term, was neglected. Its inclusion would only add a constant value to both curves if the leakage flux is indeed independent of the gap over the range considered and if

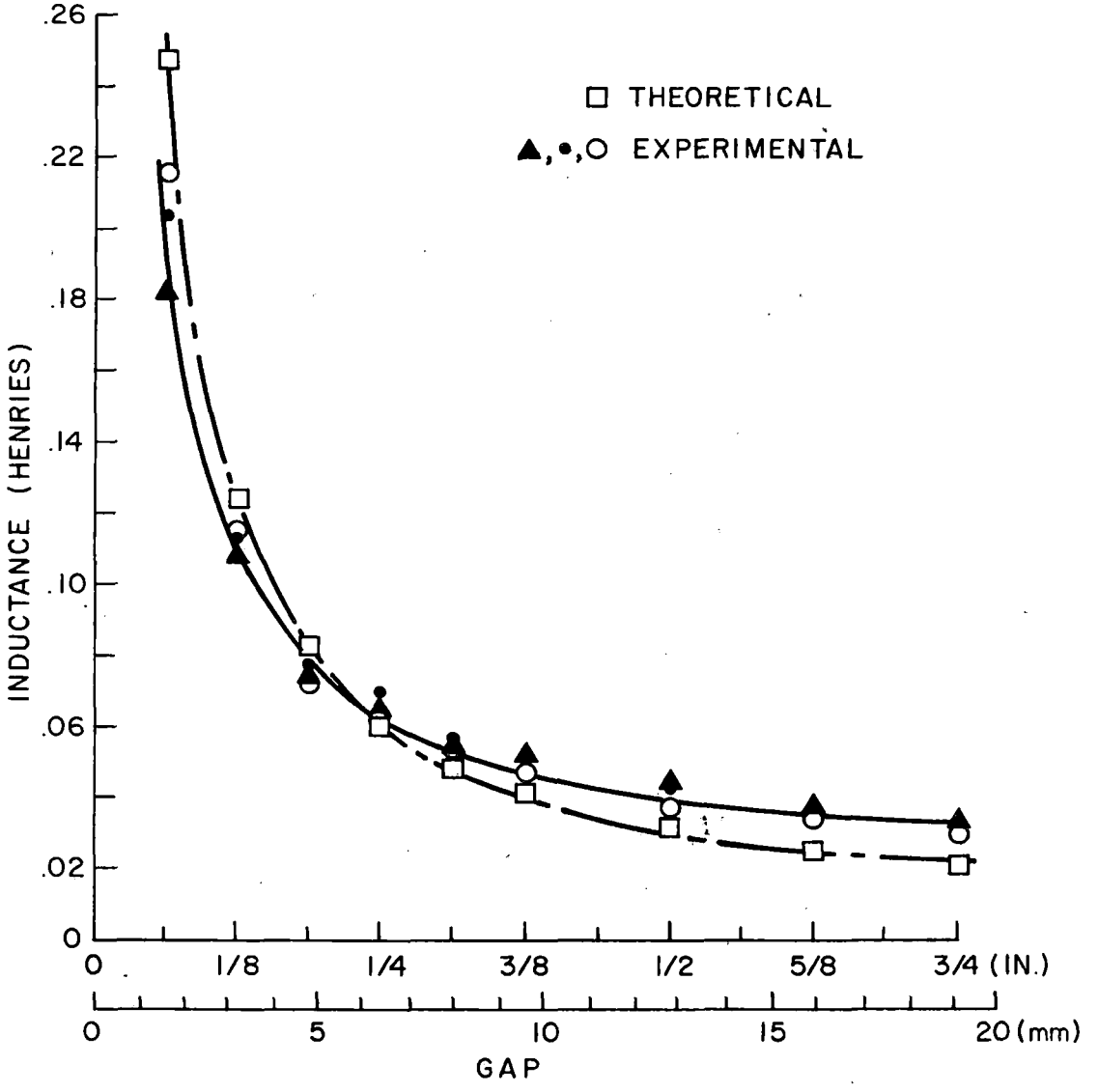

Fig. 3.12. Inductance vs air gap for small magnet.

the core reluctance is negligible. Such a constant term does not contribute to the force on the magnet.

Since the two curves of Figure 3.12 do not agree exactly, we conclude that either the neglect of track reluctance [Eq. (3.62)] is unjustified or the effective pole-face area is changing as a function of gap. In any case, the "experimental" inductance obtained from (3.59) is probably a better indication of the gap-dependent inductance of the system.

The current required for levitation can be computed given the inductance versus air gap curve of Figure 3.12, since

$$W = \frac{1}{2} L(z) I^2 \tag{3.63}$$

and

$$F_L = \frac{-dW}{dz} = -\frac{1}{2} I^2 \frac{dL(z)}{dz} , \tag{3.64}$$

assuming that I is constant. dL/dz can be obtained from (3.62) or by graphical differentiation of the "experimental" curve in Figure 3.12.

If a stable equilibrium position can be achieved with a control system (i.e. $\dot{z}, \ddot{z} = 0$), then the average lift force is mg so that

$$mg = \overline{F}_L = -\frac{1}{2} \overline{I^2} \frac{dL(z)}{dz} \tag{3.65}$$

and

$$I^2_{rms} = \overline{I^2} = -2mg/(dL/dz). \tag{3.66}$$

Thus, the current required to levitate the magnet can be calculated from (3.66). The resultant values of levitation current versus air gap for the theoretical and experimental cases are shown in Figure 3.13. Also shown in this Figure is the measured rms value of the current required to levitate the magnet with our feedback control system controlling the magnet current. Note that the current is indeed quite linear over a fairly large range of gaps.

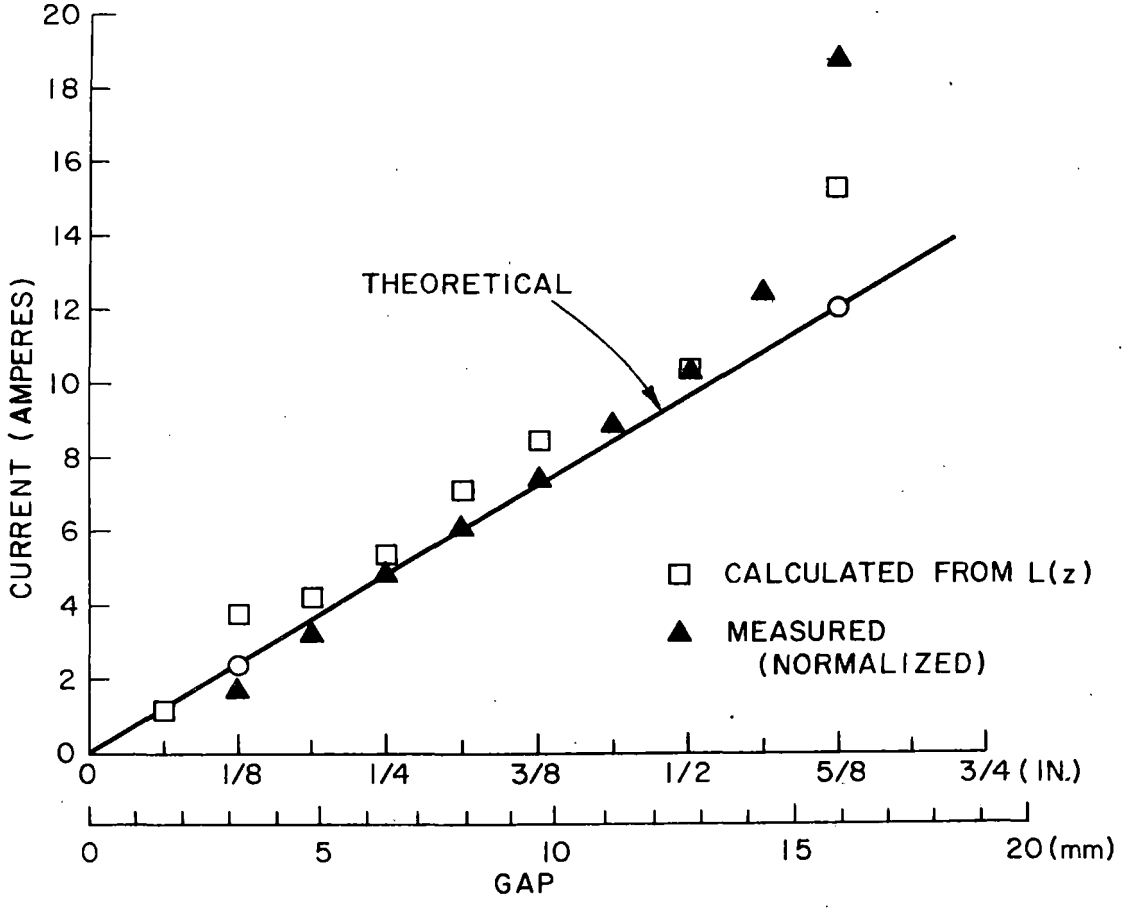

Fig. 3.13. Levitation current vs air gap (small electromagnet).

It should be noted that the measured current is normalized in Figure 3.13 so that it is equal to that obtained using the calculated L(z) at a gap of 1/2 inch. The measured current was, in fact, somewhat lower than that predicted either theoretically or calculated using the "measured" L(z). There are,however, several factors which, if considered, could improve the agreement; these are (i) the effective air gap area is really larger than the pole face area, and (ii) the experimental gap is not uniform along the length of the magnet as is assumed in the calculations.

The real power required to levitate the magnet can be calculated from the current, and obviously increases as the gap increases. For a gap of 1/8 inch this power requirement is 0.28 watts/lb. whereas at a gap of 1/4 inch this degrades to 1.77 watts/lb. For the size of the magnet considered here, the nominal operating gap should probably be less than or equal to 1/4 inch. These figures agree quite well with the figures given elsewhere for comparable levitation weight to gap ratios, eg. in Meisenholder and Wang[16].

3.5.2. Design of Control System

The idea behind the control system for the magnet current control is quite straightforward and is discussed in Meisenholder and Wang.[16] (Also, any control system analysis would be similar to that in Wilkie[45] for the superconducting suspension system except for a change in the sign of the spring constant term in the linearized equations.) Thus, the theory is not discussed in detail here. Basically, the idea is that the control current must be made proportional to the deviation of the magnet

gap from its equilibrium value in order to overcome the negative spring constant of the magnetic force. This will guarantee that any errors in the gap due to disturbances will not grow exponentially. Such a control system requires sensing the magnet-to-track gap. In order to damp out any disturbances and avoid oscillatory responses, it is necessary to add a term to the control current which is proportional to the vertical velocity of the magnet. Finally, if it is desired that the equilibrium gap height should be independent of the load, a term must be added to the control current which is proportional to the integral of the gap error.

A schematic diagram of a feedback control system to control the magnet position in the above described manner is shown in Figure 3.14. When the gap is exactly equal to the equilibrium value h, $V(h) = V_{ref}(h)$ and the control current i_c is zero. The magnet current i is then equal to the equilibrium current needed for levitating the magnet at the desired gap h. The voltage supplied to the magnet is seen to be proportional to a linear combination of the gap error, vertical magnet velocity, and integral of the gap error, and thus the magnet current is proportional to this combination. There are a number of aspects of this control system which should be noted individually. First, the vertical velocity signal is shown as being obtained by differentiating the position error signal. In general, differentiators should be avoided in practical systems since they tend to aggravate any noise problems present in the system and cause stability problems. We obtained the velocity signal in this way for the small magnet because we did not have velocity sensors available, and accelerometers suitable for the application were not available at the time the control system was constructed.

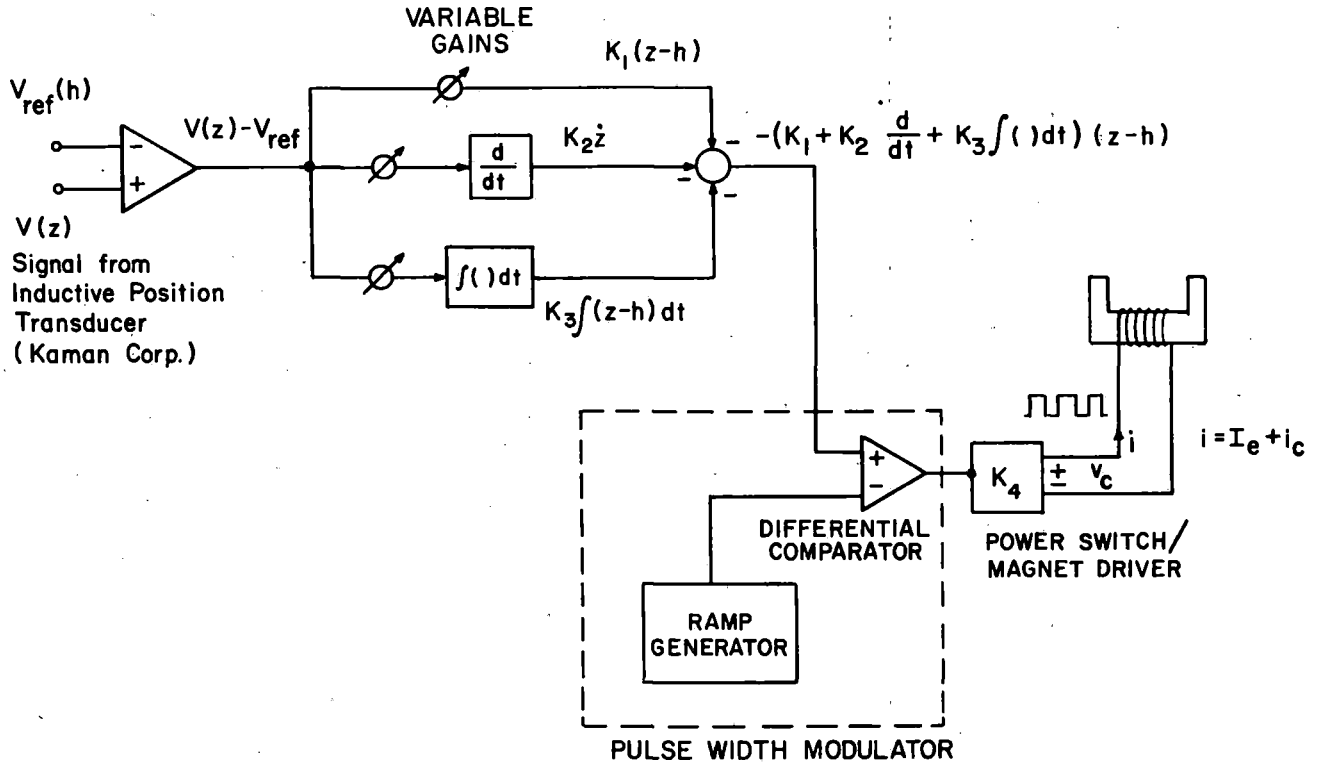

Fig. 3.14. Schematic diagram of a feedback control system to control the magnet's position.

Second, a pulse width modulator (PWM) and power switch are used to drive the magnet with the amplitude of the coil voltage V_c fixed but its pulse width variable. The pulse frequency used was 4kHz. This PWM and power switch could easily have been replaced by a linear amplifier for our purposes here. However, the PWM - power switch combination is inherently much more efficient than a straightforward linear amplifier and is desirable in an eventual real system. We thus felt it desirable to use this approach to the magnet voltage control.

Finally, in the circuit of Figure 3.14, the magnet voltage is controlled to be proportional to the linear combination of position error, integral of position error, and vertical velocity, whereas it was stated above that the magnet current should be proportional to these quantities. Since the magnet voltage is

$$V_c = L_c \frac{di}{dt} + R_c i \tag{3.67}$$

where L_c and R_c are the magnet inductance and resistance, it is apparent that i is linearly related to V_c as long as $L_c \frac{di}{dt} << R_c i$. Thus, the magnet control should be good at the lower frequencies. However, we did experience some noise problems with our first model magnet which would be partly due to the extra time lag introduced by the L_c di/dt term which dominates the voltage at higher frequencies.

With the control system of Figure 3.14, we were able to levitate the small electromagnet over a range of gaps from about 1/8 inch to 3/4 inch. The data obtained regarding the levitation current were discussed in the previous section. We experienced some noise problems due to the differentiator in the circuit and due to controlling the voltage rather than the current. The noise problems appeared as a high frequency, small amplitude vibration about the equilibrium position.

3.5.3. Large Magnet Analysis

The large model electromagnet that we built to study the electromagnetic suspension is shown schematically in Figure 3.15 along with the important dimensions. In order to restrict the magnet motion to one degree of freedom, the magnet was mounted on an aluminum plate as shown in Figure 3.16. The hydraulic cylinder which is connected to the aluminum plate to which the iron plate (rail) is attached is controlled by our electrohydraulic shaker (Ford Mini-Servo System) to produce various vibrations of the top plate. The plates are restrained to vertical motion by linear bearings which travel along the four columns at the corners of the plates. We have modified the magnet fixture somewhat since the photograph of Figure 3.16 was taken because of problems with flexing of the plates under load and friction in the linear bearings. Each plate in the fixture now consists of two plates bolted together for structural rigidity. These added plates also have linear bearings at each corner which travel along the vertical columns. Thus, the combined plates each have two linear bearings at each corner and this greatly reduces the friction from the bearings. The total weight the magnet must lift is thus equal to the sum of its weight plus the two aluminum plates to which it is attached, and this total weight is approximately 275 lb. The coil windings were placed on the core as shown in Figure 3.15, instead of in the way indicated in Figure 3.8, for ease of construction.

Data on air gap flux density versus coil current for various gap widths between the magnet pole pieces and top plate are shown in Figure 3.17. Note that these data were obtained before the second

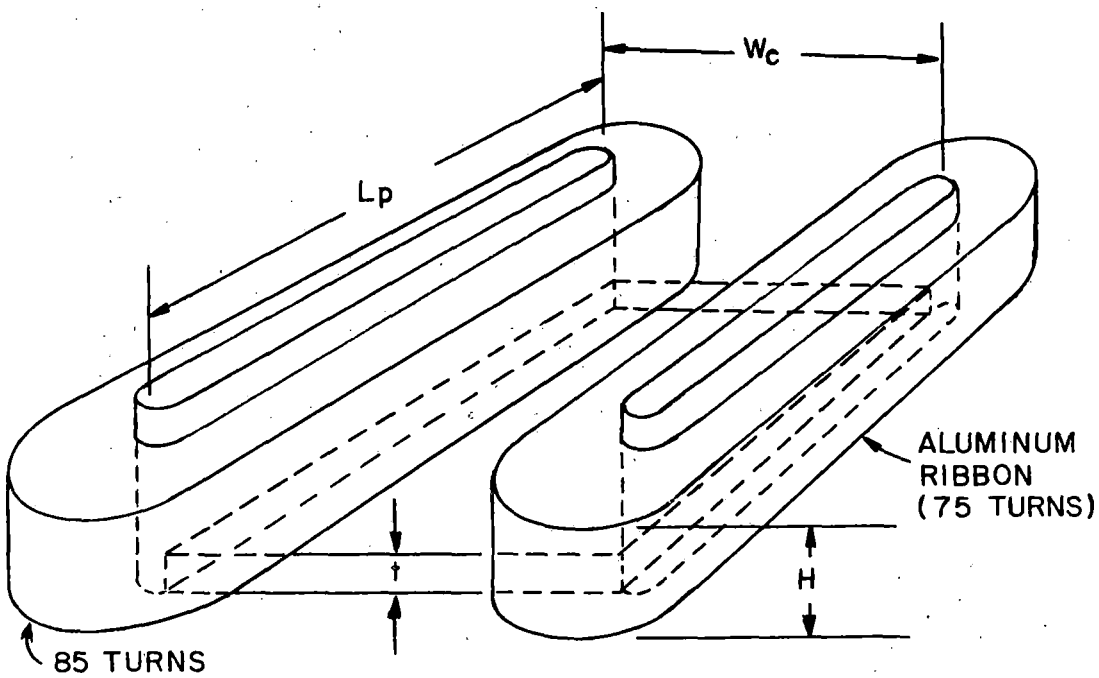

W_c = 6 IN. , L_p = 20 IN. , H = 3 IN. , t = 1 IN.

TRACK PLATE - 8 IN. BY 20 IN., 1 IN. THICK,
CORE AND TRACK ARE ARMCO STEEL

Fig. 3.15. Schematic of large electromagnet

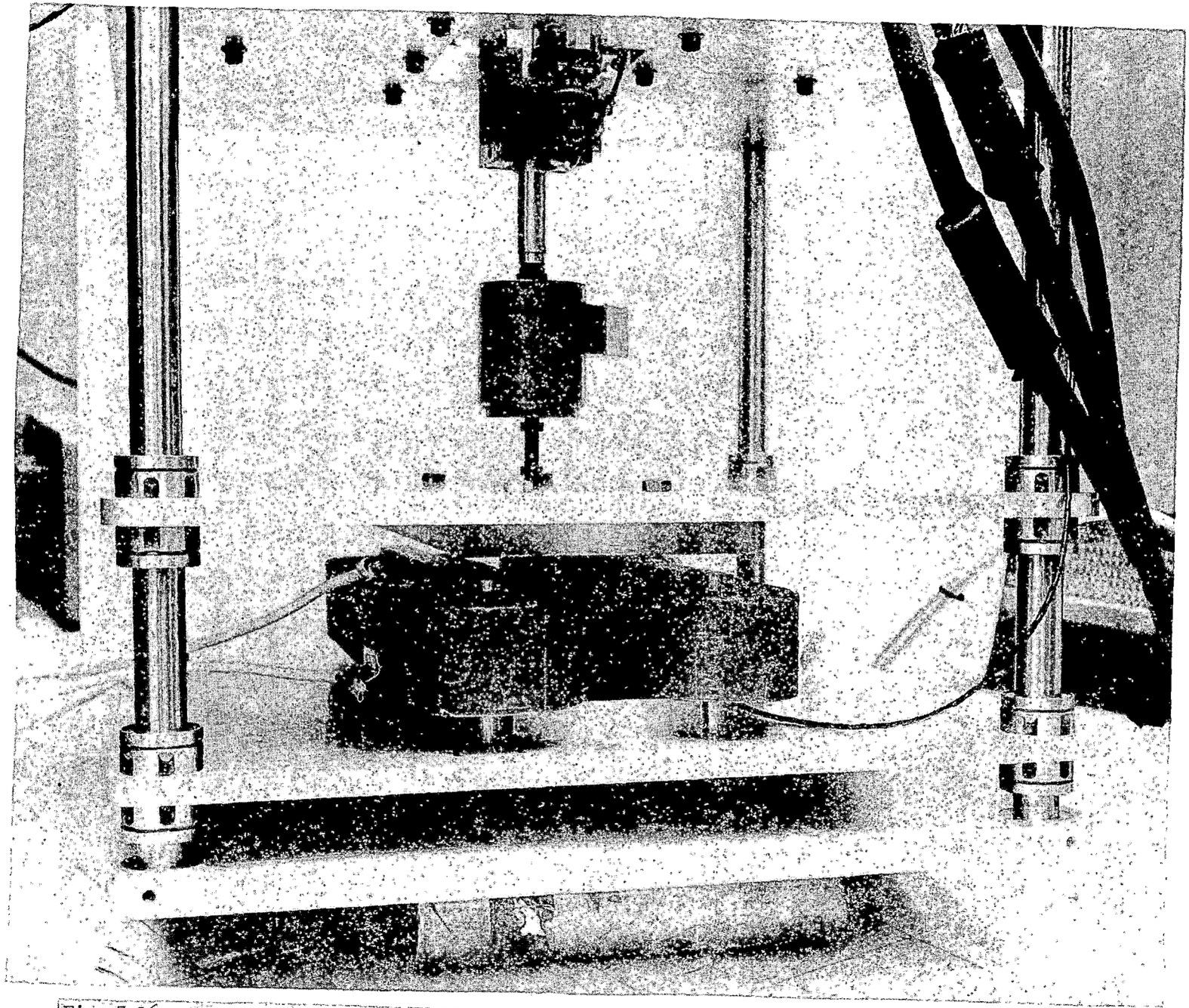

Fig. 3.16 Large electromagnet and experimental setup for study of the attractive force suspension.

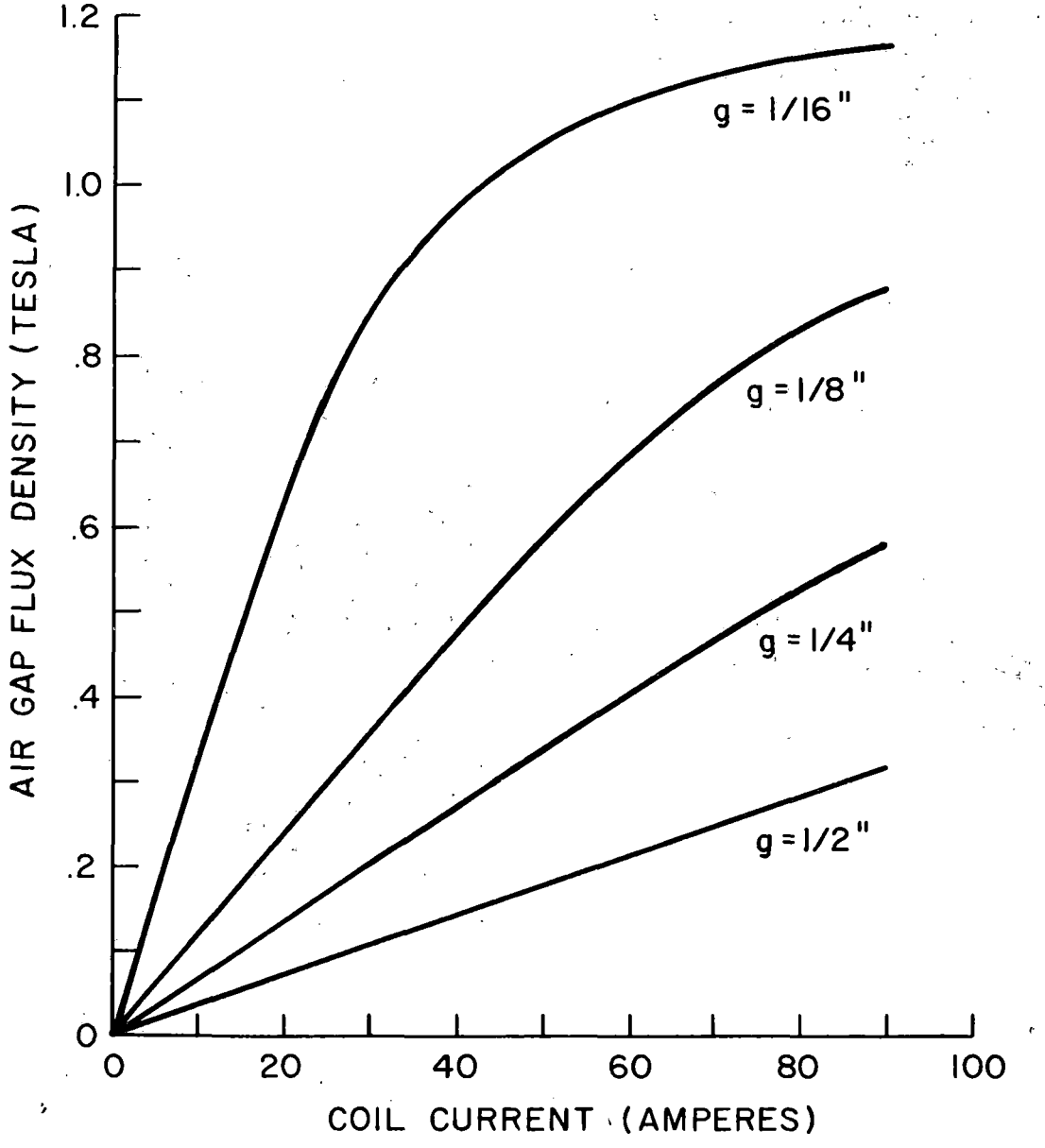

Fig. 3.17. Flux density vs. current (large electromagnet, using 85 of the 160 turns).

(75 turn) coil was wound and thus are only for the 85 turn coil. Saturation is evident for the smallest gap of 1/16 inch for currents greater than 30 amperes. The coil inductance can be calculated from the flux density versus current curves in Figure 3.17 in the same manner indicated previously for the small magnet (equation (3.58)). Also, the inductance can be calculated from the air gap reluctance as was done for the small magnet (equation (3.62)). The agreement between these curves is not particularly good for gaps below 1/4 inch and lacks explanation at this time.

The current required to levitate this magnet can be calculated as discussed previously since L(z) is known (equation (3.66)). The required derivative dL/dz can be obtained analytically from the expression for L(z) obtained from the reluctance or by graphical differentiation of the curve L(z) obtained using the measured air gap flux density versus current data. The required levitation current versus gap is plotted in Figure 3.19. The straight line (labelled theoretical) is obtained using the analytical expression for dL/dz that follows from differentiation of equation (3.62). The points marked ⊛ correspond to the current calculated using the values for dL/dz obtained by graphical differentiation of the L(z) curve obtained from the air gap flux density versus current data, and the points marked with a circle indicate the measured values of current with the magnet control system operating and the magnet levitated at the various gaps. The agreement between the theoretical and measured values is not particularly good. However, this is not surprising. Recall that in the theoretical calculation of the inductance and its derivatives that the effective area of the air gap was taken to be the pole face area.

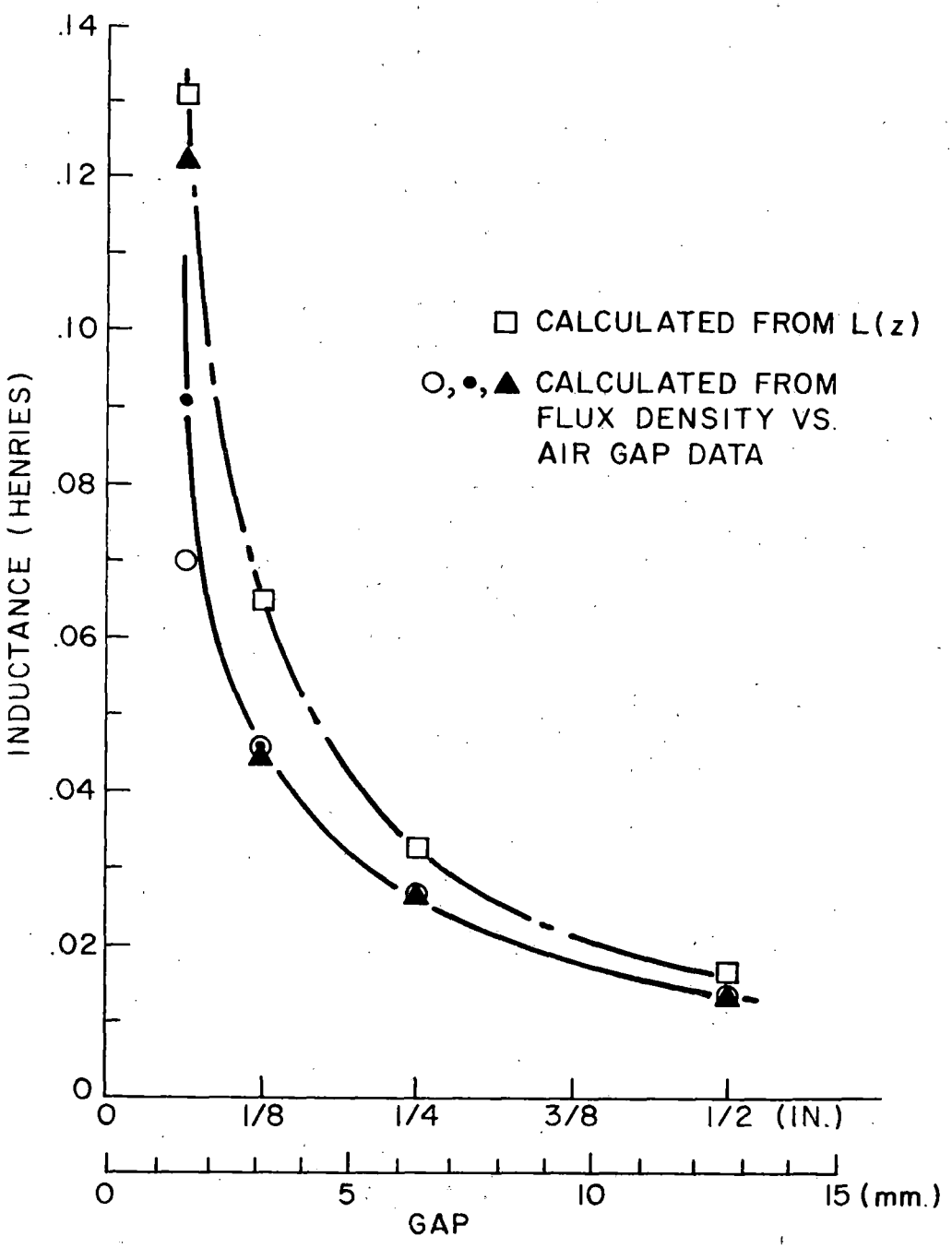

Fig. 3.18. Inductance vs. gap (large electromagnet).

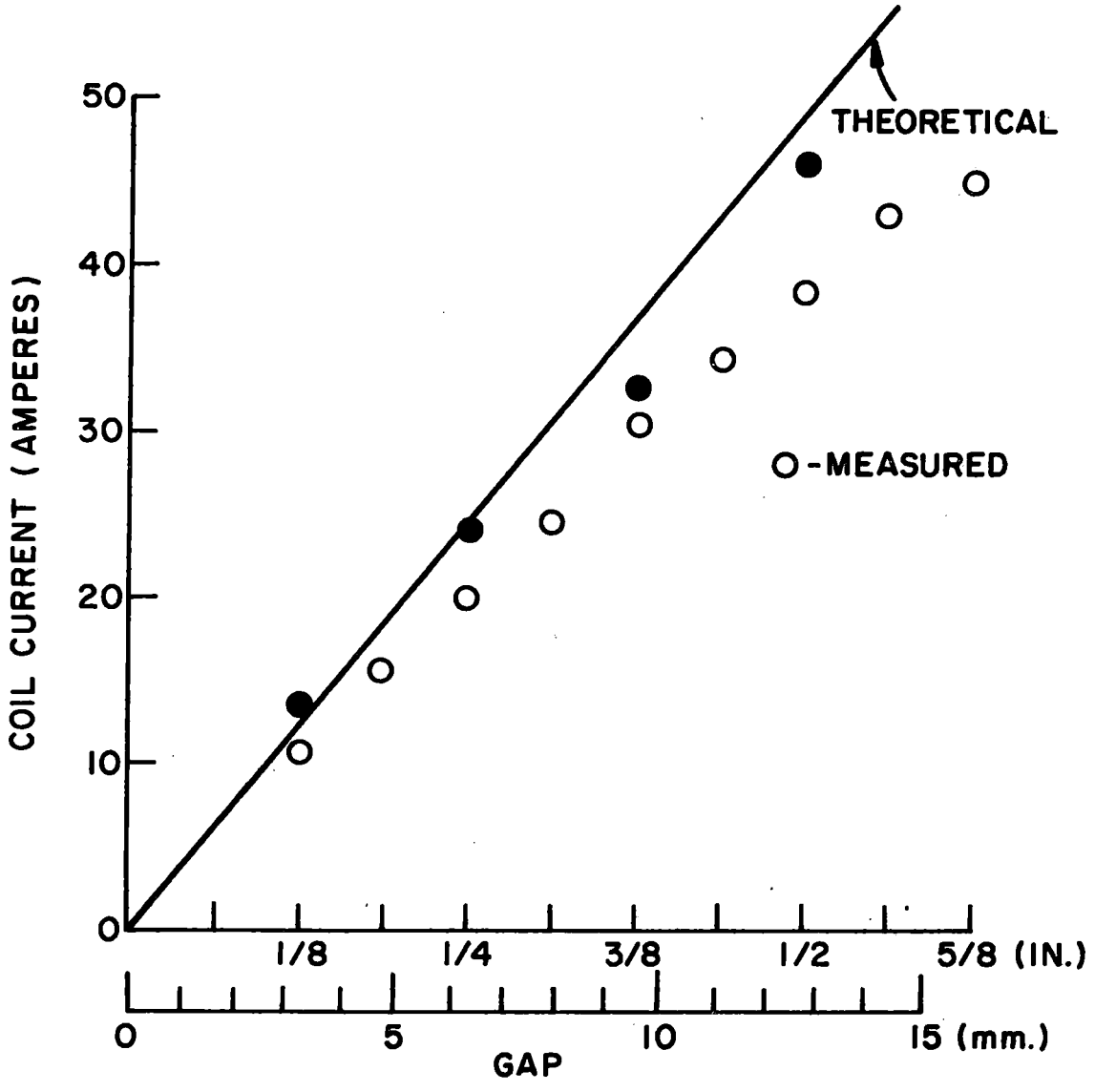

Fig. 3.19. Levitation current as a function of magnet to track gap for the large electromagnet.

In fact, as the air gap is increased, the effective air gap area will increase causing larger values for L(z) (eq.(3.62)) and its derivatives. This then implies lower values of the levitation current would be required than those calculated assuming a constant air gap area. If the effective air gap area increased linearly from the pole face area at zero gap to 1.5 times the pole face area at 1/2 inch gap, the theoretical and measured curves for the levitation current required for a given gap would agree almost exactly.

The power required for levitation can be calculated from the levitation current versus gap data since the coil resistance is known to be 0.15 ohms. The required levitation power per ton for various gaps is given in Table 3.6.

TABLE 3.6. Required Levitation Power
(275 lb. electromagnet of Figure 3.15)

gap (in.)	levitation power* (kw/ton)
1/4	0.44
3/8	1.2
1/2	1.62
5/8	2.22

* Calculated using measured values of current

These data indicate good agreement with other studies of such a system[16] and indicate we have an efficient magnet design.

3.5.4. Analytical and Experimental Study of Control System

In this section we analyze various control system designs for the large model electromagnet and compare the resulting suspension characteristics with our experimental results.

The equation of motion for the levitated magnet which is subjected to disturbances which perturb it from its equilibrium position is directly obtained from the previous discussions in which the lift force as a function of magnet-to-track gap was obtained. From equation (3.64) and using the coordinate system in Figure 3.20, it follows that

$$m\,\ddot{Z}_m = mg - F_L(Z_r) = mg + \frac{1}{2} I^2 \frac{dL(Z_r)}{d(Z_r)} \tag{3.68}$$

where $Z_r = Z_m - Z_t$. Linearizing equation (3.68) about the nominal equilibirium position, define

$$\Delta Z_m = Z_m - Z_m^e \quad , \quad \Delta Z_t = Z_t - Z_t^e \quad , \tag{3.6 }$$

and assuming ΔZ_m is small compared to the equilibrium gap, Z_r^e , and further, assuming that the current is given by

$$I = I_e + i_c \tag{3.70}$$

where i_c is the control current and I_e the equilibrium levitation current, $i_c \ll I_e$, then we obtain

$$\Delta\ddot{Z}_m = \frac{1}{2} \frac{I_e^2}{m} \left.\frac{d^2L}{dZ_r^2}\right|_e (Z_r - Z_r^e) + \frac{I_e}{m} \left.\frac{dL}{dZ_r}\right|_e (I - I_e) \quad . \tag{3.71}$$

The subscripts and superscripts, e, imply equilibrium values. This can be furthur simplified to

$$\Delta\ddot{Z}_m = a(\Delta Z_m - \Delta Z_t) + b\, i_c \quad , \tag{3.72}$$

where

$$a = \frac{1}{2} \frac{I_e^2}{m} \left.\frac{d^2L}{dZ_r^2}\right|_e \quad \text{and} \quad b = \frac{I_e}{m} \left.\frac{dL}{dZ_r}\right|_e \quad .$$

The voltage across the magnet coil is then given by

$$E_{coil} = RI + L \frac{dI}{dt} + I \frac{dL}{dt} \quad , \tag{3.73}$$

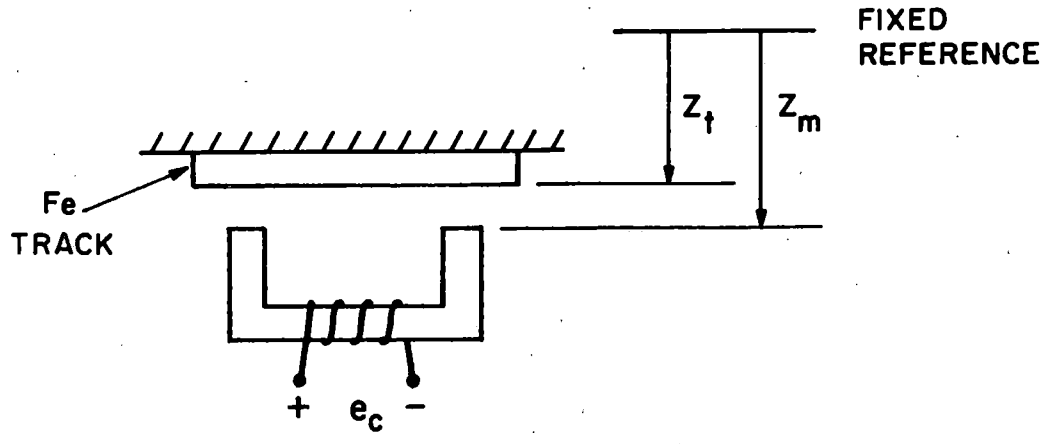

FIGURE 3.20 - MAGNET AND TRACK COORDINATES

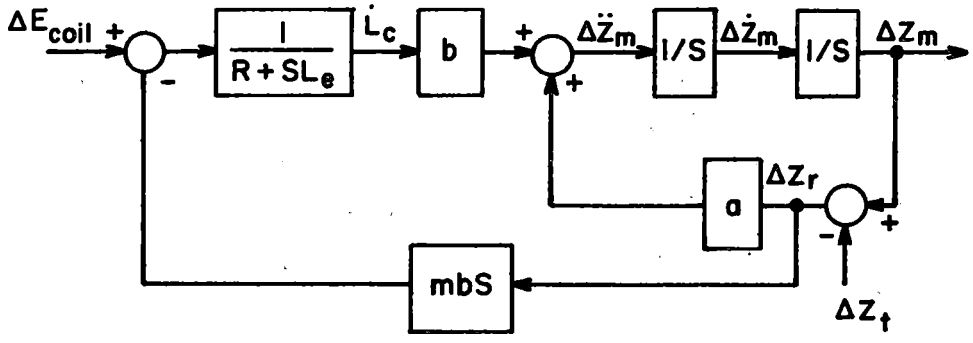

FIGURE 3.21 - BLOCK DIAGRAM REPRESENTATION OF LINEARIZED MAGNET EQUATIONS

which in terms of the small signal variables can be written

$$\Delta E_{coil} = E_{coil} - RI_e = Ri_c + L_e\frac{di_c}{dt} + I_e \left.\frac{dL}{dZ_r}\right|_e \frac{dz_r}{dt} \quad . \qquad (3.74)$$

Taking the Laplace transform of equations (3.72) and (3.74) we obtain,

$$s^2\Delta Z_m = a(\Delta Z_m - \Delta Z_t) + b\, i_c \qquad (3.75a)$$

$$\Delta E_{coil} = (R+SL_e)i_c + mb\cdot S\cdot z_r \quad , \qquad (3.75b)$$

where it is important to remember that $\Delta Z_m, \Delta Z_t, i_c, \Delta Z_r$ and ΔE_{coil} all represent the Laplace transforms of the respective time variables defined in equations (3.69) through (3.74), and S is the Laplace transform variable $\sigma + j\omega$. The block diagram representation of equations (3.75a,b) is given in Figure 3.21.

The various control strategies used to obtain a stable equilibrium with the magnet are indicated schematically in Figure 3.22. We have the capability of using both the magnet-track gap information and magnet absolute acceleration in various control strategies. The gap sensor used is a Kaman inductive sensor which gives an output of 1 volt per inch of magnet-to-track gap and the accelerometer is a Kistler servoaccelerometer which produces an output of 1/4 volt per g of acceleration. Thus, various linear combinations of absolute acceleration, absolute velocity, and relative (magnet-track) position can be used to obtain different suspension characteristics for the levitated magnet. Furthermore, this linear combination of signals can be passed through a compensation network as indicated in the figure to further alter the suspension characteristics. The control strategies we investigated fall into the following three categories:

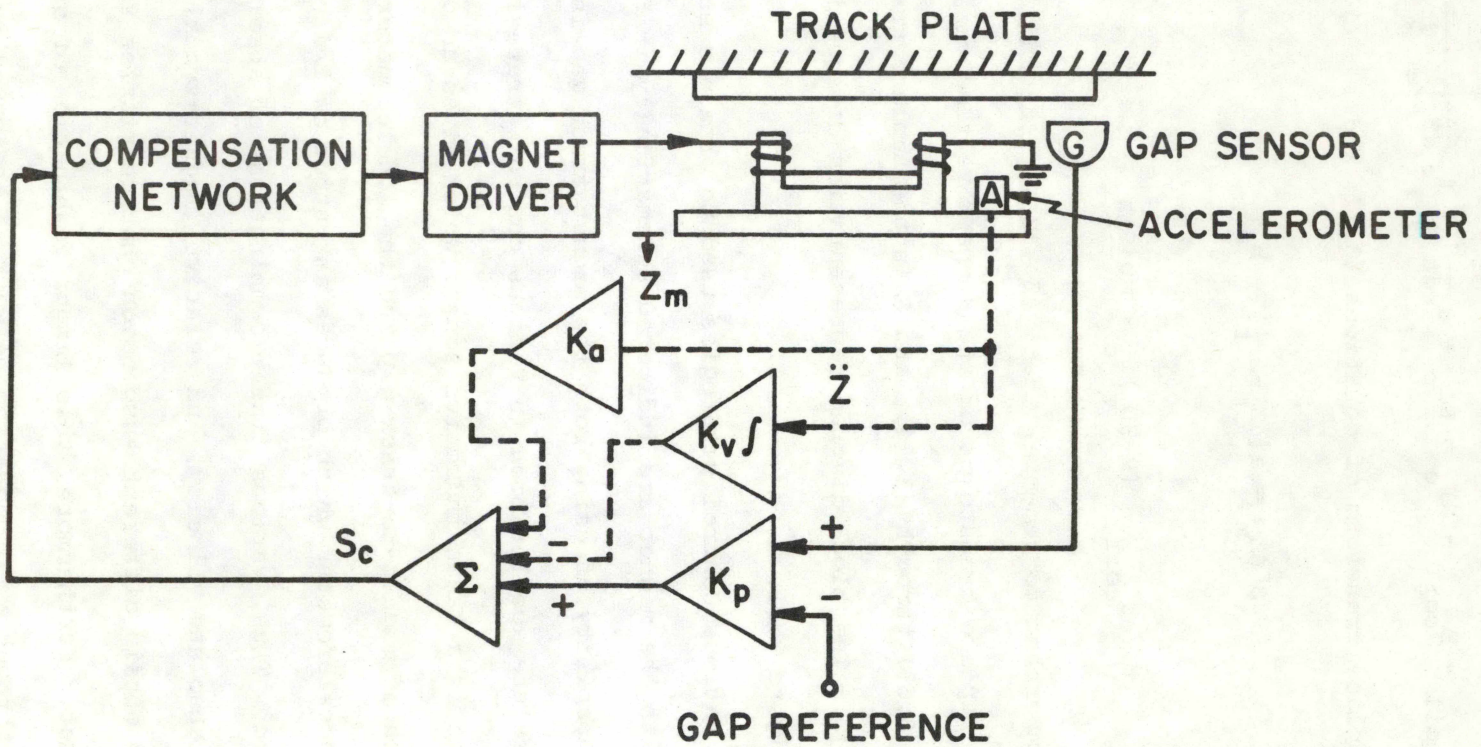

FIGURE 3.22 - SCHEMATIC OF MAGNET CONTROL SYSTEM

Type I : Position and velocity feedback $K_a = 0$, $K_v > 0$, $K_p > 0$ and the compensation network is not used. This results in a fairly soft, slow suspension with a high frequency resonance in the vicinity of 10Hz which can be altered very little by the adjustment of K_v and K_p.

Type II : Position, velocity, and acceleration feedback, $K_a > 0$, $K_v > 0$, $K_p > 0$ and the compensation network is not used. This results in a stiffer, quicker suspension.

Type III: Relative position feedback with compensation, $K_a = 0 = K_v$, $K_p > 0$ and a compensation network with a transfer function of the form $\frac{(S+a)(S+b)}{(S+c)(S+d)}$ is used. This approach requires extremely large values for the gain, K_p, and results in a very stiff suspension. However, it is very susceptible to noise problems because of the very high gains and wide bandwidth.

In each of these approaches, the control signal is used as the input to a pulse width modulator which then drives a power amplifier which drives the magnet. Thus, the control signal is used to vary the duty cycle of a fixed amplitude voltage pulse train with a 4 kHz frequency which is used to energize the coil. It is important to distinguish this approach from the case where the magnet is driven by a power supply in which the current in the coil is directly controlled since similar control signals to the input of the power amplifier would produce different dynamic characteristics of the magnetic suspension. We chose the voltage control approach because we felt that it would be more efficient in an eventual full-size vehicle, since it appears that less power would be dissipated

in the power amplifier itself using this approach. However, neither the voltage control nor current control approach should be considered to be the "only way to do it" at this time.

The Laplace transform block diagram representing the magnet including all of the control variables we investigated is shown in Figure 3.23. The blocks labeled PWM and PA represent the pulse width modulator and power amplifier. These blocks were approximated in our analysis by a simple linear gain of 1.66 which was determined experimentally. The results of the analysis indicate this was a good approximation. We proceed now to a comparison of the analytical and experimental results using the various control approaches.

Type I Control System: Position and Velocity Feedback

In all cases, the transfer function of interest is the transfer function from Z_t to ΔZ_m, i.e., we are interested in knowing how the magnet responds to disturbances in the track position. In this case, the transfer function obtained by setting $K_a = 0$ and not using a compensation network (as defined above for the Type I control approach) and applying Mason's Gain Formula is found to be

$$\frac{\Delta Z_m}{Z_i} = \frac{1}{\tau_I}\,(mb^2/L-a)\;\cdot\;\frac{N(S)}{D(S)}\quad, \qquad \text{(a)} \qquad (3.68)$$

$$N(S) = [S - (K_p b/L - a/\tau_c)]\;(\tau_I S+1) \qquad \text{(b)}$$

$$D(S) = S^4 + \frac{1}{\tau_p}S^3 + S^2\left(\frac{1}{\tau_I\tau_c} - K_v\frac{b}{L} + \frac{mb^2}{L} - a\right) + S\left(-K_p\frac{b}{L} - a/\tau_p + \frac{mb^2}{L\tau_I}\right) - \frac{K_p b}{L\tau_I} - \frac{a}{\tau_I\tau_c} \qquad \text{(c)}$$

where $\tau_c = L/R$,

$\tau_p = \tau_I\tau_c/(\tau_I+\tau_c)$

τ_I = integrator time constant .

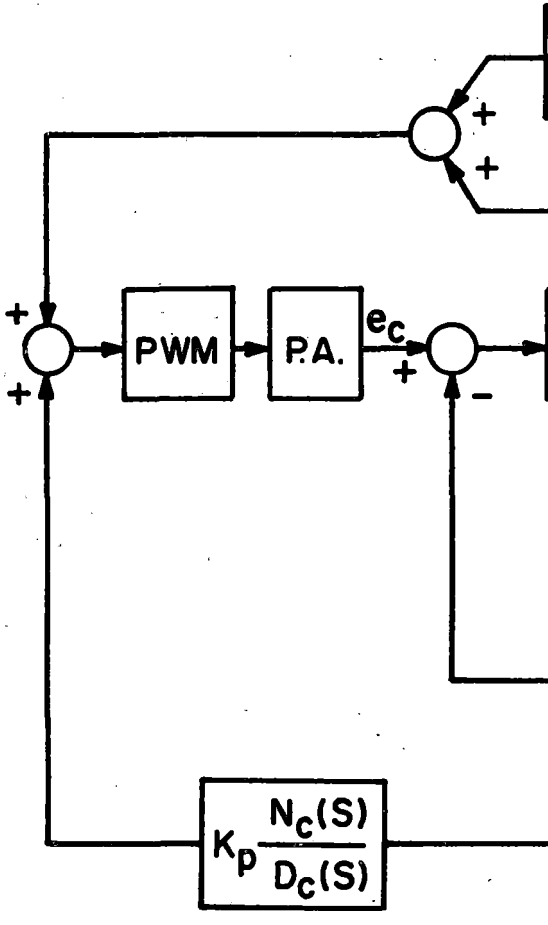

BLOCK DIAGRAM -

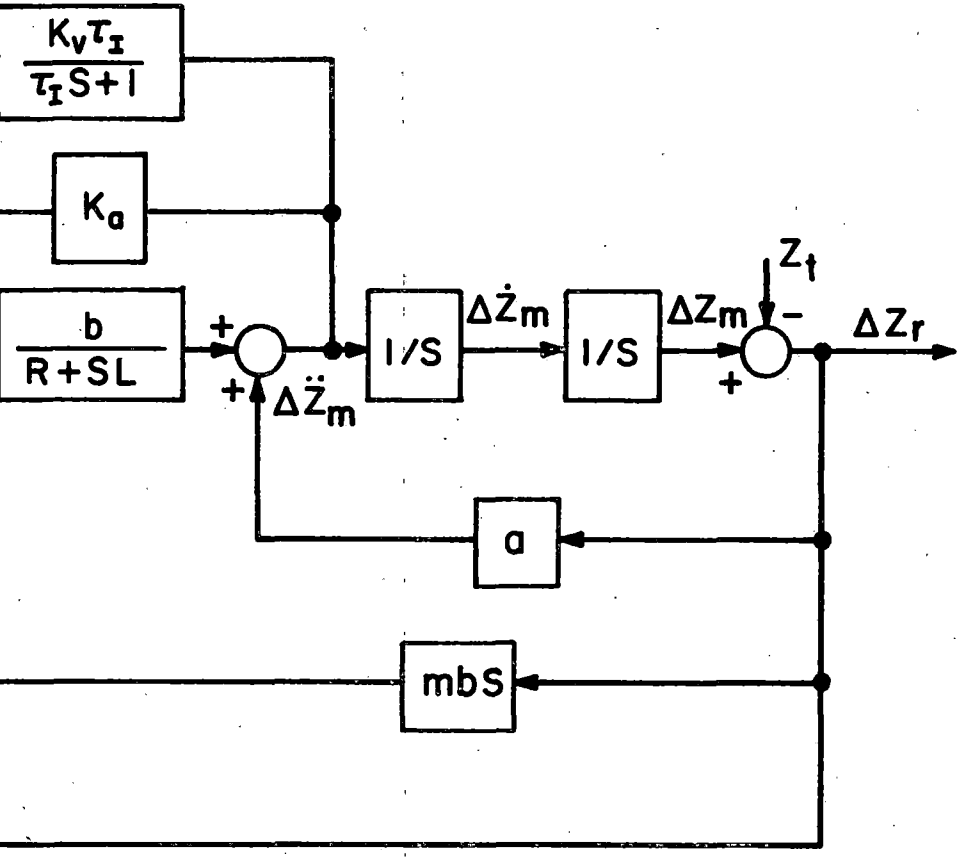

FIGURE 3.23
MAGNET WITH FEEDBACK CONTROL

Note that we use a non-ideal integrator with a time constant τ_I to obtain the velocity signal. This is done because of limitations in the electronic circuitry which prevent good operation of the circuit for very large τ_I. However, this does not have a major effect on the response for $\tau_I \geq 1$ sec., and we have used $\tau_I = 1$ sec. in most cases. Note also that at low frequencies, i.e., $S \rightarrow 0$, $\Delta Z_m/Z_t \rightarrow 1$ and at high frequencies, i.e., $S \rightarrow \infty$, $\Delta Z_m/Z_t \rightarrow 0$. This is the desired behavior since the magnet should follow the track at low frequencies and ignore it at high frequencies.

The frequency response typical of this control strategy is shown in Figure 3.24. It is characterized by a first order rolloff occurring above about 0.6 Hz and a rather undamped resonant peak occurring in the region from 8-12 Hz for reasonable values of the two gains K_v and K_p. This suspension is basically rather soft due to the rolloff around 1 Hz and thus has a slow transient response. The resonance in the 10 Hz region causes difficulties in control because it leads to saturation of the rather low voltage control electronics we used.

If one investigates the root contours for this system, i.e., the movement of the roots of the characteristic equation in the complex plane as K_v and K_p are varied, it is found that the response shown in Figure 3.24 cannot be improved upon by any combination of K_v and K_p. The low frequency rollof and lightly damped high frequency resonance will always be present. Thus, while it is difficult to define an optimal suspension for this approach, it is reasonable to say that the responses in Figure 3.24 are about the best that can be achieved.

It should be noted that the parameters of curve A correspond to those measured experimentally when the frequency response data shown were taken. Curve B, which agrees better with the experimental results,

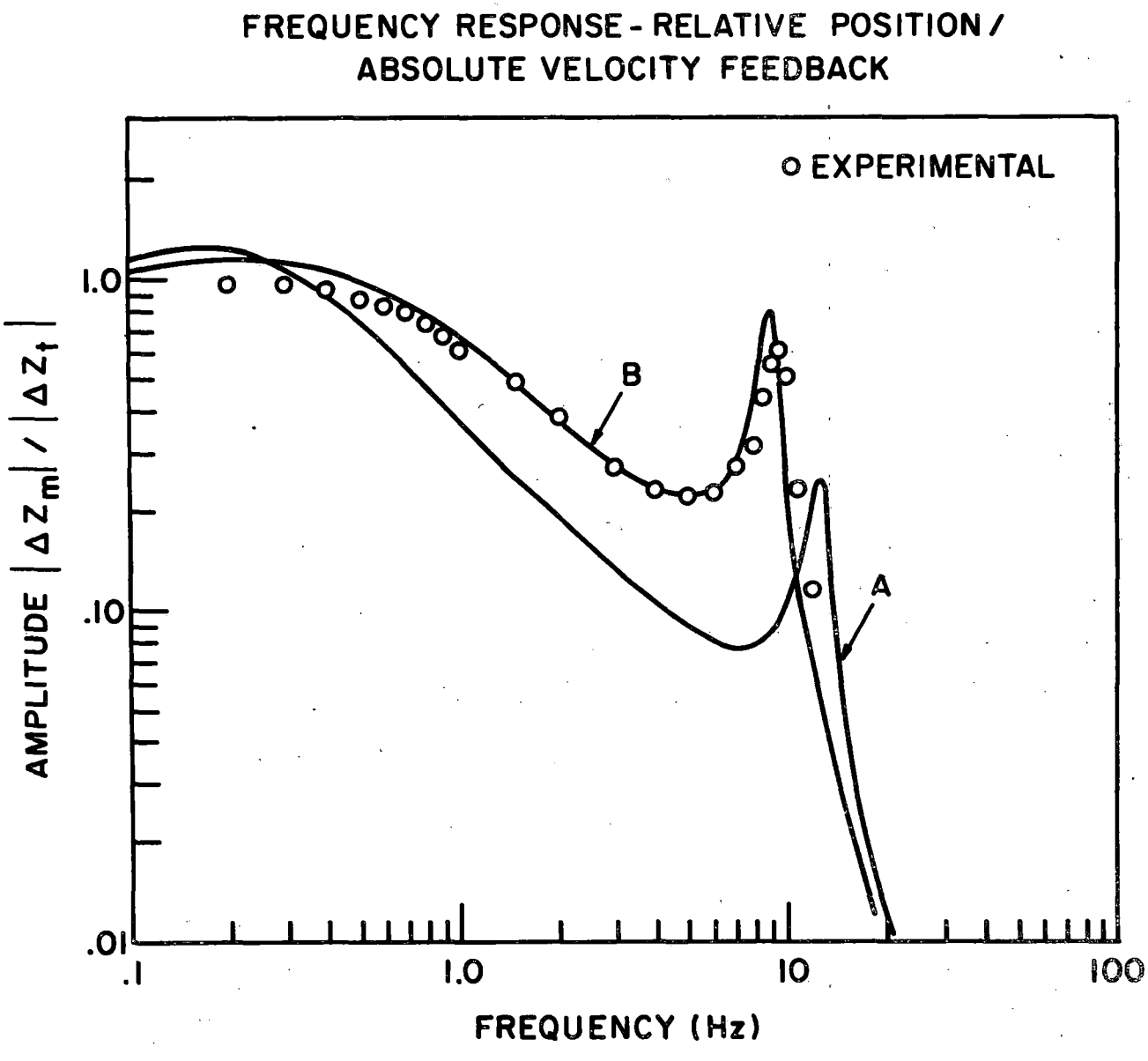

Fig. 3.24. Frequency response curves for electromagnetic suspension. The parameters are: Curve A - τ_I = 1 sec, K_v = 77.5 volt sec/ft, K_p = 319 volt/ft. Curve B - K_v = 38.75, all other parameters the same. The experimental results were obtained using the values of curve A.

was generated using K_v equal to one half the measured value. We feel that the agreement between the experimental and analytical results is very good despite this minor discrepancy. Qualitatively, the agreement between analysis and experiment is always excellent. We have strong experimental indications that a simple constant R and constant L equivalent circuit for the magnet as used in our analysis cannot precisely describe the behavior of the magnet for frequencies above about 5 Hz. Due to eddy currents in the core, the magnet resistance increases with frequency and the inductance decreases. Furthermore, it appears that the leakage inductance is not independent of the gap and could affect the results. However, because the basic agreement between analysis and experiment is so good, we do not feel that the minor numerical disagreement is cause for concern.

Finally, the phase shift curves for the given frequency responses are not shown since they do not convey much additional information. Generally the phase lag increases from about zero degrees at 0.1 Hz to about 60 degrees at 10 Hz.

Type II Control System: Position/Velocity/Acceleration Feedback

In this case, the transfer function is found to be

$$\frac{\Delta Z_m}{Z_t} = \frac{1}{\tau_I}\left(\frac{mb^2}{L} - a\right) \cdot \frac{N(S)}{D_a(S)} \qquad (3.69a)$$

where N(S) is the same as for the Type I control system (eq. (3.68)(b)) and

$$D_a(s) = S^4 + S^3\left(\frac{1}{\tau_p} - \frac{K_a b}{L}\right)$$

$$+ S^2\left\{\frac{1}{\tau_I \tau_c} + \frac{mb^2}{L} - a - (K_v + K_a/\tau_I)\frac{b}{L}\right\}$$

$$+ S\left(-K_p b/L - a/\tau_p + \frac{mb^2}{L\tau_I}\right) - K_p b/L\tau_I - a/\tau_I\tau_c \quad . \qquad (3.69b)$$

Typical frequency response curves for the suspension resulting from this control approach are shown in Figure 3.25. As before, the experimental points are marked by a • and curve A was obtained from equations (3.69a) and (3.69b) using the experimentally measured values for K_a, K_v, and K_p. Once again, excellent agreement is obtained between the analytical and experimental results if a value for K_v is used which is somewhat less than half the measured value. We feel that this relatively minor disagreement results from the somewhat simplified model of the magnet as discussed earlier.

Basically, the use of acceleration feedback allows higher values of K_p to be used without generating a lightly damped high frequency resonance. The higher K_p leads to a stiffer, quicker suspension as exemplified by the fairly flat response out to 10 Hz. The phase lag at 10 Hz for curve B is about 90°.

We feel that the response of curve B is the best response in terms of suspension stiffness, quickness, and stability which we could obtain. Such a suspension could easily follow a track of reasonable roughness if electronic circuitry with a high enough voltage rating were used. However, we will see that the ride quality without a secondary suspension would not be acceptable.

Type III Control System: Compensation Network/Position Feedback

In this approach, the accelerometer signal is not included in the control signal. The relative position signal is passed through a compensation network in order to obtain the desired stability. With a compensation network of the form

$$K_c \frac{(S+Z_1)(S+Z_2)}{(S+P_1)(S+P_2)} \qquad (3.70)$$

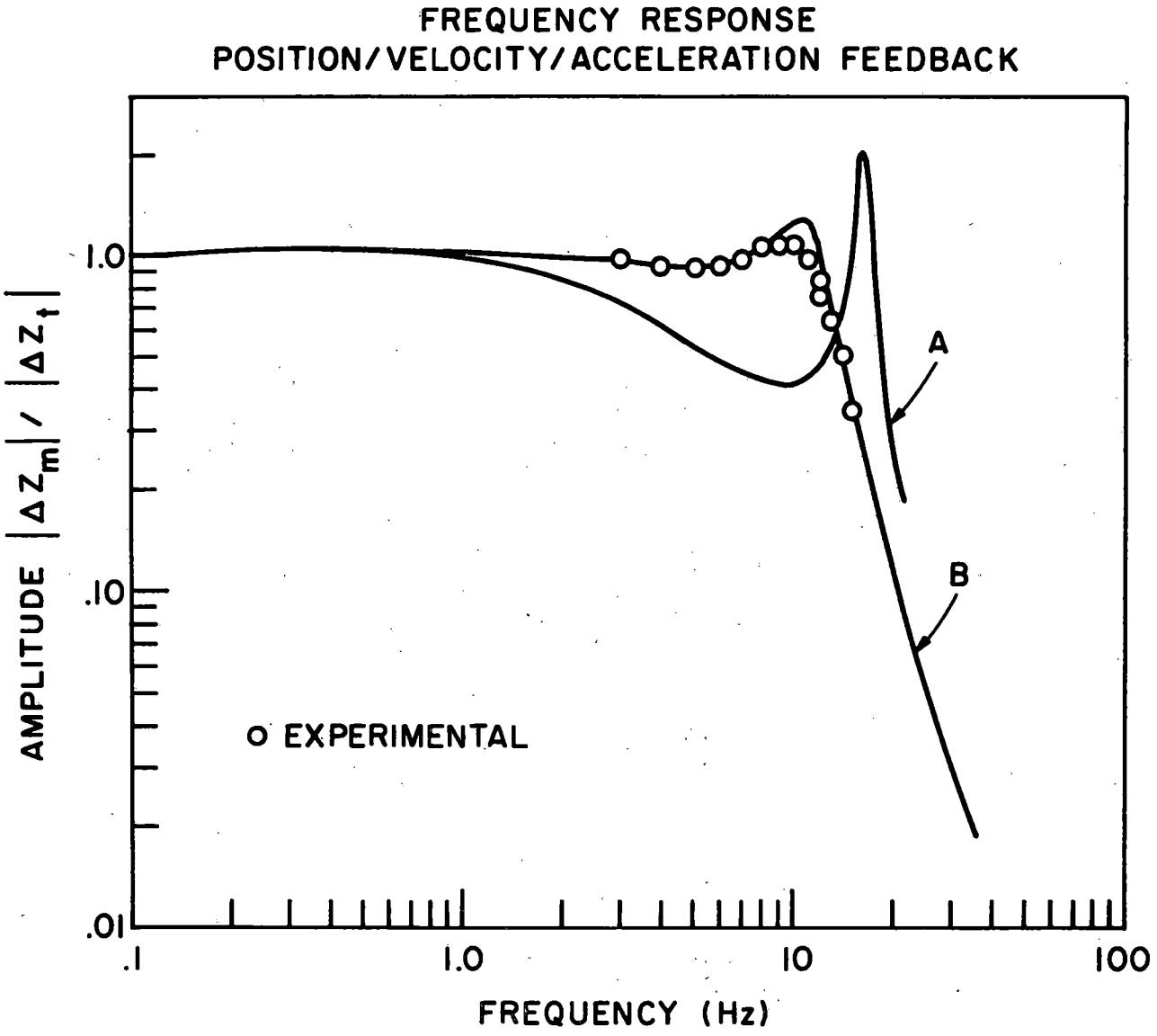

Fig. 3.25. Frequency response curves for electromagnetic suspensions. The parameters are:
Curve A and experimental - K_a = 0.775 volt sec^2/ft, K_p = 2380 volt/ft, K_v = 129 volt sec/ft.
Curve B - K_v = 50 volt sec/ft, all other parameters the same.

the transfer function $\Delta Z_m/Z_t$ is found to be

$$\Delta Z_m/Z_t = \left(\frac{mb^2}{L} - a\right) \frac{N_c(S)}{D_c(S)} \qquad \text{(a)} \qquad (3.71)$$

where

$$N_c(S) = S^3 + \left(P_1 + P_2 + R/L - \frac{K_c b}{L} \cdot \frac{1}{\left(\frac{mb^2}{L} - a\right)} \right) S^2$$

$$+ S \left\{ P_1P_2 + P_1R/L + P_2R/L - \frac{K_c b}{L} \frac{(Z_1+Z_2)}{\left(\frac{mb^2}{L} - a\right)} \right\}$$

$$+ \frac{P_1P_2R}{L} - \frac{K_c b}{L} \frac{Z_1Z_2}{\left(\frac{mb^2}{L} - a\right)} \qquad \text{(b)} \qquad (3.71)$$

and

$$D_c(S) = S^5 + (P_1+P_2+R/L)S^4 - \frac{K_c b}{L} Z_1Z_2 - a\, P_1P_2R/L$$

$$+ S^3 \left(P_1P_2 + P_1R/L + P_2R/L + \frac{mb^2}{L} - a\right)$$

$$+ S^2 \left\{ P_1P_2R/L - a(P_1+P_2+R/L) + \frac{mb^2}{L} (P_1+P_2) - \frac{K_c b}{L} \right\}$$

$$+ S \left\{ \frac{mb^2}{L} P_1P_2 - \frac{K_c b}{L}(Z_1+Z_2) - a(P_1P_2 + P_1R/L + P_2R/L) \right\} \quad . \qquad \text{(c)} \qquad (3.71)$$

This control approach corresponds to a more classical control approach than those dicussed earlier. The network of eq. (3.70) is known as a double phase lead network and is easily realized using resistor/capacitor networks with operational amplifiers as buffers. The zeroes, Z_1 and Z_2, must be much less than the poles P_1 and P_2 in order to be able to stabilize the unstable magnet equilibrium. However, for any choice of these zeroes and poles, extremely high values of the gain K_c are needed to drive the

the poles of the system (i.e., the roots of D(S) = 0) into the left half of the complex S plane as required for stability. The movement of the system poles in the complex plane as K_c is varied can be studied for various compensation poles and zeroes by finding the roots of (3.71c). Such root loci studies indicate that a compensation network given by

$$K_c \frac{(S+20)(S+25)}{(S+800)(S+900)} \tag{3.72}$$

yields about the best response. The minimum value of K_c needed for stability with this network is about 6×10^4, with values of K_c in the range 2.5×10^5 giving the best system responses as indicated by the transfer function.

The transfer function $\Delta Z_m/Z_t$ of a magnet with this type of feedback control with two different values for K_c is shown in Figure 3.26. The extremely large gain values lead to very wide bandwidth responses and an incredibly stiff suspension. However, it is apparent that noise would be a severe problem with such high gains as would saturation of the control electronics. For example, a signal of 50μ volt at the transducer would be 2.5 volt after the gain of 5×10^5. However, such a signal corresponds to a movement of only 50 microns. Furthermore, unless the signal-to-noise ratio of the transducer is of the order of 1000, electronic noise will be a problem with such high gains.

Experimentally, with great care we were able to get such a suspension to be statically stable. However, any movement of the track or variation of the reference signal caused saturation of the control circuitry and noise problems made the static stability very precarious. Thus, it was impossible to obtain a frequency response experimentally.

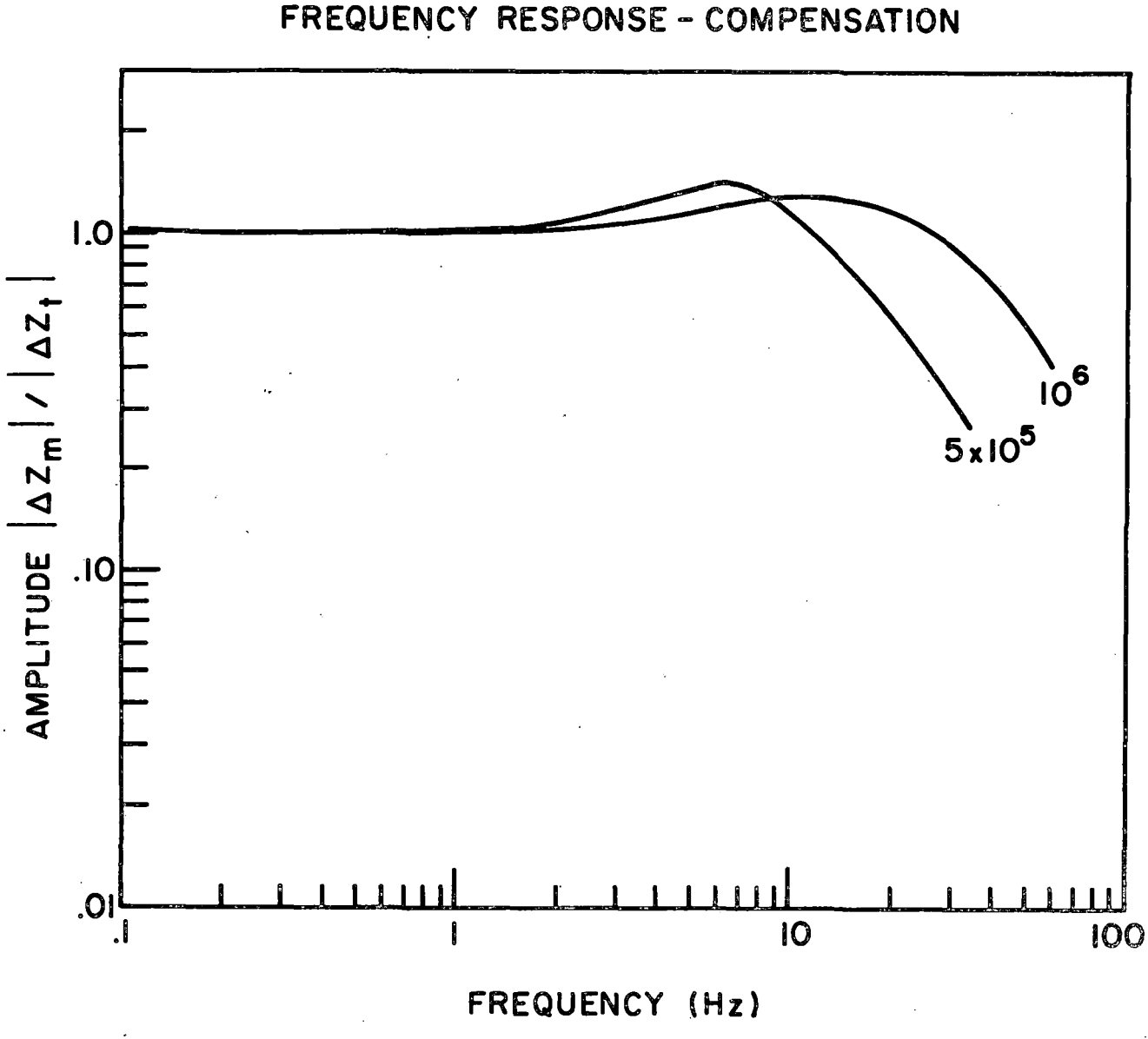

Fig. 3.26. Theoretical frequency response curves for electromagnetic suspension with compensation network. The compensation network has the transfer function $K_c \frac{(S+20)(S+25)}{(S+800)(S+900)}$ and the numbers by the curves correspond to values of K_c.

While this type of control leads to a suspension which would follow the track exactly to about 50 Hz, we do not feel it would be at all practical due to the noise problems and control circuit saturation associated with the extremely high gains.

Control Power Requirements

The nature of the limiting behavior of the levitated magnet when subjected to disturbances due to track roughness depends on the control strategy, the capabilities of the electronic circuitry used to control the magnet power supply, and on the power available from the power supply. Thus, whether the magnet strikes the track first or "falls out of control" first when subjected to sinusoidal signals of increasing magnitude depends very much on the particular details of the control system used and generalizations regarding "control limits" are somewhat difficult to make. However, it is seen in the analyses which follow that rather modest amounts of control power will be required to allow a vehicle to travel at 300 mi/h over typical guideways of random roughness without "falling out of control", and the control limit will be defined by the condition when the magnet repeatedly strikes the track.

We experimentally determined the limit when our magnet would begin striking the track by shaking the upper plate (track), using our mini-servo system, at varying amplitude for various frequencies. Because of an idiosynchrosy in our pulse width modulation circuitry, the magnet would clamp to the track once it began to strike the track, and thus the limit of striking the track in terms of the input disturbance amplitude was rather easy to determine experimentally. The control limit in

terms of track amplitude versus frequency is shown in Figure 3.27. These results were obtained using Control Type I as discussed earlier, i.e., using relative position and absolute velocity feedback control of the magnet voltage. The frequency response for the suspension obtained with the parameters $K_v = 56$, $K_p = 338$ as used in this test was very similar to those shown in Figure 3.24. This control strategy was used to determine the control limits mainly because it was the one with which we had had the most success at the time this test was run. Unfortunately, because of the nature of the magnet voltage and current, i.e., a pulse width modulated 4 KHz pulse train, it was not practical to measure the average voltage and current at the control limit. Thus, we do not have measured quantities to indicate what control power was being expended at the limit when the magnet struck the track. However, the magnet voltage and current resulting from the track vibrating at the amplitude given by the control limit curve can be calculated from a linear analysis by the same techniques as were used to determine the transfer function $\Delta Z_m/Z_t$ in earlier analyses. The transfer functions for the control voltage and current can be shown to be

$$\frac{E_c(S)}{\Delta Z_t(S)} = \frac{S^2(S+R/L)[mb\tau_I S^2 + S(mb - K_p\tau_I) - aK_v\tau_I - K_p]}{\tau_I D(S)} \qquad (3.73a)$$

and

$$\frac{I_c(S)}{\Delta Z_t(S)} = \frac{E_c(S)}{R+SL} \quad , \qquad (3.73b)$$

where D(S) is as given in equation (3.68c). Recall that the total voltage across the coil, E_{coil}, is

$$E_{coil} = e_c(t) + RI_e \qquad (3.74)$$

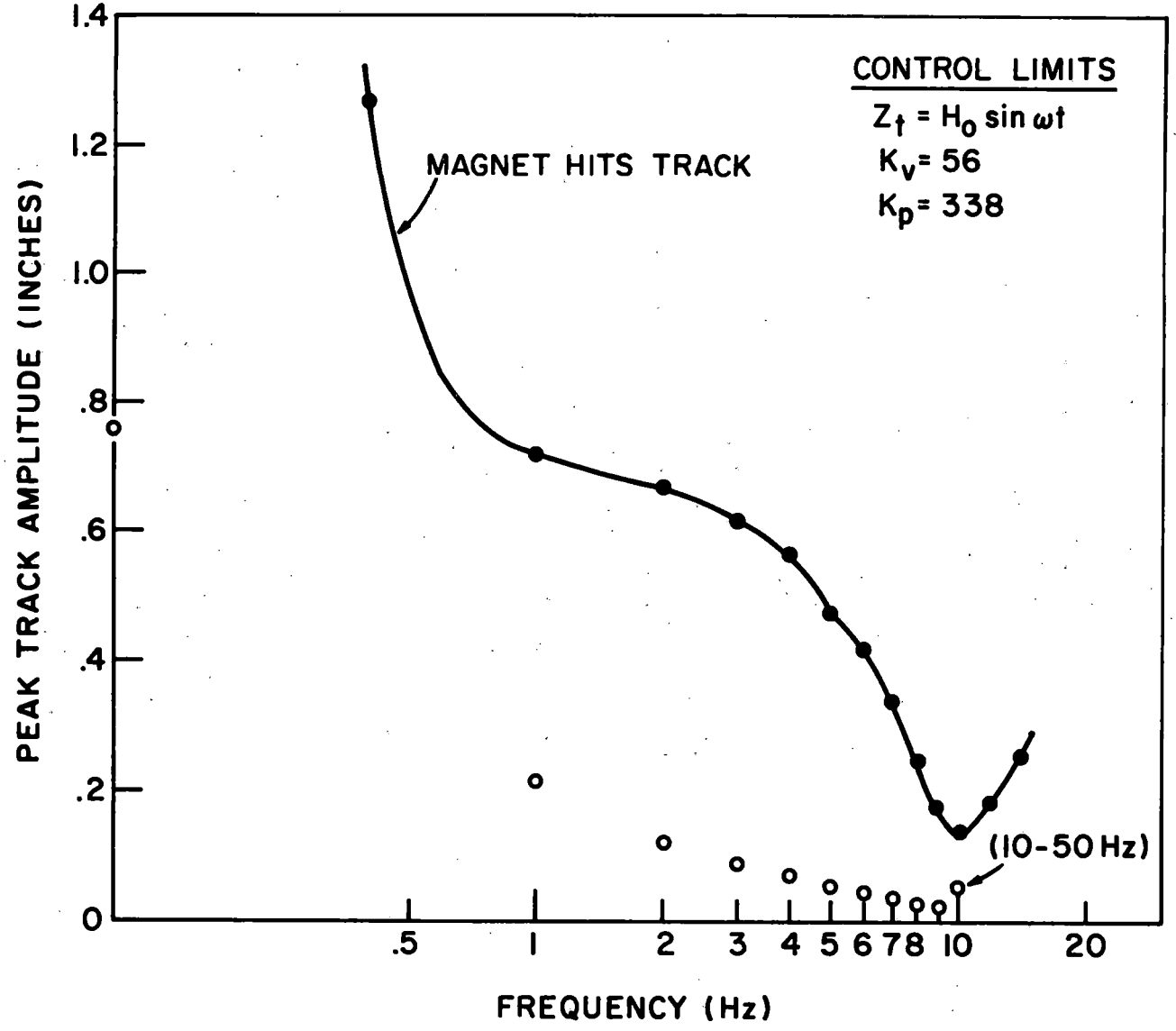

Fig. 3.27. Control limit response of electromagnetic suspension obtained using relative position/absolute velocity feedback with gains K_v = 56 volt sec/ft, K_p = 338 volt/ft. The magnet "latched" to the track when it hit. The points marked o correspond to the peak amplitude in a 1 Hz bandwidth about the various frequencies for a track with random roughness power spectral density A/Ω^2, A = 5 x 10^{-6} ft.

where R is the coil resistance and I_e the equilibrium coil current, and the total current through the coil is

$$I_{coil} = i_c(t) + I_e \quad . \tag{3.75}$$

Then $E_c(S)$ and $I_c(S)$ are the Laplace transforms of $e_c(t)$ and $i_c(t)$, respectively. The average power supplied to the coil is

$$P_{av} = \overline{E_{coil} I_{coil}} = \overline{e_c i_c} + \overline{e_c I_c} + \overline{R I_e i_c} + \overline{R I_e^2}$$

$$P_{av} = \overline{e_c i_c} + \overline{R I_e^2} \quad . \tag{3.76}$$

Where the two terms $\overline{e_c I_e}$ and $\overline{R I_e i_c}$ are zero for sinusoidal signals. The mean squared voltage and current are thus given by

$$E_{rms}^2 = \overline{E_{coil}^2} = \overline{e_c^2} + \overline{(R I_e)^2} \tag{3.77}$$

and

$$I_{rms}^2 = \overline{I_{coil}^2} = \overline{i_c^2} + \overline{I_e^2} \quad . \tag{3.78}$$

The apparent power supplied to the coil, which is a measure of the peak rating that the magnet power supply must have, is given by

$$P_{app} = E_{rms} I_{rms} \quad . \tag{3.79}$$

The various quantities of interest, eg. control power, average power, apparent power, etc. as calculated for our magnet when subjected to sinusoidal track oscillation at the amplitude indicated for the control limit in Figure 3.27 are given in Table 3.7.

TABLE 3.7. Power Quantities at the Control Limit (Fig. 3.27)

Frequency (Hz)	$\|E_c\|$ (Volts)	$\|I_c\|$ (Amps)	$P_{control}$ (Watts)	$P^*_{average}$ (Watts)	$P^*_{apparent}$ (Volt-Amps)
1.	10.6	58.4	256	477	840
2.	14.1	56.4	238	460	1042
3.	21.7	64.3	313	535	1677
4.	28.1	65.6	322	543	2178
5.	31.7	60.5	274	495	2306
6.	37.0	59.6	266	487	2653
7.	38.0	52.8	209	430	2508
8.	32.6	39.9	119	340	1831
9.	27.6	30.1	68	289	1377
10.	23.2	22.8	39	260	1069

* Calculated using measured equilibrium current.

It should be reemphasized that E_c and I_c were calculated using (3.73 a,b) and assume a strictly linear system. Thus, they do not correspond to the amplitudes that would be directly measureable in our system with the pulse width modulator since the voltage applied to the coil is fixed in amplitude, is only positive, but has a variable duty cycle. However, the power quantities calculated should correspond to the power quantities delivered by the power supply in the real case were there no saturation of either the power supply or the control circuitry. In this case it appears that there may have been saturation of both of these and thus the power calculated is an upper limit for the power which was actually being expended.

It is seen from Table 3.7 that the control power expended at the disturbance amplitude at which the magnet hit the track is at the most about 1 watt/lb. at 5 Hz. The static levitation power of 221 watts

is thus about the same as the maximum control power. However, the apparent power, which peaks at 6 Hz with a value of 2.653 KVA reaches about 10 VA/lb. Thus, the power supply must provide peak currents and voltages which are larger than would be inferred from the average power requirements, and this will be important in power supply design.

The power, both real and apparent, which would be required for a magnet subjected to a random track roughness with roughness power spectral density given by

$$P_{z_t z_t} = Av/\omega^2 \quad , \tag{3.80}$$

as used in the ride quality analyses, can also be calculated. It is easy to show that the power would be infinite if ω is taken to vary from some lower cutoff frequency ω_c to ∞, since the coil voltage power spectral density approaches a constant for high frequencies. However, if we assume that a low pass filter with a cutoff frequency of 50 Hz is used in the control loop to eliminate frequencies above 50 Hz, the real and apparent power delivered to the coil can be calculated. This power can be calculated to a good approximation by approximating the random roughness by discrete sinusoidal components at 1 Hz intervals with an rms amplitude corresponding to the rms signal present in the random signal in the 1 Hz band of frequencies. The amplitudes calculated in this manner for an A coefficient of 5×10^{-6} ft and a velocity of 300 mi/h are indicated in Figure 3.27. Note that the contribution of all frequency components above 10 Hz are included in the amplitude at 10 Hz. Then, in a manner similar to that above, E_{c_i} and I_{c_i}, the voltage and current components in the i^{th} frequency band can be calculated. Then the quantities of interest are

$$P_{average} = \sum_i \overline{e_{c_i} i_{c_i}} + RI_e^2 \qquad (3.81)$$

$$E_{rms}^2 = \sum_i \overline{e_{c_i}^2} + (RI_e)^2$$

$$I_{rms}^2 = \sum_i \overline{i_{c_i}^2} + I_e^2 \quad .$$

The control power, average power, etc. as calculated for the track with roughness described by (3.80) are given in Table 3.8.

TABLE 3.8. Power Requirement over Guideway with Roughness Power Spectral Density Av/ω^2, at 300 mi/h.

A	$P_{control}$	$P_{average}$	$P_{apparent}$
5×10^{-6} ft	70 watts	281 watts	622 volt amps
	.254 watts/lb	1.02 watts/lb	2.26 voltamp/lb

While these calculations were made for our magnet with a lift/weight ratio of 2.5, a total levitated weight of 275 lb, and dimensions as indicated in Figure 3.15, we feel that the per pound values given in Table 3.8 are valid for magnets of various sizes and weights. This is born out by our studies with the smaller magnet and the unpublished results of others.

Thus, we can conclude that a total average power of about 1 watt per pound is sufficient for operation over a guideway with statistical roughness parameter $A = 5 \times 10^{-6}$ ft at 300 mi/h. However, the peak power supply rating would be almost double that amount. Since the control power increases linearly with A, a value of A of 20×10^{-6} ft would

require a control power of 1 watt/lb and average power of almost 2 watts/lb. It appears however, that the limit of operation is really determined by the point at which the magnet strikes the track rather than when it falls out of control.

Two important points regarding control should be noted. First, there are other control strategies that could be tried and which would yield different frequency responses. Two examples are magnet current control instead of magnet voltage control, and adding a feedback term proportional to the magnet current. In essence these are both similar strategies which would yield frequency responses similar to that of the Type I control system but without the peak around 10 Hz. This would be desireable from a ride quality point of view but would probably not be useable because of clearance requirements. We used a voltage control approach since it seemed inherently more efficient than a current controlled power supply. However, this tradeoff should be investigated in more depth if the controlled current approach could be shown to have definite advantages.

The second point to note is that the voltage rating of the control system electronic circuitry is an important factor in limiting the performance of the magnetic suspension. We found that the control circuitry which we used (15 volt supply) saturated and degraded the system performance for rather small track amplitudes with frequencies in the range of 10 Hz. We would recommend using electronics with at least a 100 V (and preferably higher) rating.

Ride Quality

The ride quality resulting from traveling over a guideway with random roughness characterized by the power spectral density in equation

(3.80) can be determined for the various control approaches with the ferromagnetic suspension from the frequency responses depicted in Figures 3.24-3.26. The resulting vertical acceleration power spectral densities at 300 mi/h over a guideway of roughness parameter A= 5 x 10^{-6} ft for typical responses of each of the three control strategies are shown in Figure 3.28. It is seen that each of these greatly exceeds the Urban TACV specification. There is no possibility of meeting the specification with either the Type II or Type III control approach without a secondary suspension. However, based on the studies in Section 6, we conclude that the characteristics of such a secondary suspension (i.e., natural frequency ~.4 Hz., stroke~ 6 inches peak to peak, static load carrying capability~ 25,000 lb.) would require that it be an active secondary suspension. Furthermore, the lateral ride quality specification is slightly more stringent and would probably imply the need for an active lateral secondary suspension. This certainly adds to the complexity of such a system and greatly lessens its advantages. Using the current control strategy with the Type I control system would probably help to eliminate the resonance near 10 Hz which would make the ride quality almost acceptable. However, our previous studies indicate that the resulting rms value of the change in magnet to track clearance would be about equal to the gap of 1/2 inch. This is not acceptable. We thus conclude that the ferromagnetic suspension cannot be used over a guideway with roughness parameter A = 5 x 10^{-6} ft at 300 mi/h without using a secondary suspension to achieve ride quality. If a secondary suspension is used, there are strong indications it will have to be active.

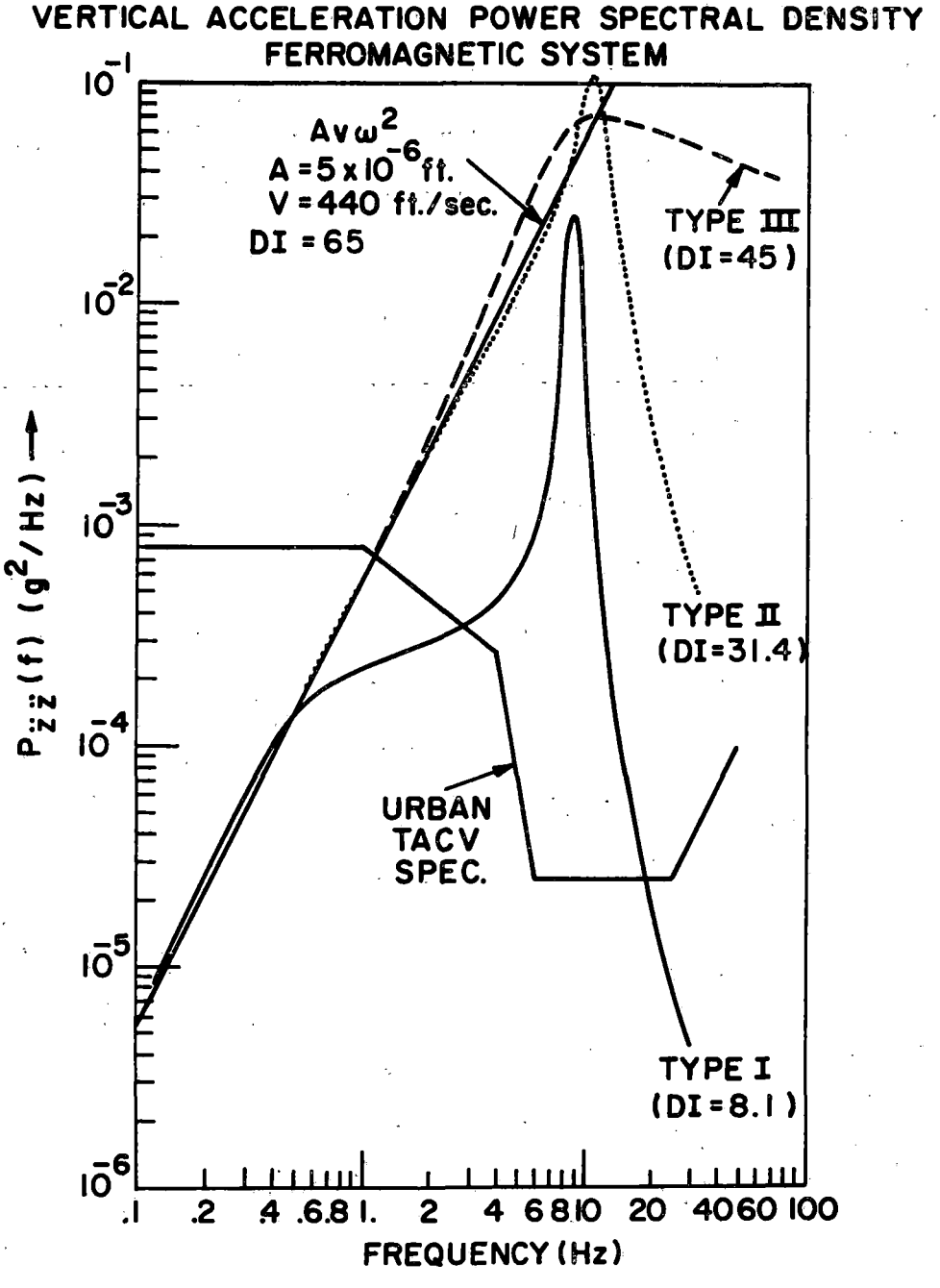

Fig. 3.28. Vertical acceleration power spectral densities for various electromagnetic suspension characteristics as discussed in the text.

4. PROPULSION

It has been determined that a 50 ton magnetically-suspended vehicle requires approximately 10,000 lb of thrust at 300 mi/h to overcome aerodynamic and magnetic drag forces.[1] To have the capability of 0.1 g acceleration, an additional 10,000 lb of thrust is required, making a total (at peak speed) of 20,000 lb (8.9×10^4 N). Four propulsion systems capable of supplying thrust of this order of magnitude are considered: (i) the linear induction motor (LIM), (ii) two forms of the newly proposed rotating superconducting motors, (iii) the linear synchronous motor (LSM), and (iv) the Q-fan turbojet engine. Aside from the obvious differences in construction between a double-sided LIM and a single-sided LIM, these two motors have essentially the same operating characteristics for our purposes. Hence, we restrict our attention to the double-sided motor. Most of the useful literature on the LIM can be found in Refs. 18-29, or references cited therein.

A double-sided LIM is currently being tested by the Department of Transportation at its Pueblo test facility. Two different motors have been built by Garrett Research Corporation: a 2,500 hp motor for testing in the LIM rail vehicle and a 4,000 hp motor for the TACRV (research TACV).

The design specifications for the 4,000 hp Garrett LIM call for 7,500 lbs peak thrust for 1.5 min. This is not enough thrust for the 100,000 lb revenue vehicle we are considering, but presumably multiple units could be built to give 20,000 lb peak thrust. The continuous cruise thrust of the Garrett LIM is to be 10,000 lb for twin 4000 hp LIMS which is adequate for the magnetically suspended vehicle to cruise at 300 mi/h.

The principal disadvantage of the LIM for our application is its weight (approximately 26,000 lb for the unit discussed above including power conditioning equipment, etc., but exclusive of LIM air cushions). The small gap, (0.3125 inch per side between the reaction rail and the ablative surface of the primary) which is required to obtain efficiencies of 60-80% and reasonable power factors, might appear to be incompatible with the large clearance of the superconducting suspension system. An analysis of this problem is given in Section 4.2. The small gap is of no particular disadvantage to the ferromagnetic system. An additional problem is that of wayside power collection. A system which must ultimately collect megawatts of power at 300 mi/h is currently under test and development by Garrett for DOT.

4.1. LIM Studies

No three-dimensional analysis of the linear induction motor has been published thus far to our knowledge. (K. Oberretl of Brown Boveri Co., Zurich has informed us of his work on the 3-D LIM. His techniques are different from ours and will be published soon.) Standard analysis assumes an infinitely wide motor, although finite length effects have been studied.[24,25] Since the width of a real motor is generally less than the pole pitch, such two-dimensional models are not completely realistic. As we have had experience in Fourier transform analysis of 3-D problems, i.e., the calculation of lift and drag on moving magnets, it was thought to be desirable to apply these techniques to the 3-D LIM problem.

We consider two types of motors. (i) series connected-constant current LIM and (ii) parallel connected-constant voltage LIM. A schematic drawing of (i) is shown in Fig. 4.1. The primary is assumed to consist of an infinite iron core with permeability $\mu = \infty$ and conductivity $\sigma = 0$. The windings are replaced by a sinusoidal current sheet in the region $0 < x < L$

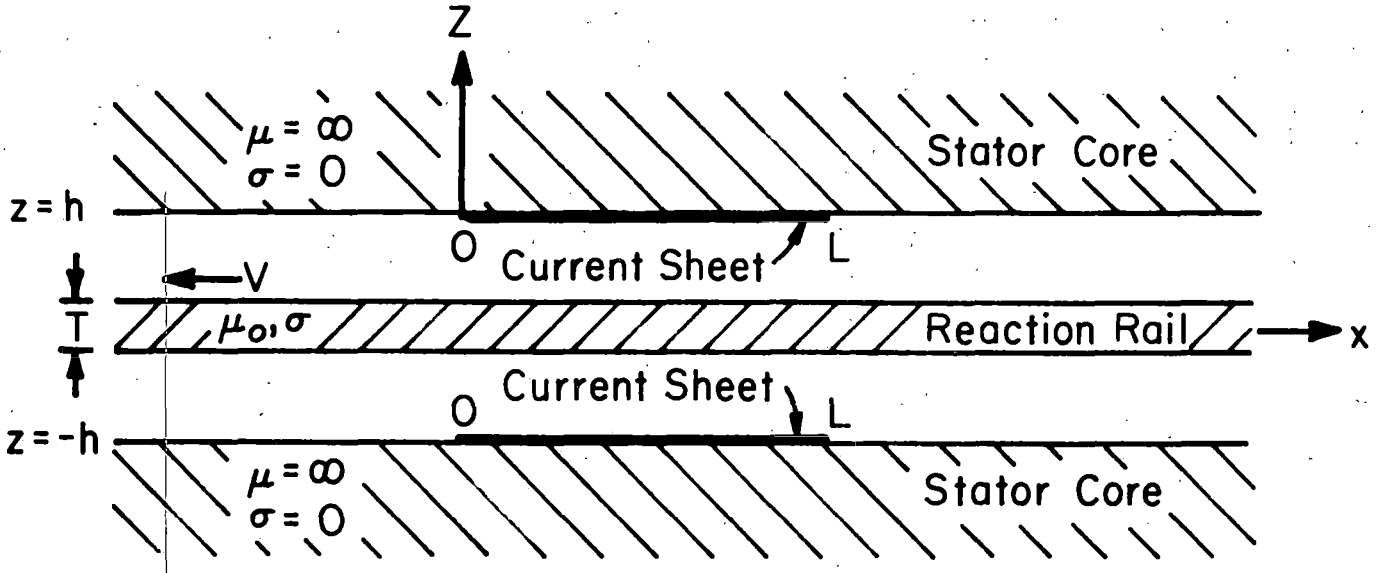

Model for Linear Induction Motor

Fig. 4.1. Coordinate system and schematic model of LIM. The y coordinate is perpendicular to the plane of the drawing, pointing inward.

and $-a < y < a$ for $z = \pm h$. In the interest of simplicity, the model further assumes that the reaction rail can be treated as a thin plate (conducting sheet) with a characteristic velocity $w = 2/\mu_o \sigma T$. This last assumption can be relaxed and the more general skin-depth problem can be solved. The more serious assumptions concerning the boundary conditions at $z = \pm h$, however, are difficult to generalize in the Fourier transform method. More accurate calculations would require more complicated numerical techniques such as relaxation methods of solving for the fields in the motor.[28]

The resulting expressions for the thrust and power loss due to joule heating in the reaction rail are

$$\langle F_x \rangle = \frac{8\mu_o i_o^2 w}{\pi^2} \int_{-\infty}^{\infty} dk_x \int_0^{\infty} dk_y \frac{k^2}{k_x} \frac{(\omega - k_x v)}{D} \frac{\sin^2 k_y a}{k_y^2} \frac{\sin^2 (q-k_x)L/2}{(q-k_x)^2} \quad (4.1)$$

and

$$\langle P_{rr} \rangle = \frac{8\mu_o i_o^2 w}{\pi^2} \int_{-\infty}^{\infty} dk_x \int_0^{\infty} dk_y \frac{k^2}{k_x^2} \frac{(\omega - k_x v)^2}{D} \frac{\sin^2 k_y a}{k_y^2} \frac{\sin^2 (q-k_x)L/2}{(q-k_x)^2} \quad (4.2)$$

where

$$D = (kw)^2 \sinh^2 kh + (\omega - k_x v)^2 \cosh^2 kh \quad , \quad (4.3a)$$

$$k = (k_x^2 + k_y^2)^{1/2} \quad , \quad (4.3b)$$

$$i_y(x,y,t) = \mathrm{Re}\{i_o e^{i(qx + \omega t)}\} \quad , \quad (4.3c)$$

$$q = 2\pi/\lambda \quad , \quad \lambda/2 = \text{pole pitch} \quad , \quad (4.3d)$$

$$\omega = 2\pi f \quad , \quad f\lambda = v_\phi = \text{phase velocity} \quad , \quad (4.4d)$$

$$v = \text{vehicle velocity} \quad (4.4e)$$

The efficiency neglecting any stator losses is

$$\text{Efficiency} = \frac{\langle F_x \rangle v}{\langle F_x \rangle v + \langle P_{rr} \rangle} \quad . \quad (4.5)$$

The evaluation of $\langle F_x \rangle$ and the efficiency are shown in Figs. 4.2 and 4.3 for a motor similar to, but not identical to, the Garrett TACRV machine. A comparison is made between the 3-D results and the 2-D results ($a \to \infty$). The thrust is normalized to the peak thrust/unit area for an infinitely long and wide machine ($L,a \to \infty$): $\mu_o i_o^2/\sinh(2q\ h)$. Gap $\equiv$ h. We note that the thrust/unit area is larger in the 3-D case, but the efficiency is lower. The peak efficiency is about 60% at a slip ($= 1 - v/v_\phi$) of 0.2. This estimate neglects stator losses so that the overall efficiency would be lower, perhaps only 50-55%.

One of the methods suggested to overcome the degradation of the LIM performance is to have a parallel connected, constant voltage primary. Leaving aside any practical problems involved in operating in such a mode, let us examine the predicted performance.

The model used to calculate the performance was based upon the assumption that the appropriate boundary condition at z = h in Fig. 4.1 (stator surface) is

$$B_z(x,y,h,t) = B_o \cos(qx+\omega t) \quad , \quad 0 < x < L \text{ and } -a < y < a \quad , \tag{4.6}$$

$$= 0 \quad , \quad \text{otherwise} \quad .$$

In this case, the thrust and power loss are

$$F_x = \frac{8\ B_o^2\ w}{\mu_o\ \pi^2} \int_{-\infty}^{\infty} dk_x \int_0^{\infty} dk_y \frac{k_x(\omega - k_x v)}{D'} \frac{\sin^2 k_y a}{k_y^2} \frac{\sin^2 (q-k_x)L/2}{(q-k_x)^2} \quad , \tag{4.7}$$

$$\langle P_{rr} \rangle = \frac{8\ B_o^2\ w}{\mu_o\ \pi^2} \int_{\infty}^{\infty} dk_x \int_0^{\infty} dk_y \frac{(\omega - k_x v)}{D'} \frac{\sin\ k_y\ a}{k_y^2} \frac{\sin\ (q-k_x)L/2}{(q-k_x)^2} \tag{4.8}$$

where

$$D' = (kw)^2 \cosh^2 kh + (\omega - k_x\ v)^2 \sinh^2 kh. \tag{4.9}$$

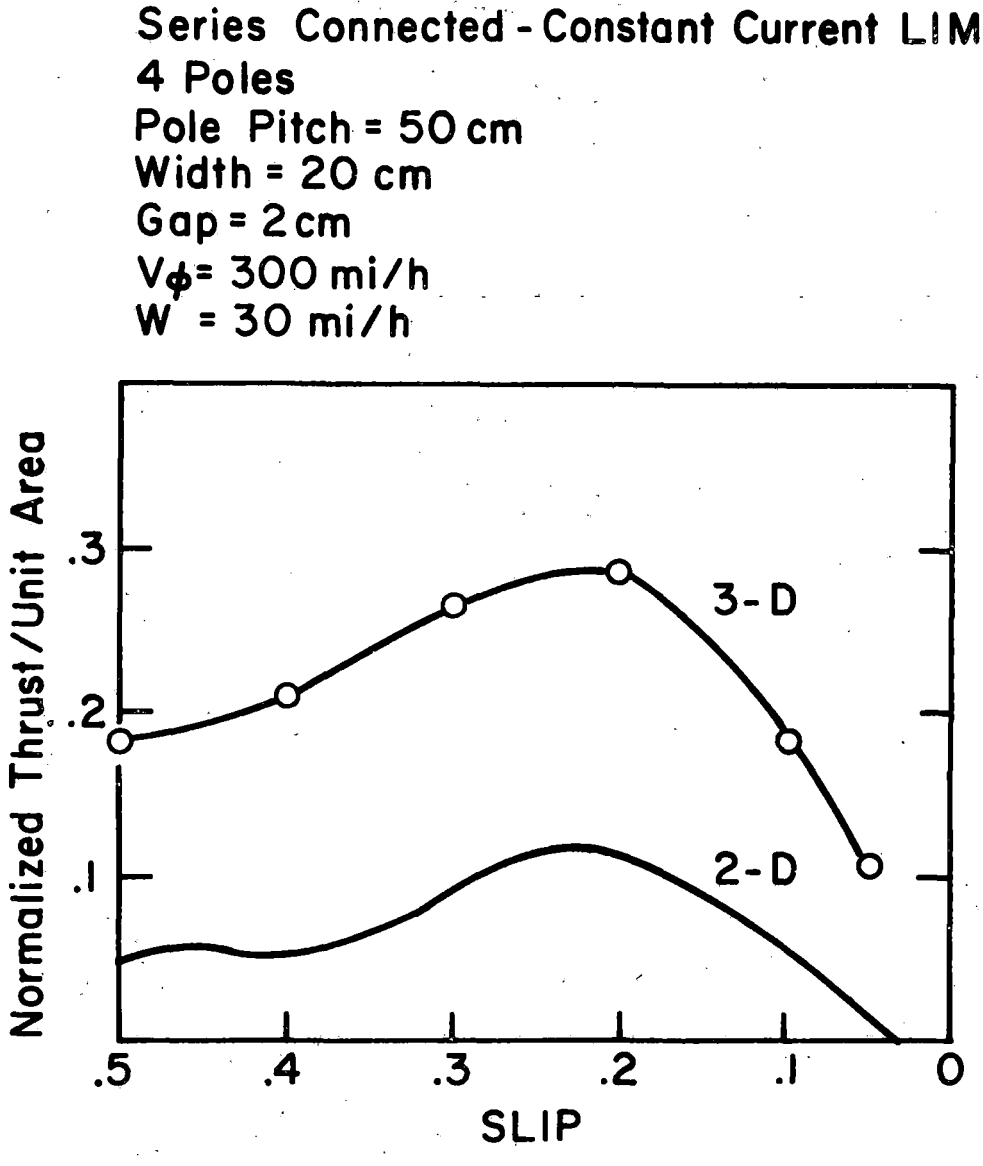

Fig. 4.2. Thrust vs slip for a 2-dimensional and a 3-dimensional model of the series connected, constant current LIM.

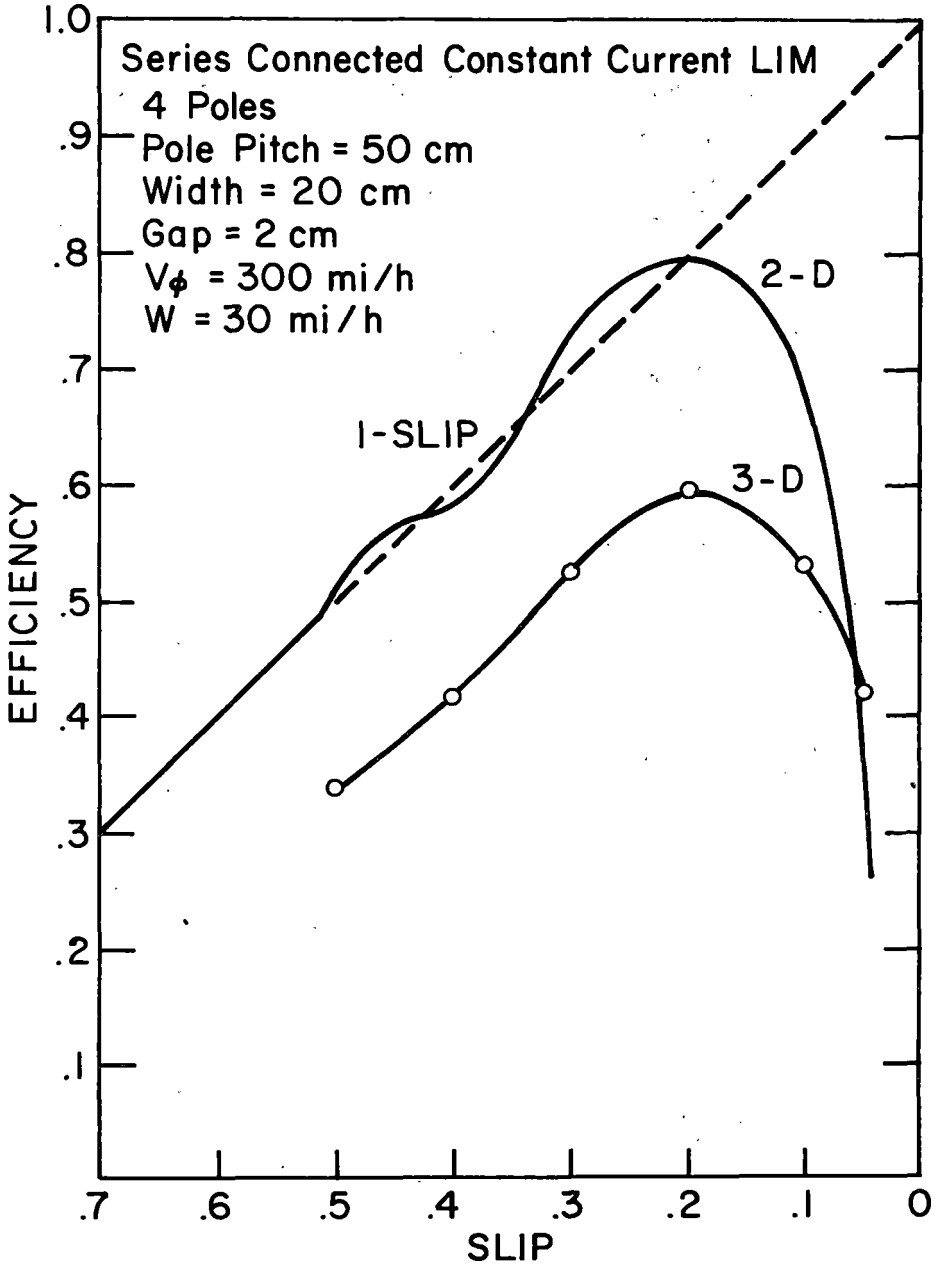

Fig. 4.3. Efficiency vs slip for the two models shown in Fig. 4.2.

In Fig. 4.4, the thrust/unit area vs. slip is shown for a motor with the same parameters as that of Fig. 4.2 and 4.3. The thrust is normalized to B_o^2/μ_o sinh 2qh , the peak thrust/unit area, for an infinitely long and wide motor. We note that the 3-D model has considerably less thrust than the 2-D case and the shape of the curves for both models is different from that of the series connected, constant current motor.

The efficiency is shown in Fig. 4.5. In the parallel connection, the 3-D model has the higher efficiency, about 50% at a slip$\approx$ 0.25. This is somewhat lower than the series connected case. It is far below the 1-slip curve, a result predicted by Iwamoto, et. al,[25] for this case.

Two main conclusions follow from our analysis. First, the correlation between two and three dimensional models is poor. It is difficult to reliably predict motor performance from a 2-D model. Second, the efficiency predicted by the 3-D models is substantially lower than that predicted by others.

4.2. Integration of LIM with High Clearance Suspension

Consider the situation in which a linear induction motor (LIM) is used for propulsion with a high clearance superconducting magnet levitation and guidance scheme. In such a scheme, some means of support and guidance must be provided for the LIM, and due to the small gap between the motor pole faces and the reaction rail, the motor position with respect to the rail must be quite rigidly maintained. One approach to controlling the motor position is to have an active lateral suspension between the motor and vehicle with the motor position controlled by reacting against the vehicle. Since the LIM is apparently quite insensitive to vertical position variations, we can assume the motor is rigidly connected to the vehicle

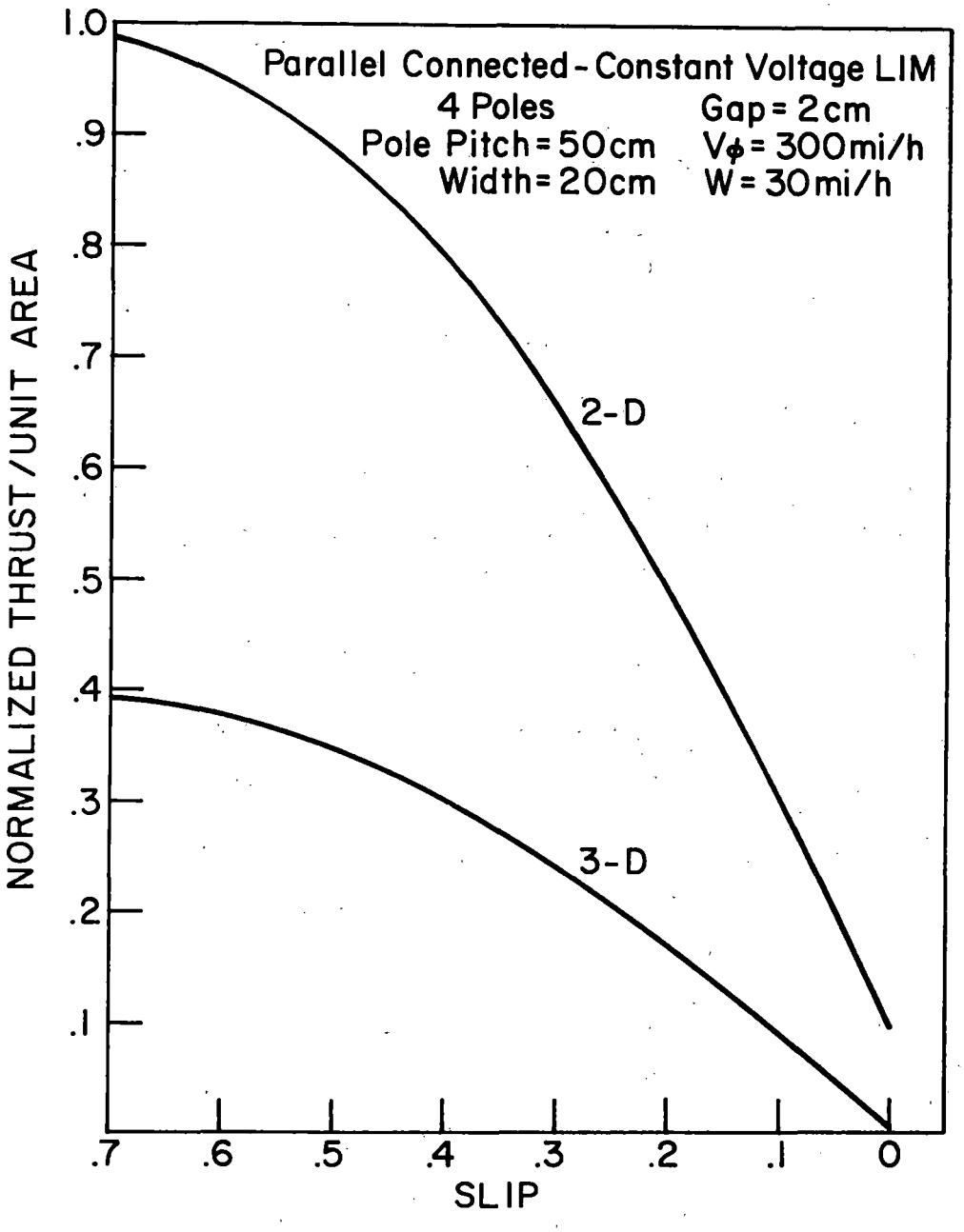

Fig. 4.4. Thrust vs slip for a 2-dimensional and a 3-dimensional model of the parallel connected, constant voltage LIM. Machine parameters are the same as in Figs. 4.2 and 4.3.

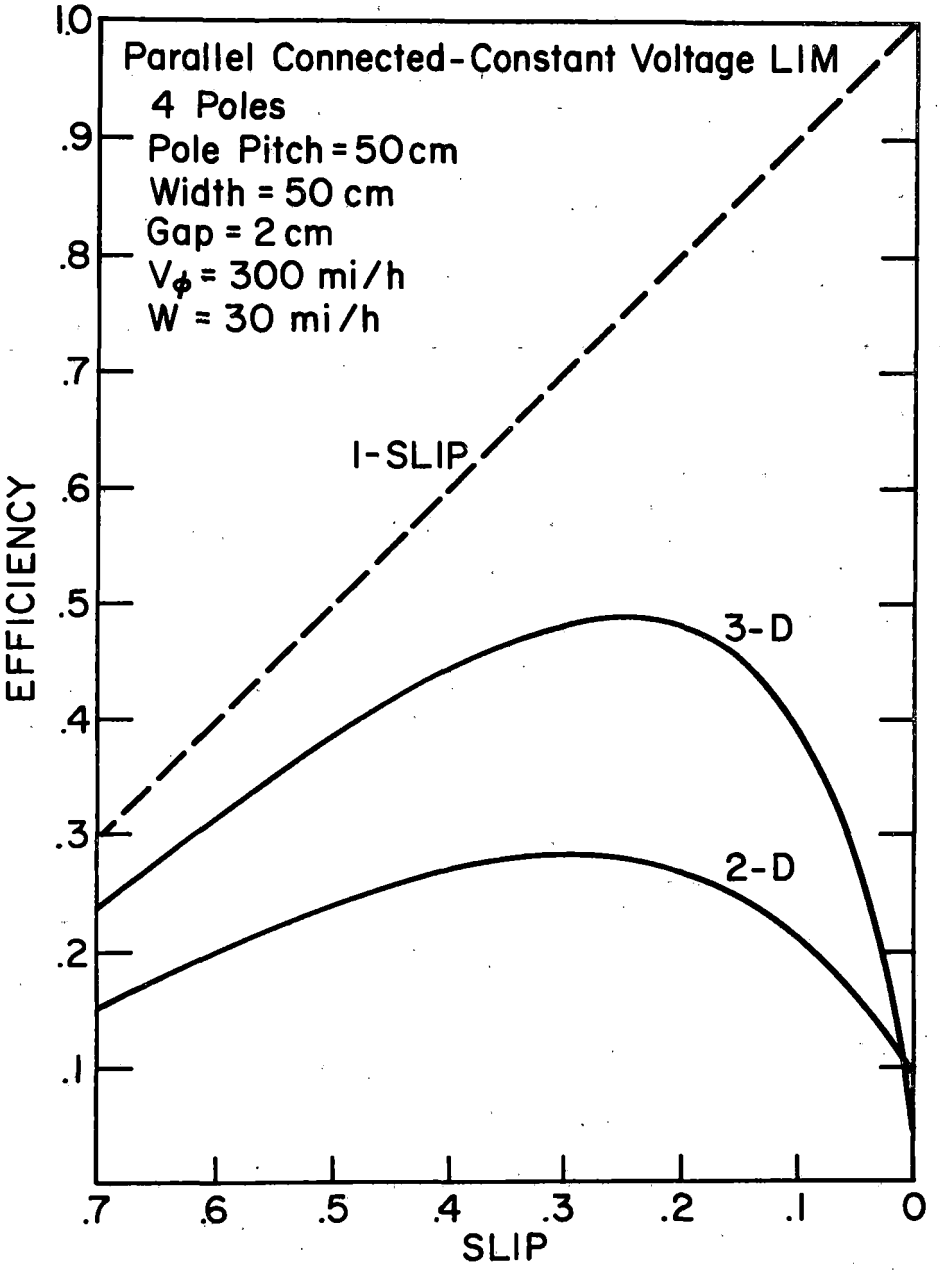

Fig. 4.5. Efficiency vs slip for the two models shown in Fig. 4.4.

in that direction. This approach to integrating the high clearance suspension with a low clearance propulsion system has been critizied because it would seem that the motor position could not be controlled well enough without degrading the passenger compartment ride to an unacceptable level. We have thus analyzed an approximate model of the lateral dynamics to determine the effect on lateral ride quality of a secondarily suspended LIM.

The scheme analyzed is that shown in Figure 4.6. The lateral magnetic suspension is represented by the lateral spring and damper characteristics k_ℓ and D_ℓ . Note that absolute velocity damping is assumed in the lateral direction. Such a lateral suspension characteristic can be achieved using separate guidance magnets and/or perhaps by suitable control of the current in the lift magnets.

The lateral suspension between the vehicle and motor is represented merely by the forces, F_s , exerted on the vehicle and the motor. This suspension is assumed to be active since there is only a small centering force of the motor on the reaction rail but yet the motor must be controlled with respect to the rail. Finally, the roll motion which is characteristically coupled to lateral motion is not included in the analysis. This effect can be included, but at this stage we merely want to demonstrate the feasibility of separate motor suspension.

The lateral equations of motion for the coupled vehicle motor system are then

$$m\,\ddot{x}_m = -F_s \tag{4.10}$$

$$M\,\ddot{x}_v = -k_\ell(2x_v - h_2 - h_3) - 2D_\ell\dot{x}_v + F_s \tag{4.11}$$

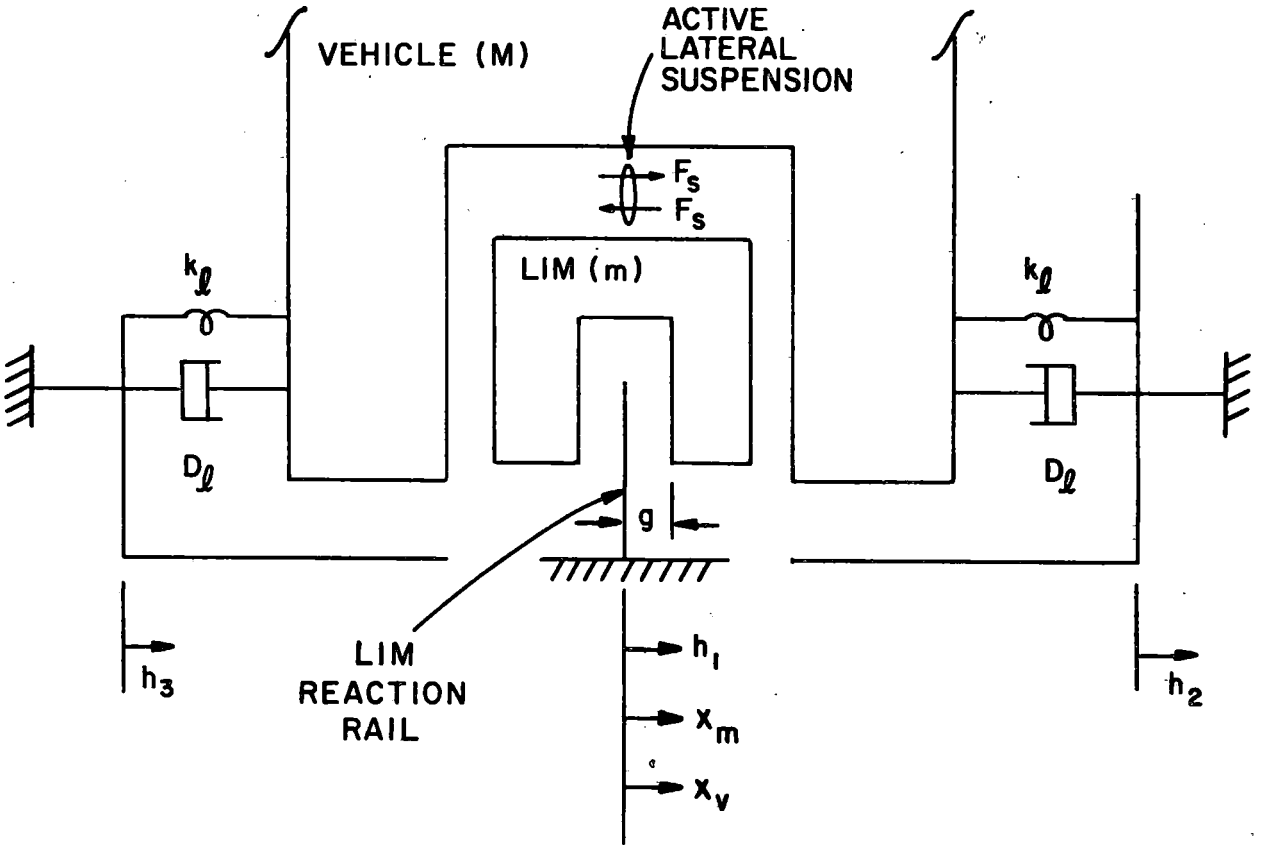

Fig. 4.6. Active suspension of LIM.

where F_s is the disturbance force on the vehicle resulting from the motor position control system. Ideally, we would like the motor to follow the track exactly (maintaining constant gap) up to some cutoff frequency, f_c, and to ignore track variations above f_c. Thus, if we ignore control system dynamics and assume an ideal control system, then

$$\ddot{x}_m = \begin{cases} \ddot{h}_1 & \text{for } f \leq f_c \\ \ddot{x}_v & \text{for } f > f_c \end{cases} \quad . \tag{4.12}$$

Substituting (4.12) into (4.10) and (4.11) and taking the Fourier Transform yields the results

$$(\omega_\ell^2 - \omega^2 + j\, 2\delta_\ell \omega_\ell \omega)\, x_v(j\omega) = \frac{\omega_\ell^2}{2}(H_2(j\omega)+H_3(j\omega)) + \frac{\omega^2 m}{M} H_1(j\omega) \quad , \omega < \omega_c \tag{4.13}$$

and

$$(\hat{\omega}_\ell^2 - \omega^2 + j\, 2\hat{\delta}_\ell \hat{\omega}_\ell \omega)\, x_v(j\omega) = \frac{\hat{\omega}_\ell^2}{2}(H_2(j\omega)+H_3(j\omega)) \quad , \quad \omega > \omega_c \quad . \tag{4.14}$$

where

$$\omega_\ell^2 = \frac{2k_\ell}{M} \quad , \qquad \delta_\ell \omega_\ell = \frac{D_\ell}{M}$$

$$\hat{\omega}_\ell^2 = \omega_\ell^2 \left(\frac{M}{M+m}\right) \qquad \hat{\delta}_\ell = \delta_\ell \Big/ \sqrt{1+m/M} \quad .$$

If we further assume that h_1, h_2, and h_3 are uncorrelated random variables that all have the same basic power spectrum, say

$$\frac{1}{\rho} P_{h_1 h_1}(\omega) = P_{h_2 h_2}(\omega) = P_{h_3 h_3}(\omega) = A\, v/\omega^2 \tag{4.15}$$

then the lateral acceleration power spectrum is given by

$$P_{\ddot{x}_v\ddot{x}_v}(\omega) = \begin{cases} \dfrac{Av\omega^2(\omega_\ell^4/2 + \omega^4(m/M)^2\rho)}{(\omega_\ell^2-\omega^2)^2 + (2\delta_\ell\omega_\ell\omega)^2}, & \omega \le \omega_c \\ \dfrac{Av\omega^2\hat{\omega}_\ell^4}{2[(\hat{\omega}_\ell^2-\omega^2)^2 + (2\hat{\delta}_\ell\hat{\omega}_\ell\omega)^2]}, & \omega > \omega_c \end{cases} \tag{4.16a}$$

$$\hat{\omega}_\ell^2 = \omega_\ell^2 \frac{M}{M+m} \qquad \hat{\delta}_\ell = \delta_\ell \Big/ \sqrt{1+m/M} \ . \tag{4.16b}$$

For frequencies below ω_c, the motor gap is constant. However, for frequencies above ω_c, we must consider the change in the gap. Assuming $x_m = x_v$ for $\omega > \omega_c$, the power spectrum of the change in the gap, $P_{\Delta g\Delta g}(\omega)$ can be found and the resulting mean square change in the gap is

$$\langle \Delta g^2 \rangle = \int_{\omega_c}^{\infty} \left(\frac{\hat{\omega}_\ell^4 + 2\rho[(\hat{\omega}_\ell^2 - \omega^2)^2 + 4\hat{\delta}_\ell^2\hat{\omega}_\ell^2\omega^2]}{(\hat{\omega}_\ell^2 - \omega^2)^2 + 4\hat{\delta}_\ell^2\hat{\omega}_\ell^2\omega^2} \right) \cdot \frac{Av}{2^2} d\omega \ . \tag{4.17}$$

We must thus choose a high enough value for ω_c so that the change in the gap is still sufficiently small. (Note that ω_c cannot be determined explicitly from (4.17) given Δg^2 since a transcendental equation results).

Some examples of lateral acceleration power spectra for different control cutoff frequencies are shown in Figure 4.7. The lateral natural frequency and damping are the same as those chosen for the vertical suspension for a good ride, since the lateral acceleration specification is very similar to the vertical one and since the A parameter of the vertical guidance panels has been assumed to be $A = 5 \times 10^{-6}$ ft. While this choice for A may seem arbitrary, there is no evidence to indicate that another value would be more valid. The A coefficient of the LIM reaction rail has been taken as 2.5×10^{-6} ft. (Apparently the LIM rail at the Pueblo test site corresponds to an A of 1.5×10^{-6} ft.) In any case, the results are not overly sensitive to ρ as long as $\rho < 1$. The mass ratio is about the best that can be expected. Any lowering of this mass ratio results in a degraded ride.

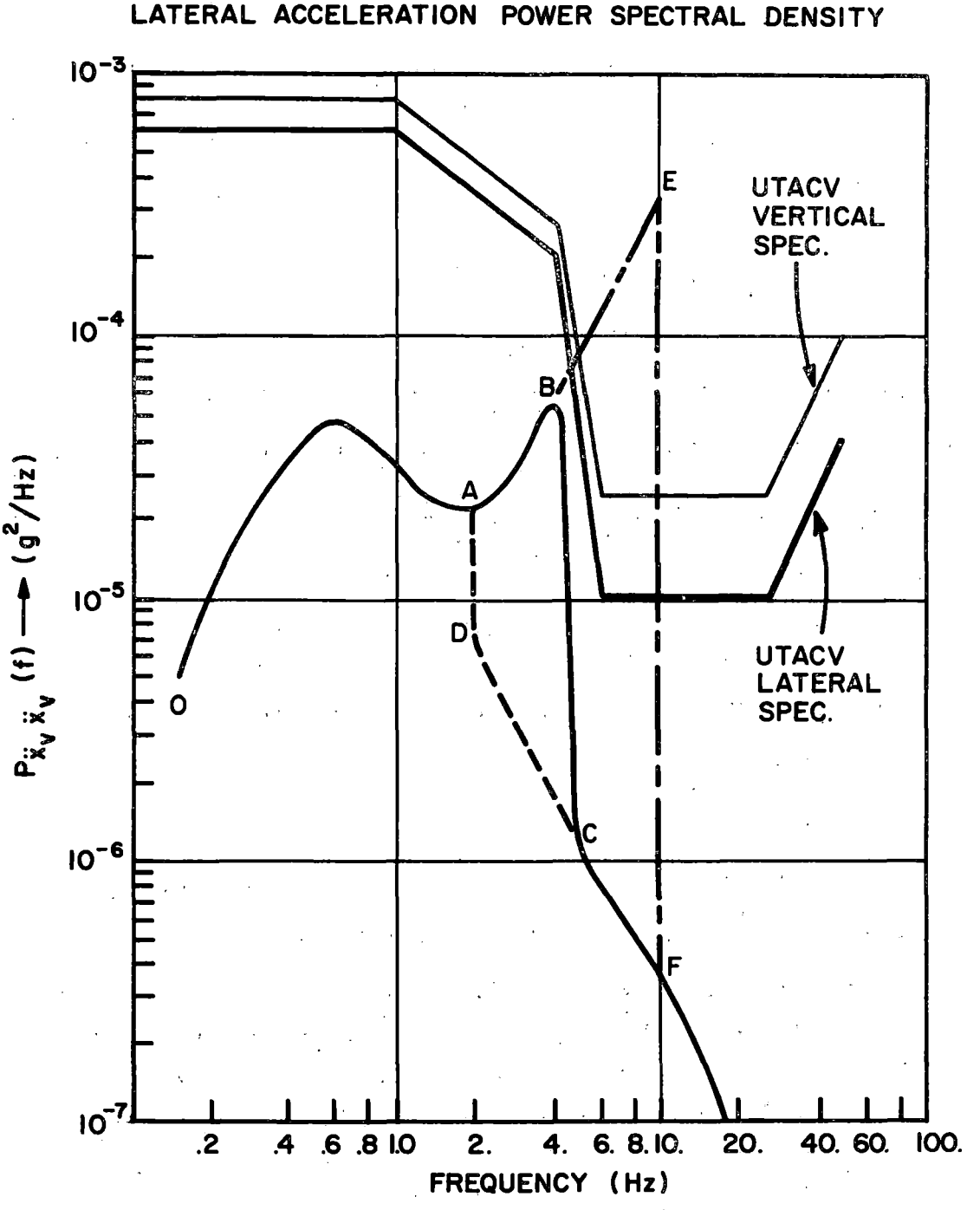

Fig. 4.7. Lateral acceleration psd for various control cutoff frequencies. (f_ℓ = 0.6 Hz, δ_ℓ = 0.707, M/m = 9, ρ = 0.5, A = 5 x 10^{-6} ft, v ≅ 300 mi/h)---f_c = 2 Hz, —— f_c = 5 Hz, — — f_c = 10 Hz.

The PSD's in Figure 4.7 look somewhat strange since they are discontinuous at the cutoff frequency. This is because an "ideal" control system has been assumed. Any real system would of course smooth out these discontinuities. For a cutoff frequency of 10Hz the curve OABEF is the PSD; OABCF corresponds to f_c = 5Hz , and OADCF corresponds to f_c = 2Hz. The rms values of vehicle acceleration, vehicle displacement, and change in the motor gap for the various curves are given in Table 4.1.

TABLE 4.1.

f_c	$\ddot{x}_{v_{rms}}$ (g's)	$x_{v_{rms}}$ (in.)	Δg_{rms} (in.)
2Hz	.008	.292	.108
5Hz	.014	.292	.068
10Hz	.034	.292	.045

For cutoff frequencies up to 5Hz , it is seen that the ride quality meets the specification. The clearance requirement for a LIM is .3125 in. rail to primary ablative surface[27]. Thus, even with the cutoff frequency as low as 2Hz the gap of the motor is less than the 2σ level in Δg. With an ablative surface on the primary, this is probably good enough. However, simply by increasing the cutoff frequency to 5Hz the gap is considerably greater than the 3σ level.

In summary, it appears that the control of the linear induction motor gap by an active control system reacting laterally against the main vehicle body may be feasible without degrading the lateral ride quality to an unacceptable level. Such a control system would require sensing the motor gap.

4.3. Rotating Superconducting Motors

We consider here two on-board propulsion systems that can provide adequate propulsive forces over a large clearance gap; and with the use of a prime mover such as a gas turbine or diesel engine, current collection problems would be eliminated. These two systems utilize physically moving static magnetic fields produced by superconducting coils, and thus minimize the a.c. loss problem. We choose to call these systems the (1) superconducting paddle wheel and the (2) superconducting screw or helix.

4.3.1. Superconducting Paddle Wheel

The superconducting paddle wheel derives its forward thrust similar to any induction motor. Namely, a moving magnetic field near a conducting surface generates eddy currents in the medium and these eddy currents produce a force opposing the motion of this field. In the conventional induction motor the moving magnetic field is created with multi-phase power. However, in order to take advantage of the large fields produced by superconductors and to avoid severe a.c. loss problems, only d.c. currents can be used. Hence, the moving magnetic field must be generated by mechanically moving the static magnetic field. One method of doing this is to mount the coil on the face of a drum and rotate the drum in proximity to the reaction rail.

Figure 4.8 shows a sketch of a paddle wheel version of such a propulsion unit. This unit consists of two paddle wheels rotating in opposite directions and using the guidance rails as the reaction member of the motor. Mounting the paddle wheels in this fashion would tend to give a more even thrust as the vehicle moves about in the guideway.

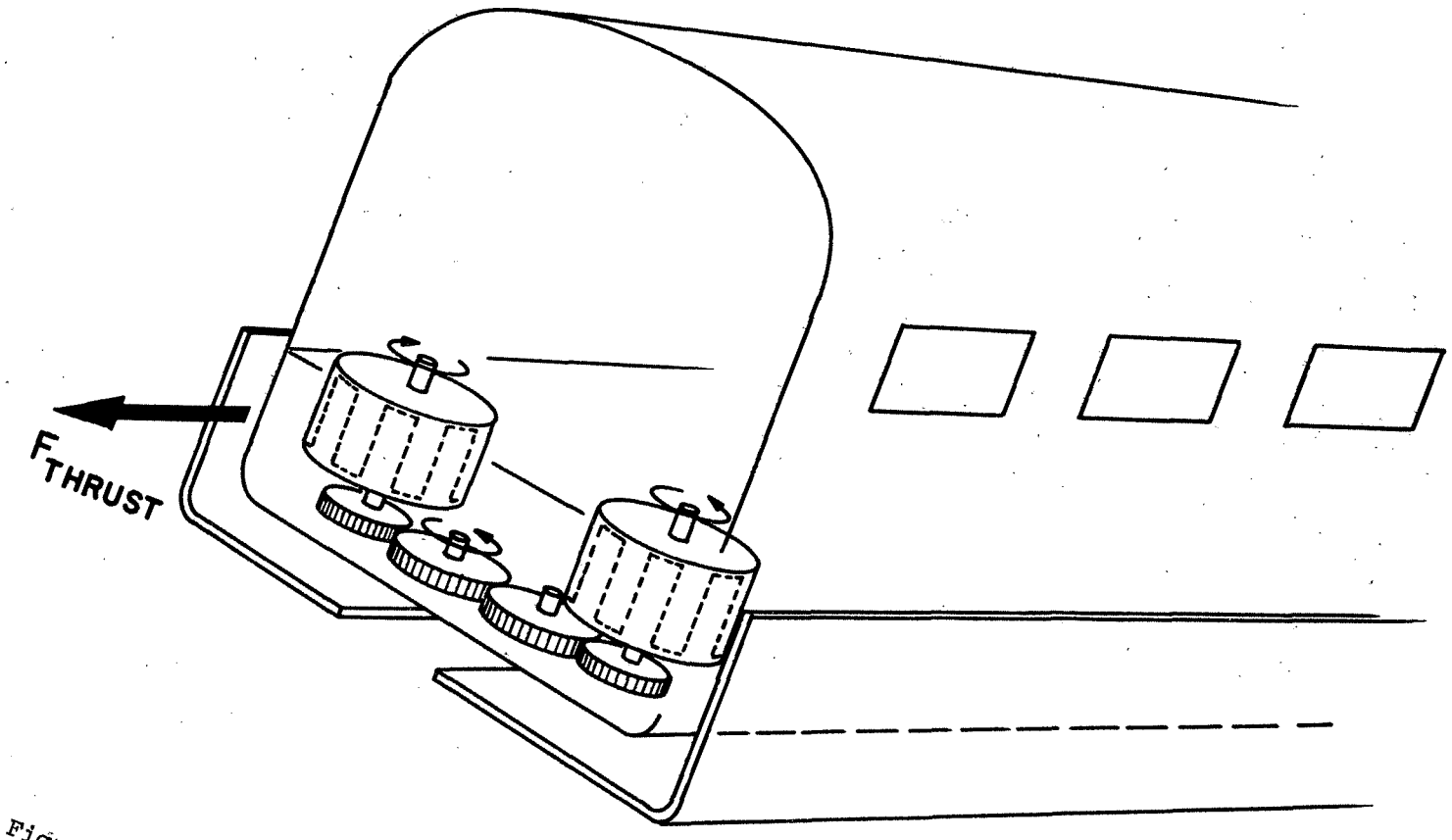

Fig. 4.8. Possible installation of superconducting paddle wheel in high speed ground vehicle.

Let us analyze a two-dimensional model of the magnetic paddle wheel. A schematic diagram is shown in Fig. 4.9. Around the perimeter of the wheel, p infinitely long wire bundles are placed parallel to the axis of the paddle wheel. In Fig. 4.9 p = 8. Each bundle is made up of N wires, each wire carrying a current I. The paddle wheel is of radius R and rotates about its axis with angular frequency ω. The velocity of the axis in the x direction is v_o. The paddle wheel is a distance z_o above an infinitely wide conducting plate of thickness T, permeability $\mu_o = 4\pi \times 10^{-7}$ (mks units), and conductivity σ.

We assume that the thickness T is small compared to the skin depth δ for the dominate frequencies involved in the magnetic field. The assumption of a thin plate allows us to apply the thin-plate theory of eddy currents. In the event that $\delta < T$, we can replace T by δ in the formulas given below.

In the thin-plate theory, the magnetic field of the eddy currents induced in the conducting plate is given by

$$\underline{B}(x,z,t) = \sum_{n=1}^{p} I_n \{ - \underline{b}[x-x_n(t),\ z + z_n(t)] - w \int_0^\infty \frac{\partial \underline{b}}{\partial z} [x-x_n(t-\tau),\ z+w\tau + z_n(t-\tau)]d\tau \} , \quad (4.18)$$

where

$$w = 2/\mu_o \sigma T \quad . \quad (4.19)$$

In 4.19 $I_n = \pm NI$, $\underline{b}(x,z)$ is the field of a wire at the origin carrying unit current in the -y direction, and the position of the $n^{\underline{th}}$ wire is denoted by $[x_n(t),\ z_n(t)]$.

The force on the $m^{\underline{th}}$ wire bundle (per unit length) is

$$F_m = \underline{I}_m \times \underline{B}(x_m(t),\ z_m(t),\ t) \quad . \quad (4.20)$$

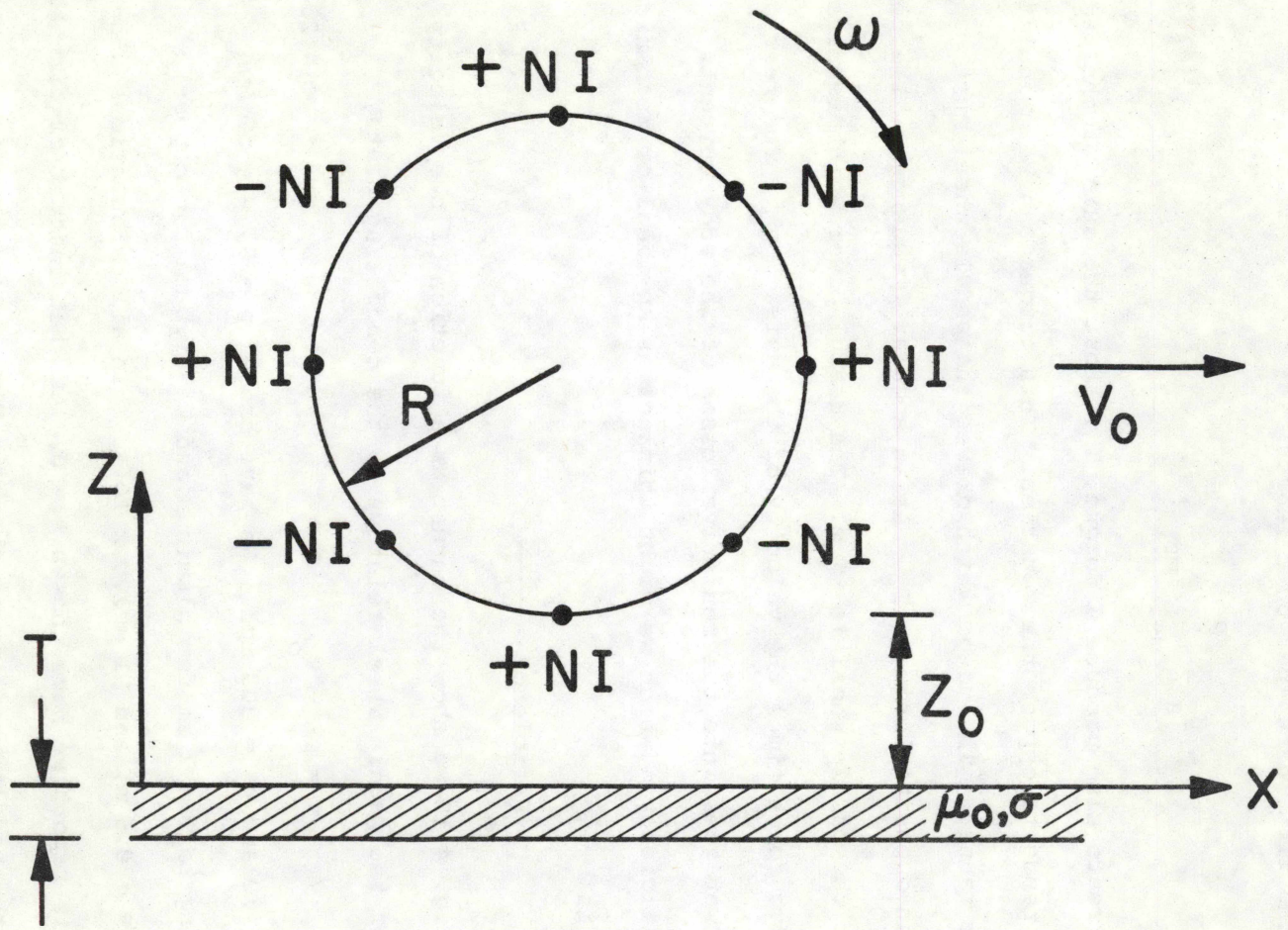

Fig. 4.9. Schematic diagram of the two-dimensional model of the paddle wheel.

The thrust (per unit length) is total force in the x direction on the paddle wheel,

$$F_{thrust} = F_x = \sum_{m=1}^{p} F_{mx} \quad . \tag{4.22}$$

Similarly, the lift force (per unit length) is

$$F_L = F_z = \sum_{m=1}^{p} F_{mz} \quad . \tag{4.23}$$

The eddy currents also produce a torque, T_y, about the axis of the paddle wheel which tends to oppose the rotation. This torque can be calculated in a similar manner. The motor which drives the paddle wheel must supply an equal, but opposite torque, $-T_y$. At an angular frequency ω, the power delivered to the paddle wheel is $-T_y\omega$. The useful power which results is the propulsive force times the velocity of the axis, $F_x v_o$. The rest of the input power goes into the resistive losses of the eddy currents. Hence the efficiency, (which we might think of as an ideal or mechanical efficiency) is

$$\text{Efficiency} = \frac{F_x v_o}{-T_y \omega} \tag{4.24}$$

In Fig. 4.10 we show the thrust as a function of the velocity of the bottom of the paddle wheel relative to the conducting plate,

$$v = \omega R - v_o \tag{4.25}$$

for both $v_o = 0$ and $v_o = 300$ mph. We have chosen $p = 8$, $w = 50$ mph (corresponding to $T = 2$ mm for aluminum and $T = 1.2$ mm for copper) $z_0 = 0.2$ m, $R = 0.5$ m, and $NI = 1.0 \times 10^6$ A. In all calculations displayed in this report we have chosen $t = 0$. At that instant of time the position of the paddle wheel is as shown in Fig. 4.9. There is a small periodic variation of the force on the paddle wheel. We note that for $v_o = 0$, the propulsive force rises to a maximum near, but slightly less

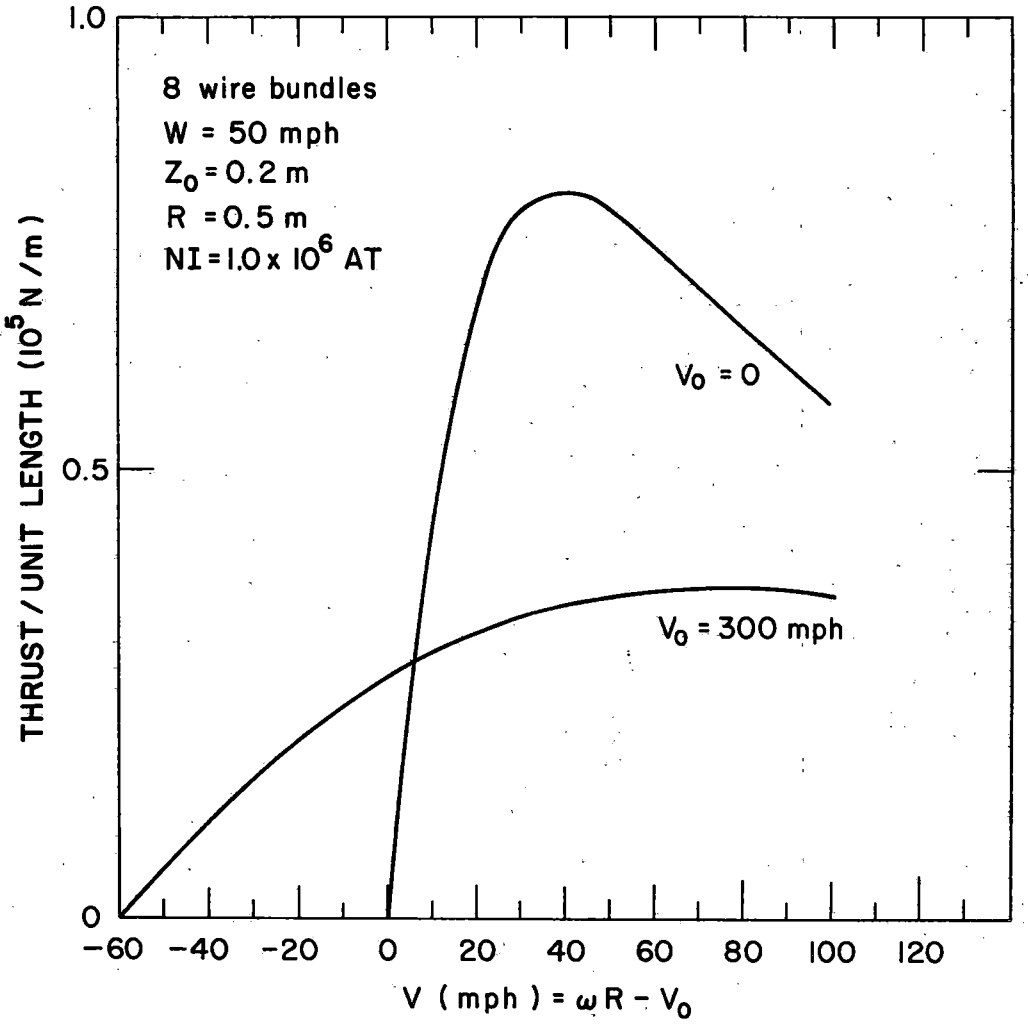

Fig. 4.10. Propulsive force as a function of the relative speed of the bottom of the paddle wheel and the guideway, $v = \omega R - v_o$. Results are shown for two different velocities of the axis of the paddle wheel, $v_o = 0$ and $v_o = 300$ mph. For $v_o = 0$, $F_{thrust}(-v) = -F_{thrust}(v)$.

than $v = w$ and then drops off with increasing v. This curve is similar to the drag force on a rectangular magnet moving with velocity v at a height z_o above a conducting plate.

For v_o = 300 mph, the maximum of the thrust is at higher speeds and is only 45% of the maximum at $v_o = 0$. Also the shape of the curve is much different. Whereas for $v_o = 0$, $F_{thrust} \to 0$ as $v \to 0$, the value of F_{thrust} at $v_o = 300$ is not very sensitive to v, the relative speed for $v > 0$. However, when v becomes negative, F_{thrust} decreases to zero near -60 mph and becomes negative. For v_o = 300 mph and $v = 0$ (i.e. $\omega R = v_o$), $F_{thrust} = 2.68 \times 10^4$ N/m. For four paddle wheels, each 1 m long this amounts to 24,000 lbs. of thrust. Even allowing for some degradation due to end effects, this amount of thrust is adequate.

In Fig. 4.11 the lift force is plotted for the same set of parameters as in Fig. 4.10, except that only $v > 0$ is shown. For $v < 0$, and v_o = 300 mi/h, F_L is rather insensitive to v down to at least -100 mph. In general the lift force is larger than the thrust. It is conceivable that this lift force could be used to lift the vehicle if the paddle wheel is arranged as in the schematic diagram, Fig. 4.9, instead of as pictured in Fig. 4.8. That is, with the axis horizontal in place of vertical. For four paddle wheels, each 1 m long the lift force for v_o = 300 mph and $v = 0$ is 100,000 lbs.

Also shown in Fig. 4.11 is the efficiency for v_o = 300 mph. (For $v_o = 0$, the efficiency is identically zero.) It can be seen that the efficiency is rather insensitive to v, being about 60% over a wide range of values. We also noted from our numerical studies that the power loss in the eddy currents, $(-T_y\omega) - F_x v_o$, is approximately wF_L. (This is rigorously true for the time averages of these quantities.)

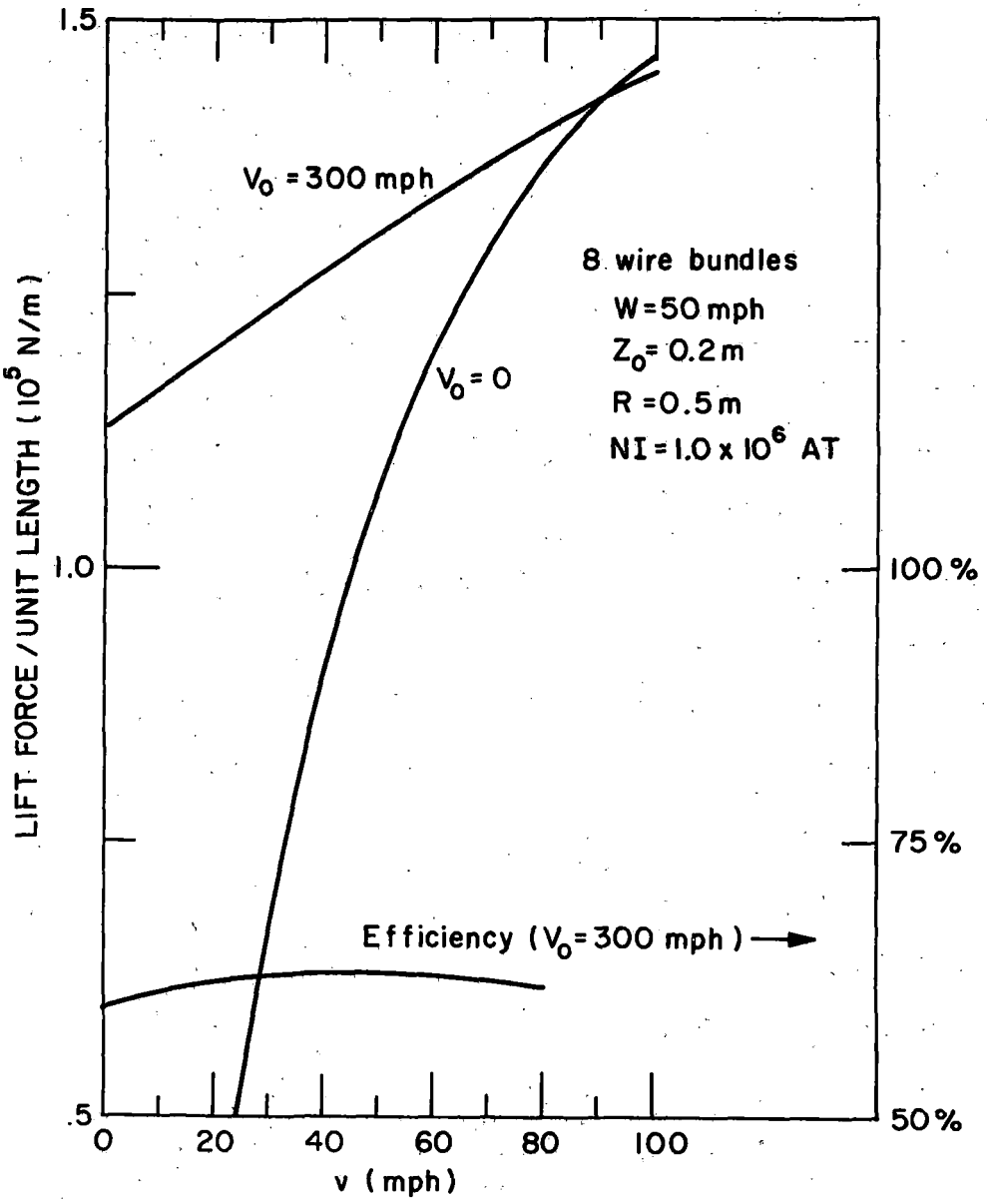

Fig. 4.11. Lift force and efficiency as a function of relative speed.

We have made similar calculations for several heights for both this paddle wheel and others with differing numbers of wire bundles, p. While the efficiency increases slightly for more wire bundles the thrust decreases, being a maximum at p = 8.

4.3.2. Superconducting Helix

One disadvantage of the superconducting paddle wheel is caused by the cycloid motion of one of the rotating conducting wires. Examining this motion one sees that forward thrust is obtained only for a short duration of the wire's cycle while the major portion of the wire's motion is in the forward direction, producing a reverse thrust and thus reducing the efficiency. The fact that the efficiency for the paddle wheel is not lower than it is, is probably due to the more complicated multi-pole arrangement.

One way of arranging the superconducting wire to provide continuous forward thrust as the wire is moved, is to form the wire into the shape of a helix. Then by rotating the helix so that the wire appears to move backward relative to the reaction rail a forward thrust is developed. In this arrangement the helix appears to move as a screw. An additional advantage of the helix over the paddle wheel is that the fluctuating component of the force should be considerably smaller if the helix is long.

Such a motor is depicted in Figure 4.12 where as an alternative arrangement, the track configuration is an inverted U-Channel.

In Fig. 4.13 we show a section of an infinitely long double helix, consisting of two identical interpenetrating helices. Each helix carries NI ampere turns of current, but in opposing directions. This arrangement produces considerably more thrust than the single helix shown in Fig. 4.12, and is probably degraded less by end effects. The radius of the helices is R. They rotate with angular frequency $\omega = 2\pi f$ and have a uniform

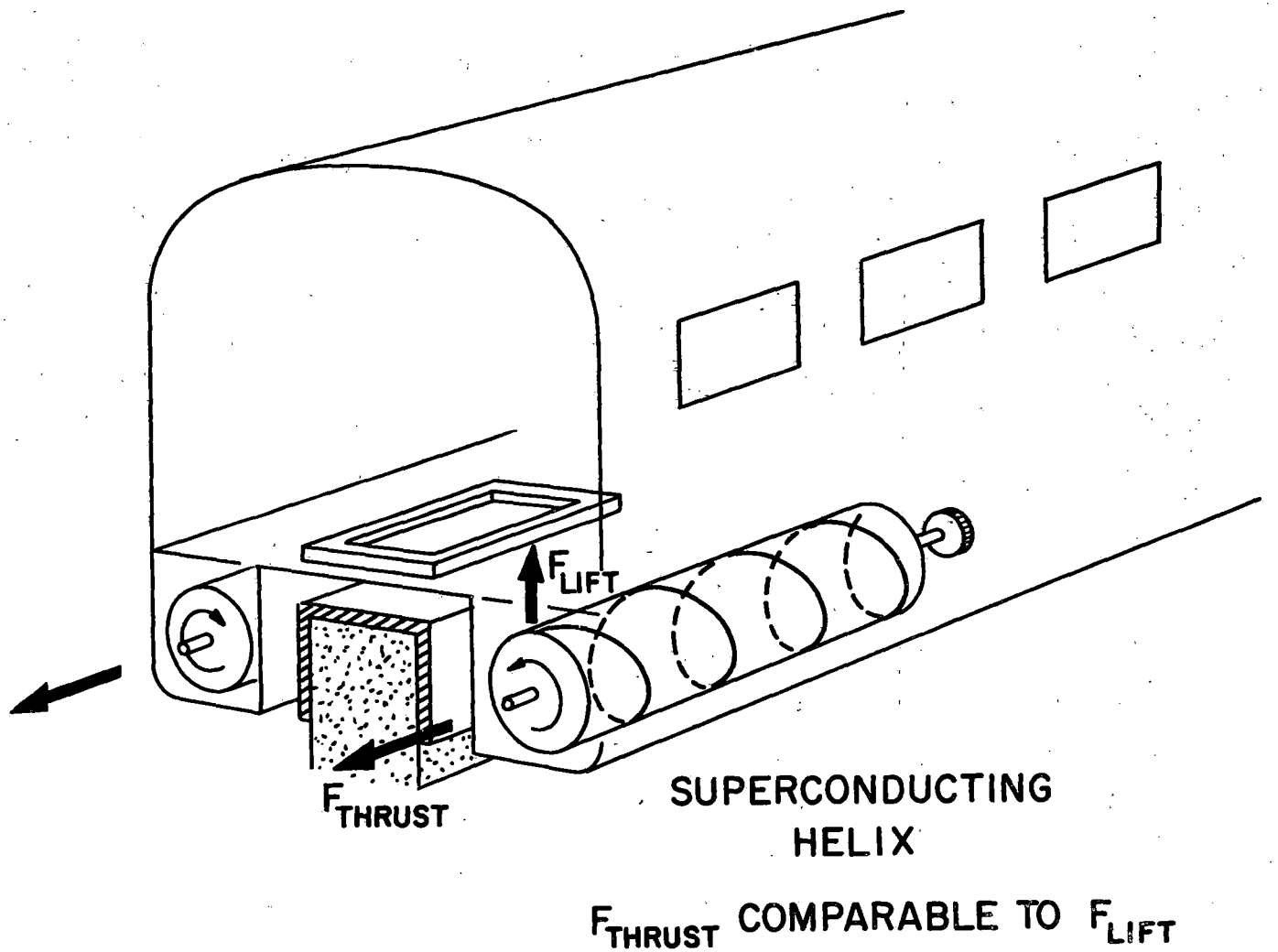

Fig. 4.12. Possible installation of superconducting screw in high speed ground vehicle.

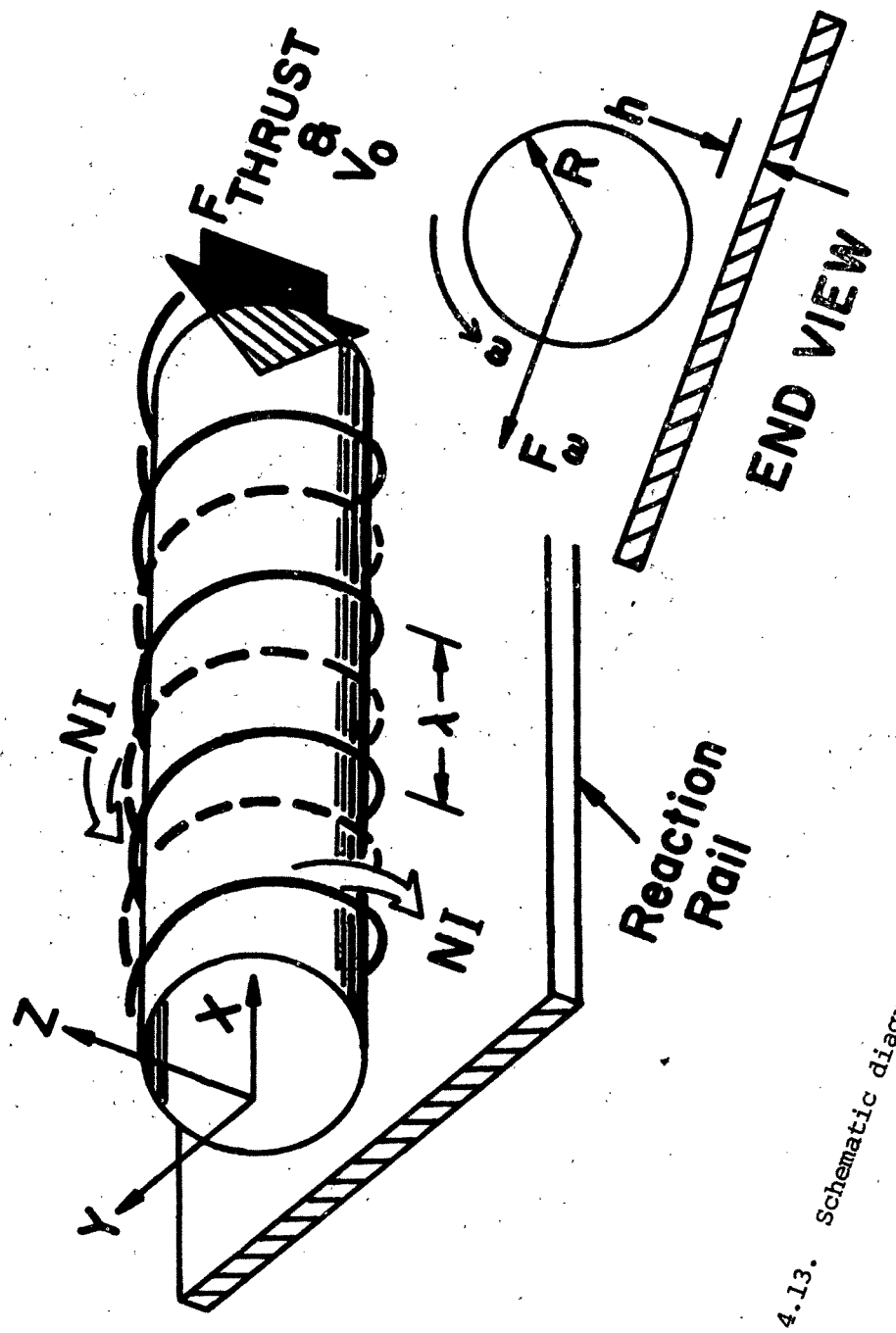

Fig. 4.13. Schematic diagram of a section of an infinitely long, double helix.

velocity of translation v_o in the negative x-direction (parallel to the axis of the helices). The pitch is λ and the gap between the helices and a conducting plate is h. As in the analysis of the paddle wheel, the plate is characterized by a speed w [See Eq. 4.20] .

It is clear that the effect of the rotational and the translational motion combined is equivalent to translational motion at velocity $v = \lambda f - v_o$ in the positive x direction without rotation. Hence, we see that

$$F_{thrust} = -F_x(v,h), \tag{4.25}$$

and

$$F_\omega = F_y(v,h). \tag{4.26}$$

The above forces are per pitch and are obtained by solving for the forces in the case where $\omega = 0$ and $v_o = -v$. It can be shown that

$$F_z(v,h) = \frac{-v}{w} F_x(v,h), \tag{4.27}$$

so that the power dissipated in the track (conducting plate) is

$$\text{power dissipated} = wF_z(v,h) \tag{4.28a}$$

$$= -vF_x(v,h). \tag{4.28b}$$

The efficiency is thus

$$\text{Efficiency} = \frac{v_o F_{thrust}}{v_o F_{thrust} + \text{power dissipated}}, \tag{4.29a}$$

$$= \frac{v_o}{v_o + v} = \frac{v_o}{\lambda f} \tag{4.29b}$$

From the thin-plate theory, it is straightforward to show that for any magnetic source

$$\underline{F} = \underline{f}(0,0,2z_o) + \frac{w}{2} \frac{\partial}{\partial z_o} \int_o^\infty d\tau \, \underline{f}(v\tau,0,2z_o + w\tau) \quad , \tag{4.30}$$

where $\underline{f}(x,y,z)$ is the force on the source due to its image when the centroid of the source is displaced by $\underline{r} = (x,y,z)$ from the image. In (4.30), z_o is the height of the centroid above the conducting plate; for the helix $z_o = R+h$.

We write $\underline{f}$ in the form

$$\underline{f} = \frac{-\mu_o (NI)^2}{4\pi} \oint \oint \underline{dl_1} \cdot \underline{dl_2} \frac{\underline{r}_{12}}{r_{12}^3} \quad , \tag{4.31}$$

where $\underline{dl_1}$ is integrated around the source loop (helix) and $\underline{dl_2}$ is around the image. To obtain force per pitch, $\underline{dl_1}$ is integrated over only one pitch but $\underline{dl_2}$ is over all the image. By doing the τ integration first, one can reduce the problem to a double numerical integral. The results of such a calculation are shown in Fig. 4.14 where F_{thrust} and F_ω as a function of relative speed $v = \lambda f - v_o$ are plotted. Both forces are linear in v for small v, reach a peak near $v = w$, and decrease as v^{-1} for large v. The maximum thrust per unit length is about 6.4×10^4 N /m for 10^6 ampere turns, which is comparable to the peak thrust per unit length of the paddle wheel for $v_o = 0$, but is about twice the peak thrust for v_o = 300 mph (see Fig. 4.10.) -- even though the current is more dense in the paddle wheel. It appears that superconducting screws of reasonable size can, therefore, provide adequate thrust.

No attempt has been made to actually design the cryogenic system or other features of these motors. However, high power, rotating electrical machinery of about this size, current density, and rotation speed are under development for other purposes.[30]

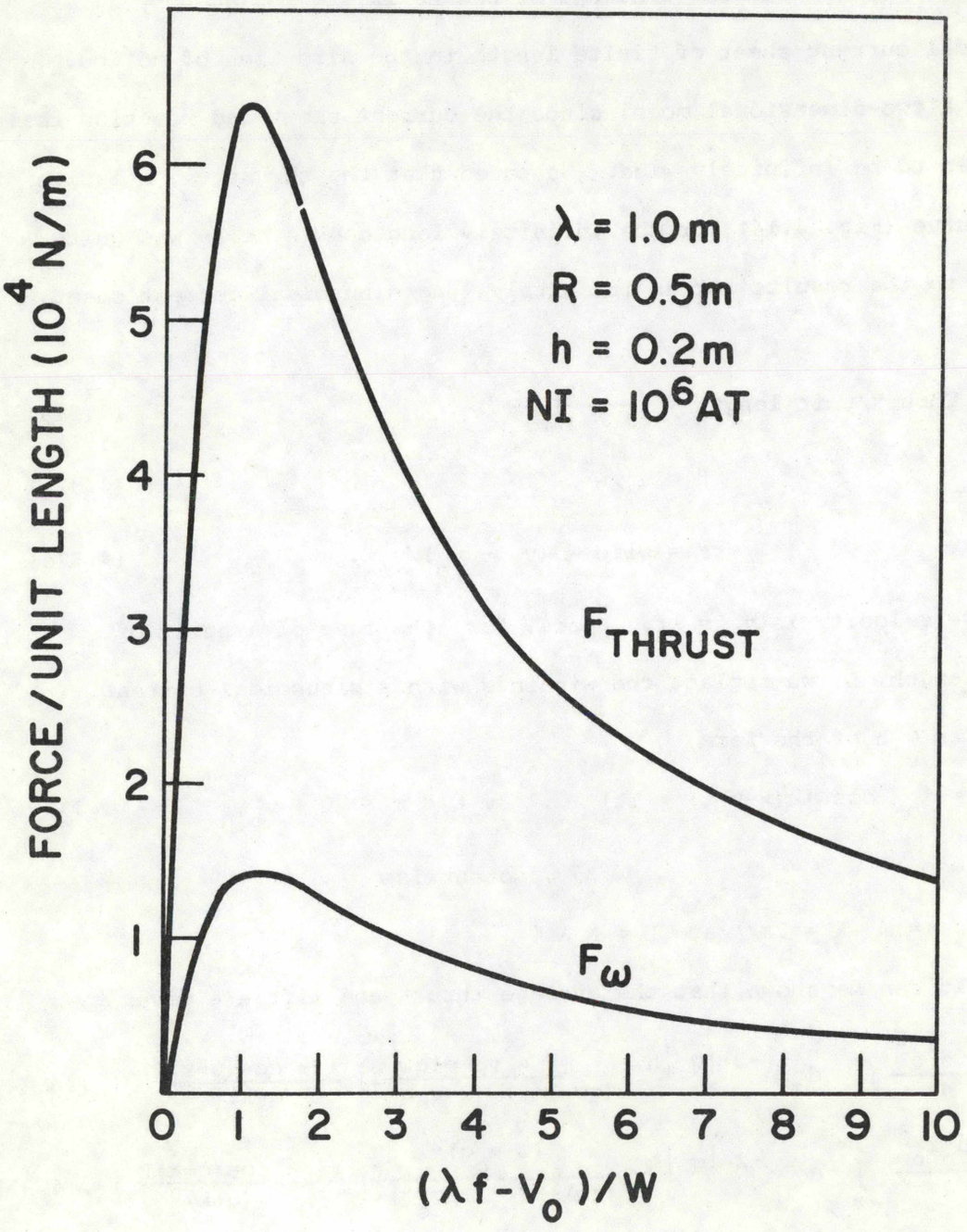

Fig. 4.14. Thrust and transverse force vs relative speed, $v = \lambda f - v_o$, for the helix. The lift force is given by $F_L = (v/w)F_{thrust}$.

4.3.3. End Effects in Linear Induction Propulsion Systems

We have adapted a model of the end effects in a LIM[24] to the calculation of end effects in the superconducting helix of finite length. In this model, the current windings of the helix are replaced by a sinusoidal current sheet of finite length in the direction of motion. This is a two-dimensional model since the current sheet and reaction rail are taken to be infinitely wide. We noted that the thrust vs. relative speed curve (Fig. 4.14) for the infinitely long double helix was quite similar to the results for an infinitely long sinusoidal current sheet, namely

$$\text{Thrust/unit length} \propto \frac{\beta s}{1 + (\beta s)^2} \tag{4.32a}$$

where $$\beta = v_\phi / w \tag{4.32b}$$

and $$s = \text{slip} = (v_\phi - v_o)/v_\phi \ . \tag{4.32c}$$

The phase velocity is $v_\phi = \lambda f$. Hence, for the case of a helix of finite length, L, we replace the windings with a sinusoidal current sheet at z = h of the form

$$i_y(x,t) = i_o \cos [k(x - v_o t) + \omega t] \quad , \quad v_o t < x < L + v_o t \tag{4.33}$$

$$= 0 \quad , \quad \text{otherwise} \quad ,$$

where $kv_\phi = \omega$, $k = 2\pi/\lambda$ and $L = N_o \lambda$.

It can be shown that the average thrust and lift are given by

$$\langle F_x \rangle = \frac{\mu_o i_o^2}{4\pi} \int_{-\infty}^{\infty} dq \, e^{-2|q|h} \, \frac{(\omega - v_o q) qw}{(qw)^2 + (\omega - v_o q)^2} \left[\frac{1 - \cos(q-k)L}{(q-k)^2} \right] , \tag{4.34}$$

$$\langle F_z \rangle = \frac{\mu_o i_o^2}{4\pi} \int_{-\infty}^{\infty} dq \, e^{-2|q|h} \, \frac{(\omega - v_o q)^2}{(qw)^2 + (\omega - v_o q)^2} \left[\frac{1 - \cos(q-k)L}{(q-k)^2} \right] . \tag{4.35}$$

Furthermore, it can be shown that the average power dissipated in the reaction rail is $w\langle F_z \rangle$. Hence the efficiency is

$$\text{Efficiency} = \frac{\langle F_x \rangle v_o}{\langle F_x \rangle v_o + w \langle F_z \rangle} \quad . \tag{4.36}$$

(This is the ideal or mechanical efficiency and does not include any losses in the windings.)

In Fig. 4.15 we show the results of varying the number N_o (i.e., varying N_o and L with λ fixed). Even for $N_o = 8$, the normalized thrust is somewhat lower than the results for $N_o = \infty$ although the shape is similar, except near zero slip where the thrust for a finite length motor does not vanish. The normalized thrust is the actual average thrust per unit length divided by $\frac{\mu_o}{4} i_o^2 e^{-2kh}$.

In Fig. 4.16, the efficiency is shown. For $N_o = \infty$, the efficiency is 1 - s. The motors with N_o finite show the curious behavior of the efficiency first rising sharply to a peak and then decreasing as the slip is made larger.

In Figs. 4.17 and 4.18, the effect of changing v_ϕ / w from 10 (in Figs. 4.15 and 4.16) to 50 is displayed. This is equivalent to increasing the conductivity of the reaction rail. The thrust is severely reduced at low slip, but the efficiency is increased somewhat.

Due to the approximate nature of the model, the results in Figs. 4.15 - 4.18 should be viewed as giving the general trends as parameters are varied, not as precise quantitative calculations. It is clear that $N_o \gtrsim 4$ and $v_\phi / w \lesssim 10$ are required to obtain a significant fraction of the predicted operating performance of the infinitely long helix.

4.4. LSM Studies

A number of authors[31-34] have discussed the possibility of using superconducting magnets on board the vehicle and an active track to form a linear synchronous motor. Propulsion is obtained from a traveling flux wave (from the track) pulling on the superconducting magnets. With these

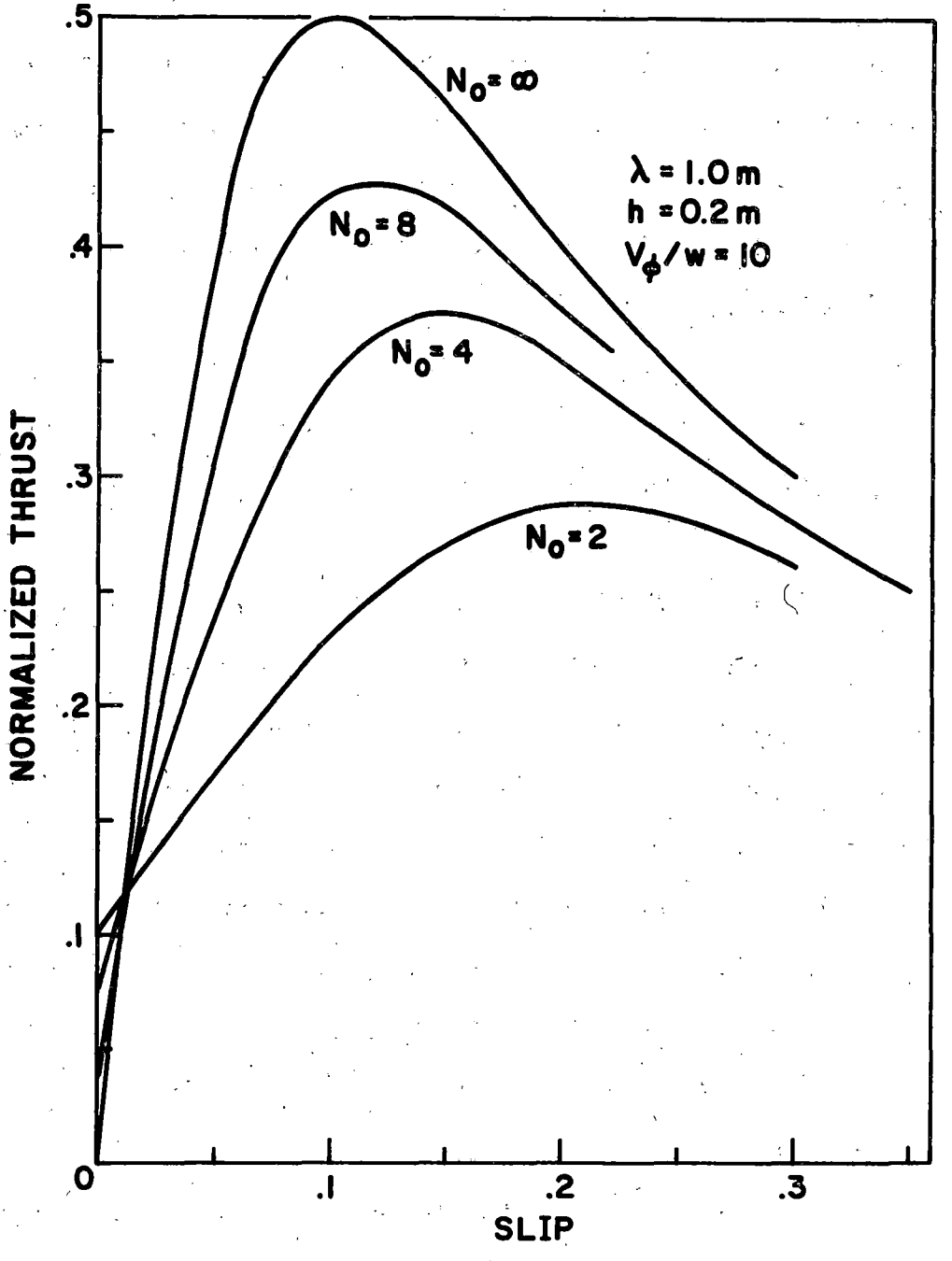

Fig. 4.15. Thrust vs slip for various $N_o = L/\lambda$ (end effect in the helix for different lengths).

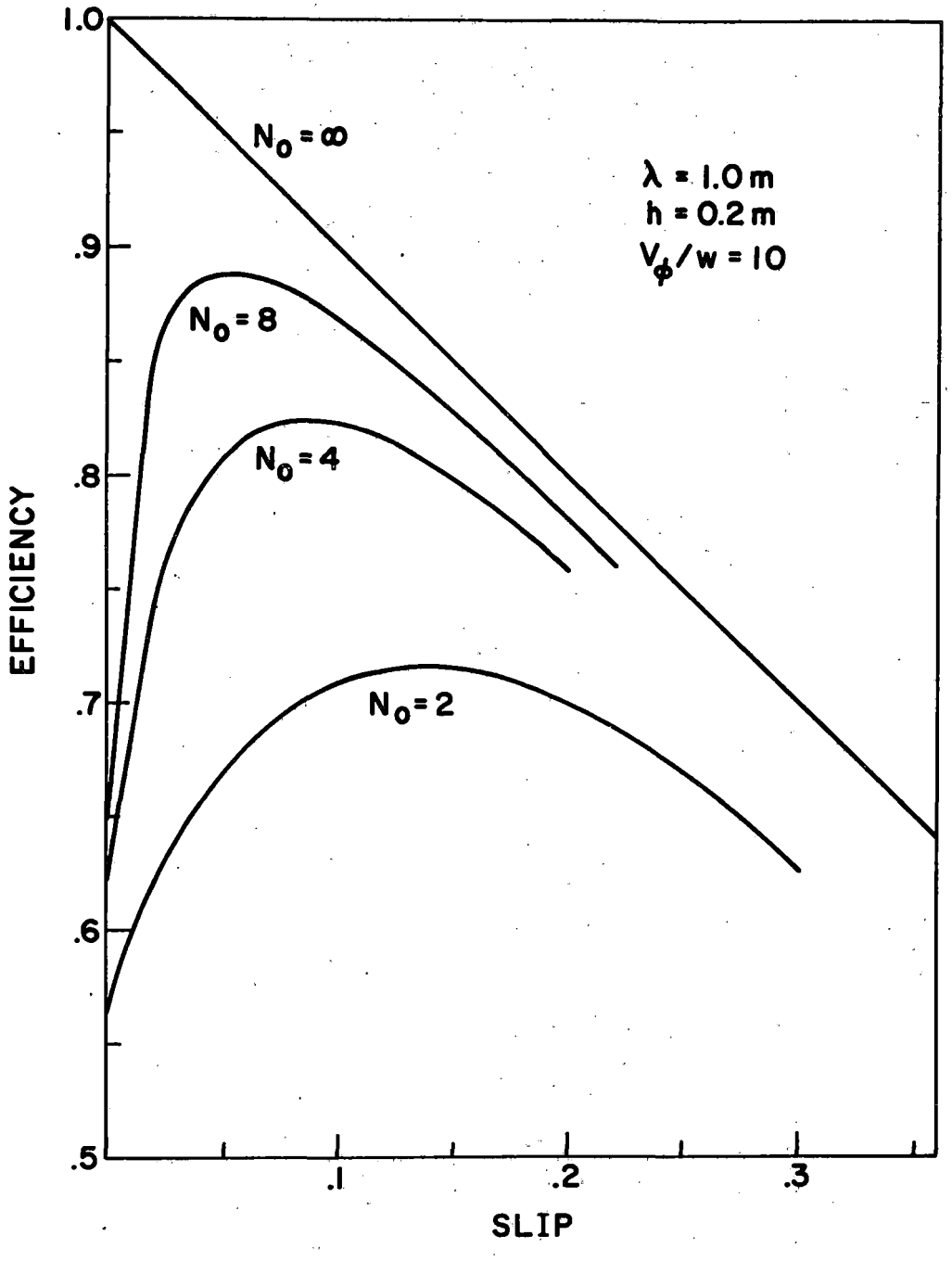

Fig. 4.16. Efficiency vs slip. Same parameters as Fig. 4.15.

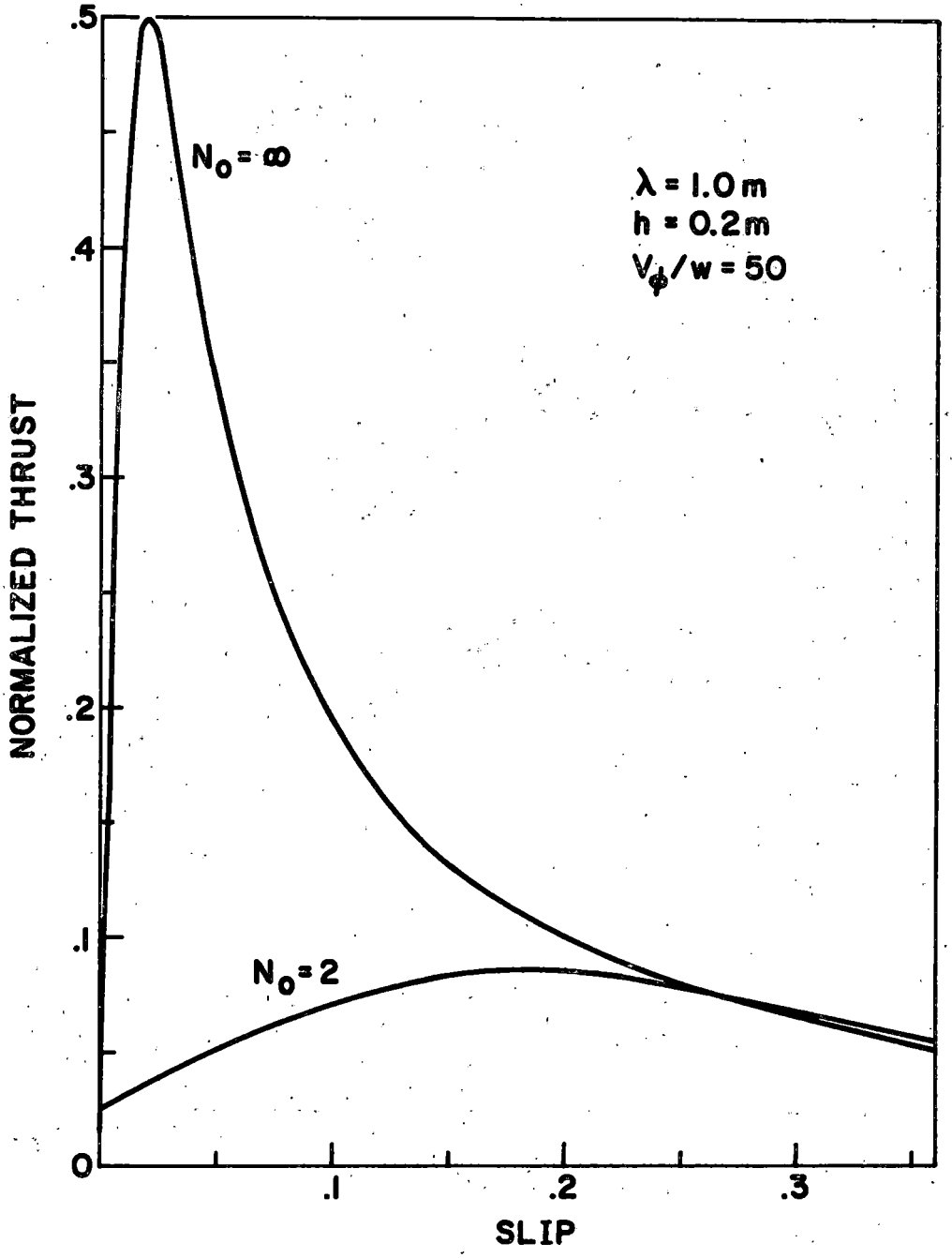

Fig. 4.17. Thrust vs slip for larger v_ϕ/w than in Figs. 4.15 and 4.16. This is equivalent to an increase in the conductivity of the reaction rail.

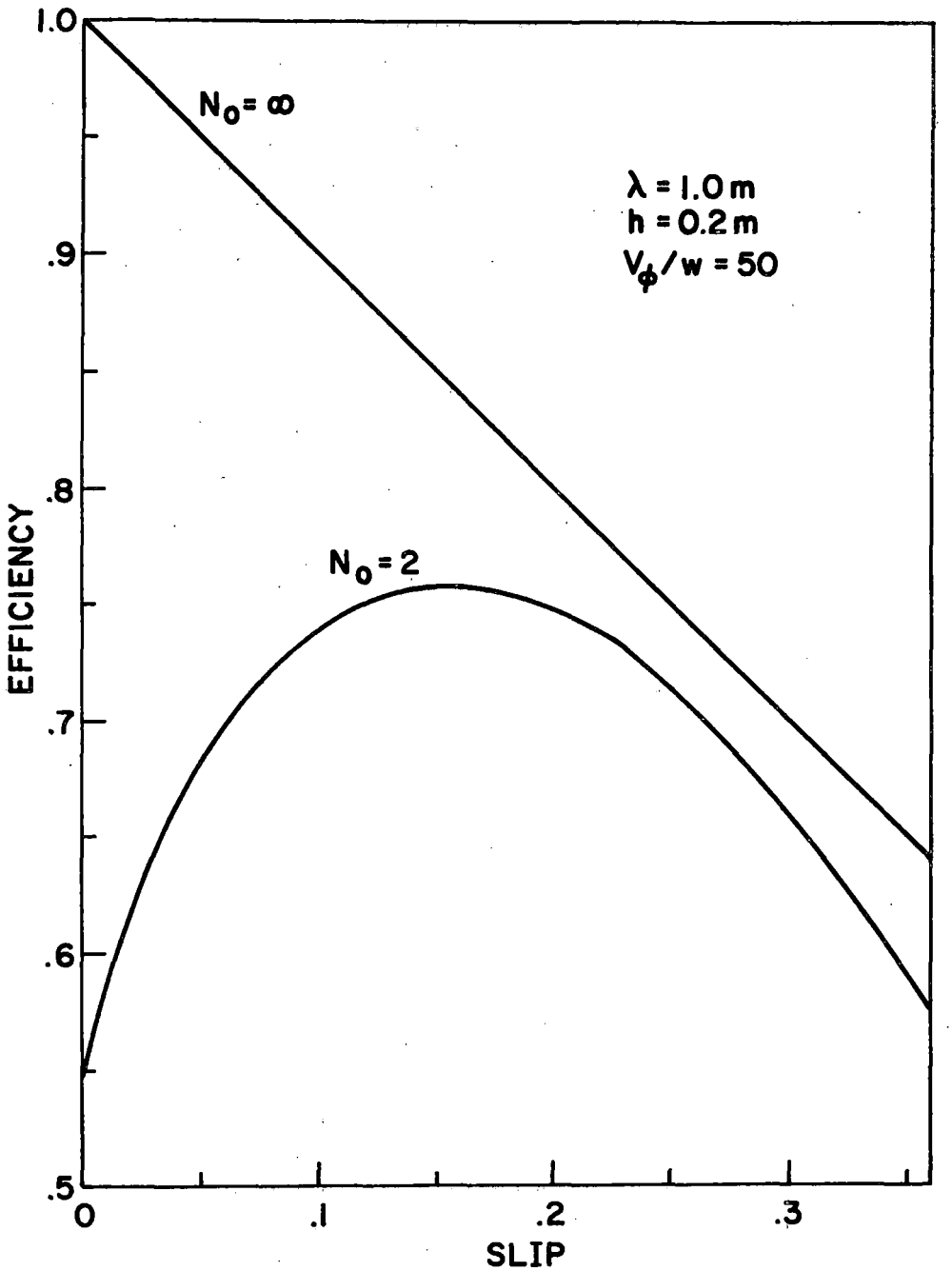

Fig. 4.18. Efficiency vs slip. Same parameters as Fig. 4.16.

high-field magnets, large clearances between the vehicle and track (as large as the suspension height in the superconducting levitation system) can be obtained with reasonable currents in the track (1 - 2000 A). Wayside power collection would not be required and some weight savings as compared to the LIM should be realized. The disadvantages of the system are the cost and complexity of an active track including a wide-range variable-frequency power supply[32] and the increased number of superconductors required on the vehicle. The latter necessitates not only additional cryogenic equipment, but also additional shielding.

We consider a simple model of the LSM shown in Fig. 4.19. Only one phase of a three-phase track system is shown. The other two phases are coplanar with the one shown but displaced by c and 2c, respectively. Only one vehicle magnet is shown, although many magnets in equivalent force positions will be present in an actual design. We will calculate the forces on each magnet separately. The magnet carries a constant current I_v.

It greatly simplifies the problem to assume that the track carries a balanced current excitation, i.e., the current in the n^{th} loop whose center is at $x = nc$ is

$$i_n(t) = I_o \cos(\omega t - n\pi/3) \quad . \tag{4.37}$$

The phase velocity (synchronous velocity) is then

$$v_\phi = 3\omega c/\pi = 6c\, f \quad . \tag{4.38}$$

The vehicle magnet has dimensions $a \times b$ with b parallel to the vehicle velocity v. The track coils are the same size as the vehicle coil. In addition, we shall take $c = b/3$. The mutual inductances between the vehicle coil and a track coil whose centers are separated by (x,z) is denoted by $M(x,z)$. (An expression for M is given in ref. 35)

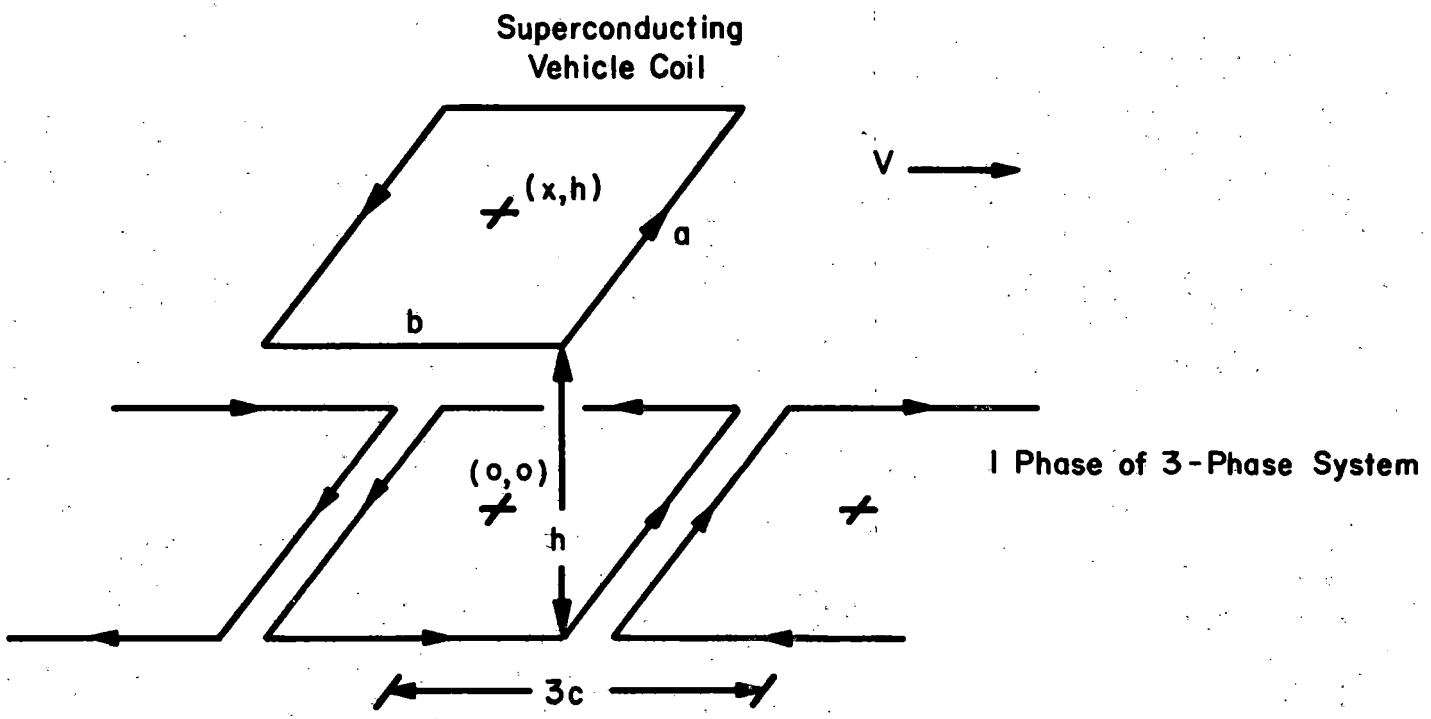

Fig. 4.19. Schematic diagram of a LSM. Only one phase of a 3 phase track system is shown.

The flux linking the vehicle coil with its center at (x,z) and the track is

$$\Phi = \sum_n M(x-nc,z)\, i_n(t). \tag{4.39}$$

The forces on the coil are

$$F_x = I_v \frac{\partial \Phi}{\partial x} , \tag{4.40}$$

and

$$F_z = I_v \frac{\partial \Phi}{\partial z} . \tag{4.41}$$

For $x = x_o + v_\phi t$ and $z = h$, the average forces are given by

$$< F_\alpha > = \frac{I_v\, I_o\, v_\phi}{c} \sum_n \int_0^{t_1} dt\, M_\alpha(x_o + v_\phi t - nc, h) \cos(\omega t - n\pi/3), \tag{4.42}$$

where $\alpha = x,z$,

$$M_\alpha = \frac{\partial M}{\partial \alpha} , \tag{4.43a}$$

$$t_1 = c/v_\phi . \tag{4.43b}$$

After some manipulation, and recalling M(x,h) is an even function of x, one can show that

$$< F_x > = \frac{2 I_v\, I_o}{c} \sin\left(\frac{\pi x_o}{3c}\right) \int_0^\infty dx \frac{\partial M}{\partial x}(x,h) \sin\left(\frac{\pi x}{3c}\right) \tag{4.44}$$

$$< F_z > = \frac{2 I_v\, I_o}{c} \cos\left(\frac{\pi x_o}{3c}\right) \int_0^\infty dx \frac{\partial M}{\partial z}(x,h) \cos\left(\frac{\pi x}{3c}\right) . \tag{4.45}$$

Integrating by parts in the $< F_x >$ equation gives the alternative forms

$$< F_x > = \frac{-2\pi I_v\, I_o}{3\, c^2} \sin\left(\frac{\pi x_o}{3c}\right) \int_0^\infty dx\, M(x,h) \cos\left(\frac{\pi x}{3c}\right) \tag{4.46}$$

and

$$< F_z > = \frac{-3c}{\pi} \cot\left(\frac{\pi x_o}{3c}\right) \frac{\partial}{\partial h} < F_x > . \tag{4.47}$$

(Alternatively, we could have evaluated the average forces from just one phase of the three phase system, and then tripled the result to find the total.)

Some simple analytic results follow if we take $a >> b$, h. In this instance, it can be shown that (setting $c = b/3$)

$$< F_x > = \frac{-6\mu_o \, a \, I_v \, I_o}{b} \sin\left(\frac{\pi x_o}{b}\right) e^{-\pi h/b} \quad , \tag{4.48}$$

and

$$< F_z > = \frac{-6\mu_o \, a \, I_v \, I_o}{b} \cos\left(\frac{\pi x_o}{b}\right) e^{-\pi h/b} \quad . \tag{4.49}$$

Atherton[34] first suggested that for a given height h and width a , there is an optimum length b . Maximizing $< F_x >$ with respect to b gives $b = \pi h$. For smaller a , numerical studies give a broad maximum at $b \simeq 3.7\ h$ for $a = 1m$ and $b \simeq 4.2\ h$ for $a = 0.5$ m , where $h = 0.3$ m. These results differ by about a factor of 2 from Atherton's. We believe our results to be correct.

The absolute magnitude of the thrust on a single vehicle coil for some typical parameters,

$$\begin{aligned} I_o &= 1500 \text{ A} \quad , \\ I_v &= -\ 5 \times 10^5 \text{ A} \quad , \\ h &= 0.3 \text{ m} \quad , \\ a &= 1m \quad , \\ b &= 1.1 \text{ m} \quad , \end{aligned} \tag{4.50}$$

is

$$< F_x > \ = 452 \text{ lb.} \ \sin\left(\frac{\pi x_o}{b}\right) \tag{4.51}$$

Eq. (4.51) results from the numerical evaluation of (4.46).

We have shown that the peak thrust requirement of a magnetically levitated vehicle is approximately 20,000 lb. Hence, about 44 vehicle magnets are required.

The magnet length b in (4.50) has been chosen to give maximum thrust for a given height, width, coil current, and track current. To completely optimize the system one would also have to consider track costs, magnet weight and shielding, etc. so that some other aspect ratio may be more favorable. No attempt was made to perform this type of optimization. In addition, we note that the propulsion magnets have a different aspect ratio (1 x 1.1 m) than the lift magnets (0.5 x 3 m), which suggests that either a compromise design is needed, or that separate magnets are required for propulsion and lift. Certainly, if we use the parameters in (4.50) and (4.51) more magnets (44) are needed for propulsion than lift (4.8). It is also evident from Eqs. (4.48) and (4.49) that $< F_z >$ is an attractive force in the region where $< F_x >$ is positive and stable (i.e., where $< F_x >$ increases for a decrease in x_o.) From the approximate results (4.48) and (4.49), we see that $< F_z >$ can be as large as $< F_x >$ Since $< F_z >$ is attractive, it acts to increase the effective weight of the system in an arrangement such as Fig. 4.19.

One important property of a LSM is its stability. A simple model of the dynamical behavior allows us to put bounds on the velocity error which is allowed. It is reasonable to assume that $z \simeq h$, and at any instant of time

$$F_x \simeq F_o \sin(kx-\omega t) \tag{4.52}$$

where

$$F_o = \frac{-2\pi\ I_v\ I_o N_v}{3c^2} \int_0^\infty dx\ M(x,h)\ \cos\left(\frac{\pi x}{3c}\right), \qquad (4.53a)$$

$$k = \frac{\pi}{3c} = \frac{\pi}{b} \quad , \qquad (4.53b)$$

and

$$v_\phi = \omega/k \quad . \qquad (4.53c)$$

For convenience we take $F_o > 0$. The number of magnets on the vehicle is N_v. If m is the mass of the vehicle, then

$$m\frac{dv}{dt} = -F_D(v) + F_o \sin(kx-\omega t) \quad , \quad v = \frac{dx}{dt} , \qquad (4.54)$$

where $F_D(v)$ is the drag force. Let $x' = x - v_\phi t$, then

$$m\frac{dv'}{dt} = -F_D(v_\phi+v') + F_o \sin kx' \quad , \quad v' = \frac{dx'}{dt} , \qquad (4.55)$$

Now $v' \ll v_\phi$, so

$$F_D(v_\phi+v') = F_D(v_\phi) + F_D'(v_\phi)\ v' + \ldots \quad . \qquad (4.56)$$

We can rewrite the equation of motion as

$$m\frac{dv'}{dt} = -f_D(v') - \frac{dV}{dx'} \qquad (4.57)$$

where

$$f_D(v') = F_D'(v_\phi)v' + \ldots \qquad (4.58a)$$

and

$$V(x') = F_D(v_\phi)\ x' + \frac{F_o}{k}\cos kx' \quad . \qquad (4.58b)$$

$V(x')$ can be thought of as an effective potential energy.

Synchronous operation corresponds to operation at a local minimum in $V(x')$, i.e., at $x' = x_o$ where $F_o \sin kx_o = F_D(v_\phi) \equiv F_D$. (See Fig. 4.20). The point $b-x_o$ gives the same thrust as x_o, but corresponds to an unstable equilibrium (potential maximum). Clearly the system is stable if $(1/2)mv'^2 + V(x') < V_2$. Hence, if the vehicle is given a

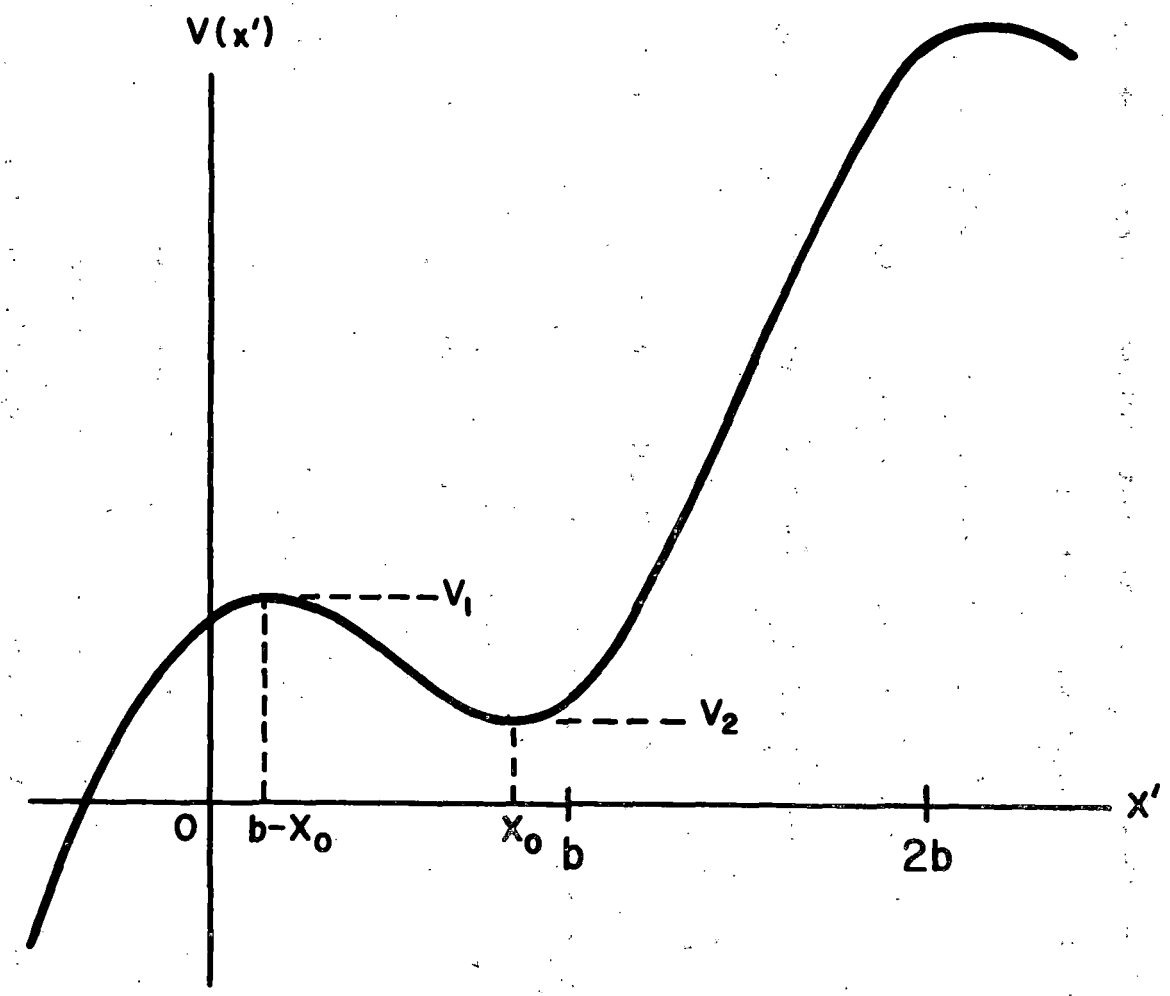

Fig. 4.20. Effective potential energy $V(x')$ vs x'. Stability is obtained if the operating point remains in the local minimum about x_o.

velocity error $\Delta v = v' = v - v_\phi$, but no position error, stability is obtained if $1/2m(\Delta v)^2 < (V_2 - V_1)$ or

$$(\Delta v)^2 < \frac{4b\,F_o}{\pi m}\left[(1-F_D^2/F_o^2)^{1/2}\,\frac{F_D}{F_o}\cos^{-1}\frac{F_D}{F_o}\right] . \tag{4.59}$$

Take $\cos^{-1}x$ to be positive, but less than $\pi/2$. This result is similar to a rough estimate given by Richards and Tinkham[32].

For $b = 1.1m$, $mg = 100{,}000$ lb, $F_o = 20{,}000$ lb and $F_D = 10{,}000$ lb, we find

$$|\Delta v| \lesssim 1m/s = 2.2\ mi/h . \tag{4.60}$$

Unless one goes to larger F_o, the permissible velocity error is rather small.

It is desirable to calculate the efficiency of the LSM. The track is energized in sections of length L. The efficiency at cruise is

$$\text{Efficiency} = \frac{F_D v}{F_D v + P_t} \tag{4.61}$$

where P_t is the energy dissipated in the track,

$$P_t = \frac{3}{2} N_t R I_o^2 , \tag{4.62}$$

The number of track loops in one phase is $N_t = L/b$ and the resistance of a single loop is $R = \rho 2(a+b)/A$ where ρ is the resistivity and A is the cross-sectional area of the conductor. Substituting into (4.61), we find that

$$\text{Efficiency} = \frac{1}{1 + \left(\frac{3LRI_o^2}{2bF_D v}\right)} \tag{4.63}$$

For an aluminum conductor ($\rho = 2.8\ \mu\ \Omega$-cm) of 2.5 cm x 2.5 cm cross section and with $I_o = 1500$ A, a = 1.0 m, b = 1.1 m, $F_D = 10{,}000$ lb, and v = 300 mi/h, we find that

$$\frac{3RI_o^2}{2bF_D v} = 0.97 \times 10^{-4}\ m^{-1} \simeq \frac{1}{10km} \qquad (4.64)$$

Hence,

$$\text{Efficiency} \simeq \frac{1}{1 + (\frac{L}{10km})} \quad . \qquad (4.65)$$

Clearly, high efficiencies are available if short sections of track are energized (e.g., if L = 2km, then the efficiency = 83%) .

In Fig. 4.21 we show a possible arrangement of the propulsion magnets and the lift magnets. In this case, the height of the propulsion magnets above the track is taken to be 0.15 m.

The full clearance of the suspension system is probably not required for the propulsion system since the dynamic stroke is < 0.1 m. In addition, control coils and/or damping plates must also fit below the lift coils which makes the suspension height as large at 0.3 m. Reducing h to 0.15 m decreases the required number of vehicle magnets to 24 as compared to 44 for h = 0.3 m. The peak thrust F_o vs. magnet length b is shown in Fig. (4.22). A maximum occurs at b = 0.5 m. For L = 2 km, the efficiency is shown in Fig. 4.23 where I_o is adjusted at each value of b so that $F_o = 2F_D = 20{,}000$ instead of being fixed as in Fig. 4.22.

1b/ There is a broad maximum in the efficiency at $b \approx 0.8$ m. As a function of L, Eq. (4.65) gives the efficiency for $b \approx 0.8$ m to a good approximation. In Figs. (4.24) and (4.25), the resistance and conductor volume/km of track are shown as functions of b. We note these quantities increase rapidly with decreasing b for $b \lesssim 0.4$ m. Such curves are useful in optimizing the system.

4.5. Propulsion by a Turbojet Engine

It has generally been concluded that propulsion by a jet engine is not an available option for the magnetically levitated revenue vehicle. The reasons are noise and air pollution. The noise problem does not, however,

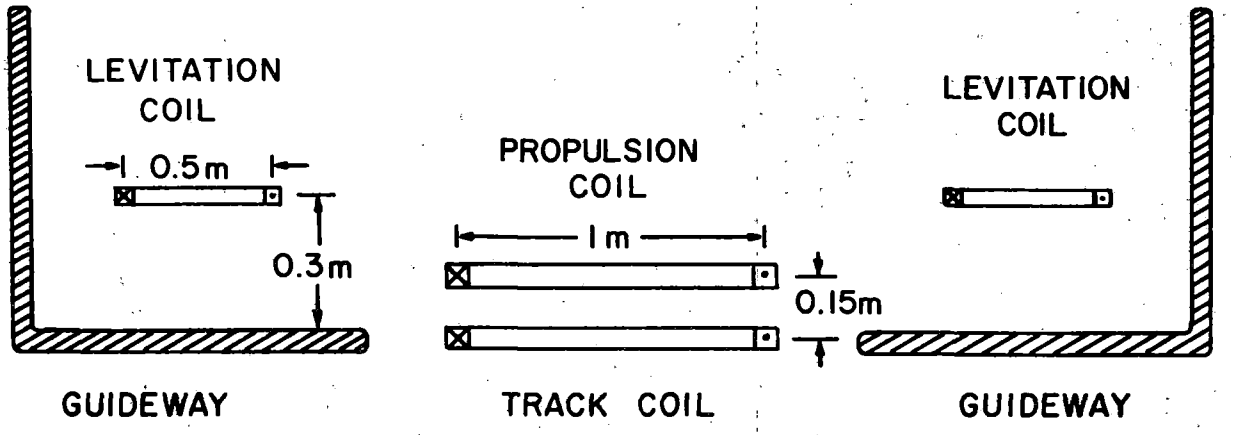

Fig. 4.21. Possible configuration of lift magnets and propulsion magnets for LSM.

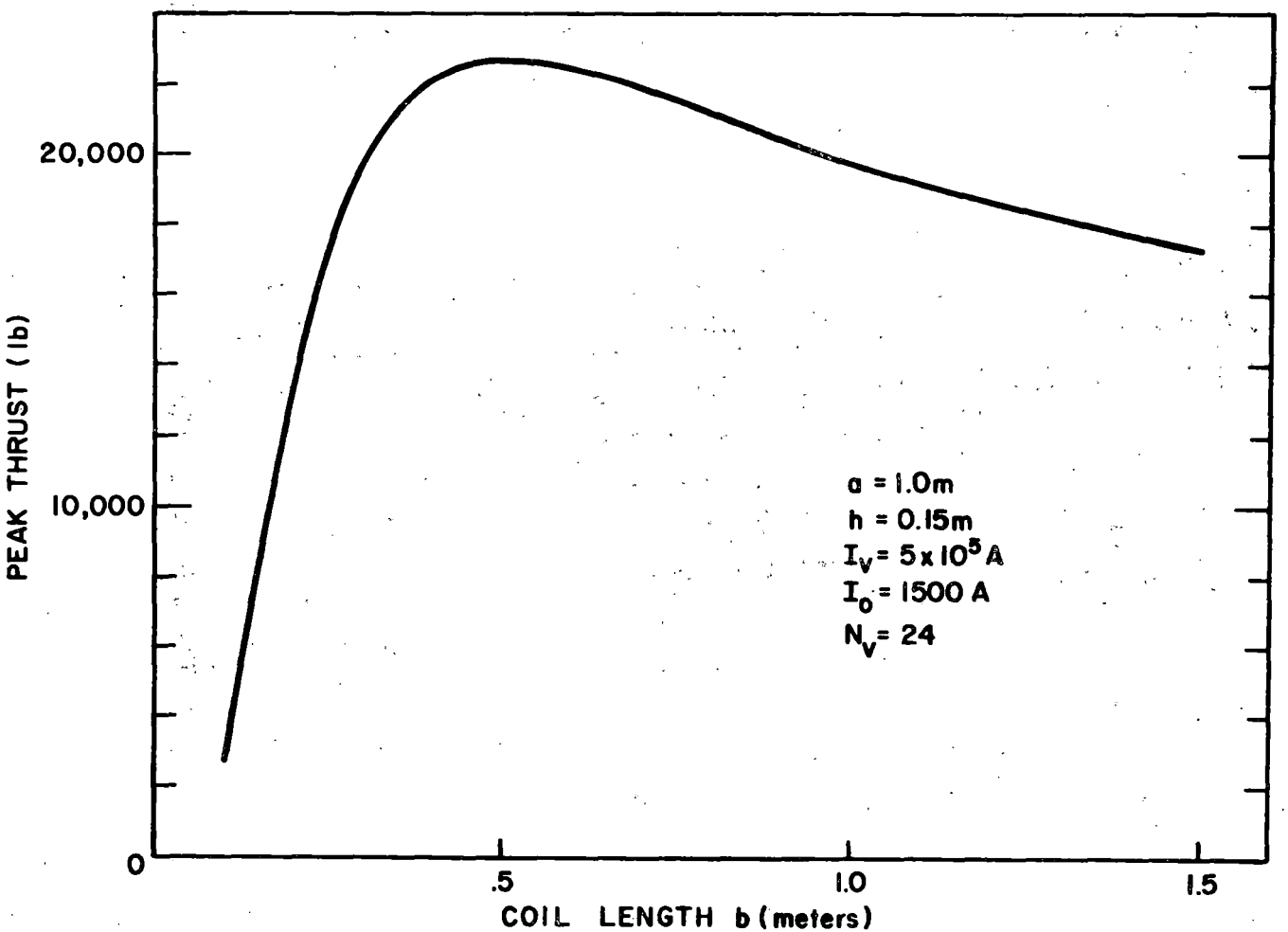

Fig. 4.22. LSM peak thrust for 1m wide coil at 0.15m height as a function of magnet length. The vehicle is assumed to have 24 magnets on board, each carrying 5×10^5A. The track current I_o is 1500 A (I_o is the peak track current, not r.m.s.).

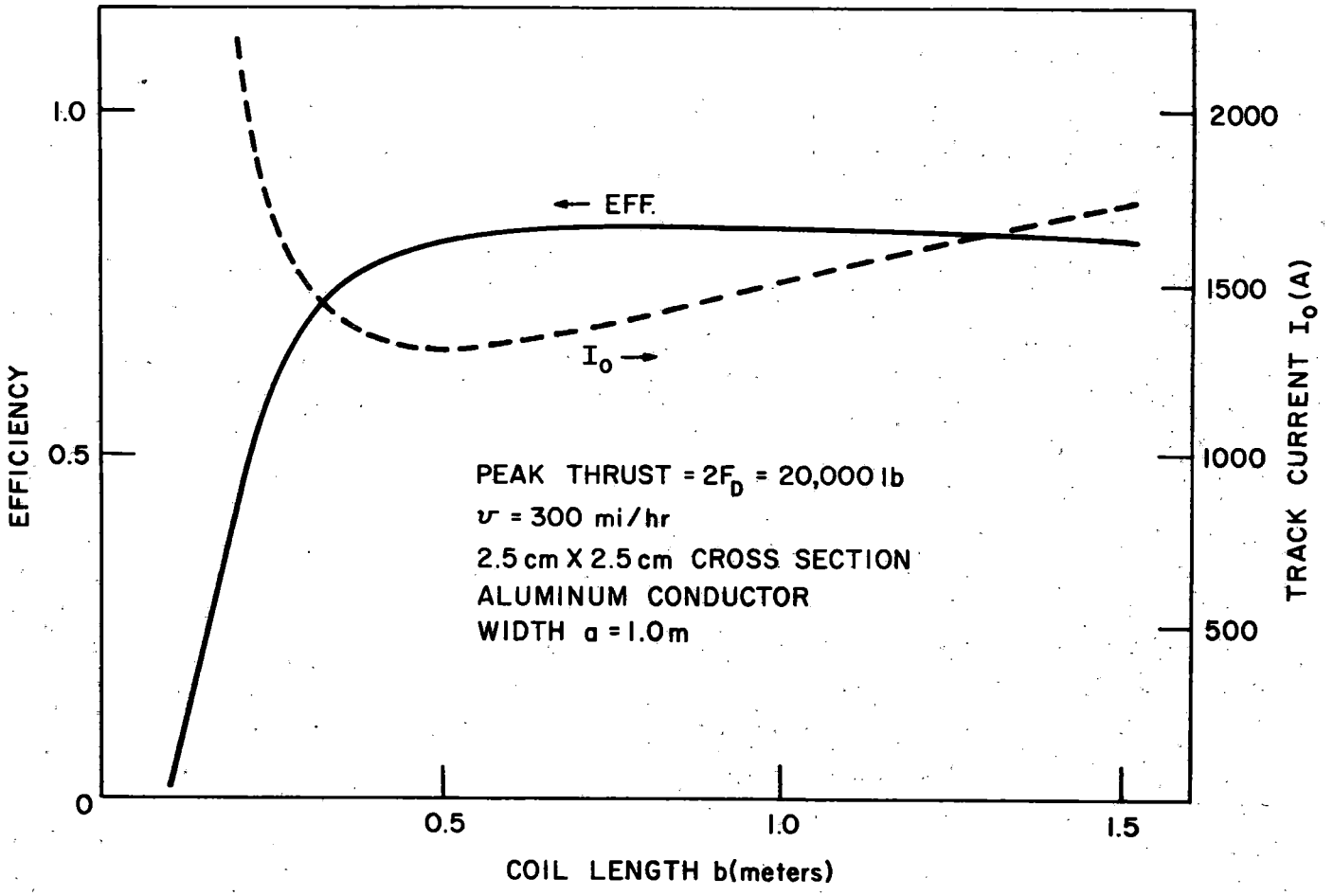

Fig. 4.23. Efficiency and track current vs coil length b. The track current is adjusted so that the peak thrust is 20,000 lb at each value of b. Other parameters are the same as in Fig. 4.22. The efficiency is calculated for an energized track length of 2km.

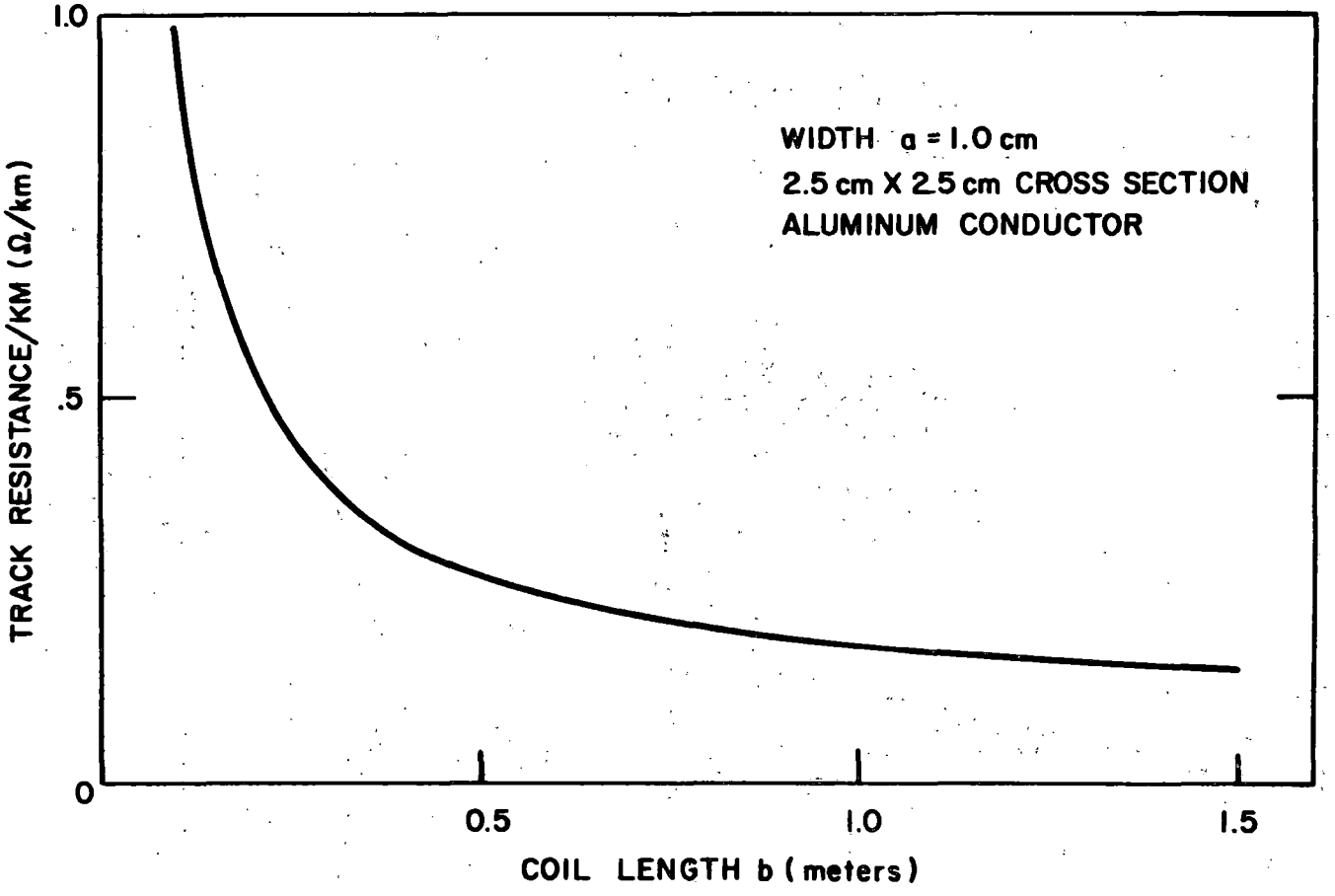

Fig. 4.24. Resistance/km of track (1 phase) vs coil length b.

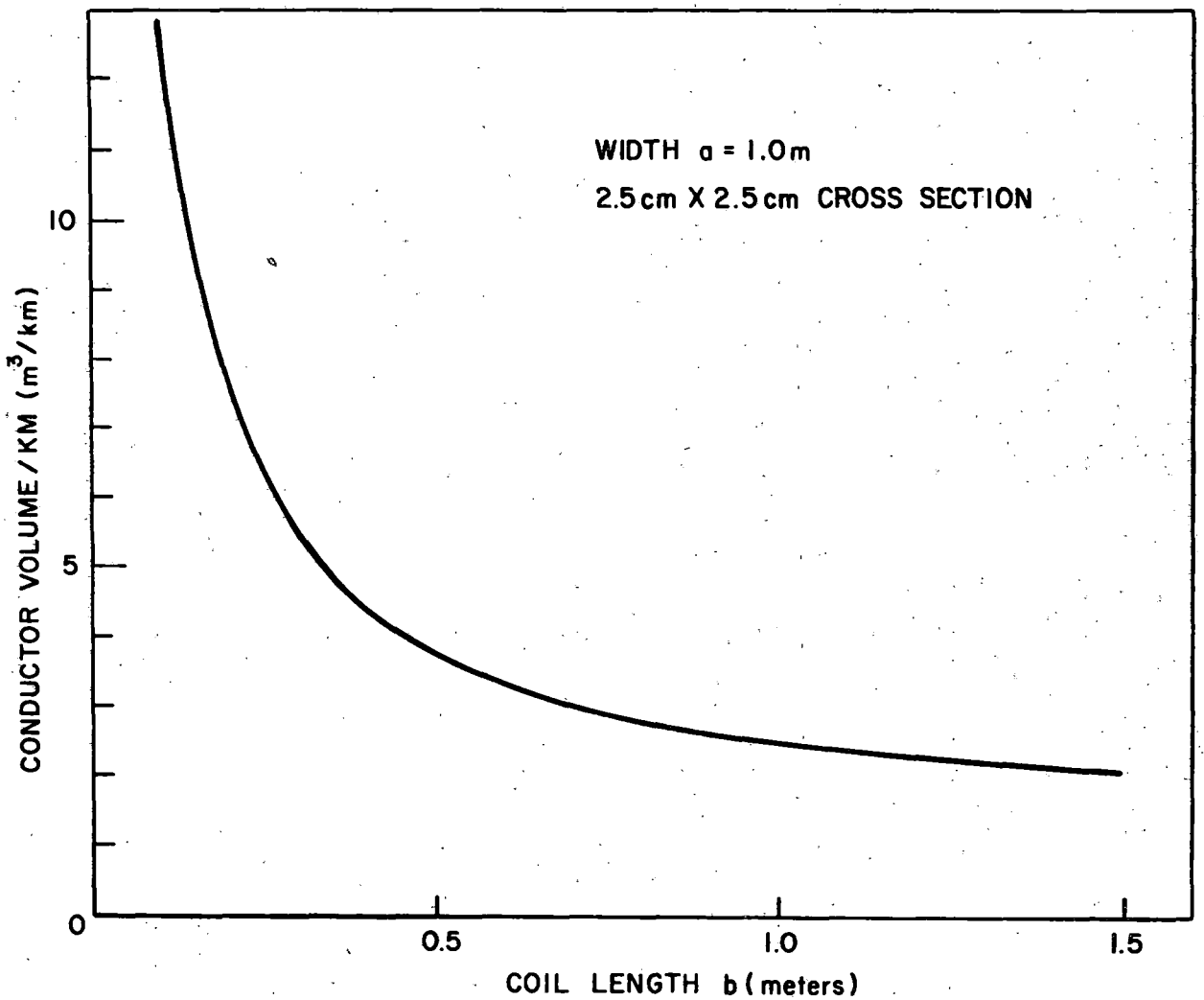

Fig. 4.25. Volume of conductor/km of track (1 phase) vs coil length b.

appear to be insurmountable since it has been shown that a substantial reduction in jet noise can be achieved through appropriate engine design; in this connection the Q-fan design[36] by Hamilton Standard is the one which has received the most development. The current status of noise and pollution control for jet engines has been discussed in a recent article by Beheim et al.[36] The turbojet engine has many desirable features as a propulsive power unit for a magnetically levitated vehicle, particularly for a vehicle with a repulsive-type suspension. The engine is light weight (even with fuel for a 300 mile trip), requires no wayside power pickup and no close-gap reaction surface. It does not preempt any part of the track area, thus allowing greater freedom in guideway choice.

The noise from a jet engine is from two sources: from fan noise and from the mixing of the high velocity jets with ambient air. Fan noise can be reduced by locating the fan deep in the nacelle and by an acoustical treatment of the nacelle. The jet noise can be reduced by going to larger bypass ratios. The bypass ratio is the flow rate in the fan stream compared to the flow rate in the jet core. From an efficiency standpoint a bypass ratio of about 4.5 is optimum, but the efficiency does not degrade very much as one goes to higher bypass ratios. However, the noise level drops by about 10 EPNdB (effective perceived noise level) for each increase of 5 in the bypass ratio.

The Q-fan, developed by Hamilton Standard, uses a fan with 8 to 15 blades (with subsonic tip speed), and a bypass ratio as large as 30. The fan diameter is somewhat larger than that of a conventional fan engine. The Q-fan has a desirable thrust characteristic; it provides about 50% larger thrust at low speeds than at cruise, which would be an advantage in overcoming the drag peak. Experiments on the Q-fan, which have been carried

out in part under a NASA contract, show that the high-bypass feature does indeed produce much lower noise levels.

A study by Hamilton Standard for the application of Q-fan propulsion to high-speed ground transportation showed that two 4.5 ft diameter Q-fans, each rated at 3600 shaft HP, are sufficient to propel the 50 ton revenue vehicle to a speed of 280 mi/h. The noise level is projected at 81 dbA at 50 ft. This is an acceptable level for intercity operation. (For comparison the Bertin aerotrain with the shrouded propeller produces 106 dbA at 50 ft.) In order to reach a lower noise specification for in-station operation (61 dbA at 50 ft.), the engine would have to be throttled to 25% maximum thrust.

The other problem area for jet engines is polluting emissions. Hydrocarbons and CO emissions can be reduced substantially by modifications in combustor design, but control of nitrogen oxide emissions is more difficult. Various approaches for accomplishing the latter goal use water injection or electronic engine control. In any case it seems probable that emission standards will be defined for aircraft engines in the near future, and considerable developmental effort will be expended to meet these goals.

5. VEHICLE AERODYNAMICS

5.1. Aerodynamic Drag

The principal drag force on a magnetically levitated vehicle at 300 mi/h is the aerodynamic drag force, unless the vehicle operates in an evacuated tube. Since evacuated tube operation is not anticipated at the present, it is important to have as accurate an estimate of the drag as possible. The aerodynamic drag force can be written as

$$F_{AD} = \frac{1}{2} C_D A \rho \ v^2 \tag{5.1}$$

where C_D is the drag coefficient, A is the frontal area (generally assumed to be 100 ft^2), ρ is the density of air (taken to be 2.38×10^{-3} $slug/ft^3 \approx 1.2$ milligram/milliliter), and v is the vehicle velocity. The dynamic pressure, $\frac{1}{2}\rho v^2$, at 300 mi/h is 230 lb/ft^2. Hence for A = 100 ft^2 and v = 300 mi/h, $F_{AD} = 2.30 \times 10^4 \ C_D$ lbs.

Previously[1] we estimated that $C_D = 0.26$, which gives $F_{AD} = 6000$ lb.

A more thorough study of the drag coefficient has been done by AVCO.[37] In this study, the drag coefficient is sum of four contributions: nose drag, base drag, skin friction drag, and drag to due to protuberances.

$$C_D = C_{nose} + C_{base} + C_{skin} + C_{prot.} \tag{5.2}$$

We summarize their results.

5.1.1. Nose Drag

Although the nose drag depends to a certain extent on the exact shape of the nose, making the nose exceptionally pointed does not reduce the drag significantly, but probably results in an uneconomical use of space. It was concluded that for a practical design

$$C_{nose} = 0.08. \tag{5.3}$$

5.1.2. Base Drag

If the hydraulic radii of the base and frontal areas are equal, then

$$C_{base} = \frac{0.029}{\sqrt{C_{skin}}} \tag{5.4}$$

The base drag depends upon the skin friction coefficient because the skin friction partially determines the flow by the trailing edge. For $C_{skin} = 0.07$, we find that

$$C_{base} = 0.11. \tag{5.5}$$

(See following section for the determination of C_{skin}.)

5.1.3 Skin friction drag

The skin friction drag is composed of two parts, that due to the wetted area of the vehicle adjacent to the guideway, A_{gap}, and that due to the rest of the area A_o. So

$$C_{skin} = C_{f,gap} \frac{A_{gap}}{A} + C_f \frac{A_o}{A} \quad , \tag{5.6}$$

where $C_{f,gap}$ is the skin friction coefficient for the gap region (i.e., the region adjacent to the guideway) and C_f is the coefficient for the rest of the vehicle. (Recall A is the frontal area.)

To determine $C_{f,gap}$ and C_f, it is necessary to know the flow Reynolds number

$$Re_L = vL/\nu \tag{5.7}$$

where L is the vehicle length (100 ft) and ν is the dynamic viscosity (1.7×10^{-4} ft^2/sec). We find that $Re_L = 2.7 \times 10^8$ at 300 mi/h. The flow is clearly turbulent. For these conditions the thickness of the (velocity) boundary layer is

$$\delta = 0.37L/Re_L^{0.2} \quad . \tag{5.8}$$

For a 100 ft vehicle, δ = 9 inches (23 cm) which is the same order of magnitude as the clearance between vehicle and track for a system using the superconducting suspension. (Note that h = 0.3 m = 12 inches corresponds to the distance between the track and the magnet midplane or center. Parts of the dewar, the damping plate and/or control coils must fit below the magnet so that the clearance is less than 0.3 m. The clearance is therefore probably 15-20 cm. In (5.8), δ is the boundary layer thickness at the trailing edge of the vehicle. At the leading edge, the boundary layer is zero, increasing nearly linearly with distance to the trailing edge. Hence, we do not expect that the influence of the guideway will be significant. For smaller gaps, the flow becomes turbulent Couette flow. It is difficult to reliably estimate the drag in this case since there are several competing phenomena occurring simultaneously; (1) Couette flow increases $C_{f,gap}$, (2) venting of the guideway causes the relative velocity in the gap to decrease below v, and (3) a rough guideway surface can maintain the relative gap velocity close to v, even with venting. (1) and (3) represent increases in $C_{f,gap}$ while (2) represents a decrease. It is concluded that for close gaps (e.g., 1 inch) and also for the larger gaps that the most reliable estimate is

$$C_{f,gap} = C_f \quad , \tag{5.9}$$

i.e., the ground effect can be neglected. The uncertainties associated with the ground effect are smaller than other uncertainties, e.g., those in C_{prot}.

Therefore, from (5.6) we find that

$$C_{skin} = C_f \, A_{wet}/A \quad , \tag{5.10}$$

where A_{wet} is the total wetted area of the vehicle, $A_{gap} + A_o$. We assume that $A_{wet} = 40A$. C_f can be estimated from the Prandtl-Schlichting skin friction formula[38].

$$C_f = \frac{0.455}{(\log Re_L)^{2.58}} - \frac{A}{Re_L} \quad , \tag{5.11}$$

where A ~1700 (depends on the transition Reynolds number).

This gives $C_f = 1.85 \times 10^{-3}$ for $Re_L = 2.7 \times 10^8$. Substituting into (5.10), we find that ($A_{wet} = 40$ A)

$$C_{skin} = 0.07 \tag{5.12}$$

This assumes that the vehicle surface is smooth as opposed to a surface with many rivets where C_{skin} may be as large as 0.2. Clearly this must be avoided.

5.1.4. Proturberance Drag

Protuberance drag is due to large scale objects such as windows. Small scale effects (surface finish, rivets, etc.) are included in C_{skin}. This contribution to the drag has the largest uncertainty of any of the four. AVCO estimates that

$$C_{prot.} = 0.1 \tag{5.13}$$

5.1.5 Total Drag Coefficient

Summing (5.3), (5.5), (5.12), and (5.13) we find that

$$C_D = 0.36 \tag{5.14}$$

The error according to AVCO, is at least $\pm$ 0.03. Eq. (5.14) then represents a 8300 lb drag force at 300 mi/h. Careful design of the body to reduce the protuberance drag could result in a 20% decrease of this force, giving 6600 lb which is about what we previously estimated.

It should be pointed out that the AVCO estimate of the ground effect was solely related to the effect on the skin friction. Any effects due to changes in the flow pattern about the vehicle such as occurs when a vehicle passes through an enclosed, or partially enclosed, guideway have not been considered. In this regard, THL[39] predicts that $C_D \simeq 0.25$ for the box and inverted "T" designs, but $C_D \simeq 0.33$ for the channel design. These calculations pertain to an air cushion vehicle of comparable width but only about 60% of the length of the vehicle considered in this report. (Air collection drag is not included, but the additional drag associated with the air pads is.)

5.2. Aerodynamic Effects on Yaw and Transverse Oscillations

Consider a vehicle of length L and width W with guidance magnets at each corner. Each magnet has a normal force (guidance force) F_G and an associated drag force F_{GD}. It is straightforward to show that the torque on the vehicle due to magnetic forces for small ψ (yaw angle) and y (transverse displacement of the center of mass which is taken at the vehicle center) is (See Fig. 5.1)

$$M_{z,mag} = (F_G 2W + F'_G L^2)\psi + 2W F'_{GD} y \tag{5.15}$$

where $F'_G = \frac{\partial F_G}{\partial h'}$ and $F'_{GD} = \frac{\partial F_{GD}}{\partial h'}$. h' is the nominal separation of the magnets from the guideway.

Likewise, the transverse force due to the magnets is

$$F_{y,mag} = 4F'_G y. \tag{5.16}$$

The aerodynamic torque is

$$M_{z,aero} = \frac{1}{2} \rho v^2 AL C_n \tag{5.17}$$

where $\frac{1}{2}\rho v^2$ is the dynamic pressure, $A = W^2$ is the frontal area, and

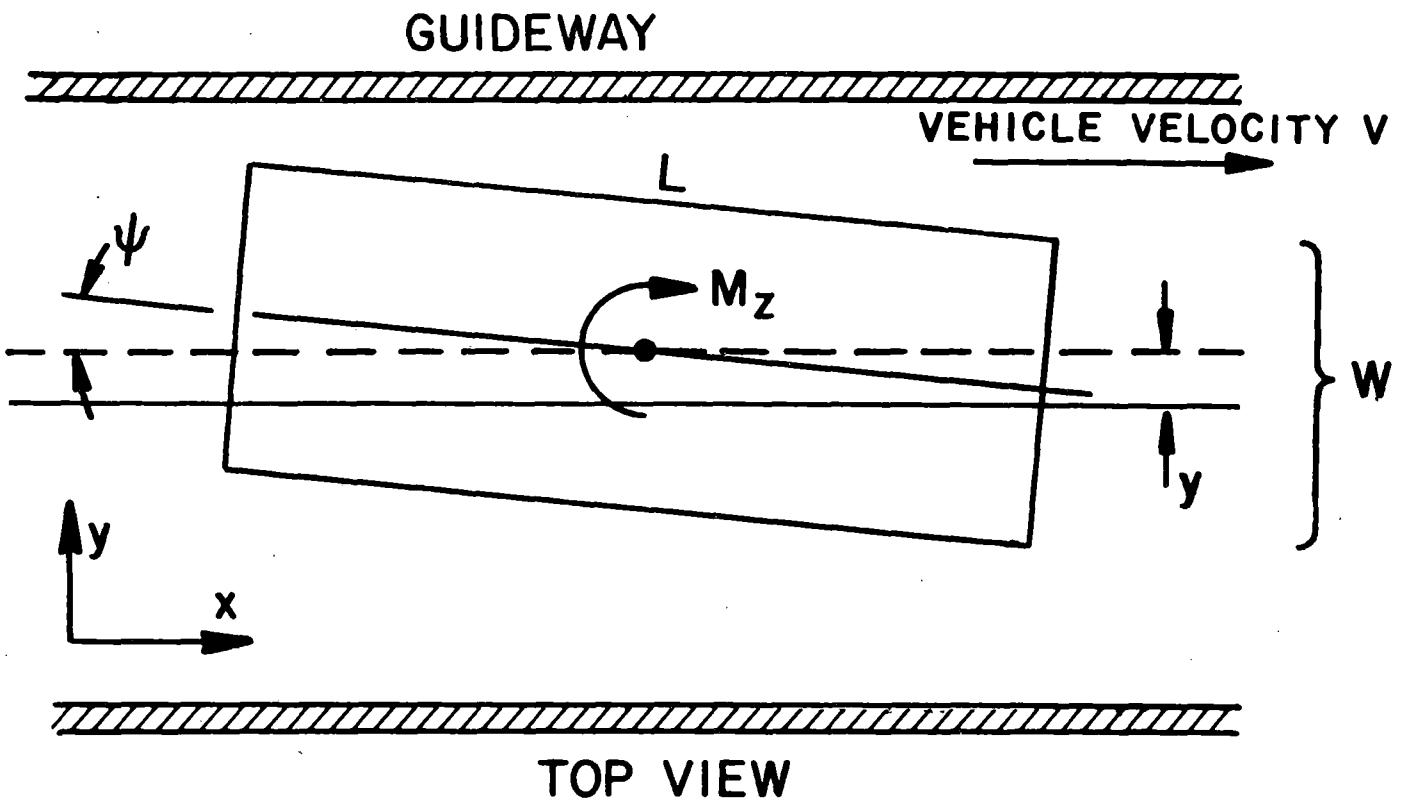

Fig. 5.1. Yaw and transverse oscillation of vehicle in guideway.

C_n is the yawing moment coefficient. For small ψ .

$$C_n = \frac{dC_n}{d\psi}\bigg)_o \quad \psi \ . \tag{5.18}$$

The transverse or side force is

$$F_{y,aero} = -\frac{1}{2}\rho v^2 \, A \, C_y \tag{5.19}$$

where $C_y = \frac{dC_y}{d\psi}\bigg)_o \psi$ for small ψ . There is no component proportional to y.

The moment of inertia is $I = \frac{1}{12} ML^2$ where M is the mass and it is assumed that L >> W and the mass is uniformly distributed. The equations of motion are:

$$I\ddot{\psi} = M_{z,mag} + M_{z,aero}, \tag{5.20}$$

and

$$M\ddot{y} = F_{y,mag} + F_{y,aero} \ . \tag{5.21}$$

We now assume that the guidance force is one half of the lift force for the corresponding lift magnet,

$$F_G = \frac{1}{2} F_L \ . \tag{5.22}$$

Also,

$$F_{GD} = \frac{w}{v} \, F_G \ . \tag{5.23}$$

(The characteristic speed w is defined in Eq. (2.2).)

We recall that the natural frequency of the vertical oscillations is

$$\omega_o^2 = -\frac{4}{M} F_L' \quad , \quad F_L' = \frac{\partial F_L}{\partial h} \tag{5.24}$$

if there are four lift magnets ($4F_L = Mg$); h is the nominal height which is taken to be equal to h'.

The coefficient of the term in $M_{z,mag}$ proportional to ψ is therefore given by

$$F_G 2W + F_G' L^2 = \frac{1}{4} MgW - \frac{1}{8} M\omega_o^2 L^2 \qquad (5.25)$$

$$\simeq - \frac{1}{8} M\omega_o^2 L^2 \quad .$$

The last approximation follows since $L >> W$ and $\frac{1}{2} \omega_o^2 L >> gW$.

Similarly,

$$2W\, F_{GD}' = - \frac{1}{4} \frac{W}{v} W\, M\omega_o^2 \qquad (5.26)$$

and

$$4F_G' = - \frac{1}{2} M\omega_o^2 \quad . \qquad (5.27)$$

From the Tracked Hovercraft Limited Report[39] it can be seen that $\left.\frac{dC_n}{d\psi}\right)_o \sim$ 1 to 2, depending upon guideway type, for the size and shape vehicle of interest. Since $\frac{1}{2} \rho v^2 \simeq 230$ lb/ft^2 at 300 mi/h, A = 100 ft^2 and L = 100 ft,

$$M_{z,aero} \sim 2\text{-}4 \times 10^6\, \psi \quad . \qquad (5.28)$$

For a 50 ton vehicle at a frequency of $\frac{\omega_o}{2\pi}$ = 1.35 Hz (appropriate to a $\frac{1}{2}$ x 3m coil)

$$M_{z,mag} \sim - 4 \times 10^8 \psi + \text{terms in } y \quad . \qquad (5.29)$$

Hence, we can neglect $M_{z,aero}$ compared to $M_{z,mag}$.

In the same report, we find that

$$dC_y/d\psi)_o \simeq 0 \text{ , channel guideway}$$
$$\simeq 6 \text{ , inverted "T" guideway} \qquad (5.30)$$
$$\simeq 8 \text{ , box guideway.}$$

These coefficients are based upon wind tunnel tests on small models in which both the guideway and the vehicle were rotated. Hence, they are only approximate for the analysis above. The data reported are more appropriate for side winds, which are discussed later.

The equations of motion become

$$\ddot{\psi} + \omega_{\psi}^{2}\,\psi = -\,k_1\,\omega_o^{2}\,\xi \quad , \tag{5.31}$$

$$\ddot{\xi} + \omega_{y}^{2}\,\xi = -\,k_2\,\omega_o^{2}\,\psi \quad , \tag{5.32}$$

where

$$\omega_{\psi}^{2} = -\,\frac{1}{I}\,\frac{\partial}{\partial\psi}\,(M_{z,mag} + M_{z,aero}) \simeq \frac{3}{2}\,\omega_o^{2} \quad , \tag{5.33a}$$

$$k_1 = -\,\frac{2W^2}{I\omega_o^{2}}\,F'_{GD} \simeq 3\,\frac{w}{v}\left(\frac{W}{L}\right)^{2} , \tag{5.33b}$$

$$\xi = y/W \quad , \tag{5.33c}$$

$$\omega_{y}^{2} = -\,\frac{1}{M}\,\frac{\partial F_{y,mag}}{\partial y} \simeq \frac{1}{2}\,\omega_o^{2} \quad , \tag{5.33d}$$

and

$$k_2 = \frac{\rho v^2 A}{2MW\omega_o^{2}}\,\frac{dC_y}{d\psi}\bigg)_{o} \tag{5.33e}$$

Both k_1 and k_2 are small, dimensionless numbers ($k_1 \sim 10^{-3}$, $k_2 \sim 10^{-1}$).

One normal mode of oscillation has a frequency $\simeq \omega_{\psi} \simeq \sqrt{3/2}\,\omega_o$ in which $\xi \simeq k_2\psi$ and the second has a frequency $\simeq \omega_y \simeq \omega_o/\sqrt{2}$ with $\psi \simeq -\,k_1\xi$. The degrees of freedom are only slightly coupled.

In general we do not expect the aerodynamic forces to affect the normal modes of oscillation of the vehicle to any great extent since the magnetic forces are much larger. AVCO[37] gives the relevant coefficients for the other modes (pitch, heave, and roll).

5.2.1. Side Winds

A 60 mi/h side wind corresponds to a yaw angle of 11° when the vehicle is traveling 300 mi/h. According to THL,[39] the side force coefficient at 11° is

$$\begin{aligned} C_y &\simeq 0 \quad , \text{ channel guideway} \\ &\simeq 1.1, \text{ inverted "T" guideway} \\ &\simeq 1.7, \text{ box guideway} \end{aligned} \tag{5.34}$$

This gives a side force of 23,000 lb. x C_y which is considerable for the inverted "T" and box guideways. Wind tunnel tests by Grumman on a TACRV model[40] indicate about 7700 lb. on a vehicle roughly $\frac{1}{2}$ the size considered above. In these tests, the guideway was similar to the channel guideway in THL's tests.

5.3. Use of Flaps for Damping:

Consider the use of four flaps, one at each corner of the vehicle, which would be controlled to produce damping of the vertical motion. The dimensions of the flaps are assumed b x c as shown in Fig. 5.2, where using standard terminology with respect to airfoils[41]

b/2 = span of wing (flap)

c = chord of wing (flap) .

The aspect ratio A for flaps in this arrangement is

$$A \equiv b^2/S$$

where S is the surface area of the wing. In the simple case of a rectangular wing (flap) as shown, S = bc so that A = b/c. This is not in general true for airfoils of more complicated shape, e.g., parabolic leading edge, in which case $A = b/c_{average}$.

The subject of the aerodynamics of airfoils is complicated and therefore the simplified analysis presented here is by no means to be

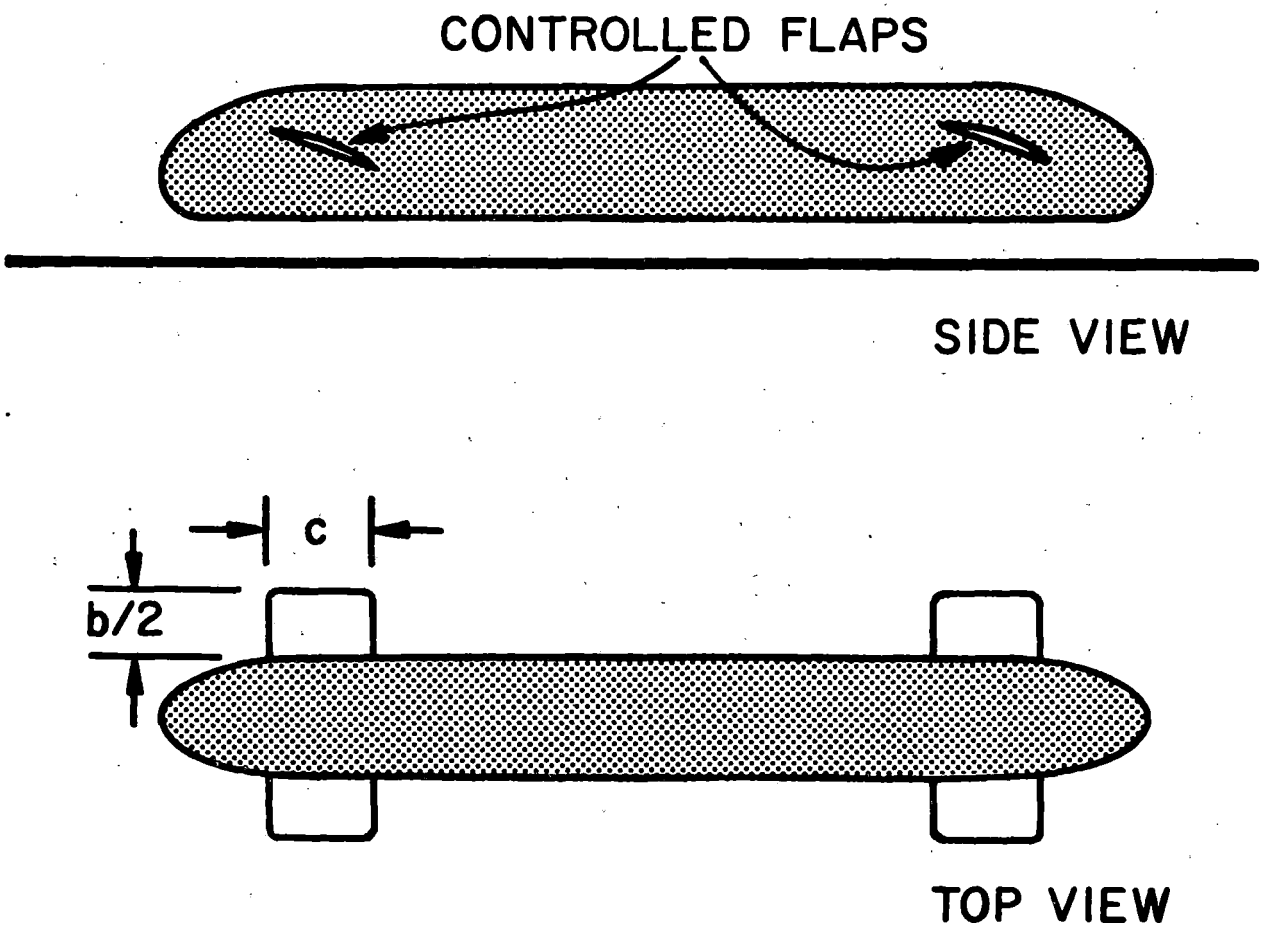

Fig. 5.2. Use of flaps for damping vertical motion of vehicle.

considered a definitive treatise. However, it should be sufficiently exact to give a feel for whether damping of the vertical motion could be obtained using flaps of reasonable size.

The limitations of the analysis are:

(1) It is assumed the flaps are far enough from the ground plane that it has no appreciable effect on the lift and drag relationships.

(2) The effect of the wings (flaps) being attached to the vehicle body is taken into account by assuming the two flaps on either side of the vehicle operate as one single flap (total span b) in free space.

(3) The flaps are assumed to be rectangular flat plates with blunt ends. Changing the profile, planform shape, or end shape of the flaps would change the results somewhat but probably not significantly.

(4) It is assumed that the flaps are operated in unison in response to vertical velocities induced by track irregularities. The rotations about the center of mass due to the front and rear flaps operating out of phase (pitch) or the side to side flaps out of phase (roll) are not considered.

5.3.1. Lift and Drag Coefficients:

The lift and drag coefficients for an airfoil are defined by

$$C_L = \frac{F_L}{(\frac{1}{2}\rho v^2)S} = \frac{F_L}{qS} \quad , \; q = \text{dynamic pressure,} \tag{5.35}$$

and

$$C_D = \frac{F_D}{qS} \quad . \tag{5.36}$$

It has been determined that for wings of any aspect ratio[41-44] and of many shapes

$$C_D = \frac{C_L^2}{\pi A} \quad . \tag{5.37}$$

(Empirically, it has been found that this relationship underestimates the drag somewhat, but provides a good order of magnitude number.)

The lift coefficient depends on the wing shape, profile, and aspect ratio. It appears that for our purposes it is very reasonable to assume that the lift coefficient for a single pair of rectangular flaps is

$$C_L = .5\ \pi\ A\ \alpha \tag{5.38}$$

and our results will certainly be valid to within a factor of two on C_L.

5.3.2. Required Flap Rate:

With the above information, we can determine the relationships between flap size, flap rate, and the desired damping. For a given degree of damping, the damping force is

$$F_D = m\ \beta\ \dot{z} \tag{5.39}$$

and the flaps must exert this vertical force so that (with n flaps)

$$\frac{m\beta\dot{z}}{n} = \left(\frac{1}{2}\ \rho v^2\right)\ x\ S\ x\ (.5\pi)\ A\ \alpha \tag{5.40}$$

or

$$\alpha = \frac{m\beta\dot{z}}{nq(.5)\pi\ \ b^2} \tag{5.41}$$

and the flap rate required is thus (rms)

$$\dot{\alpha}_{rms} = \left(\frac{m\beta}{.5\ \pi\ qb^2n}\right)\ \dot{z}_{rms}\ . \tag{5.42}$$

Since $\beta = 2\ \delta\omega_o$, and $m = w/g$

$$\dot{\alpha}_{rms} = \left(\frac{4w\delta\omega_o}{n\pi qb^2}\right)\ \frac{\ddot{z}_{rms}}{g}\ . \tag{5.43}$$

We already have computed $\ddot{z}_{rms}/g$ for various values of δ. Thus we can compute $\dot{\alpha}_{rms}$ for various flap sizes.

$$\dot{\alpha}_{rms} = \frac{4 \times 10^5\ lb\ \delta\omega_o}{4\ \pi\ (225\ lb/ft^2) \times b^2}\ \ (\ddot{z}_{rms}/g) \tag{5.44}$$

for a 1 m × 3 m coil at .3 m height $\omega_0 = 7.38$ r/sec

$$\dot{\alpha}_{rms} = \frac{1.04 \times 10^3 \, \delta}{b^2} \left(\ddot{z}_{rms}/g\right) \tag{5.45}$$

TABLE 5.1. Required Flap Rates for Aerodynamic Damping

b	α_{rms}	δ
3 ft	.9 r/sec (51.5°/sec)	.707
5 ft	.32 r/sec (18.3°/sec)	.707
3 ft	1.27 r/sec (65.5°/sec)	1.0
5 ft	.453 r/sec (25.8°/sec)	1.0

(δ = .707 → .011 g.rms)

Thus it appears that flaps of the order of 25 ft^2 per pair would be needed to obtain the required damping. (See Table 5.1) Certainly the peak to peak swing of $\pm$ 73°/sec of the 1.5 ft x 3 ft flaps would be unreasonable to expect and the analysis is probably not valid for such large deviations in the angle of attack. However, the swing of $\pm$ 26°/sec of the 2.5 ft x 5 ft. flaps at .707 = δ would perhaps be reasonable. The only way to use smaller flaps would be to use more of them.

There seem to be some definite disadvantages to using flaps to obtain damping,

(1) The flap effectiveness decreases drastically with speed. Since the flap rate varies as $\frac{1}{v^2}$ and $\ddot{z}_{rms}$ as $\sqrt{v}$, the flap rate required would be $(2)^{3/2}$ times greater at 150 mph, for example.

(2) Flaps of the order of 2.5 ft x 5 ft would be required on all four corners of the vehicle. This could cause clearance problems.

(3) Flaps could not be used in partially evacuated tubes which might be required for future operation of the system at higher speeds.

(4) The operation of the flaps in tunnels is probably very questionable.

(5) The vehicle would probably be more susceptible to disturbances caused by wind gusts if it had such flaps.

It thus appears that while the use of flaps for damping of the vertical motion would be feasible with large enough flaps (2.5 ft x 5 ft) there would seem to be little incentive to use them. Similar conclusions have been reached by AVCO.[37]

6. VEHICLE DYNAMICS AND RIDE QUALITY

6.1. Dynamics of Various Guideways

The dynamics of a magnetically levitated vehicle in various guideways of the type shown in Figure 6.1 were discussed in the final report[1] of Task I and in more detail in Wilkie[45]. However, an error has been discovered in the analysis relative to the inverted vee guideway in Wilkie where it was shown that the equilibrium obtained with the inverted vee guideway is stable. In fact, this is not the case and the equilibrium obtained with either an inverted vee or vee shaped guideway is unstable. Detailed analyses of these guideways as well as others appear in Auelmann and Schaefgen[46] and are summarized here because of the importance of these results.

Consider the case of a levitated vehicle riding above the inverted vee guideway as shown in Figure 6.2. To a first order, the vertical, longitudinal, and yaw motions of the vehicle are decoupled from the lateral motions of sway (y) and roll (α). The equations of motion describing the coupled sway and roll dynamics are[45,46]

$$\begin{bmatrix} \ddot{Y}_{CG} \\ \ddot{\alpha} \end{bmatrix} = \begin{bmatrix} A_{11} & A_{12} \\ A_{21} & A_{22} \end{bmatrix} \begin{bmatrix} Y_{CG} \\ \alpha \end{bmatrix} \tag{6.1}$$

where

$$A_{11} = \frac{4}{m} \cos^2 \Theta \, F_n^n$$

$$A_{12} = \frac{4}{m} F_n^n \cos \Theta \, (b \sin \Theta + c \cos \Theta)$$

$$A_{21} = \frac{4F_n^n}{I_{CG}} \cos \Theta \, (b \sin \Theta + c \cos \Theta)$$

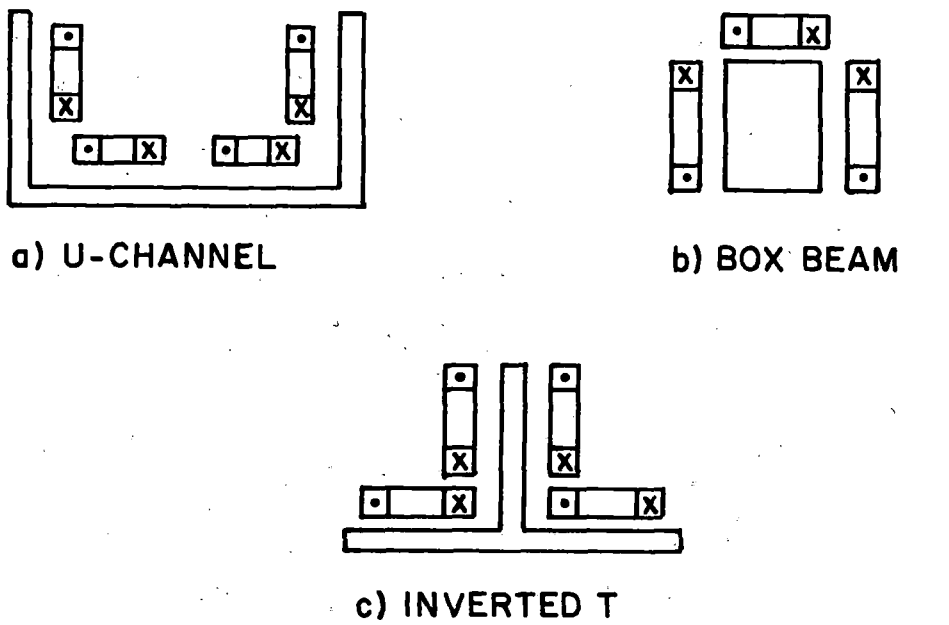

Fig. 6.1. Location of levitation-guidance magnets in various guideways.

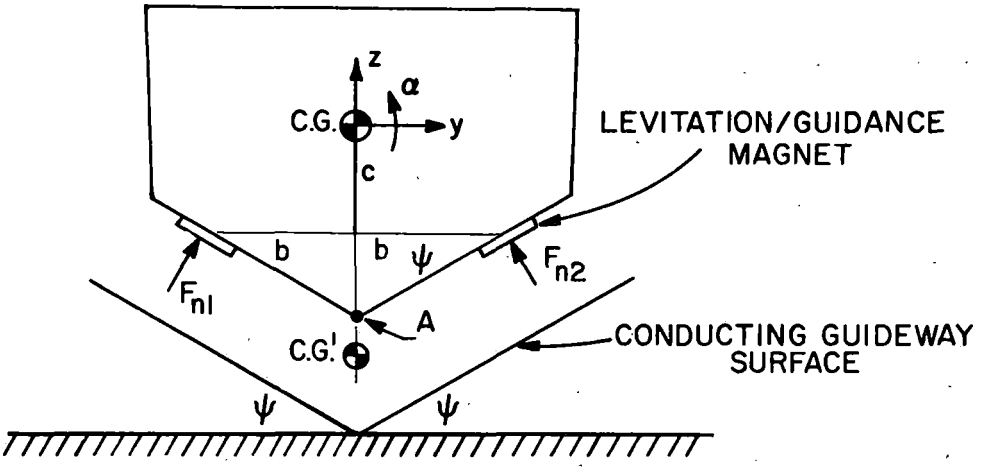

Fig. 6.3. Vehicle above vee guideway.

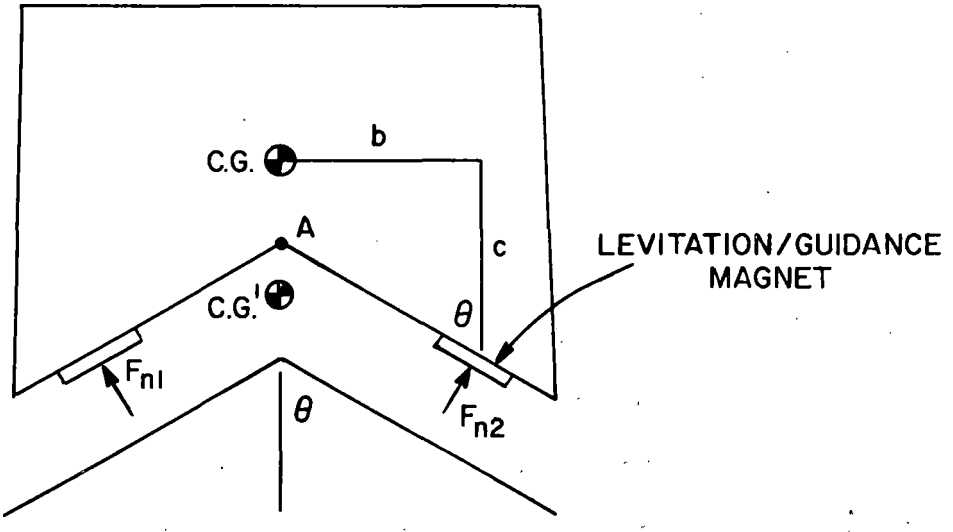

Fig. 6.2. Vehicle above inverted vee guideway

$$A_{22} = \frac{4F_n^n}{I_{CG}} (b \sin\theta + \cos\theta)^2 + \frac{Mg}{I_{CG}} (c - b \cot\theta)$$

I_{CG} = moment of inertia about roll axis

$$F_n^n = \frac{\partial F_n}{\partial n}, \quad n = \text{coordinate normal to track}$$

It is straightforward to show that a necessary condition that the roots of the characteristic equation of (6-1) all lie in the left half of the complex plane is that

$$b > c\tan\theta \tag{6.2}$$

which implies that the center of gravity must be below the point A at some point C.G.′ for stability. Otherwise any deviation from the equilibrium will lead to exponentially growing errors. (Note: The error in Wilkie[45] is the statement immediately following equation (47) which states that "for parameter values of interest, $S_{1,2}^2$ are always negative..." This statement resulted from an error in the analysis. In fact, for parameters of interest, $b > c \tan\theta$ and thus at least one value of $S_{1,2}^2$ is positive implying instability.)

Similar analysis of the vee shaped guideway leads to the condition for stability being[47]

$$-c > b \tan\psi \tag{6.3}$$

where c, b and ψ are defined in Figure 6.3.
This condition implies a location of the center of gravity below the point A at some point C.G.′ as shown in Figure 6.3.

For practical vehicle configurations and weights, the stability criteria of equations (6.2) and (6.3) imply that the vehicle would have to be suspended below the track and support magnets in monorail fashion. Thus,

the vee and inverted vee guideways without orthogonal guidance surfaces are not deemed desirable or practical.

A stable equilibrium can be achieved with a vee guideway by using interior side panels as shown in Figure 6.4. (Obviously, as the tilt angle $\psi \to 0$, the characteristics of this guideway approach those of the inverted T guideway.) This guideway has the desirable feature that both the bottom and side panels contribute lift and guidance. Furthermore, there are indications that this guideway, with $\psi \approx 20°$, provides a greater margin of stability in the roll-sway mode of the vehicle than does the inverted T, when the vehicle is controlled with just four control magnets.[46]

Each of the stable guideway configurations discussed here exhibit the somewhat undesirable characteristic that the vehicle will assume an adverse roll angle under a steady lateral load. For example, a steady load in the positive y direction in Figure 6.4 will lead to a negative equilibrium roll angle. This problem does not seem serious however since the equilibrium roll angle for a .1 g side load in either the u-channel, box beam, inverted T, or vee guideway with interior side panels are all about -1 degree.[46] This characteristic can be corrected by the control system.

The more extensive analyses that have been conducted on lateral dynamics using various guideway magnet configurations have indicated two important points regarding the use of active feedback control to obtain good ride quality.[45] First, while the simple independent magnet control philosophy discussed in Wilkie[45] is appealing because of its simplicity and ease of implementation, it may not be the most desirable in terms of the overall dynamic response of the vehicle. Second, independent guidance control is not necessary to achieve damping of all vehicle response modes;

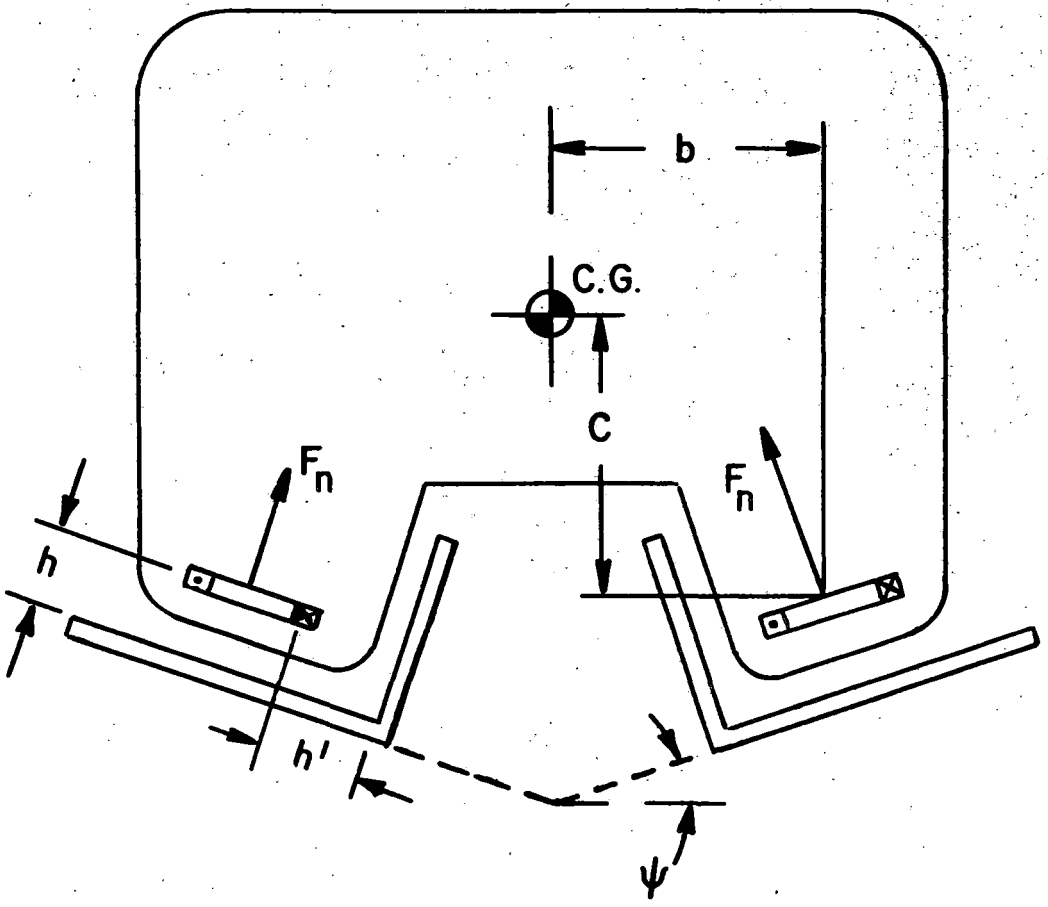

Fig. 6.4. Vehicle above canted inverted T guideway

this can be achieved in any of the stable guideway configurations discussed above with four levitation magnets and four control magnets per vehicle. This is particularly true if signal mixing is allowed in the feedback control of the control magnet currents. However, we feel that no one guideway, magnet, and control philosophy combination is clearly superior to any other at this time.

6.2. Ride Quality

6.2.1. Track Roughness

Ride quality analyses in the Task I Final Report were based upon determining the vertical acceleration power spectral density (psd) resulting from the guideway roughness power spectral density. Recall that the guideway roughness power spectral density is defined by the relationship

$$\overline{z_g^2} = \int_{\Omega_1}^{\infty} \Phi\ (\Omega)\ d\Omega \qquad (6.4)$$

where

Ω = wave number = ω/v

z_g^2 = mean squared amplitude of the guideway irregularity

Ω_1 = lower limit on the wave number spectrum,

and recall also that it has been found experimentally that most roadbeds and surfaces can be characterized by a power spectral density of the form[45, 47-49]

$$\Phi\ (\Omega) = A/\Omega^2 \quad , \qquad (6.5)$$

where A is called the statistical roughness parameter. A value of 5×10^{-6} ft. (1.5×10^{-6} m) for A is often used as a standard.

There is considerable disparity as to what value of A corresponds to different surfaces. For example, the value for airport runways[47-49] can be found in various sources to vary between 2×10^{-7} ft and 2×10^{-5} ft

(6×10^{-8} m to 6×10^{-6} m) while the value for highways is given in the range 10^{-5} to 8×10^{-5} ft (3×10^{-6} m to 24×10^{-6} m).

Another measure of guideway roughness is the mean squared mid-chord offset[50] defined by

$$< \delta^2 > = < \{ \frac{1}{2} [z_g (x + L/2) + z_g (x - L/2)] - z_g (x) \}^2 > \qquad (6.6)$$

which is obviously a function of the value of L. It can be shown that the mean squared mid chord offset for a guideway with the power spectral density of (6.5) is given by

$$< \delta^2 > = \frac{\pi A L}{4} . \qquad (6.7)$$

A value for $< \delta^2 >$ using measured data on the roughness of the linear induction motor reaction rail at the Pueblo test track has been calculated[50] and the corresponding value for A determined from (6.7) has been found to be 1.5×10^{-6} ft. However, the data did indicate some discrepancy from the A/Ω^2 model for the roughness psd at the long wavelengths.

Thus a value for A of 5×10^{-6} ft. seems to be a very reasonable standard for comparison.

6.2.2. Ride Quality Index

The form of the vertical acceleration power spectral density resulting from the track roughness depends on the means of damping used, eg. passive damping or feedback control of the magnet current, and on the natural frequency of the linearized magnet force law. The expressions for the vertical acceleration psd, $P_{zz}^{\cdots}(f)$, for various control schemes and damping mechanisms are given in the Task I Final Report[1] and in Wilkie[45].

Previous analyses of ride quality have been based upon comparing the power spectral density $P_{zz}^{\cdots}(f)$ calculated for a given control scheme or damping mechanism with the Urban TACV specification (Fig. 6.5). According to

$P_{\ddot{z}\ddot{z}}(f)$ (g^2/Hz)
5×10^{-4}
10^{-4}
5×10^{-5}
10^{-5}
5×10^{-6}
2×10^{-6}
.1

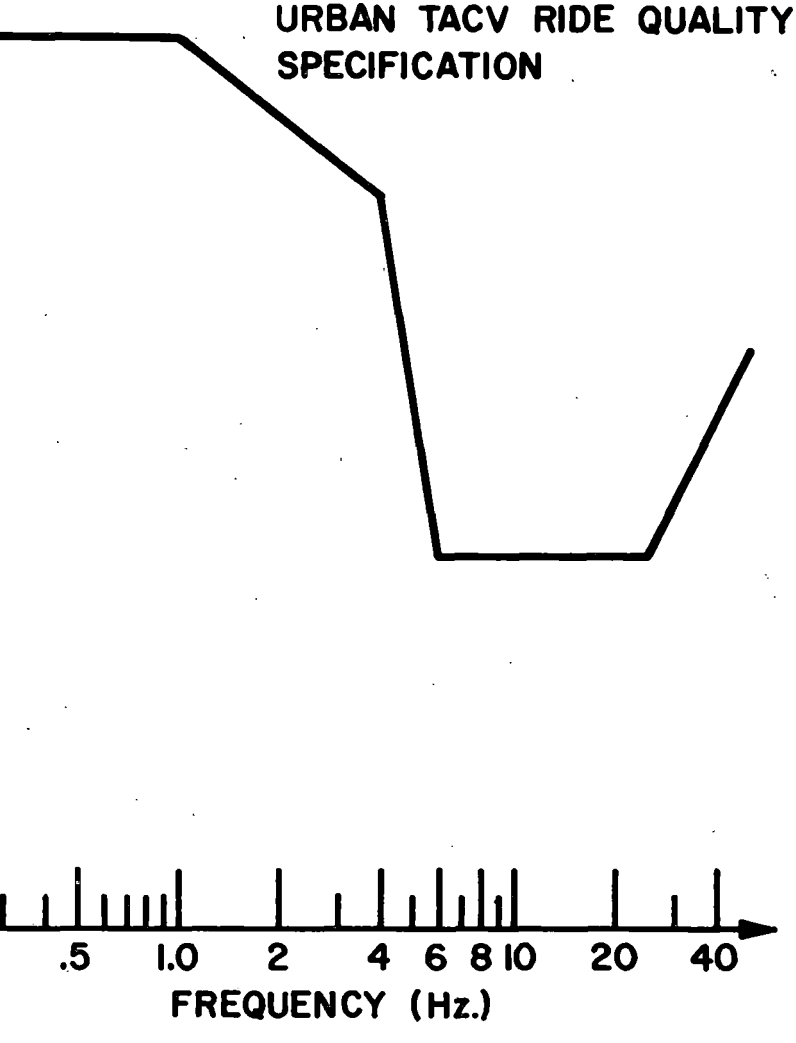

Fig. 6.5. Urban TACV ride quality specification.

this specification, $P_{zz}^{\cdots}(f)$ must be below a certain frequency-dependent limit at each frequency f for the ride to be considered good. Since the specification presumably came from measurements on rail cars having a (qualitatively judged) good ride, it is clear that any vehicle which meets the Urban TACV standards will also have a good ride. It is not clear, however, that a vehicle which exceeds the Urban TACV limit in one range of frequency, but is below it in all others, will have a poor ride. In fact, it may have a better ride. For example, suppose a vehicle underwent a sinusoidal variation at a single frequency f_o, then $P_{zz}^{\cdots}(f)$ would be an infinite spike at f_o (i.e., $P_{zz}^{\cdots}(f) \propto \delta\ (f-f_o)$, $\delta(x)$ = Dirac delta function). Clearly this exceeds the Urban TACV specification. However, if the amplitude of the variation is small enough that the peak acceleration does not exceed the ride quality standard for vertical acceleration at a single frequency (Fig. 6.6, known as the Janeway Criteria, also see reference 51) the ride should be good. Hence there should be a better method of determining ride quality than a point by point comparison of the vertical acceleration psd with the Urban TACV specification.

We believe that a better method of analyzing ride quality would be one like that developed by Butkunas[52] to evaluate the ride quality of automobiles which is very similar to an approach developed by Lee and Pradco[53] from their experimental studies of human vibration tolerance. In this approach, an index of ride quality is defined as the square root of the integral of the vertical acceleration psd multiplied by a frequency dependent weighting function, T(f). This weighting function corresponds to the human transfer function and reflects the variable sensitivity of the human to vibration as a function of frequency.

There are several possibilities for the form of T(f), but the simplest is

$$T(f) = 2/\ a^2_{max}(f) \tag{6.8}$$

where $a_{max}(f)$ is the maximum allowable acceleration at a single frequency f (Fig. 6.6 - the Janeway Criteria):

$$\begin{aligned} a_{max}(f) &= a/f \quad , && 1 < f < 6 \text{ Hz} \\ &= b \quad , && 6 \text{ Hz} < f << 20 \text{ Hz} \\ &= cf \quad . && 20 \text{ Hz} < f < 60 \text{ Hz} \end{aligned} \tag{6.9}$$

The factor of 2 appears in (6.8) because the Janeway Criterion refers to peak amplitude whereas the integral of a psd yields an rms value.

If $a_{max}(f)$ is measured in g's, then

$$\begin{aligned} a &= 0.204 \\ b &= 0.034 \\ c &= 1.7 \times 10^{-3} \quad . \end{aligned} \tag{6.10}$$

We take the range 0.2 to 50 Hz to be the range of integration so that

$$\begin{aligned} (DI)^2 &= \int df\ P_{zz}(f)\ T(f) \\ &= 2 \int_{0.2}^{50} df\ P_{zz}(f)/a^2_{max}(f) \quad . \end{aligned} \tag{6.11}$$

If $a_{max}(f)$ is in units of g's, then $P_{zz}(f)$ is in units of g^2/Hz.

Consider a simple example of a vehicle undergoing a sinusoidal vibration at frequency f_o with peak amplitude $a_{max}(f_o)$. Then

$$P_{zz}(f) = \frac{a^2_{max}}{2}(f_o)\ \delta(f-f_o) \quad . \tag{6.12}$$

The discomfort index is then

$$DI = 1. \tag{6.13}$$

The discomfort index corresponding to the weighted integral of the Urban TACV specification between 0.2 and 50 Hz is DI = 1.43. This means

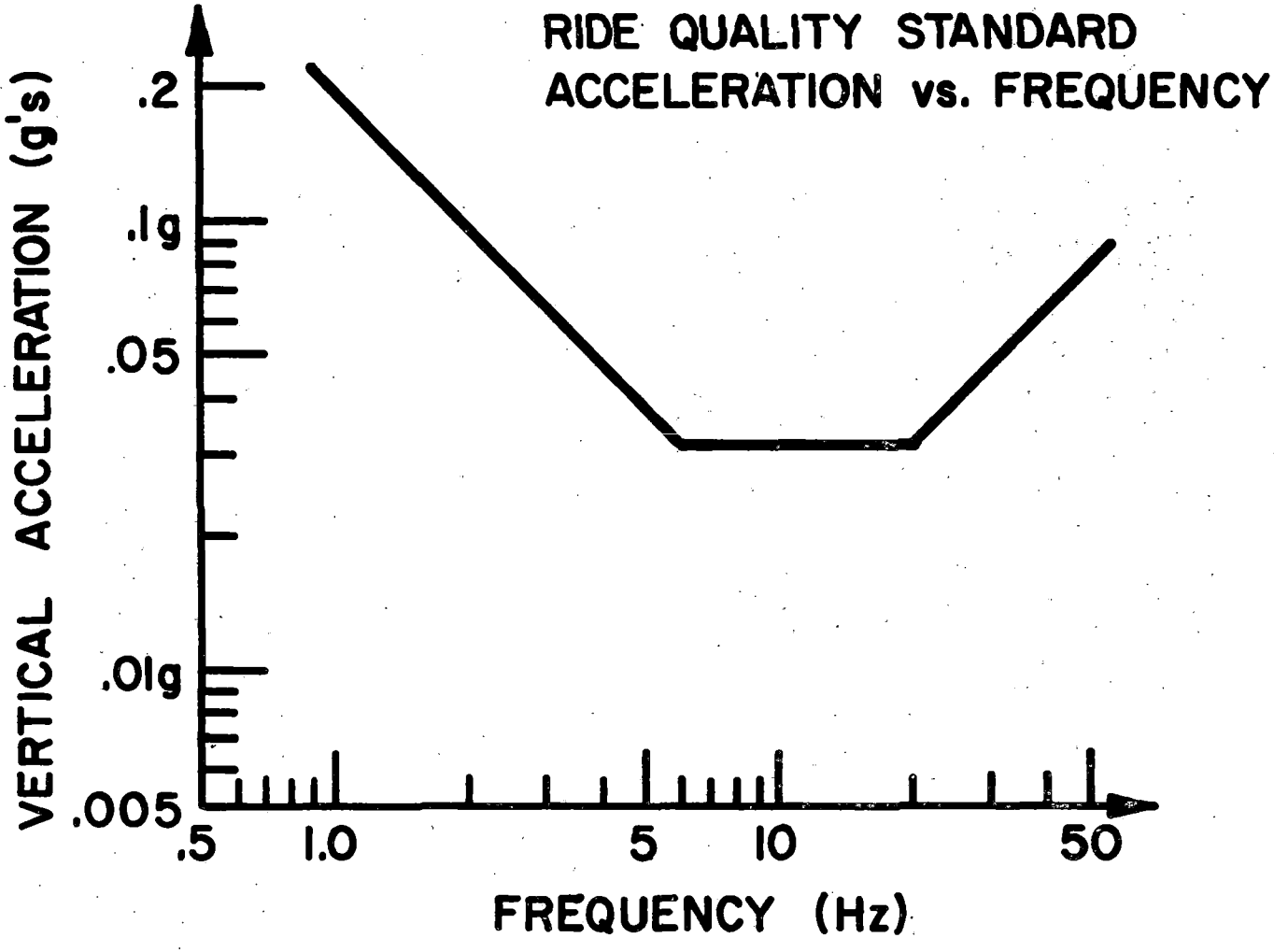

Fig. 6.6. Single frequency ride quality specification.

that the vertical acceleration psd which is known to correspond to a good ride gives a low discomfort index, which lends credibility to the proposed index.

The discomfort index corresponding to the various vertical acceleration PSD's that can be obtained using passive damping, active control, etc. have been calculated. The results for copper plate and tuned coil passive damping are shown in Figure 6.7. The discomfort indices for both cases are seen to be greater than the value 1.43 which corresponds to the URBAN TACV specification, indicating that the rides are worse. However, based on the discomfort index, the ride quality obtained using passive damping appears closer to being acceptable than might be inferred by direct comparison of the obtained vertical acceleration psd with the urban TACV specification.

Similarly, the discomfort indices were calculated for two cases of relative position/absolute velocity feedback control and are shown in Fig. 6.8. We note that the values are quite low (.15 - .19) compared to the Urban TACV. Since DI $\propto\sqrt{A}$, an increase by a factor of 100 in A would still give an acceptable ride for $\delta = 1/\omega_o\tau = 2.68$ although the control currents, required clearance, etc., would go up by a factor of 10.

Standards other than that of Janeway have been given for human vibration tolerances, and these standards might also be used in choosing T(f) for a ride index. Thus, it is instructive to compare the various criteria to determine if the weighting function T(f) in (6.11) would be significantly different if standards other than Janeway's were used.

Four different standards are shown in Figure 6.9. A discussion of each of the three standards other than Janeway's follows.

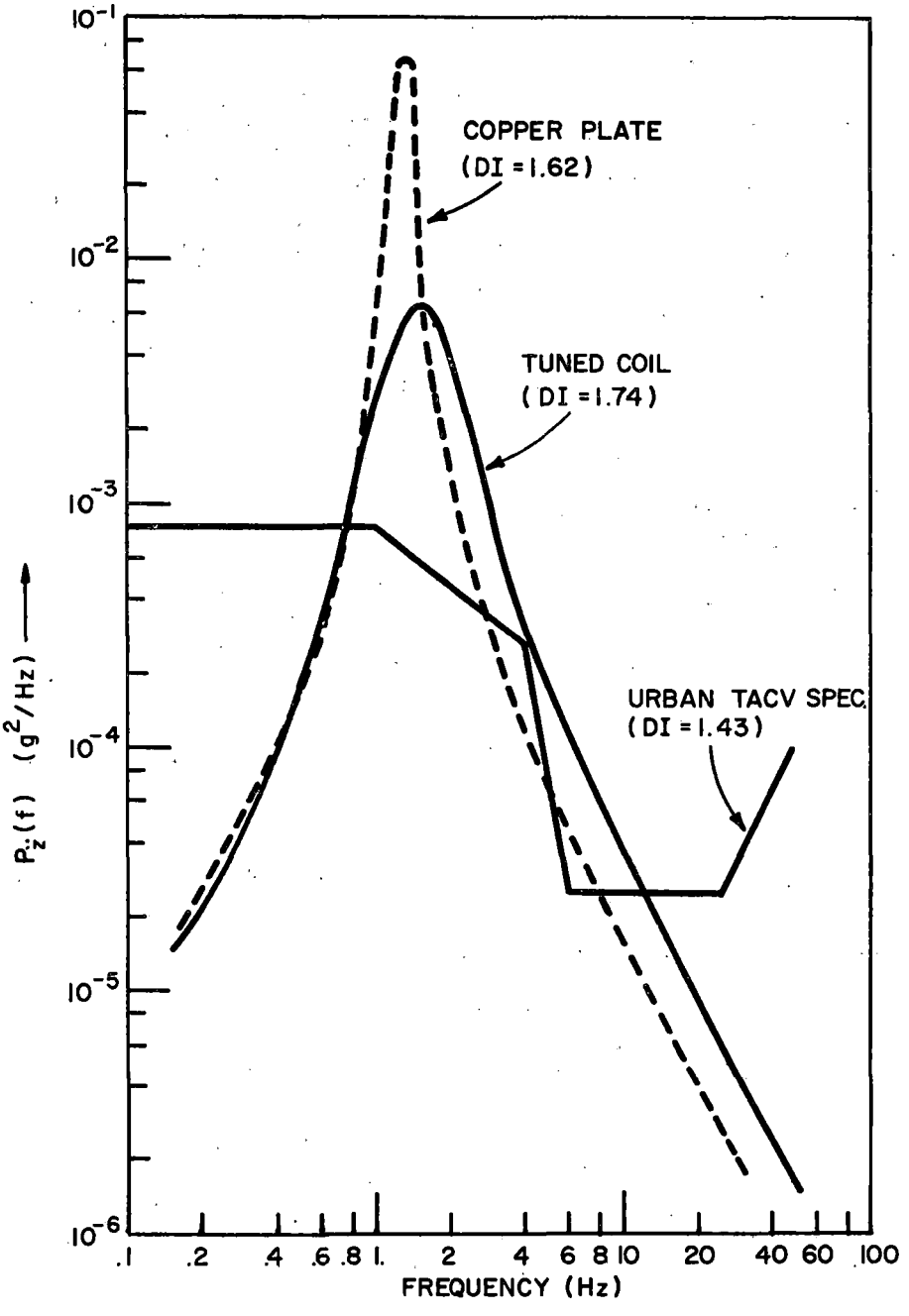

Fig. 6.7. Vertical acceleration psd for a vehicle with passive damping. v = 300 mi/h. A = 5 x 10^{-6} ft.

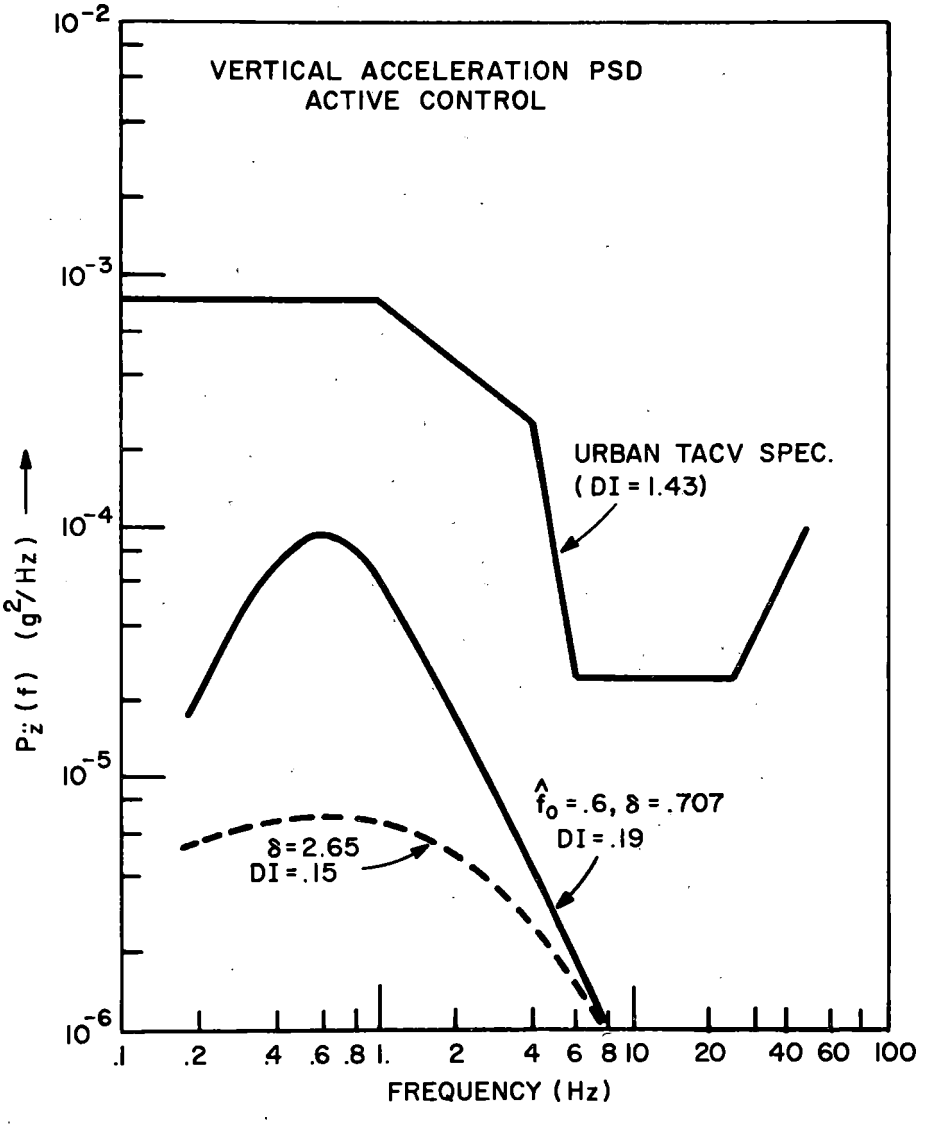

Fig. 6.8. Vertical acceleration psd for a vehicle with relative positive/absolute velocity feedback control. A = 5 x 10^{-6} ft, v = 300 mi/h.

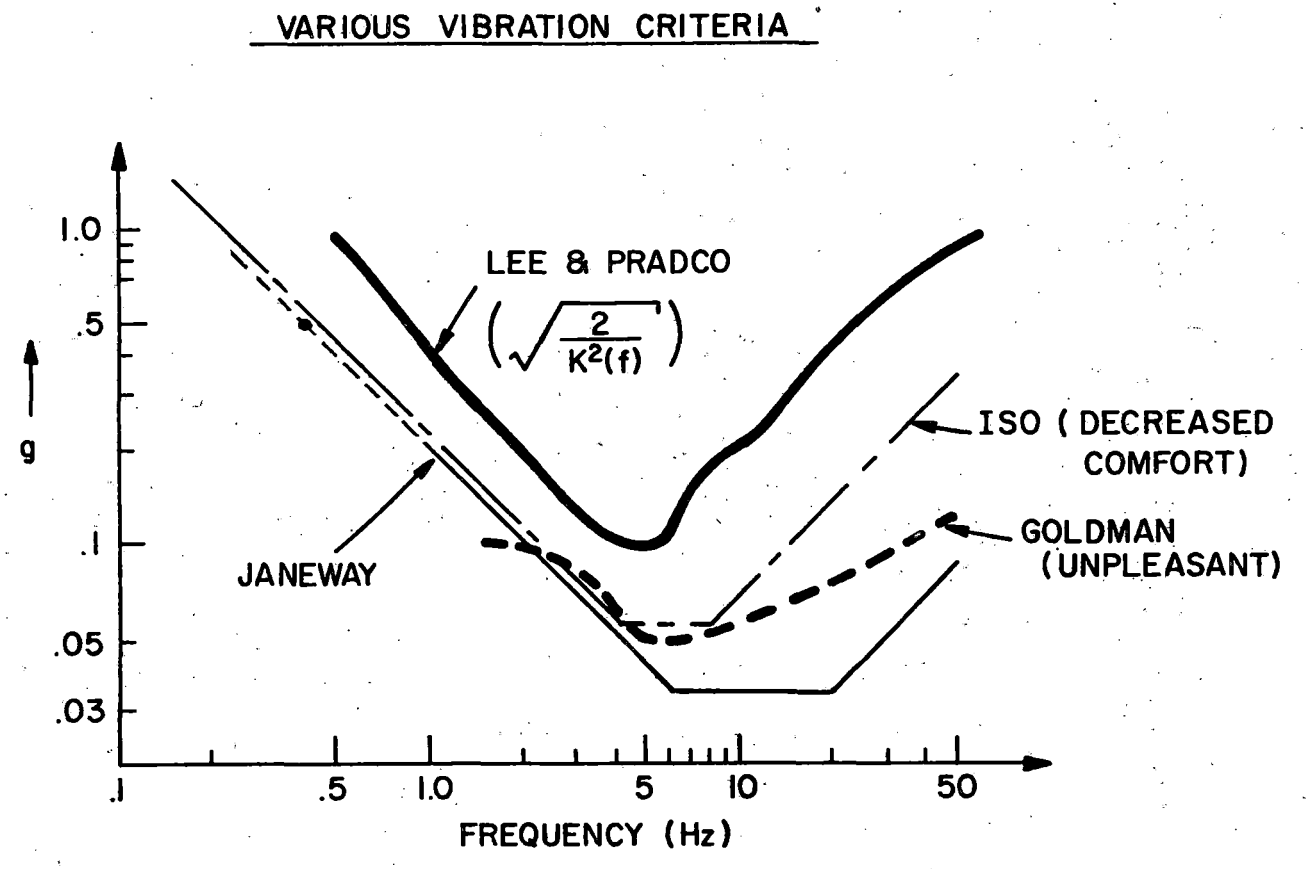

Fig. 6.9. Several different ride quality standards.

Goldman Standard

This standard is given in the "Shock and Vibration Handbook", McGraw Hill. The contour shown corresponds to the equal sensation contour denoted as unpleasant by Goldman. Butkunas[52] has used Goldman's Standard to determine T(f) in analyzing automobile ride quality. (Note that this standard is only valid down to 1.5 Hz.)

ISO Standard

This standard is referenced in "Active Vibration Isolation for Aircraft Seating" by Peter C. Calcaterra, Sound and Vibration, March, 1972, and corresponds to reduced comfort. ISO refers to the International Standards Organization and the reference for this standard is given by Calcaterra as "Equal Annoyance Contours for the Effect of Sinusoidal Vibration on Man", C. Ashley, Shock and Vibration Bulletin, No. 41 (Part 2), December, 1970, pp. 13-20.

Lee and Pradco

Lee and Pradco[53] have determined experimentally that ride quality is proportional to the power absorbed by a human. Furthermore, they determinted experimentally that the absorbed power in the vertical direction in a band of frequencies $f_1 < f < f_2$ is

$$P_{abs} = \int_{f_1}^{f_2} K(f) P_{zz}(f) df \qquad (6.14)$$

and a numerical fit for K(f) was made and is given in the above referenced paper. In order to compare with the other ride standards, $(2/K(f))^{1/2}$ is plotted in Figure 6.9.

Observations

It is seen that the Janeway standard is the most stringent of those

given. Furthermore, the various standards differ most in the region above 6 Hz, where the amplitude of the power spectral density for the ride of a magnetically levitated vehicle is typically quite small. Thus, our proposed ride index appears to be a conservative one when compared with other standards that have been used.

It should also be noted that the Lee-Pradco results were obtained for random vibrations, whereas the other curves apply to sinusoidal vibrations. Lee and Pradco noted that the human tolerance to random vibration is greater than to vibrations occurring at single frequencies.

One uncertainty which remains in the ride quality analysis results from the possibilities of motion sickness. Lee and Butkunas both noted that oscillations around 0.5 Hz can produce motion sickness and that experimental results to date have probably not considered this effect sufficiently.

We conclude that if the discomfort index is meaningful, then our previous judgments concerning ride quality based upon the Urban TACV specification may have been too stringent. Since we are dealing with power spectra which are peaked near a single resonant frequency in place of being rather broad band (as the test vehicle which gave rise to the Urban TACV apparently was), the discomfort index approach which is intimately connected with the Janeway Criteria should be better. Unfortunately, it has not been demonstrated experimentally that two vehicles with widely different power spectral densities but identical discomfort indices do in fact give equally good rides. We expect to perform experiments to determine this information in the near future.

6.3. Ride Quality with a Secondary Suspension

It is seen from our previous results[1,45] that very good ride quality can be achieved over quite rough tracks when active control of the magnet

currents (or the current in separate control coils) is used. Another alternative to achieving a good ride might be to use a secondary suspension in conjunction with a primary suspension consisting of magnets with passive damping. In order to study this alternative, the one degree of freedom motion of the mass-spring-damper shown in Figure 6.10 was investigated. The spring and damper k_2 and D_2 would be equivalent to those obtained by the linearized magnet force law and copper plate damper.

The power spectral densities for the accelerations $\ddot{z}_1$ and $\ddot{z}_2$ were obtained for various parameter combinations k_1, k_2, D_1 and D_2, and assuming the track roughness power spectral density is given by A/Ω^2 as in our previous work. The passive damping means used to obtain these results is the copper plate damping described in the final report[1] of Task I, Appendix F. The damping due to the eddy current losses in the copper plate is frequency dependent and is optimized for a given natural frequency of the coil.

The vertical acceleration power spectral density for both the magnets and passenger compartment for one set of suspension parameters and weight distribution between the primary suspended mass (magnets) and secondary mass (passenger compartment) is shown in Fig. 6.11. There are many possible combinations of suspension parameters, but the resulting responses have the same characteristics as those shown in Fig. 6.11, with a low frequency peak (0.4 - 0.6 Hz) due to the secondary suspension and a high frequency peak (6-10 Hz) due to the primary suspension. It is apparent that an acceptable ride can thus be achieved using passive damping and a secondary suspension even with a low mass ratio of $m_1/m_2 = 3$ Such a mass ratio would correspond to having a primary mass consisting of

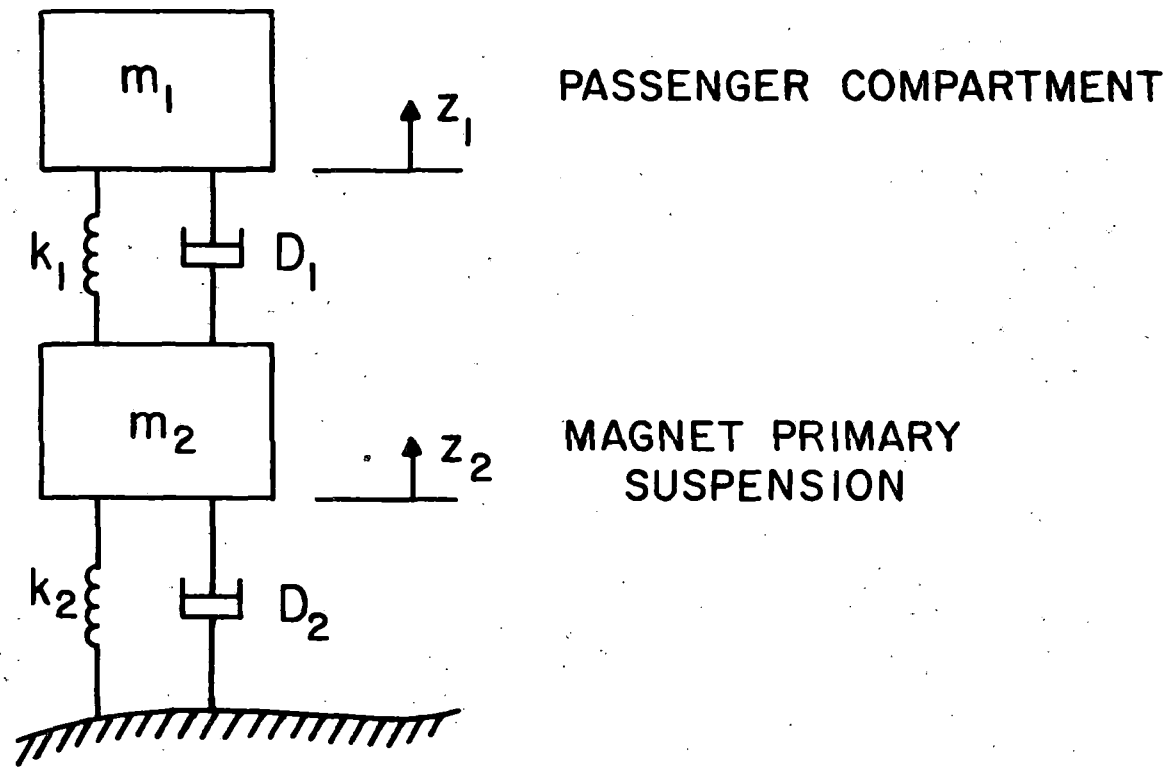

Fig. 6.10. Model of vehicle with a secondary suspension.

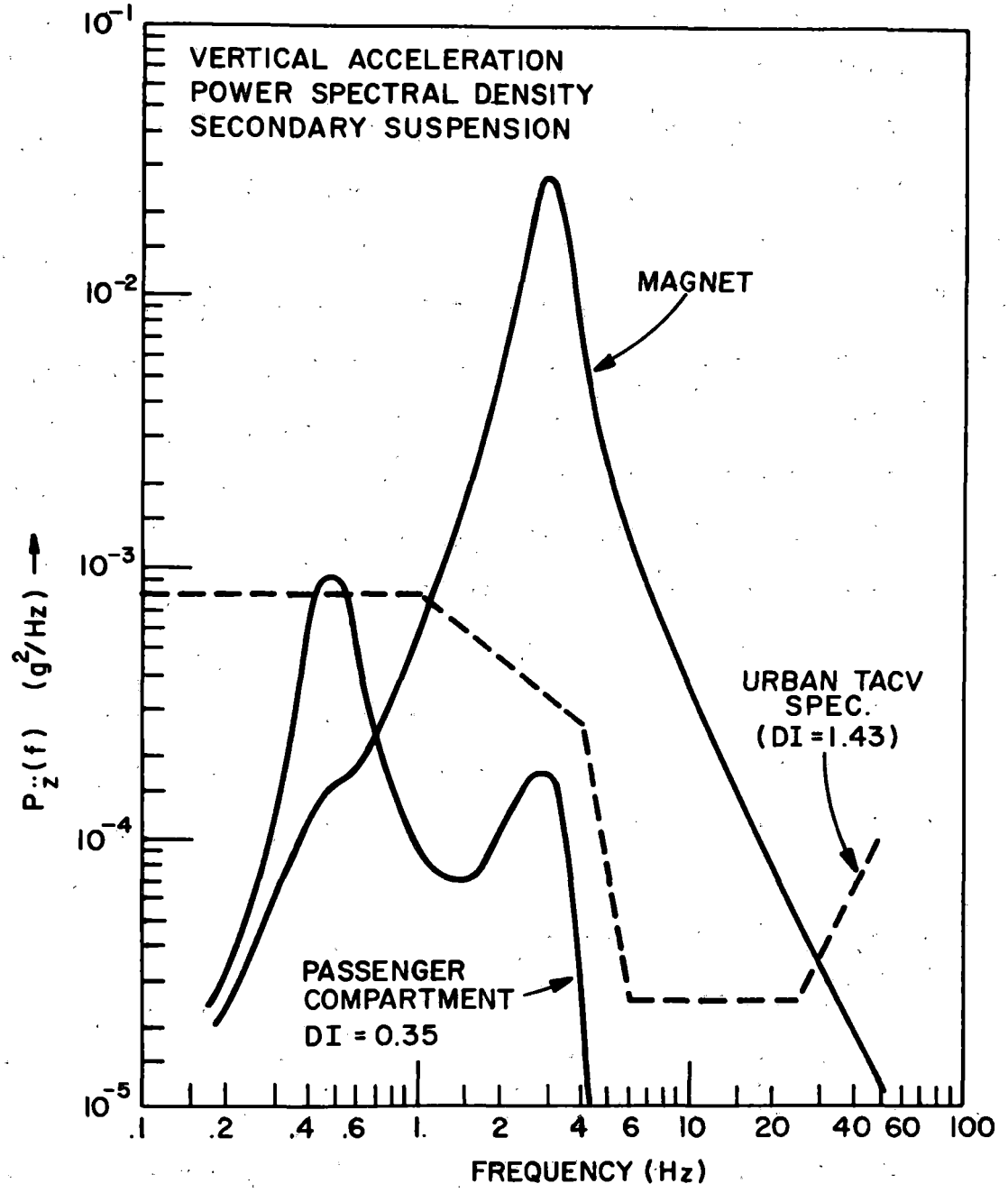

Fig. 6.11. Vertical acceleration psd for a vehicle with a secondary suspension. $m_1/m_2 = 3$, $k_1/k_2 = 0.1$, $D_1/D_2 = 0.1$. A + 5 x 10^{-6} ft, v = 300 mi/h.

the suspension magnets and the thrust elements of a 10,000 Hp linear induction motor. Furthermore, based on the discomfort index, a track 4 times rougher (A coefficient 16 times larger) should be tolerable. However, the response peaks at about 0.4 and 5 Hz would considerably exceed the Urban TACV specification for such a track.

Two important things should be noted about these results. First, the natural frequency corresponding to the secondary suspension (about 0.4 Hz) is unrealistically low when one considers the practical problem of building such a suspension with purely passive mechanical elements. Thus, either this frequency must be raised (which will degrade ride quality) or an active secondary suspension will be required. Second, even over the smooth track the magnets are subjected to rms accelerations of about 0.35 g with a considerable portion of the vibration energy near 3 Hz. Such operation will cause substantial ac loss in magnets wound with multicore wire (see Table A2), but the calculated loss with single-core wire is modest.

The complexity added by a secondary suspension, particularly an active one, is probably not justified when compared with the case of active control using separate control coils, and we do not recommend this approach.

6.4. Dynamics of Vehicle Including Pitch

All ride quality analyses made thus far[1,45] have considered the vehicle as a point mass and studied the single degree of freedom vertical motion. The yaw[1] and longitudinal[45] motion of a more realistic vehicle have been analyzed to determine stability and their fundamental characteristics, but the response at different points in a vehicle subjected to random guideway roughness have not been determined. In this section we

discuss the dynamics of a vehicle which is free to pitch as well as experience vertical translational motion.

Consider the vehicle as indicated in Figure 6.12 traveling with velocity v in the direction shown over a track with random deviations from a nominal smooth profile. The random track roughness at the forward and aft magnets is indicated by η_1 and η_2, respectively, as in Fig. 6.12. The vertical coordinates of the magnet mid-points with respect to the fixed reference are z_1 and z_2. There is an obvious relationship between the front and aft track deviations given by

$$\eta_1(t) = \eta_2(t - 2B/v) = \eta_2(t - T_D) \ , \tag{6.15}$$

where T_D is the vehicle transit time, and thus the Fourier transforms of $\eta_1(t)$ and $\eta_2(t)$ are related by

$$H_1(j\omega) = e^{-j\omega T_D} \ H_2(j\omega) \ . \tag{6.16}$$

This is the key relationship to recognize so that the pitch motion of a vehicle subjected to random track roughness can be analyzed. Assuming now that the translations and rotations are relatively small, we can make a linearized analysis of the motion of the vehicle. We assume copper plate damping is used, the high speed limit applies, and for simplicity that there is one magnet at each end of the vehicle. Then the lift force at the magnet i is given approximately by

$$F_{L_i} = \frac{Mg}{2} - \frac{M\beta}{2}(\dot{z}_i - \dot{\eta}_i) - \frac{M\omega_o^2}{2}(z_i - \eta_i - h) \tag{6.17}$$

Where z_i is the coordinate of the ith magnet, h is the nominal value of z_i, β is the damping coefficient due to copper plate damping, and ω_o^2 is the natural frequency of the magnet motion. The ratio of the lift and drag forces at the ith magnet is

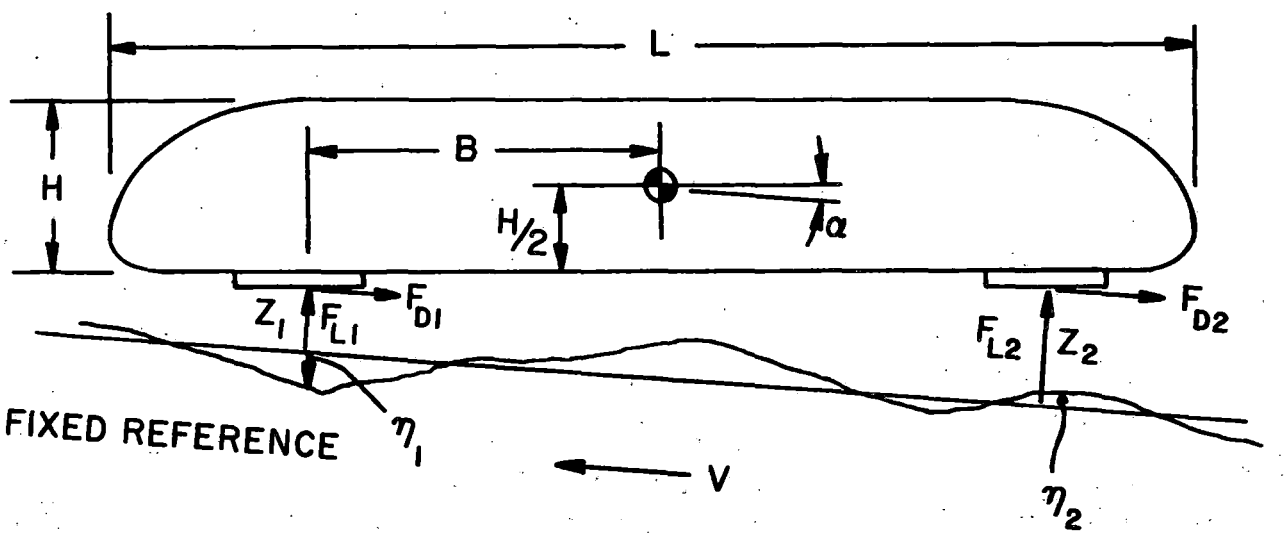

Fig. 6.12. Vehicle undergoing pitch oscillations.

$$F_{L_i}/F_{D_i} = v/w \geq 50 \quad , \tag{6.18}$$

and therefore neglecting the rotational torques due to changes in the drag forces has a negligible effect on the results while simplifying the analysis. (We assume that the nominal pitch torque due to drag is canceled by the nominal pitch torque due to the propulsion system so that the equilibrium pitch angle α is zero.) With these assumptions, the equations of motion are found to be

$$\begin{aligned} &\ddot{z}_{CG} + \beta\dot{z}_{CG} + \omega_o^2 z_{CG} = \frac{\beta}{2}(\dot{\eta}_1 + \dot{\eta}_2) + \frac{\omega_o^2}{2}(\eta_1 + \eta_2) \\ &\alpha + \frac{MB^2}{I}\beta\dot{\alpha} + \left(\frac{\omega_o^2 mB^2}{I} - \frac{MgH}{2I}\right)\alpha = \frac{MB}{2I}\left[-\beta(\dot{\eta}_1-\dot{\eta}_2) - \omega_o^2(\eta_1-\eta_2)\right] \end{aligned} \tag{6.19}$$

where z_{CG} is the vertical deviation of the center of gravity from its normal position. Taking the Fourier Transform of (6.19) and recalling (6.16), the following transfer functions can be obtained,

$$\begin{aligned} T_{z_{CG}}(j\omega) &= \frac{F[z_{CG}(t)]}{H_1(j\omega)} \quad , \\ T_\alpha(j\omega) &= \frac{F[\alpha(t)]}{H_1(j\omega)} \quad . \end{aligned} \tag{6.20}$$

From these expressions, the power spectral density of the vertical accelerations and rotations are given by

$$\begin{aligned} P_{\ddot{z}_{CG}\ddot{z}_{CG}}(\omega) &= \omega^4 T_{z_{CG}}(j\omega)\, T_{z_{CG}}(-j\omega)\, P_{h_1h_1}(\omega) \quad , \\ P_{\alpha\alpha}(j\omega) &= T_\alpha(j\omega)\, T_\alpha(-j\omega)\, P_{h_1h_1}(j\omega) \quad . \end{aligned} \tag{6.21}$$

Assuming the usual form for the track roughness power spectral density[1,45] (see also Eq. (6.5)), we obtain from (6.21)

$$P_{\ddot{z}_{CG}\ddot{z}_{CG}}(\omega) = \frac{\omega^2(\omega_o^4 + \omega^2\beta^2)\, Av\, \cos^2(\omega T_D/2)}{[(\omega_o^2-\omega^2)^2 + \omega^2\beta^2]} \tag{6.22}$$

Comparison of this with the expressions given in the final report[1] of Task I and in Wilkie[45] show that the acceleration power spectrum obtained for the one degree of freedom point mass motion with relative velocity damping is simply the envelope for the expression in (6.22); the only difference is the factor $\cos^2(\omega T_D/2)$ which modulates the amplitude. However, in the present case with rotations considered, the vertical acceleration at different points in the vehicle will differ from those at the center of gravity. Thus, over the magnets,

$$\ddot{z}_1 = \ddot{z}_{CG} - B\ddot{\alpha} \qquad (6.23)$$

$$\ddot{z}_2 = \ddot{z}_{CG} + B\ddot{\alpha}$$

From these expressions, the vertical acceleration power spectral densities at the front and rear of the vehicle can be determined. These expressions, while straightforward to obtain, are quite complicated and are not included here. The vertical acceleration power spectra at the front, center and rear of a vehicle supported at the front and rear by magnets (0.5 m x 3 m at h = 0.3 m) and with copper plate damping which is frequency dependent (see Appendix F of Task I Final Report[1]) are shown in Figure 6.13. It is seen that the point mass PSD is the envelope for all three vertical acceleration PSD's with this type of damping. The rms accelerations and discomfort indices for the three PSD's are given in Table 6.1. Thus, the discomfort index at all three positions on the vehicle is less than that made by point mass calculations* and in fact the discomfort indices are seen to be quite a bit lower (DI $\approx$ 1) than that corresponding to the Urban TACV specification (DI = 1.43), even though the PSD exceeds the specification substantially at the natural frequency for each position. Thus, it appears we can still not rule out the possibility of using totally passive damping.

* See Fig. 6.7.

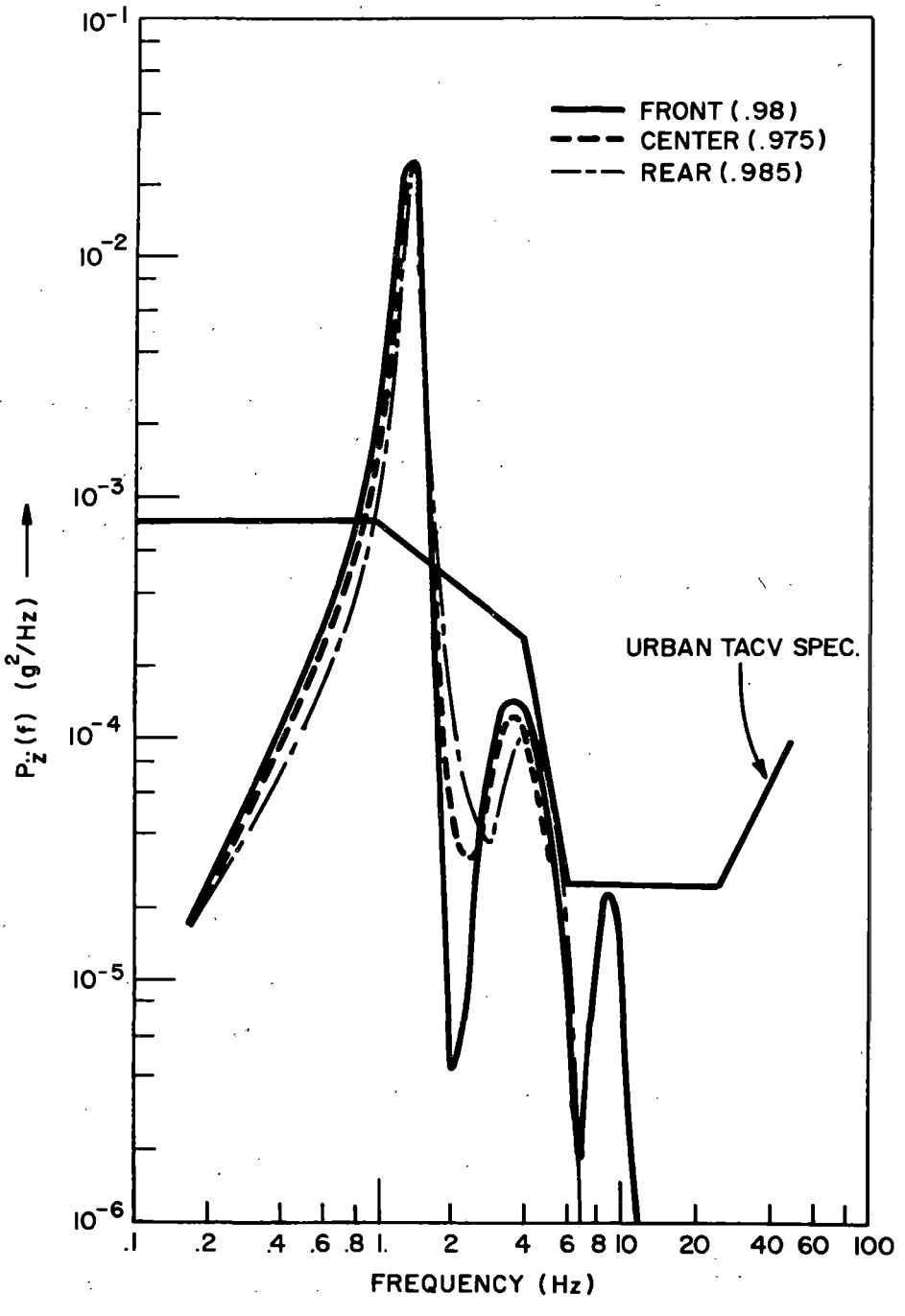

Fig. 6.13. Vertical acceleration psd for various positions in vehicle with passive (copper plate) damping. A = 5 x 10^{-6} ft, v = 300 mi/h.

TABLE 6.1. RMS Accelerations and Discomfort Indices with Passive Damping (Pitch Motion Included)

Position	RMS ACCEL (g's)	DI
Front	.0828	.98
Center	.0820	.975
Rear	.0822	.985

Similar analyses of the dynamics (including pitch) have been made by Schaefgen and Auelmann[46] for the case where feedback current control in control coils is used to give absolute velocity/relative position feedback control as discussed in Wilkie[45]. The analysis proceeds as discussed here except that the linearized force expression analogous to (6.17) would be

$$F_{L_i} = \frac{Mg}{2} - \frac{M\beta}{2}\dot{z}_i - \frac{M\hat{\omega}_o}{2}(z_i - \eta_i - h), \qquad (6.24)$$

where β is now the absolute velocity damping due to the feedback control and $\hat{\omega}_o$ is the adjusted heave natural frequency. The nominal point mass parameters that would result in $\hat{f}_o$ = 0.6 Hz and damping coefficient of 0.707 are used for comparison. The vertical acceleration PSD for the front of the vehicle is shown in Figure 6.14 and those for the center and rear are shown in Figure 6.15. In this case, the point mass results represent the envelope for the vertical acceleration of the center of gravity but not for the vertical acceleration at the front and rear of the vehicle. In fact, the front and rear accelerations have a lobe near 6 Hz which could be troublesome. However, the Urban TACV specification is still met at all points.

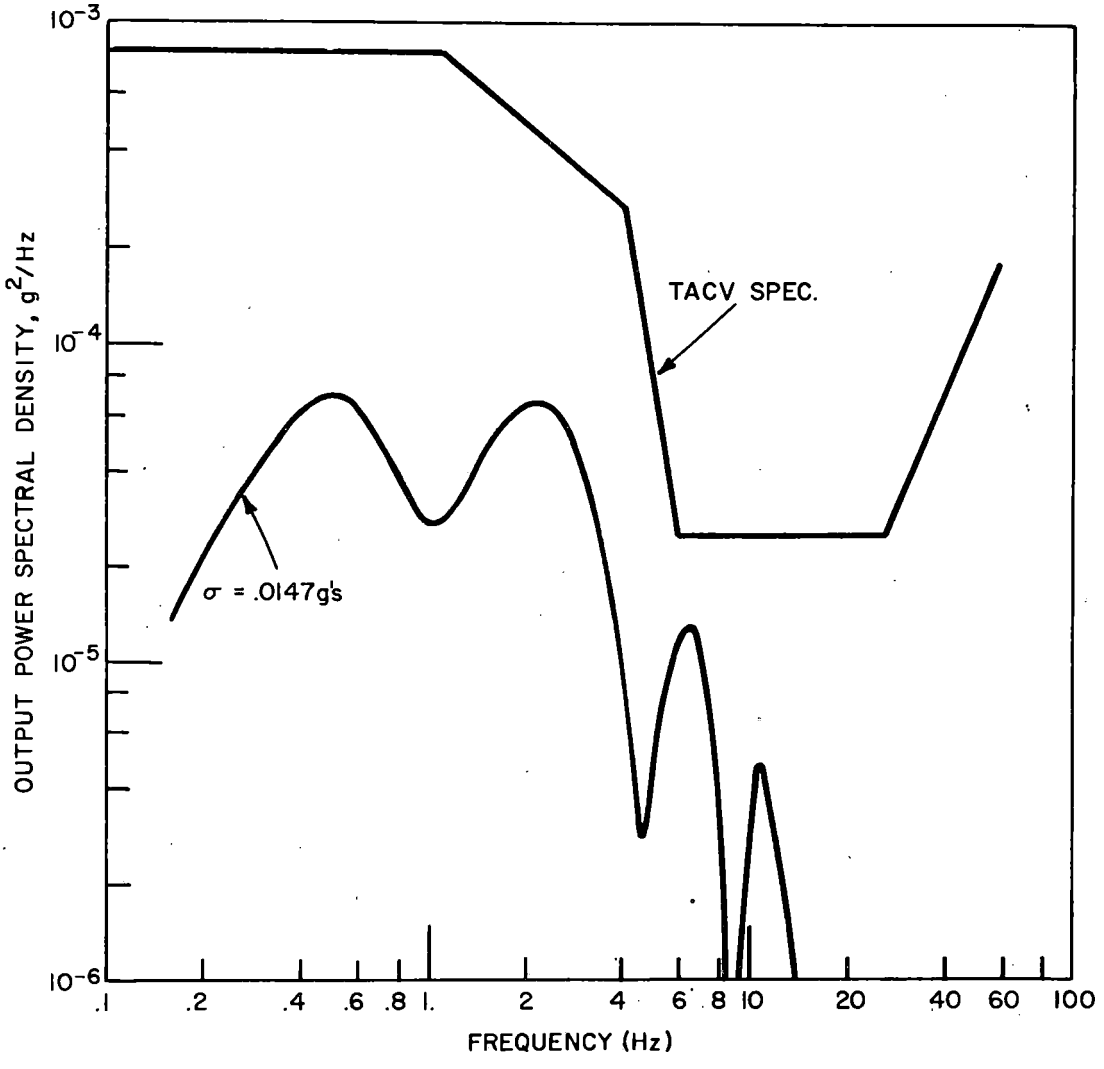

Fig. 6.14. Vertical acceleration psd for front end of vehicle for the case with feedback control. A = 5 x 10^{-6} ft, v = 300 mi/h.

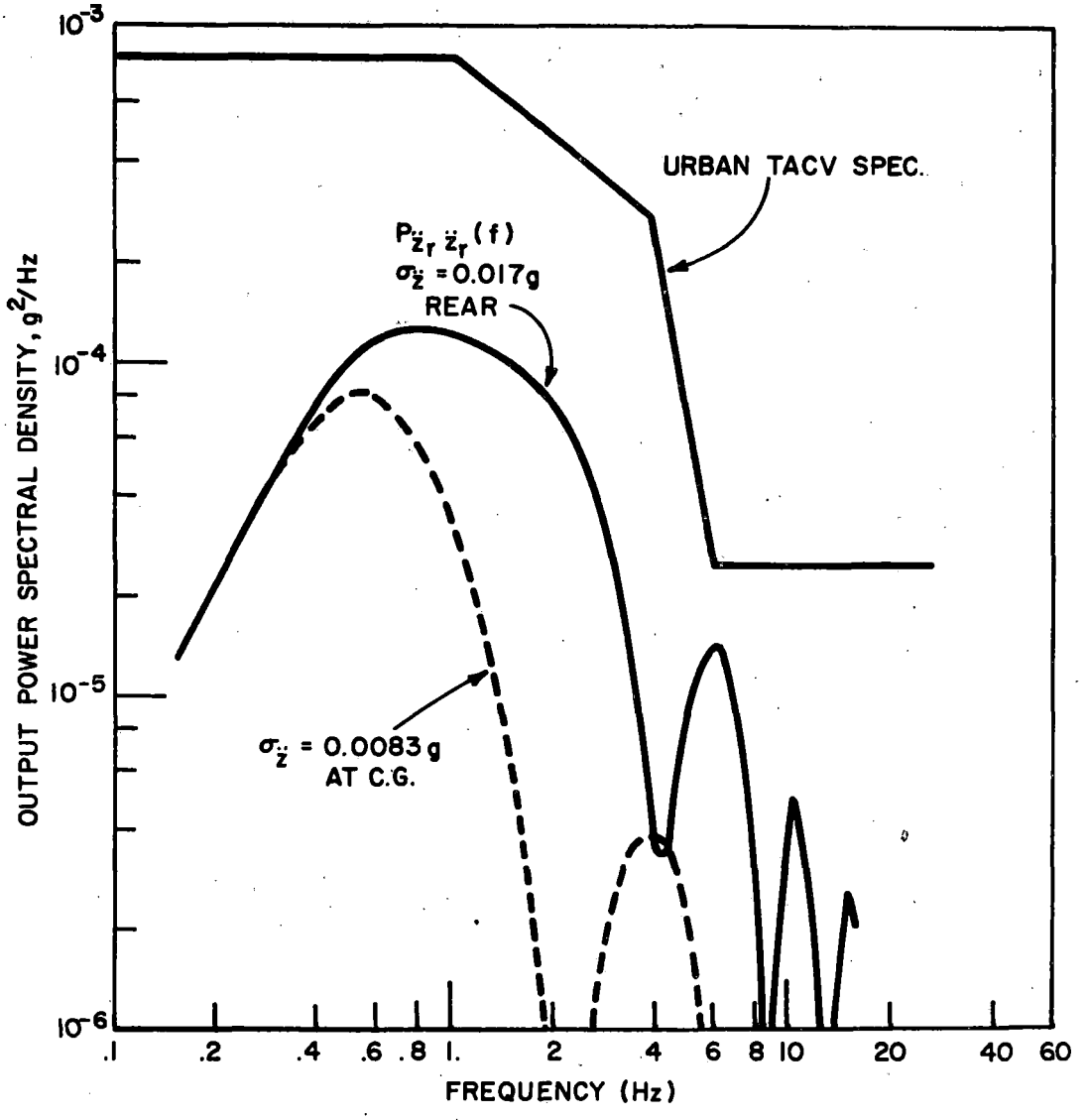

Fig. 6.15. Vertical acceleration psd for vehicle for the case with feedback control. A = 5 x 10^{-6} ft, v = 300 mi/h. Center of gravity and rear of vehicle.

It was found that the effects of aerodynamics on heave and pitch motion, for practical aerodynamic coefficients, are negligible.[46]

Also, it is felt that this will be the case for bending modes of the body structure.

Thus, we can conclude that excellent ride quality can be achieved with feedback control in all cases and with reasonable power requirements.

6.5. System Failure Analysis

In the event that current in the levitation-guidance magnets is interrupted, partial or total loss of lift and guidance will result; with the possibility that the vehicle will drop onto the guideway, or -- at a minimum -- its dynamic motion will be perturbed. In the repulsive-force suspension the most likely failure which would interrupt the magnet current is loss of superconductivity in the magnet wire; in the attractive-force suspension loss of magnet current might result from a failure in the control system. Furthermore, since the latter suspension is not inherently stable, the control system is susceptible to trigger instabilities which could produce rather bizarre dynamic effects.

Once one or more magnets has failed, the dynamic effects on vehicle motion should probably be larger for the case of the repulsive-force suspension since the free-fall distance of the vehicle is larger and the magnet redundancy is smaller in this case. On the other hand the L/R time constants for the magnets are larger in this case, the time to dissipate the magnetic energy is longer, and this would tend to ameliorate the dynamic perturbations.

In the following sections we analyze a few of the possible system failure modes, but only for the case of the repulsive-force suspension.

6.5.1. Total Loss of Lift

In the event all of the magnets fail, or the magnets at one end of the vehicle fail, there could be an immediate loss of levitation force and the vehicle would then drop onto the guideway (we neglect the magnet time constant, so that this is essentially a worst case analysis.) The amount of free-fall has an important effect on the magnitude of impact force experienced by the vehicle. The actual maximum impact force depends on the stiffness and damping characteristics of the undercarriage, whether wheels or skids. The functional relationships between the maximum impact force and these dynamic parameters are derived below, using a linear damped system as the working model. Note, however, that practical design would tend to incorporate the use of non-linear (velocity squared) damping devices.

The vehicle and undercarriage combination will be represented by a mass and a spring-damper combination. Just before impact the system is in free fall; following impact the system is governed by the equation:

$$\ddot{Z} + 2\delta\omega_o\dot{Z} + \omega_o^2(Z-Z_1) = 0 \ , \qquad (6.25)$$

where Z is the vertical position of a reference point on the vehicle, Z_1 is this reference point upon impact, $\omega_o = (k/M)^{1/2}$ is the undamped frequency of the spring-damper, k is the spring constant of the undercarriage structure, M is the vehicle mass, and δ is the damping ratio. The solution of (6.25) is

$$Z = Z_1 + \exp(-\omega_o\delta t)[A \cos \omega_1 t + B \sin \omega_1 t] \qquad (6.26)$$

where

$$\omega_1 = \omega_o(1-\delta^2)^{1/2} \ . \qquad (6.27)$$

The boundary conditions are

$$\left.\begin{aligned} \ddot{Z}_o &= -g \\ \dot{Z}_o &= -(2gh)^{1/2} \end{aligned}\right\} \quad \text{at } t = 0 \qquad (6.28)$$

Where h is the free-fall distance, or the difference of the vehicle elevations between the maximum speed condition and lift-off (assuming here that there are no retracting provisions, in which case the free-fall distance should include the retraction travel). Thus

$$\dot{Z}_o = \omega_o\ [-\delta A + (1-\delta^2)^{1/2}B]$$

$$-g = -\omega_o{}^2[(1-2\delta^2)A + 2(1-\delta^2)^{1/2}\delta B]$$

or

$$A = g\omega_o{}^{-2} - 2\delta\dot{Z}_o\omega_o{}^{-1} \tag{6.29}$$

$$B = (\delta A + \dot{Z}_o\omega_o{}^{-1})(1-\delta^2)^{-1/2} \tag{6.30}$$

Using Eqs. (6.26) to (6.30) it is relatively easy to show that

$$\ddot{Z} = -g\frac{[1-2\delta\dot{Z}_o\omega_o g^{-1} + (\dot{Z}_o\omega_o g^{-1})^2]^{1/2}}{(1-\delta^2)^{1/2}}\ \exp(-\omega_o\delta t)\ \cos(\omega_1 t+\phi) \tag{6.31}$$

where

$$\phi = \tan^{-1}[\{\delta-\dot{Z}_o/(\omega_o A + 2\delta\dot{Z}_o)\}(1-\delta^2)^{-1/2}]\ . \tag{6.32}$$

Since in practical systems $-\dot{Z}_o/\omega_o$ is greater than δA (note that δ is in the range of 0.4 to 0.6), ϕ will be in the first quadrant.

Maximum $\ddot{Z}$ occurs at a time t_1 given by

$$-\omega_o\delta\ \cos(\omega_1 t_1+\phi) - \omega_1\ \sin(\omega_1 t_1+\phi) = 0\ ,$$

or
$$\tan(\omega_1 t_1+\phi) = -\delta(1-\delta^2)^{-1/2}\ ,$$

$$\cos(\omega_1 t_1+\phi) = (1-\delta^2)^{1/2}\ . \tag{6.33}$$

Therefore:

$$|\ddot{Z}_{max}| = g[1-2\delta\dot{Z}_o\omega_o g^{-1} + (\dot{Z}_o\omega_o g^{-1})^2]^{1/2}\ \exp(-\omega_o\delta t_1) \tag{6.34}$$

For a free-fall distance h

$$\omega_o\dot{Z}_o g^{-1} = -[(k/M)(2h/g)]^{1/2}\ . \tag{6.35}$$

The maximum force felt by the vehicle is thus less than or equal to

$$F_{max} = Mg\ [1 + 2\delta(2kh/W)^{1/2} + 2kh/W]^{1/2} \qquad (6.36)$$

where W = Mg is the vehicle weight. The quantity in brackets will be called the load factor n.

For a vehicle weighing 10^5 lbs. free falling through a distance of 8 inches, $2h/W = 1.6 \times 10^{-4}$ in/lb. It is more convenient, however, to consider one corner of the vehicle (i.e., one wheel or skid) which supports 25,000 lbs. Thus $2h/W = 6.4 \times 10^{-4}$ in/lb. The load factor for various undercarriage spring constants is shown in Table 6.2.

TABLE 6.2. Load Factor for Various Spring Constants

k (lb/in)	$n = F_{max}/Mg$
1,000	1.51
5,000	2.37
10,000	3.07

The revenue vehicle system is not expected to have a free-fall distance of more than 4 or 5 inches; hence, it is concluded that a design load factor of around 2 is acceptable provided a proper choice is made for undercarriage stiffness.

6.5.2. Loss of Lift at One Corner

Failure of the levitation magnets at one corner only of the vehicle may prove to be worse than complete loss of levitation, since the vehicle would now be loaded asymmetrically. This would cause the vehicle to drop onto the guideway at the unsupported corner. Combined loss of lift and guidance at one corner would cause the vehicle to come

into contact with both the levitation and guidance surfaces of the guideway. The impact force experienced by the vehicle would be comparable to that found in the proceding section and would depend on the stiffness and damping characteristics of the structures which impact the guideway. In order to minimize the possibility of a failure of this type it is desirable to build redundancy into the levitation-guidance system.

In order to get some idea of the magnet redundancy which must be built into a magnetically-levitated vehicle, several simplified analyses of the dynamic behavior of a vehicle following magnet failure have been carried out. For these simplified studies we have considered only the levitation system and assumed that guidance is unaffected. In first approximation the dynamic responses following both loss of some lift and some guidance are additive.

If one or more of the levitation magnets fails, there will be a partial loss of lift, a drop in the center of gravity of the vehicle, and pitch and roll displacements. If the collapse of the field is sudden, oscillations in these degrees of freedom will be induced. The vehicle will assume new equilibrium in which it is either supported by the remaining magnets or it is supported by the magnets and guideway in combination. Oscillations in the degrees of freedom may cause the vehicle to come into contact with the guideway even though the new equilibrium prevents contact. The momentary loss of drag, which is later regained as the vehicle drops down, does not appear to be an important consideration even if it occurs impulsively.

As a first example we consider a vehicle supported by eight levitation magnets -- two in each corner. If one of the eight magnets fails, the vehicle will still remain floating. (We assume that the lift force varies as $F_L \propto h^{-5/3}$, where h is the suspension height.) The new

equilibrium height of the center of mass is found to be 0.917 h_o, and the pitch and roll displacements of the weakened corner are each 0.094 h_o; where h_o is the original suspension height. The new equilibrium height of the weakened corner is thus 0.73 h_o. If the collapse of the magnetic field occurs instantaneously, the combined oscillation from the three degrees of freedom will cause the corner to dip another 0.27 h_o, however, it is difficult to see how the magnetic energy can be dissipated so rapidly. A magnetic decay time of a few seconds would be sufficient to lower the vehicle into its new equilibrium in a gentle way. If we assume that the vehicle-track clearance is initially 0.75 h_o, then the vehicle does not make contact with the track even if maximum oscillation were induced. Thus, a support system which uses eight levitation magnets seems to be a very safe design.

If the field in one of the eight magnets collapses suddently the momentary loss of drag would be in the range of 0.02 to 0.003 g, depending on the vehicle speed. This would produce a series of mild propulsive jerks. If the field decays in a few seconds (or more slowly) there should be no perceptible change in drag.

As a second example we consider a vehicle supported by six levitation magnets -- one in each corner and two amidship. If one of the corner magnets fails the weakened corner will find a new equilibrium at about 0.35 h_o. This appears to be high enough to prevent contact with the guideway assuming there is no control coil below the levitation coil and provided no oscillation is induced. However, even a small amount of oscillation will cause the vehicle to slap the guideway. Thus this design would not appear to be as safe as the fully redundant design discussed above.

7. BASELINE DESIGN OF RESEARCH VEHICLE AND GUIDEWAY

A conceptual layout of the Magnetic Cushion Research Vehicle System is given in Figure 7.1. The system is comprised of the 12-passenger vehicle and its associated aluminum alloy guideway. To identify some of the packaging constraints, a LIM propulsion sub-system was incorporated, together with its Tee-shaped reaction rail and appropriate wayside power pick-up (not shown). The baseline system design shown in Figs. 7.1 and 7.2 was configured to be compatible with the TACRV guideway currently under construction at the DOT High Speed Ground Test Center at Pueblo, Colorado. Although this produces a non-optimum configuration, from the standpoint of aerodynamic drag and payload packaging, the potential cost savings of this approach are obviously quite large. Other subsystems, e.g. arresting gear, telemetry, communications, etc. would also be selected to maximize compatibility with the TACRV system.

7.1. Research Vehicle Specification

The vehicle shown in Figure 7.1 weighs approximately 53,000 lbs. and is 12 ft. high, 10 ft.-7 inches wide and 65 ft. long. It accommodates a 3-man crew, with provisions for 12 passengers - primarily to test passenger reaction, with reasonable Revenue Vehicle simulation, to the anticipated high speed environments. The vehicle has been configured for reasonably low aerodynamic drag ($C_d \sim 0.30$ to 0.35) although improvements in base shape, fineness ratio and cross-sectioned area may be necessary. No detailed structural analyses were conducted, but preliminary estimates indicate that the various loads can be accommodated effectively with conventional aircraft-type monocoque construction. An estimated weight breakdown for the vehicle is given in Table 7.1. The primary elements comprising the vehicle are identified in the following paragraphs.

FIGURE 7.1. CONCEPTUAL LAYOUT
TML RESEARCH VEHICLE SYSTEM

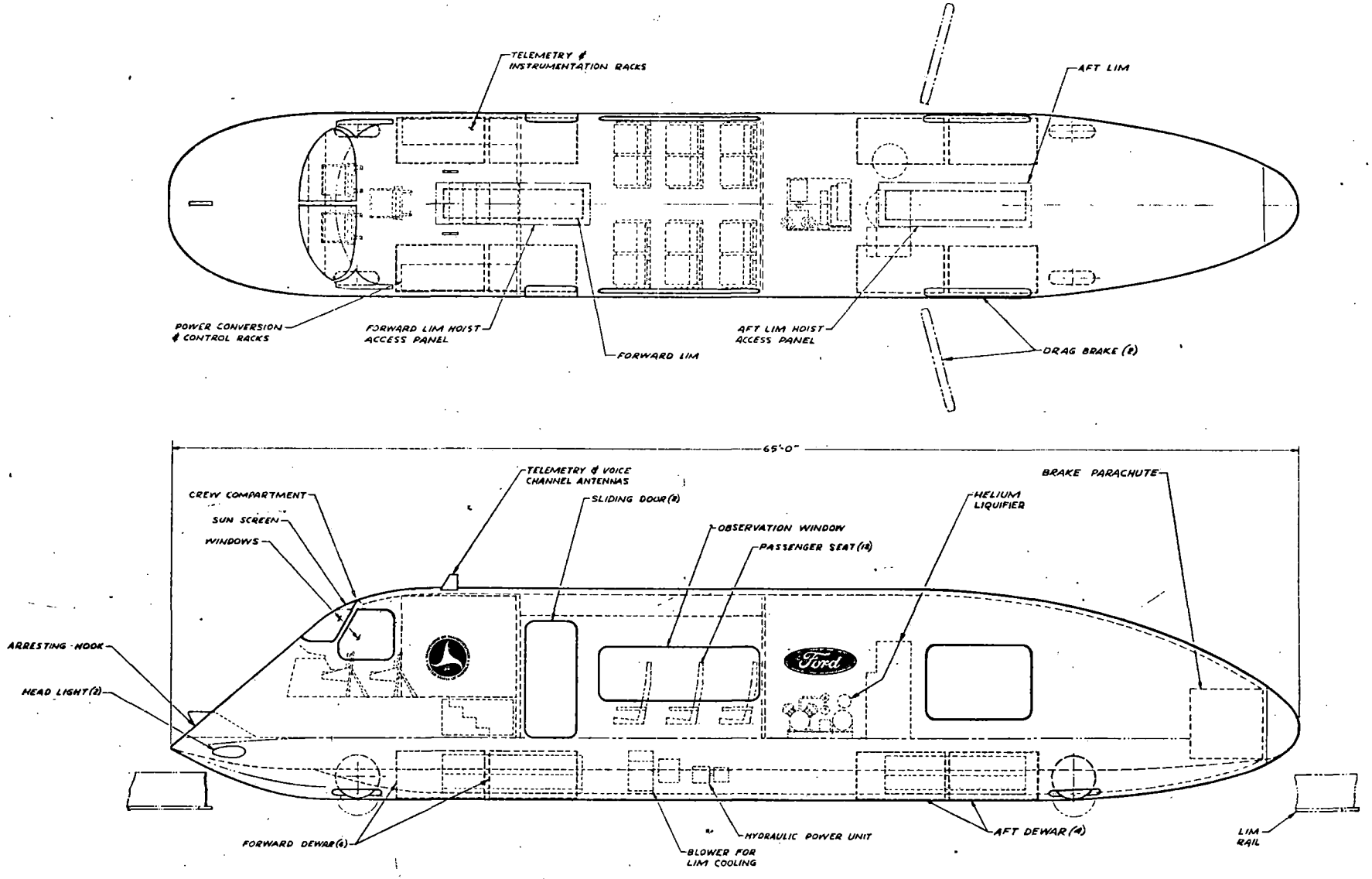

TABLE 7.1. Weight Estimate for Research Vehicle

STRUCTURE		6800
SKIN & STIFFENERS	2740	
FRAMES	750	
FLOOR	625	
BEAMS	1535	
ARRESTING HOOK SUPPORT	150	
DRAG BRAKE SUPPORT	200	
PARACHUTE SUPPORT	200	
DEWAR SUPPORTS	200	
WHEEL SUPPORTS	400	
DEWARS & MAGNETS		8000
LIMS (ELECTROMAGNETIC TRACTION UNITS)		15000
HELIUM LIQUEFIER		5300
AIR CONDITIONER		485
COOLING BLOWER		250
HYDRAULIC POWER SYSTEM		300
CREW COMPARTMENT		3805
CONTROL CONSOLE	200	
SEATS	105	
POWER CONDITIONING & CONTROLS	3000	
TELEMETRY & INSTRUMENTATION	500	
PASSENGER COMPARTMENT		1100
SEATS	600	
TRIM	500	
WHEELS & GEAR		1600
DRAG BRAKES & ACTUATORS		600
PARACHUTE		200
DUCTING & CABLING		3000
INSULATION		2200
AUXILLARY POWER		4000
TOTAL ESTIMATED VEHICLE WEIGHT		52,640 lbs.

7.1.1. Primary Suspension

Primary lift, as well as lateral support, are provided by four levitation-guidance pads. Each pad consists of two superconducting magnets (in tandem) encapsulated in separate dewars. Each dewar is approximately 72 x 32 x 22 inches on edge and contains a 0.5 x 1.5 m coil. Each dewar has a gas return line and a liquid supply line to and from the on-board helium liquefier subsystem. The helium liquefier shown in Figure 7.1 is the Cryogenic Technology, Inc. Model 1400. Note also that each dewar contains a liquid helium supply tank for additional safety in the event of liquefier failure. As described in Chapter 2, vehicle stability and ride quality are to be provided by a control system featuring auxiliary (non-superconducting) electromagnets located external to the primary lift magnets.

7.1.2. Alternate Suspension

Since no magnetic lift is available when the vehicle is at rest, a rubber-tired wheel system is provided. The wheels also serve to elevate the vehicle above the "equilibrium" position to reduce the high magnetic drag encountered at low speeds. This is particularly important when a thrust-limited propulsion system, e.g. a LIM, is employed. Preliminary study indicates that the wheels should be retracted subsequent to reaching an appropriate "lift-off" speed - primarily for clearance purposes - although some residual wheel projection below the vehicle ($\sim$4 inches) may be necessary for emergencies, i.e. where several of the lift magnets fail, rather than using skids. The tires shown in Figure 7.1 are Type VII aircraft tires, 30 inches OD x 7.7 inches wide, qualified at 300 MPH with a maximum load of 12,500 lbs. Further details of the wheeled suspesion system are given in Section 7.2.

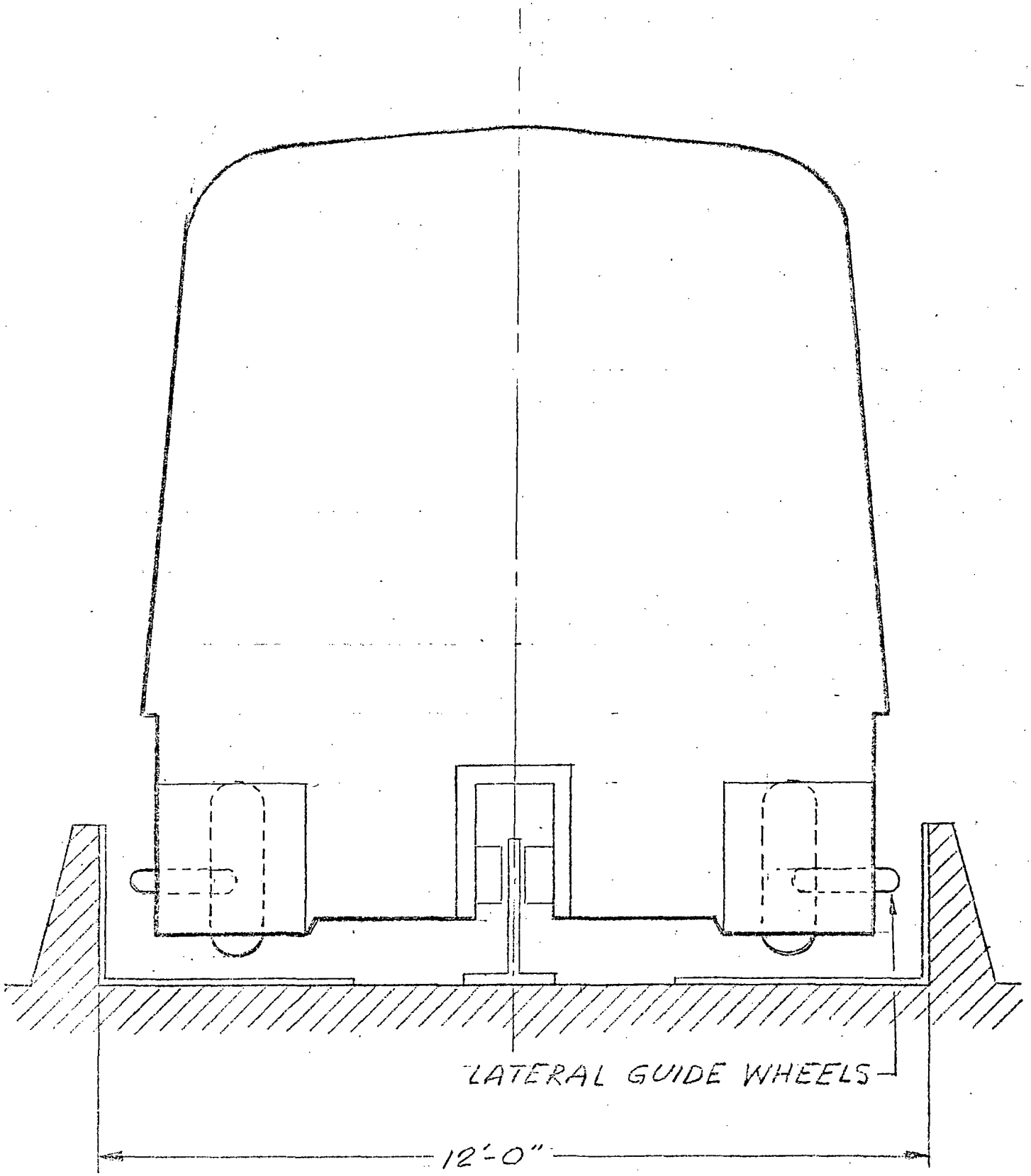

"U" SHAPED GUIDEWAY OPTION

FIGURE 7-2

7.1.3. Propulsion and Power Conversion

The research vehicle has been provided with a LIM, since electric propulsion is required and the LIM is the only such motor which has been adequately tested. Futhermore, the results of Sect. 4.2 indicate that this motor can be integrated with a high-clearance suspension. We suggest, however, that consideration be given to a quiet fan jet engine (see Sect. 4.5).

The LIM traction units (each 3000 hp) have an envelope 20 inches wide x 26 in. high x 100 in. These two units, with their suspension gear, are estimated to weigh approximately 15,000 lbs. An electrically driven blower is provided to supply cooling air for the LIM windings and stacks. Electrical power conversion equipment for propulsion, magnetic suspension, vehicle control, auxiliary power, instrumentation and communication is contained in racks within the crew compartment

7.1.4. Accommodations

The crew compartment is configured to duplicate as nearly as possible the anticipated facilities and features which would be provided in a Revenue Vehicle. Redundant controls and back-up personnel would be provided to enhance safety and reliability in the research program. The passenger compartment is styled and equipped as in a Revenue Vehicle in order to observe passenger comfort and passenger reaction to high speed ground travel. Twelve individual passenger seats are provided.

7.1.5. Braking

Five separate braking subsystems are provided for normal and emergency conditions. It is anticipated that normal braking would be accomplished by the inherent aerodynamic and magnetic drag and by LIM reversal. At low speeds (when running on the wheels) disc brakes within each wheel would be used for braking. For emergencies, aerodynamic drag brakes are provided on each side of the vehicle and a parachute brake is positioned

in the rear of the vehicle. Cable arresting gear, which would be engaged by an arresting hook on the vehicle, is also provided as a back-up system.

7.1.6 Life Support

Complete life support facilities are provided for the crew and passenger compartments. These facilities include complete air conditioning, thermal and sound insulation. Central processing units for air conditioning are located under the floor of the crew compartment.

7.2. Undercarriage Design

This section is concerned with the design of a wheeled undercarriage to support the Research Vehicle at low speeds, since the magnetic suspension becomes quite inefficient (too much drag) below about 75 mi/h. The 50,000 lb. vehicle traveling at 300 mi/h will have a magnetic drag of about 1,500 lbs at its equilibrium height of 30 cm. At 75 mi/h the equilibrium height decreases to 26 cm and the drag increases to 3,500 lbs. If the undercarriage is designed to prevent the height from decreasing below 26 cm, the maximum magnetic drag will be held to about 8,600 lbs. at a speed of about 10 mi/h. Between 75 mi/h and zero speed, the wheels are gradually lowered so that the vehicle height remains constant while the tires accept a greater share of the vehicle weight. Above 75 mi/h, the wheels can be retracted to give additional clearance, but they should be allowed to project far enough to accept the vehicle weight immediately in case of a lift system failure.

The need for retraction could be eliminated by allowing the vehicle height to decrease at low speeds, but this would increase the magnetic drag to a value greater than the total drag at 300 mi/h which is undesirable particularly for thrust-limited propulsion systems. The retractable undercarriage

also makes possible tests and demonstrations at various vehicle heights (variable lift-off).

The forward and rear units of the wheeled undercarriage are shown in Figure 7.1. The two units are similar, with the front and rear units synchronized hydraulically so that they would be raised and lowered together. Single Type VII aircraft 30 x 7.7 tires are used. Each tire is rated at 12,500 lbs at 300 mi/h, giving an allowable vehicle gross weight of 50,000 lbs. The tires bear directly on the aluminum surfaces of the guideway.

At each end of the vehicle, two additional 18 x 4.4 wheels are positioned normal to the guidance panels of the guideway. These provide side forces for turns, as well as stabilizing the vehicle at low speeds. Because of the large radius required for turns at high speed, it should not be necessary to steer the main wheels of the undercarriage. However, if it is desired to reduce the side loads on the tires in a turn, a slight castering capability similar to that used in some aircraft landing gears could be built into the undercarriage.

7.3. Guideway

The baseline vehicle was configured to operate on an aluminum guideway which could be installed on the concrete ground slab of the high-speed TACV test track at Pueblo, Colorado. The guideway has a maximum width of 12 feet and can be installed between the TACRV vertical side panels. New guideway supports would be positioned

at an appropriate spacing along the track on top of the existing slab. This is a viable alternative to a continuous concrete guideway support laid on top of the slab. These individual supports could be anchored to the slab and removed upon conclusion of the magnetic cushion research program.

The guideway geometry is illustrated in Fig. 7.2; it utilizes the "conventional" double L configuration. Other guideway options are possible; in fact, any of the stable configurations discussed in Chapter 6 (the double L, box beam, inverted Tee, or canted inverted Tee) are acceptable options.

One of the more interesting options is the canted, inverted Tee configuration (see Fig. 6.4). The dynamic analyses alluded to in Chapter 6 suggest that this configuration would provide somewhat better vehicle control than other types of guideways when only four control coils are used. This guideway could be installed on the existing TACRV track at Pueblo, but its installation would prohibit testing the TACRV in the same time frame.

7.3.1 Aluminum Specification

Each aluminum track is formed in the shape of an "L"; following the prescription discussed in Chapter 2 the levitation section is made 1.1 m wide and the guidance section is 0.7 m high. The track is 2.5 cm thick. The aluminum alloy recommended is 6101-T61 which has 92% of the electrical conductivity of high-purity aluminum but is stronger mechanically. This alloy has a yield point of 11,000 psi and an ultimate strength of 18,000 psi. The two ~~tracks~~ rails require 862,000 lbs of aluminum alloy per mile.

Although aluminum plate can be produced as rolled plate, an extrusion, or cast plate, only the first option appears suited for production of the magnetic cushion track. Rolled plate can be produced in widths up to 210 inches and in lengths up to 110 ft. Extruded shapes are limited by maximum die size and press pressure; ALCOA informs us that extrusions which they can make are limited to 33 inches width. Cast plate is still somewhat experimental and is limited to 50 inch widths.

The rolled plate must either be bent into the L shape, or two smaller width plates must be joined by butt or seam welding. 4043 aluminum is recommended for a weld filler material. If the rolled sheet is to be bent, then one is limited to about 20 ft lengths of L track. Rolled plate can be obtained for about $.47 per pound, and may possibly be obtained for less on a competitive bid basis; however, an additional fabrication cost would incur either in the bending or welding operation.

The track sections should be welded together to produce a continuous track; however, an occasional expansion joint is necessary. It was shown in reference 1 (Appendix G) that there is a momentary reduction in lift of 40% at a butt expansion joint. In section 7.3.2 it is shown that the reduction in lift at a scarfed joint is only 25% and we recommend such an expansion joint. This momentary reduction in lift should not cause any serious ride quality problems even in a passively-controlled vehicle (See reference 1, Appendix G). This reduction in lift is for a single magnet; since we are recommending redundant magnet support at each corner, the actual percentage reduction in vehicle lift is only one-half the values quoted above.

The aluminum plate will be placed in direct contact with the concrete slab or structural member. There is no compatibility or corrosion problem between aluminum and concrete provided that corrosive chemicals, such as calcium chloride which is sometimes added to concrete to facilitate curing in below zero temperatures, are not used.

7.3.2. Inductance Studies of Guideway Joints

The ac impedance technique described in Section 2.2 has been used to measure the change in lift and drag forces on a magnet at guideway joints. A 2 x 4 inch coil was moved at several fixed heights above an aluminum plate containing a transverse joint, and the inductance was measured as a function of position. Both 1/16 and 1/8 thick plate were used; essentially the same results were obtained in both cases. The measurement frequency was 1 kHz. Figure 7.3 shows the result of such a measurement for the case of a butt joint (no electrical contact). From a measurement at constant height one can obtain the change in drag force due to the joint, and from the difference between the inductances at two heights one can obtain the change in lift force due to the joint.

For the butt joint we find a maximum loss of lift of 41% in a pulse of width $\approx$ 3/4 the length of the magnet. This is in essential agreement with the calculation of reference 1 (Appendix G). The change in drag force is $\pm$ 7% of the lift force. Although this is an appreciable fraction of the steady drag force at 300 mi/h, it corresponds to an impulsive acceleration of only 0.07 g.

We next measured the coil inductance as it moved over a scarfed joint in which the joint is tapered over a length four times the thickness of the plate. There was no electrical contact at the joint. In this case the maximum loss in lift is 25% and the change in drag is only $\pm$ 5% of the steady lift.

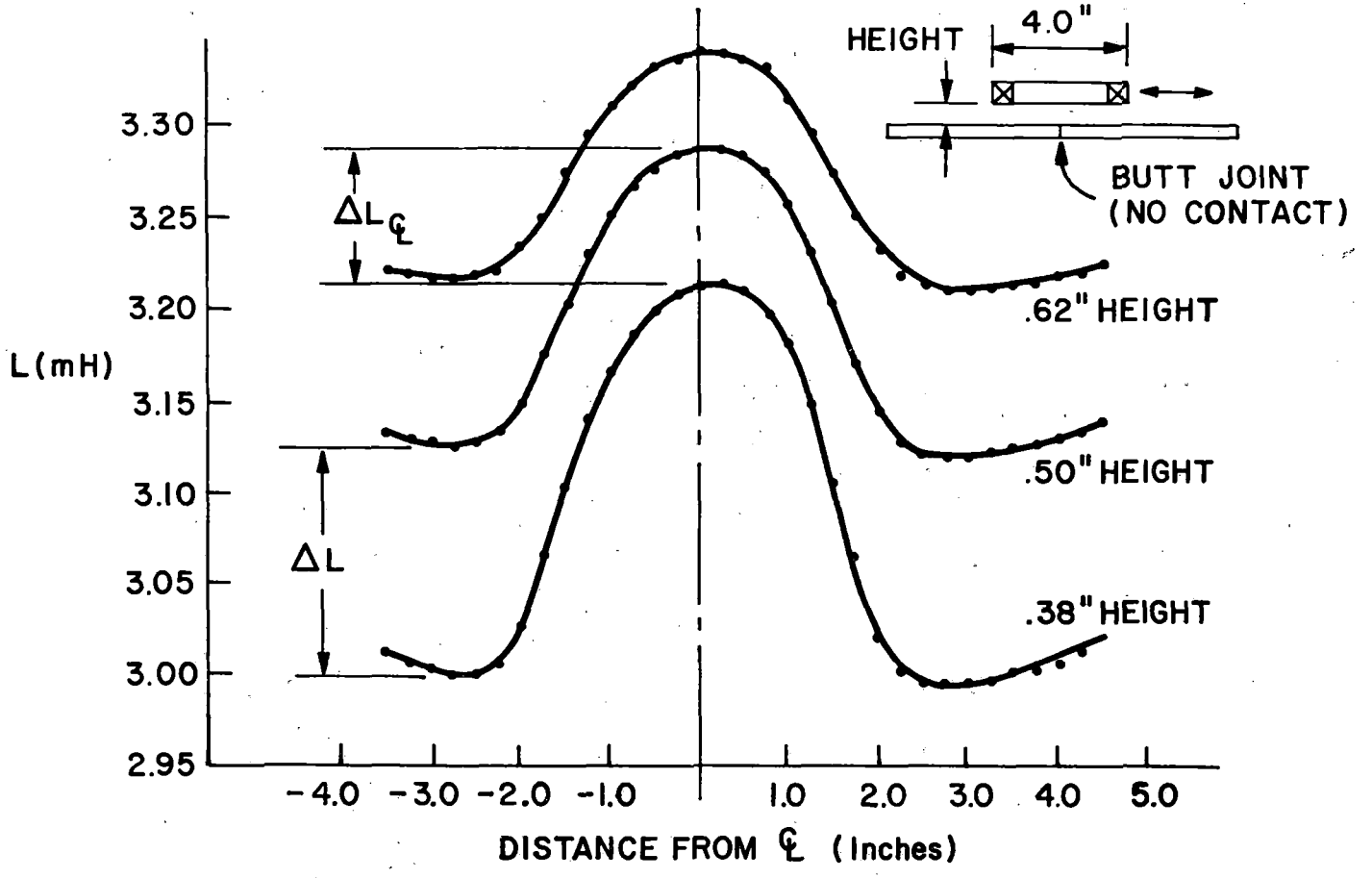

Fig. 7.3. Inductance measurement of a coil in a guideway with a butt joint.

7.3.3. Radius of Curves

A 300 mi/h vehicle executing a curve of 2-mile radius requires a 30° bank angle to eliminate lateral acceleration on the passengers. The apparent downward acceleration in this maneuver is 1.15 g, which is quite acceptable. If, however, the vehicle executes the 30° banked curve at the wrong speed, the passengers will experience lateral accelerations, and the sides of the guideway will have to supply centripetal force to the vehicle. The latter consideration offers no problem since the horizontal forces are not extremely large.

Consider, for example, a 150 mi/h vehicle executing a curve of 2-mile radius at a 30° bank angle. The centripetal acceleration required is 0.14 g but the guideway is banked to supply 0.57 g. Thus the "vertical" section of the guideway must supply a force of 0.43 Mg, and the passengers will experience a lateral acceleration of 0.43 g. This effect on the passengers is unacceptable.

There are two alternative methods for providing satisfactory ride quality while the vehicle is executing curves. One is to make the curve radii large enough that the lateral accelerations experienced by the passengers are always small, even when the curve is executed at the wrong speed for the bank angle. The other is to provide either active or passive means for the passenger compartment to achieve the proper bank angle while the undercarriage and levitation magnets follow the prescribed guideway bank angle. The latter alternative should definitely be explored for a revenue system, but is a detailed study which we cannot pursue here. We shall therefore, consider only the first alternative.

The specification for the Sanyo Rail Line in Japan is for a minimum curve radius of 4000 m at a speed of 250 km/h. This gives a centripetal acceleration of 0.123 g. If we use the same criterion (same centripetal acceleration) for our 300 mi/h system, then the minimum radius of curvature is 14,900 m or 9.25 miles.

7.3.4. Switching

High-speed switching of a magnetically levitated vehicle can be accomplished by moving sections of the guideway or by introducing auxiliary magnet-track configurations (possibly close gap) which can be powered to deflect the vehicle to one side (or other) of the guideway. If the first alternative is chosen, large sections of the guideway must be moved. This follows since the vehicle should not move on a track of radius smaller than the minimum allowed radius, and the switch track must be displaced by at least the guideway width. If the guideway width is d, then the length of the track L which must be moved is $L = (2dR)^{1/2}$ where R is the minimum curve radius. For d = 12 ft and R = 9.25 miles, L = 1100 ft. The movement of such large sections of guideway does not appear to be practical.

On the other hand high-speed switching does not appear to be necessary. The main purpose of switching in a revenue system is to allow some vehicles to leave the high-speed track and enter a station. This can be accomplished at much lower speeds (below 50 mi/h), and here the vehicle will be operating on wheels.

If the vehicle is operating on wheels and moving at relatively low speeds there are many standard techniques available for switching. One side of the guideway will have to be opened (either by moving it sideways or by lowering it) but because the vehicle is moving at low speed only one hundred feet or so of the guideway need be moved.

The only remaining problem for switching involves the linear induction motor. The standard double-sided LIM requires a reaction rail down the middle of the guideway; this reaction rail would have to be moved also in a switching operation. In the simplest type of switch the LIM reaction rail would be lowered below grade in the switch section, one side of the guideway would be opened, and the vehicle would be pulled through the switch by an active propulsive unit in the guideway; when the switch is restored for high-speed, through operation, it would function like any other part of the guideway.

7.4. Cryogenic Magnet Design and Refrigeration Requirement

An engineering design of a superconducting coil and cryogenic container for a levitation-guidance pad for a TMC research vehicle was carried out by Magnetic Corporation of America under subcontract to the present contract with DOT. This design is discussed in detail in MCA-TP124 (reference 8) so that the results are only summarized briefly here. The coil for each pad is a flat racetrack coil having an overall length of 2 m, a width of 0.5 m, and 300,000 ampere turns, which provides a lift force (at 300 mi/h speed) of 12,500 lbs when the plane of the coil is 30 cm above the track surface. Four such coils are capable of supporting the research vehicle.

As discussed in Section 7.1.1. we are now proposing a fully redundant levitation-guidance system with eight magnets. Each magnet is a flat racetrack coil of dimensions 1.5 m x 0.5 m. x 0.5 m. We have used the MCA design with each magnet (and cryogenic container) shortened by 0.5 m.

The basic configuration of the MCA design is shown in Fig. 7.4. The coil consists of a twisted composite superconducting winding with

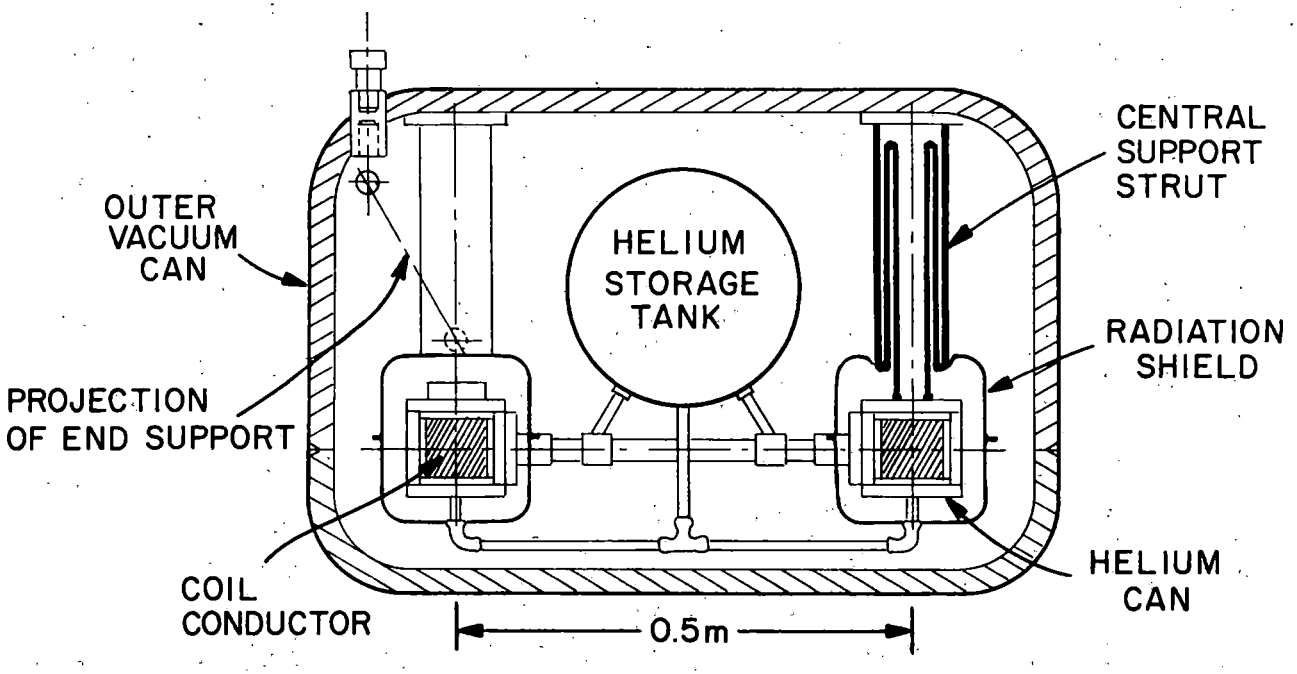

Fig. 7.4. Basic configuration of MCA magnet and dewar.

helium passages to stabilize the superconductor and to remove the losses caused by time-varying magnetic fields. The windings are contained in a stainless steel can which is supported by six stainless steel reentrant-type supports that are slanted to take loads in more than one direction. The ac losses and heat leak generate helium gas which is used for the vapor-cooled electrical leads as well as to cool the radiation shield which surrounds the helium temperature components. It should be emphasized that the MCA magnet design is conservative, not incorporating some of the more novel features found in the Ford magnet, e.g., all-aluminum cryostat, G-10 epoxy-fiberglas struts and potted windings (see Section 2.6.1). The reason for the conservative design is that for the first research vehicle one would like to use a safe, proven magnet design since it is the suspension concept which is being tested. Once the testing program is underway additional magnets incorporating more novel features should be built to replace one or more of the original magnets.

A helium container with suitable internal baffling is placed above the coil and supplies helium by gravity to the windings. The room-temperature outer vacuum can is made of aluminum. To minimize heat leak the system operates in the persistent mode with removable current leads and a thermally-actuated, permanently-connected persistent switch.

The pad is designed with an internal helium reservoir with sufficient storage capacity for 8 hour operation. This configuration allows for batch operation as well as maintains the helium level above the windings under various dynamic operating conditions. The MCA design is able to maintain liquid level above the coil windings under sustained

longitudenal acceleration of 0.1 g. The shorter magnets used in the baseline design will maintain liquid level above the windings under sustained acceleration of 0.13 g. Higher accelerations can be provided for by either raising the helium reservoir or by providing some flow restrictions in the vent lines. Such a provision would appear to be necessary if emergency braking up to 0.4 g is allowed for the vehicle. The reservoir configuration of the MCA design allows for either open-cycle operation or the possibility of hookup to a closed-cycle refrigerator.

Two designs for the levitation-guidance pad were presented by MCA. These are the lightly-damped design and the maximum self-damping design. Since the self-damping is due to eddy currents generated in the outer vacuum can, the only difference in the two designs is the amount of aluminum in the outer can. Both designs are structurally sound. The weight of the lightly-damped pad is 948 lbs and the weight of the maximum-damped pad is 1654 lbs. These weights do not include magnetic shielding.

In order to utilize the MCA levitation pad design in the baseline design of the research vehicle presented in Section 7.1 we have adopted the following procedure. We use the lightly-damped pad since control coils will be used and we do not need maximum self damping. The weight of the baseline magnet and cryogenic container is obtained by taking that of the MCA design and subtracting off the component weights in the 0.5 m section which is removed in obtaining the shorter pad. The 8000 lb entry for DEWARS & MAGNETS in Table 7.1 includes the weight of the eight cryogenic magnets and the control coils.

The heat leak per pad has been estimated by MCA as 3.8 W when 1000 ampere leads are used, and as 2.6 W when 500 ampere leads are used. To this must be added approximately 1.0 W for ac losses. The cryogenic requirement for 8 pads can be supplied by the Model 1400 helium refrigerator, made by Cryogenic Technology, Inc. (CTI), and two compressors. The combined weight of this refrigeration system is 5700 lbs. Substantially lighter refrigeration systems are possible but are not commercially available at the present time. Based on experimental refrigerators which have been built for flight applications it is estimated that the refrigerator weight could be made as low as 1500 lbs. We recommend open-cycle operation for the magnets in the research vehicle, thus saving the weight of a refrigeration system; we have, however, included a 5700 lb refrigerator in the system weight (Table 7.1) in case closed-cycle operation is desired.

No magnetic shielding is being recommended for the research vehicle in order to let experience with the unshielded magnets determine the shielding requirements, if any, for a revenue system. According to the MCA design the magnetic field at the floor of the vehicle in the vicinity of the magnet is 420 gauss. This can be reduced to 230 gauss with an iron shield 2 cm thick. Four 2 cm iron shields for the eight levitation-guidance magnets would weigh about 6000 lbs. Thus, 2 cm magnetic shielding can be incorporated, or 4 cm magnetic shielding can be used with the aft magnets and no shielding on the forward magnets, without increasing the weight of the system (Table 7.1) provided open cycle cryogenic operation is utilized. Shielding of the aft magnets with at least 2 cm of iron might prove necessary if it is determined that the unshielded field would be deliterious to electrical equipment

in the aft compartment, and if such equipment cannot be located at a sufficiently remote location from the magnets. Shielding of the rear 1/3 of the forwarded magnets might be desirable to reduce the field in all parts of the passenger compartment below 200 gauss.

It was noted in Section 2.8 and also in the MCA report[8] that magnet shielding with iron or other ferromagnetic materials requires a substantial weight penalty. Superconducting shielding (either by a coil or by superconducting material) requires a much smaller weight penalty but involves a more complicated magnet design. Superconducting shielding should certainly be explored for the revenue vehicle, but it appeared to us that the simpler racetrack magnets should be used in the research vehicle, at least initially.

8. CONCLUSIONS

The present study (Tasks II and III) has been concerned with certain critical problem areas relative to magnetic suspension of high-speed vehicles, and with the baseline design of a TMLRV (tracked magnetically levitated research vehicle). Although Task I (see reference 1) established the basic feasibility of magnetic levitation as a suspension system for high-speed ground vehicles, certain aspects of the overall system problem were either not addressed or addressed only briefly. Areas not treated include propulsion, system failure, and magnetic shielding. Furthermore no effort was expended in Task I on the design of a control system for the attractive force suspension.

The situation is complicated by the fact that there are two viable magnetic suspension schemes, the electrodynamic (or repulsive-force) suspension and the electomagnetic (attractive-force) suspension, and the critical problem areas are different in the two cases. For the repulsive-force suspension the unresolved problem areas are: superconducting magnet design, ac loss in the superconducting magnets, magnetic shielding, and choice of a compatible propulsion system. For the attractive-force suspension the problem areas are: control system design and basic control strategy, eddy-current drag at high-speeds due to magnetic saturation of the track, maximum allowable track roughness, and the need for a secondary suspension. Both suspension systems have been treated in the present study. It was felt that detailed analyses of critical areas might show problems serious enough to rule out future consideration of one of the suspension systems. This has not proved to be the case, however. Both suspensions appear capable of guiding a

vehicle at 300 mi/h, but the system specification will be different in the two cases. We discuss the results for each suspension separately.

8.1. Repulsive-Force Suspension

A full scale superconducting magnet design for a levitation-guidance pad of a magnetically-supported, high-speed vehicle has been carried out by Magnetic Corporation of America under subcontract; this design is summarized in Section 7.4. The calculated thermal loss of such a pad is of the same order as the estimate made in reference 1, and is thus manageable. One of the serious problems anticipated in the operation of superconducting magnets is the large ac loss expected in the coils when they are disturbed from equilibrium by interaction with guideway irregularities or by fields due to control currents. Some estimates have suggested that this loss will contribute from 1/3 to 1/2 the total cryogenic loss. For this reason a series of experiments was performed on model superconducting coils for which the operating conditions on a revenue vehicle coil were simulated. The measured ac losses were actually smaller than our original estimates;[1] for an actively controlled vehicle operating on a guideway with $A = 5 \times 10^{-6}$ ft* the ac loss is less than 0.5 watt per coil. Thus, ac loss is not a major problem. Our experiments also indicate that single-core superconducting wire is preferable to multicore wire as far as ac losses are concerned.

Concerning magnetic shielding, it appears that the magnetic field of the levitation coils can be attenuated to below 200 gauss (in the passenger compartment) without an excessive weight penalty. Such fields do not appear to be detrimental to human beings and can probably be accepted as a natural part of the high-speed environment, much as reduced air pressure is accepted in aircraft. However, if

* See Section 6.2.1 for a definition of A.

linear synchronous motor (LSM) propulsion is used the magnetic shielding problem will be much more severe, and a substantial weight penalty will be required to reduce the fields in the passenger compartment to the 200 gauss level.

Various types of propulsion systems have been investigated for the high-speed, magnetically supported vehicle (LIM, LSM, superconducting paddlewheel and screw, and quiet-fan jet engine) in the present study. The propulsive system currently under development for the tracked air cushion vehicle is the linear induction motor (LIM), and it has been suggested that the LIM be used to propel the TMC vehicle. The principal problem here is that relatively small clearance is required between the LIM and its reaction rail for efficient operation, and this is not compatible with the large clearance between the levitated vehicle and track. It is shown in Section 4.2, however, that control of the LIM gap by an active control system reacting laterally against the main vehicle body appears feasible without degrading the lateral ride quality to an unacceptible level. Thus the LIM appears to be an acceptable propulsion system. The ideal propulsion system for this type of TML vehicle is the quiet-fan, turbojet engine; this engine is light weight, requires no wayside power pickup and no close-gap reaction surface. It does not preempt any part of the track area, thus allowing greater freedom in guideway choice.

The repulsive-force suspension is completely stable but has poor inherent damping. Although acceptable ride quality can probably be achieved (for a guideway with $A = 5 \times 10^{-6}$ ft) with passive control and a secondary suspension, superior ride quality can be obtained without

a secondary suspension using active control. The control power requirement is modest: 1.2 kW/ton supported weight for a guideway with $A = 5 \times 10^{-6}$ ft. The control power is proportional to the guideway A-coefficient.

Of the various guideway configurations studied, the canted, inverted T appears to be the best, but is only marginally superior to the double L, or inverted T guideways. Because guideway tolerance is not critical, it would appear that slip-cast concrete techniques can be used with normal highway construction practice in the guideway construction. Guideway costs for an inverted T guideway can perhaps be estimated from previous estimates made for the UTACV guideway: $400,000 per mile for grading and concrete work, to which must be added approximately $400,000 per mile for aluminum. If jet engine propulsion is used no additional cost would be required; however, if a LIM is used there will be an additional cost for the LIM rail and wayside power pick-up.

One characteristic of this suspension system is the low-speed drag peak, which poses a problem to thrust-limited propulsion systems. However, several methods for circumventing the drag peak were outlined in reference 1.

8.2. Attractive-Force Suspension

Two model electromagnets with their required feedback control systems were built and tested during the present study. These were built for purposes of demonstration and for studying the characteristics of the attractive-force suspension. Both magnets were constrained to move vertically (one degree of freedom), and both control systems used

pulse-width modulation to control the current in the magnet. Various control strategies were studied; the most effective one uses displacement and acceleration sensors with feedback signals proportional to gap displacement, magnet acceleration, and integral of magnet acceleration. At one-half inch gap the static control power required is approximately one watt per pound of supported weight; the control power to handle a dynamic perturbation equivalent to a guideway with A-coefficient $= 5 \times 10^{-6}$ ft is quite small but requires a power supply with capacity of 2 volt-amp/lb supported weight.

An analytic study of the lift and drag forces in the attractive-force suspension has uncovered a serious problem for high-speed operation. The problem arises because the magnetic flux in the track must be carried in the skin depth. The skin depth depends on conductivity and permeability of the track, as well as on vehicle velocity, but is of the order of 1 mm for magnets of 1 m length.
at 300 mi/h / This small skin depth causes the flux density in the track to approach saturation and the permeability to drop precipitously. As a result the eddy-current losses in the track are much larger than would be obtained if there were no saturation. This problem can be largely avoided if the track is laminated; however, such a procedure would increase the cost of the suspension system substantially. The problem can be minimized by making the levitation magnets very long, and it is felt that by appropriate magnet design the eddy-currents losses can be kept within reasonable bounds. With 10 m long magnets, estimates scaled from the calculations of Sections 3.1 and 3.2 indicate a lift-to-drag ratio of between 70 and 120 for a pure levitation system. This will be degraded somewhat when guidance is included.

Our studies have shown that there is a maximum guideway roughness which this type of suspension will tolerate; however, this guideway is substantially rougher than the standard ($A = 5 \times 10^{-6}$ ft) so that this does not appear to be a problem. On the other hand, satisfactory ride quality cannot be obtained without a secondary suspension unless the track is very smooth ($A < 5 \times 10^{-7}$ ft); furthermore, an active secondary suspension appears necessary.

The attractive-force suspension is a good low-speed suspension which appears capable of guiding and supporting a vehicle at speeds up to 300 mi/h. It does not require wheels, except possibly for emergency landing. It integrates well with the linear induction motor (LIM). Methods for accomplishing high-speed switching, without moving sections of the guideway, have been proposed by Krauss-Maffei and Messerschmitt-Bolkow-Blohm.

Because the vehicle magnets must hang below the steel track, most guideway designs which have been proposed use an elevated guideway. Such a guideway would probably be made from pre-cast concrete sections. Because tolerances are more stringent here than with the repulsive-force suspension, it is expected that guideway construction costs will be higher, although the metal track costs will clearly be lower.

8.3. Baseline Design of TML Research Vehicle

Baseline specifications of the guideway and TML research vehicle, including a full scale magnet design, are discussed in Chapter 7 (see, e.g. Figure 7.1). This has been carried out for a system using the repulsive-force suspension as required by our contract with the Federal Railroad Administration. However, both types of magnetic suspension appear to be contenders for the TMLV system.

9. RECOMMENDATIONS

The present study has turned up no problems serious enough to definitely rule out one of the competing magnetic suspensions (repulsive-force or attractive force) proposed for high-speed ground transportation. The next phase of the magnetic levitation program should focus on high-speed comparison tests of these two suspensions. The rocket sled program proposed by the Department of Transportation, in which model vehicles supported by one or the other of these suspensions are accelerated to speeds of 300 mi/h and their dynamic behavior studied, would appear to be a direct way of accomplishing this objective.

The ultimate choice of a suspension for a high-speed transportation system will be determined by which system design can achieve the desired ride quality objective at the lowest overall system cost. Although accurate information relative to this goal can probably only be obtained through operation of research vehicles, important supporting information can be obtained from additional model studies of the type carried out in the present program. We propose, therefore, a follow-on program to address the following problems: attractive-force system, (i) quantitative assessment of the magnetic drag at high-speeds, (ii) determination of the necessity for an active secondary suspension and the power requirement of the suspension; repulsive-force system, (iii) guideway configuration studies aimed at reducing the amount of aluminum in the guideway. (We have noted that aluminum cost will be a substantial fraction of overall guideway costs.)

Finally, we would like to propose that serious consideration be given to a high-speed system design using the repulsive-force suspension

and using a quiet-fan jet engine in each vehicle for propulsion. Although electric propulsion has been proposed for this mode of transportation because of environmental reasons (noise, pollution), experiments on large by-pass turbojet engines have shown that the noise can very likely be reduced to acceptable levels. The jet engines are light weight and their use would eliminate substantial transmission power losses. Furthermore, this combination of suspension and propulsion systems would appear to be compatible with a lower cost guideway than that required for other combinations.

10. REFERENCES

1. L. C. Davis, J. R. Reitz, D. F. Wilkie and R. H. Borcherts, "Technical Feasibility of Magnetic Levitation as a Suspension System for High-Speed Ground Transportation Vehicles", U.S. Department of Transportation Report PB 210-506 * (1972).

2. H. T. Coffey, F. Chilton and L. O. Hoppie, "The Feasibility of Magnetically Levitating High Speed Ground Vehicles", U.S. Department of Transportation Report PB 210-505* (1972).

3. H. T. Coffey, private communication.

4. J. R. Reitz and L. C. Davis, "Force on a Rectangular Coil Moving above a Conducting Slab", J. Appl. Phys. 43, 1547 (1972).

5. R. H. Borcherts and L. C. Davis, "Force on a Coil Moving over a Conducting Surface Including Edge and Channel Effects", J. Appl. Phys. 43,2418 (1972).

6. C. A. Guterjahn, S.L. Wipf, H. J. Fink, R. W. Boom and K. E. MacKenzie, "Magnetic Suspension and Guidance for High Speed Rockets by Superconducting Magnets", J. Appl. Phys. 40, 2133 (1969).

7. W. Gautachi and W. F. Cahill in Handbook of Mathematical Functions, ed. by M. Abramowitz and J. A. Stegun (Natl. Bur. Std., Washington, D.C., 1964), Appl. Math. Sci. 55, p. 231.

8. Z. J. J. Stekly, T. A. deWinter, J. A. Vitkevich, J. M. Tarrh and A. E. Emanuel, "Design Study of Superconducting Magnetic Levitation Pads", Magnetic Corporation of America Report MCA-TP 124 (1972).

9. The epoxy used in the tests was Crest 3170/7133 from Crest Products Co., Santa Ana, California 92075.

10. Suggested by Professor Y. Ishizaki, Univ. of Tokyo.

11. S. L. Wipf, Proc. 1968 Summer Study on Superconducting Devices and Accelerators, Brookhaven Nat. Lab. BNL 50155, 511 (1968).

12. C. P. Bean, Phys. Rev. Letters 8, 250 (1962); H. London, Phys. Letters 6, 162 (1963).

13. R. G. Rhodes, E. C. Rogers, and R. J. A. Seebold, Cryogenics 4, 206 (1964).

* Available from National Technical Information Service, U.S. Dept. of Commerce.

14. J. A. Oberteuffer and P. J.Plasse, Bibliography of Recent Literature on Bio-Magnetic Effects (M.I.T. National Magnet Lab. 1972); M. F. Barnothy, Biological Effects of Magnetic Fields (plenum Press, New York 1964); H. Aceto, C. A. Tobias and I. L. Silver, "Some Studies on the Biological Effects of Magnetic Fiels", IEEE Trans. on Magnetics MAG-6, 368 (1970).

14a. A. M. Byalov and P. I. Shpilberg, "Effect of Magnetic Fields under Industrial Conditions on the Central Nervous System", GIG SANIT 34, 30 (1969).

14b. H. Friedman, R.O. Becker, and C. H. Backman, "Effects of Magnetic Fiels on (Human) Reaction Time Performance", Nature 213, 949 (1967).

14c. M. F. and J. M. Barnothy, Nature 225, 1146 (1970); D. E. Beischer and J. C. Knepton, NAMI-972 (1966); W. C. Levengood, Nature 209, 1009 (1966).

14d. Z. J. J. Stekly, "State of the Art Superconducting Magnets", J. Appl. Phys. 42, 65 (1971).

15. J. T. Harding, "Progress in Magnetic Suspension Applied to High Speed Ground Transportation", Seventeenth Annual Conference on Magnetism and Magnetic Materials, Chicago 1971; G. Bohn et al, "A Contribution to Electromagnetic Levitation Technology", Fourth Int. Cryogenic Eng. Conf. and Exhibition, Eindhoven, 1972.

16. S. G. Meisenholder and T. C. Wang, "Dynamic Analysis of an Electromagnetic Suspension System for the Suspended Vehicle System", U.S. Dept. of Transportation Report PB 211-592 (1972).

17. K. Oberretl, "Magnetic Fields, Eddy Currents, and Losses, Taking the Variable Permeability into Account", IEEE Trans. Power Apparatus and Systems, PAS-88, 1646 (1969).

18. E. R. Laithwaite, Induction Machines for Special Purposes (Chemical Publishing Co. Inc., New York, 1966).

19. C. H. Lee, "Study of Linear Induction Motor, Its Feasibility for High-Speed Ground Transportation", U.S. Clearing House, Report No. PB-174866.

20. K. M. Chirgwin et al., "Linear Induction Motor for High-Speed Tracked Vehicle", Fourth Intersociety Energy Conversion Engineering Conference, Washington, D.C., 1969.

21. G. P. Kalman et al., "Electric Propulsion System for Linear Induction Motor Test Vehicle", Fourth Intersociety Energy Conv. Eng. Conf., Washington, D.C. 1969.

22. B. T. Ooi and D. C. White, "Traction and Normal Forces in the Linear Induction Motor", IEEE Trans. Power Apparatus and Systems PAS-89, 638 (1970).

23. T. C. Wang, "Linear Induction Motor for High-Speed Ground Transportation", IEEE Trans. Industry and General Applications IGA-7, 632 (1971).

24. S. Yamamura, H. Ito and Y. Ishikawa, "Theories of the Linear Induction Motor and Compensated Linear Induction Motor", IEEE Trans. Power App. and Systems PAS-91, 1700 (1972).

25. M. Iwamoto, E. Ohno, T. Ito and Y. Shimyo, "End-Effect of High Speed Linear Induction Motor", Seventh Annual Meeting of the IEEE Industry Applications Society, Philadelphia 1972, p. 323.

26. J. K. Dukowicz, "Attraction/Repulsion Forces in a Single-Sided Linear Induction Motor", FRA-RT-71-78 (PB 200 685) March 1971.

27. "Development and Manufacture of a Linear Induction Motor Propulsion System for the Tracked Air Cushion Research Vehicle", AiResearch Manuf. Co. (Garrett Corporation), FRA-RT-72-35, April 1971.

28. H. J. Holley, S. A. Nasar and L. del Cid, Jr., "Computations of Fields and Forces in a Two-Sided Linear Induction Motor" (to be published).

29. Review Articles: E. R. Laithwaite and S. A. Nasar, "Linear-Motion Electrical Machines", Proc. IEEE 58, 531 (1970); M. Poloujadoff, "Linear Induction Machines I. History and Theory of Operation", IEEE Spectrum, p. 72 (Feb. 1971); II. Applications, IEEE Spectrum, p. 79 (Mar. 1971).

30. Z. J. J. Stekly and H. H. Woodson, "Rotating Machinery Utilizing Superconductors", IEEE Trans. on Aerospace 2, 826 (1964); H. H. Woodson, J. L. Smith, Jr., P. Thullen and J. L. Kirtley, "The Application of Superconductors in the Field Windings of Large Synchronous Machines", IEEE Trans. PAS-90, 620 (1971); P. Thullen, J. C. Dudley, D. L. Greene, J. L. Smith, Jr., and H. H. Woodson, "An Experimental Alternator", IEEE Trans. PAS-90, 611 (1971); "Industrial Promise of the 'Super-Motor'", New Scientist, p. 157 (Dec. 16, 1971).

31. J. R. Powell and G. T. Danby, "The Linear Synchronous Motor and High Speed Ground Transport", Sixth Intersociety Energy Conv. Eng. Conf., Boston (1971).

32. P. L. Richards and M. Tinkham, "Magnetic Suspension and Propulsion Systems for High-Speed Transportation", J. Appl. Phys. 43, 2680 (1972).

33. H. H. Kolm and R. D. Thornton, "The Magneplane: Guided Electromagnetic Flight", Applied Superconductivity Conference, Annapolis, 1972.

34. D. L. Atherton, L. E. G. Love and D.O. Prentiss, "Magnetic Levitation: Linear Synchronous Motor Efficiency", Can. J. Phys. (to be published).

35. J. R. Reitz, J. Appl. Phys. 41, 2067 (1970).

36. M. A. Beheim, R. J. Antl and J. H. Povolny, "Advanced Propulsion, Cleaner and Quieter", Astronautics and Aeronautics (August 1972); "Hamilton-Standard Q-Fan", Aviation Week and Space Tech., Oct. 16, 1972, p. 59.

37. R. A. Johnson, "Aerodynamic Drag and Stability Characteristics of a Magnetically Levitated Vehicle", AVCO Report No. AVSD-0391-72-CR, Nov. 1,1972.

38. Hermann Schlichting, Boundary Layer Theory (McGraw-Hill Book Co., New York 1968).

39. "A Comparison of Three Tracked Air Cushion Vehicle Configurations", Tracked Hovercraft, Ltd (England), prepared for U. S. Dept. of Transportation. Report FRA-RT-71-68.

40. J. Pierson and J. Helgesen, "Tracked Air Cushion Research Vehicle Aerodynamic Analysis", Grumman Corp., March 1971.

41. Bryan Thwaites, editor, Incompressible Aerodynamics (Oxford University Press, Oxford, England, 1960).

42. L. M. Milne-Thomson, Theoretical Aerodynamics (D. Van Nostrand Co., New York, 1952), 2nd ed.

43. S. F. Hoerner, Aerodynamic Drag (Publ. by Author,1951).

44. C. D. Perkins and R. E. Hage, Airplane Performance - Stability and Control (John Wiley and Sons, New York, 1957), 6th printing.

45. Dennis F. Wilkie, "Dynamics, Control and Ride Quality of a Magnetically Levitated High Speed Ground Vehicle", Transpn. Res. (1972).

46. R. R. Auelmann and H. W. Schaefgen, "Longitudinal and Lateral Dynamics of a Maglev Vehicle",unpublished Philco-Ford report (December 1972).

47. J. C. Houbolt, "Runway Roughness Studies in the Aeronautical Field", Proc. Amer. Soc. Civil Engr., J. Air Transp. Div. 89, No. AT-1 (March 1961).

48. D. A. Hullender, D. N. Wormley, and H. H. Richardson, "A Preliminary Study of Actively Controlled Air Cushion Suspensions", MIT Elec. Proj. Lab. Report EPL-70-76110-11, prepared for D.O.T. under contract C-85-65, June 15, 1972.

49. B. D. Van Deusen, "A Statistical Technique for the Dynamic Analysis of a Vehicle Traversing Rough Yielding and Non-Yielding Surfaces", NASA report CR-659, prepared by Chrysler Corp. under contract NASW-1287, April 1967.

50. "Statistical Analysis of LIMRV Reaction Rail Survey Data", Mitre Corporation working paper WP-10125, Nov. 30, 1972.

51. "Technical Extracts from Tracked Air Cushion Vehicle System Study and Analysis Report", TRW Report 06818-6008-R000, prepared for the Office of High Speed Ground Transportation, D.O.T., October 1967.

52. A. A. Butkunas, "Power Spectral Density and Ride Evaluation" S.A.E. paper 660138, presented at the Society of Automotive Engineers Congress, January 1966.

53. Richard A. Lee and Fred Pradco, "Analytical Analysis of Human Vibration", S.A.E. paper 680091, presented at the Society of Automotive Engineers Congress, January 1968.

54. L. C. Davis, J. Appl. Phys. 43, 4256 (1972).

55. M. Tinkham, J. APPL. Phys. 44 (to be published, 1973).

APPENDIX A. STUDIES OF AC LOSS

A.1. Field Geometry Calculations

In order to model properly the revenue-coil operating conditions on our sample coil system we must know the field distribution in our drive coil-sample coil system. The coil dimensions of that system are given below.

TABLE A1. Coil Dimensions

	Drive Coil	Sample Coils (7,8,9)
Length	14.0 cm	2.6 cm
ID = $2r_1$	9.5 cm	3.85 cm
OD = $2r_2$	11.9 cm	6.20 cm
No. of turns N	5790	1090
Wire Diam.	.051 cm	.042 cm

We have used a relation given by Terman* for the mutual inductance between two concentric coils to obtain the relation between the drive coil current I_d and the induced sample coil current I_s. For our system of the dimensions shown this yields $I_s = 1.94\ I_d$.

Because the relative field distributions over the wire bundles of the sample and revenue coils are quite different, we must consider that the ac and dc fields are correctly modeled only when the appropriately averaged fields are made equal rather than when the fields at the wire bundle surfaces are equal. We have performed a numerical calculation of the total field over the windings of the sample coil by summing the induced self-field due to I_s and the applied field of the drive coil.

*F. E. Terman, Radio Engineers Handbook (McGraw Hill) (1943) p. 71

As we shall see in A.2 the losses for a given ac field level are, in all regimes, expected to be proportional to the surface area of superconducting wire exposed to the field. This means that the volume averaged B fields are the ones we should be comparing between sample and revenue coils. We have carried out this averaging numerically for the sample coil field distribution, and it is easily performed in the approximation that only the self-field component matters for the revenue coil. For the sample coil the averaged B field is given by $\bar{B} = .0383\ I_d$ (Tesla). For the revenue coil the field $\bar{B}$ is that occuring at a radius $\bar{r} \approx .7\ a$ where a is the outer radius of the round wire bundle. Once we have determined, for the various control strategies, the appropriate ac field variation for the revenue coil we may then deduce the value of I_{do} at which we should examine our experimental loss data.

A.2. Loss Calculations

The ac loss calculations are performed for a slab geometry using the macroscopic Bean-London critical state model[12] which insists that in type II superconductors the current density has only the values $J = J_c, 0$ and no others. This leads to a linear decrease of the magnetic field with distance into a superconducting material and to a penetration depth $\delta = B_s/\mu_o J_c$ where B_s is the surface field. In an ac field where $B = B(t)$ then clearly $\delta = \delta(t)$ also and for part of each cycle the field does not fully penetrate the sample. There is thus a distinction in the loss behaviour for wires of radius b greater or less than $\delta(B_{max})$ for the maximum amplitude ac field.

$b > \delta_{max}$

For this case the field never fully penetrates the wire and falls to zero linearly as $B = B_s - \mu_o J_c x$ with distance x from the surface.

One first integrates $\underline{E} \cdot \underline{J}_c \, dv$ over the penetrated volume and then averages the loss over a complete cycle of the ac field. The resulting loss per cycle and per unit surface area of the slab is

$$Q/_{cycle} = \frac{2B_o^3}{3\mu_o^2 J_c} \tag{A1}$$

where B_o is the peak ac field amplitude. In order to approximate our situation we take the surface area to be that of the two sides of a square wire of the same cross-sectional area as our actual round wire and use the volume averaged field in the wire bundle. The volume averaged field is $\overline{B}_o = .038\ I_{do}$ for our sample coils. The superconducting core radius of SC 8-15 wire is $b = 1 \times 10^{-4}$ m and the equivalent square wire has side $c = 1.77 \times 10^{-4}$ m. The resultant predicted loss from (A1) is just $Q/_{cycle} = .467 \times 10^{-3} I_{do}^3$ joules.

$\underline{b < \delta_{max}}$

For this case of full field penetration of the wire each cycle carries the system from below penetration to beyond it. The analysis is essentially the same as that above and leads to the relation

$$Q/_{cycle} = 2J_c b^2 \ B_o - 4/3\ \mu_o J_c^2 b^3 \tag{A2}$$

for the loss per unit surface area. Eq. (A2) underestimates our measured loss for the experimental multicore coils by about a factor of 2 whereas Eq. (A1) gives a much better fit to the data for the #7 single core coil.

In this study it is of primary importance to estimate, using our experimental data, the ac loss to be expected from a revenue vehicle coil. We do this for each of the control strategies discussed in Section 2.7

of the main report. These strategies all call for ac levels producing very small losses in our restricted sample geometry and good data at these low levels are difficult to obtain. We therefore cite the range of values for the loss using both cubic and linear extrapolation from the data.

For the single core coil #7 we use the successful cubic fit to the data of Fig. 2.31 to deduce at 1.18 Hz the relation $\dot{Q} = 0.04 \times 10^{-3} (I_{do})^3$ watts. From the best low field data (taken at the higher frequencies) we can do a linear extrapolation according to $\dot{Q} = 10^{-3} I_{do}$ watts.

For the multi-core coils we have carried out only the linear extrapolation from our lowest values. The data at higher fields are not linear but do not fit the theory well at all. The linear extrapolation will surely err on the side of predicting somewhat higher losses and we have therefore adopted this conservative approach. The table shows the predicted loss levels for the different strategies and the two wire types.

TABLE A2. Predicted ac loss per coil in a revenue for different control strategies

	"SC8-15" Single-Core Wire	"Kryoconductor" Multi-Core Wire
Lift Coil-Direct Control	0.7 watts	8.5 watts
Separate Control Coil	.08 to .3 watts	2.5 watts
Secondary Suspension Optimized Damping	.016 to .21 watts	5.8 watts

We believe that the larger values shown in the table represents an upper limit to the ac loss to be expected for well ventilated and well supported coils at these very low ac field levels. It is probable that

the multi-core loss values are somewhat exagerated for the last two cases where full penetration of the field does not occur except near the coil bundle surface. This would bring the multi-core coil also into the cubic regime but with its much larger wire surface area it will still be expected to have larger losses at these low fields than the comparable single-core coils. The single-core coil data agrees rather well with the theoretical calculation both in magnitude and field dependence and we thus expect that the upper, linearly extrapolated limits in Table A2 are overly pessimistic.

APPENDIX B. DERIVATION OF LIM EQUATIONS

The purpose of this Appendix is to derive Eqs. (4.1), (4.2) and (4.7) concerning the performance of the linear induction motor (LIM). The computational model is shown in Fig. 4.1. A reaction rail is located midway between two identical primary windings (stators). We approximate each stator by a semi-infinite block of iron with infinite permeability and zero conductivity. The current windings are replaced by current sheets at $z = \pm h$. Whereas the stator cores extend to infinity in the x and y directions, the stator currents are confined to a finite region. The reaction rail is replaced by a thin plate (conducting sheet) of surface resistivity $1/T$ which is characterized by a velocity

$$w = 2/\mu_o \sigma T \quad . \tag{B.1}$$

In a coordinate system where the reaction rail moves to the left with velocity v, the current in the reaction rail is given by

$$i'_x = \sigma T \, E_x \tag{B.2}$$

and

$$i'_y = \sigma T \, (E_y + vB_z) \quad . \tag{B.3}$$

At $z = 0^+$ (i.e., just above the reaction rail), we find from Ampere's circuital law neglecting displacement currents that

$$B_x = \frac{\mu_o}{2} \, i'_y \tag{B.4}$$

and

$$B_y = -\frac{\mu_o}{2} \, i'_x \quad . \tag{B.5}$$

We note that B_x and B_y are odd functions of z while B_z is even.

From (B.2) and (B.3)

$$\frac{\partial i'_y}{\partial x} - \frac{\partial i'_x}{\partial y} = \sigma T \left[\text{Curl } E)_z + v \frac{\partial B_z}{\partial x} \right]_{z=0^+} . \tag{B.6}$$

Substituting (B.4) and (B.5) into (B.6) and recalling that

$$\text{curl } E)_z = - \frac{\partial B_z}{\partial t} ,$$

we find that at $z = 0^+$

$$\frac{\partial B_x}{\partial x} + \frac{\partial B_y}{\partial y} = \frac{\mu_o \sigma T}{2} \left(- \frac{\partial B_z}{\partial t} + v \frac{\partial B_z}{\partial x} \right) \tag{B.7}$$

making use of (B.1) and

$$\text{div } B = 0 , \tag{B.8}$$

gives the boundary condition at $z = 0^+$

$$w \frac{\partial B_z}{\partial z} = \frac{\partial B_z}{\partial t} - v \frac{\partial B_z}{\partial x} . \tag{B.9}$$

If we assume that all time variations are of the form $e^{i\omega t}$, then (B.9) becomes

$$w \frac{\partial B_z}{\partial z} = i\omega B_z - v \frac{\partial B_z}{\partial x} , \quad z = 0^+ . \tag{B.10}$$

In the region $0 < z < h$ we write the magnetic field in terms of its Fourier components,

$$B_\alpha = \int_{-\infty}^{\infty} dk_x \, e^{ik_x x} \int_0^{\infty} dk_y \cos k_y y \, (a_\alpha e^{-kz} + b_\alpha e^{kz}), \quad \alpha = x, z \tag{B.11}$$

and

$$B_y = \int_{-\infty}^{\infty} dk_x \, e^{ik_x x} \int_0^{\infty} dk_y \sin k_y y \, (a_y e^{-kz} + b_y e^{kz}) , \tag{B.12}$$

where

$$k = \sqrt{k_x^2 + k_y^2} \quad . \tag{B.13}$$

We assume that the motor is symmetric about the xz-plane (in addition to the symmetry about the xy-plane).

To satisfy (B.8) and

$$\text{curl } B)_z = 0 \quad ,$$

requires that

$$a_y = i\, k_y\, a_x/k_x \quad , \tag{B.14}$$

$$a_z = i\, k\, a_x/k_x \quad , \tag{B.15}$$

$$b_y = i\, k_y\, b_x/k_x \quad , \tag{B.16}$$

and

$$b_z = -i\, k\, b_x/k_x \quad . \tag{B.17}$$

To satisfy (B.10) it is required that

$$wk\,(-a_z + b_z) = i(\omega - k_x v)\,(a_z + b_z) \quad ,$$

or that

$$b_z = \Gamma\, a_z \quad , \tag{B.18}$$

where

$$\Gamma = [kw + i(\omega - k_x v)]/[kw - i(\omega - k_x v)] \quad . \tag{B.19}$$

From Eqs. (B.16), (B.17) and (B.18), we find

$$b_z = i\, k\Gamma\, a_x/k_x \quad , \tag{B.20}$$

$$b_x = -\Gamma\, a_x \quad , \tag{B.21}$$

and

$$b_y = -ik_y \Gamma a_x/k_x \quad . \tag{B.22}$$

The force on the stators is equal and opposite to that on the reaction rail. Hence, the time-averaged thrust is

$$\langle F_x \rangle = -\tfrac{1}{2}\mathrm{Re} \int_{-\infty}^{\infty} dx \int_{-\infty}^{\infty} dy\, i_y'^{*}\, B_z \tag{B.23}$$

$$= -\mathrm{Re} \int_{-\infty}^{\infty} dx \int_{0}^{\infty} dy\, \frac{2}{\mu_o}\, B_x^{*}\, B_z \tag{B.24}$$

where B_x and B_z are evaluated at $z = 0^+$. Eq. (B.24) follows from (B.23) by substitution of (B.4) and from the symmetry in the y direction. Similarly, the average power loss in the reaction rail is

$$\langle P_{rr} \rangle = \frac{1}{2\sigma T} \int_{-\infty}^{\infty} dx \int_{-\infty}^{\infty} dy\, (|i_x'|^2 + |i_y'|^2) \tag{B.25}$$

$$= \frac{4}{\mu_o^2 \sigma T} \int_{-\infty}^{\infty} dx \int_{0}^{\infty} dy\, (|B_x|^2 + |B_y|^2) \tag{B.26}$$

Substitution of Eqs. (B.11) and (B.12) into (B.24) and (B.26) gives after some manipulation

$$\langle F_x \rangle = -\frac{2\pi^2}{\mu_o} \mathrm{Re} \int_{-\infty}^{\infty} dk_x \int_{0}^{\infty} dk_y\, (a_x+b_x)^{*}\, (a_z+b_z) \tag{B.27}$$

and

$$\langle P_{rr} \rangle = \frac{4\pi^2}{\mu_o^2 \sigma T} \int_{-\infty}^{\infty} dk_x \int_{0}^{\infty} dk_y\, (|a_x+b_x|^2 + |a_y+b_y|^2) \quad . \tag{B.28}$$

Making use of Eqs. (B.1), (B.14), (B.15), and (B.18)-(B.22), we find that

$$\langle F_x \rangle = \frac{8\pi^2 w}{\mu_o} \int_{-\infty}^{\infty} dk_x \int_{0}^{\infty} dk_y\, \frac{k^2}{k_x}\, \frac{(\omega - k_x v)\, |a_x|^2}{(kw)^2 + (\omega - k_x v)^2} \tag{B.29}$$

and

$$\langle P_{rr} \rangle = \frac{8\pi^2 w}{\mu_o} \int_{-\infty}^{\infty} dk_x \int_{0}^{\infty} dk_y \frac{k^2}{k_x^2} \frac{(\omega - k_x v)^2 \, |a_x|^2}{(kw)^2 + (\omega - k_x v)^2} \quad . \tag{B.30}$$

Thus far we have not made use of the boundary condition at $z = h^-$ (i.e., just below the stator),

$$B_x = -\mu_o \, i_y(x,y) \quad , \tag{B.31}$$

where $\underline{i}(x,y)$ is the stator current (on one stator).

Inserting (B.11) into (B.31), we find after inverting the Fourier transform

$$a_x e^{-kh} + b_x e^{kh} = -\mu_o \, \tilde{i}_y \, (k_x, k_y) \tag{B.32}$$

where

$$\tilde{i}_y(k_x,k_y) = \frac{1}{\pi^2} \int_{-\infty}^{\infty} dx \, e^{-ik_x x} \int_{0}^{\infty} dy \cos k_y y \, i_y(x,y) \quad . \tag{B.33}$$

From (B.19), (B.21), (B.29), (B.30) and (B.32), we have

$$\langle F_x \rangle = 2\mu_o \pi^2 w \int_{-\infty}^{\infty} dk_x \int_{0}^{\infty} dk_y \frac{k^2}{k_x} \frac{(\omega - k_x v)}{D} \, |\tilde{i}_y(k_x,k_y)|^2 \tag{B.34}$$

and

$$\langle P_{rr} \rangle = 2\mu_o \pi^2 w \int_{-\infty}^{\infty} dk_x \int_{0}^{\infty} dk_y \frac{k^2}{k_x^2} \frac{(\omega - k_x v)^2}{D} \, |\tilde{i}_y(k_x,k_y)|^2 \, , \tag{B.35}$$

where

$$D = (kw)^2 \sinh^2 kh + (\omega - k_x v)^2 \cosh^2 kh \quad . \tag{B.36}$$

If we approximate the stator currents by a finite sinusoidal current sheet of length L and width 2a, then

$$i_y(x,y) = i_o e^{iqx} \quad , \quad 0 < x < L \ , \ |y| < a$$

$$= 0 \quad , \quad \text{otherwise} \ . \tag{B.37}$$

Continuity of current is implicit in our analysis so (B.37) implies that the appropriate line currents in the x-direction exist at $y = \pm a$, and that $qL = N_o 2\pi$ where N_o is the number of pole pairs. ($L = N_o\lambda$ where $\lambda = 2\pi/q$ is the wavelength).

From (B.33), we find for this model that

$$\tilde{i}_y(k_x,k_y) = \frac{i_o}{\pi^2} \frac{\sin k_y a}{k_y} \frac{e^{i(q-k_x)L}-1}{i(q-k_x)} \tag{B.38}$$

Substituting into (B.34) and (B.35) gives

$$\langle F_x \rangle = \frac{8\mu_o i_o^2 w}{\pi^2} \int_{-\infty}^{\infty} dk_x \int_0^{\infty} dk_y \frac{k^2}{k_x} \frac{(\omega-k_x v)}{D} \frac{\sin^2 k_y a}{k_y^2} \frac{\sin^2(q-k_x)L/2}{(q-k_x)^2} \tag{B.39}$$

and

$$\langle P_{rr} \rangle = \frac{8\mu_o i_o^2 w}{\pi 2} \int_{-\infty}^{\infty} dk_x \int_0^{\infty} dk_y \frac{k^2}{k_x^2} \frac{(\omega-k_x v)^2}{D} \frac{\sin^2 k_y a}{k_y^2} \frac{\sin^2(q-k_x)L/2}{(q-k_x)^2} \ . \tag{B.40}$$

These results correspond to the constant current-series connected LIM (Eqs. (4.1) and (4.2)).

In the limit $a,L \to \infty$ (infinite machine) it can be shown that

$$\langle F_x \rangle / 2aL \to \mu_o i_o^2 (v_\Phi - v) w / [w^2 \sinh^2 qh + (v_\Phi - v)^2 \cosh^2 qh] \ , \tag{B.41}$$

where

$$v_\Phi = \omega/q \ . \tag{B.42}$$

The peak thrust/unit area occurs at

$$v_\Phi - v = w \tanh qh \tag{B.43}$$

and is

$$\langle F_x \rangle / 2aL\Big|_{\text{peak}} = \mu_o \, i_o^2 / \sinh 2qh \quad . \tag{B.44}$$

Now, instead of specifying the stator current at z = h and using the boundary condition (B.31), let us write $\langle F_x \rangle$ and $\langle P_{rr} \rangle$ in terms of the field just below the stator surface, $B_z(x,y,h^-)$. We do this by noting that (B.29) and (B.30) could have been written in terms of a_z since

$$a_x = -ik_x \, a_z / k \quad , \tag{B.45}$$

according to (B.15). From (B.11) we have

$$a_z \, e^{-kh} + b_z \, e^{kh} = \tilde{B}_z \, (k_x, k_y) \quad , \tag{B.46}$$

where

$$\tilde{B}_z(k_x,k_y) = \frac{1}{\pi^2} \int_{-\infty}^{\infty} dx \, e^{-ik_x x} \int_0^{\infty} dy \cos k_y y \, B_z(x,y,h^-) \quad . \tag{B.47}$$

The quantity b_z can be eliminated from (B.46) by use of (B.18) so that

$$a_z = \tilde{B}_z(k_y,k_y) / (e^{-kh} + \Gamma \, e^{kh}) \quad . \tag{B.48}$$

After some manipulation, making use of (B.19), (B.29), (B.45), and (B.48), we find that

$$\langle F_x \rangle = \frac{2\pi^2 w}{\mu_o} \int_{-\infty}^{\infty} dk_x \int_0^{\infty} dk_y \, \frac{k_x(\omega - k_x v)}{D'} \, |\tilde{B}_z(k_x,k_y)|^2 \tag{B.49}$$

and

$$\langle P_{rr} \rangle = \frac{2\pi^2 w}{\mu_o} \int_{-\infty}^{\infty} dk_x \int_0^{\infty} dk_y \, \frac{(\omega - k_x v)^2}{D'} \, |\tilde{B}_z(k_x,k_y)|^2 \quad , \tag{B.50}$$

where

$$D' = (kw)^2 \cosh^2 kh + (\omega - k_x v)^2 \sinh^2 kh \quad . \tag{B.51}$$

If we approximate the field at the stator by

$$B_z(x,y,h^-) = B_o e^{iqx} \qquad 0 < x < L\,,\ |y| < a$$

$$= 0 \qquad , \qquad \text{otherwise,} \tag{B.52}$$

then

$$\langle F_x \rangle = \frac{8B_o^2 w}{\mu_o \pi^2} \int_{-\infty}^{\infty} dk_x \int_o^{\infty} dk_y \frac{k_x(\omega - k_x v)}{D'} \frac{\sin^2 k_y a}{k_y^2} \frac{\sin^2(q-k_x)L/2}{(q-k_x)^2} \tag{B.53}$$

and

$$\langle P_{rr} \rangle = \frac{8B_o^2 w}{\mu_o \pi^2} \int_{-\infty}^{\infty} dk_x \int_o^{\infty} dk_y \frac{(\omega - k_x v)^2}{D'} \frac{\sin^2 k_y a}{k_y^2} \frac{\sin^2(q-k_x)L/2}{(q-k_x)^2} \quad . \tag{B.54}$$

This corresponds to the constant voltage-parallel connected case (Eq. (4.7)).

If we let $a, L \to \infty$, then

$$\langle F_x \rangle / 2aL \to \frac{B_o^2 w}{\mu_o} \frac{(v_\Phi - v)}{w^2 \cosh^2 qh + (v_\Phi - v)^2 \sinh^2 qh} \tag{B.55}$$

The peak thrust/unit area occurs at

$$v_\Phi - v = w \coth qh \tag{B.56}$$

with a value of

$$\langle F_x \rangle / 2aL \Big|_{peak} = B_o^2 / \mu_o \sinh 2qh \quad . \tag{B.57}$$

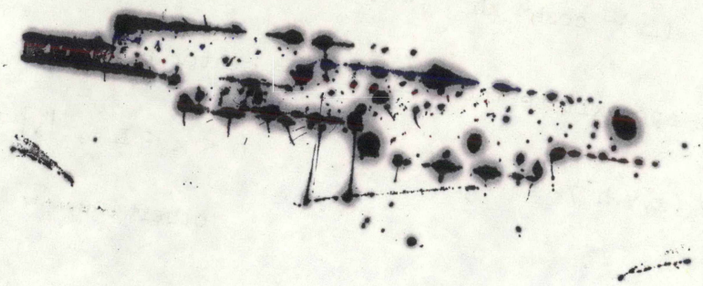

Preliminary Design Studies of Magnetic Suspensions for High Speed Ground Transportation, 1973, FRA/RT 73/27, 11-Advanced Systems